

# **EXPERIMENTAL DETERMINATION OF SOIL DAMPING**

Application to the residual soil from Porto granite

**ABÍLIO RENATO MATOS OLIVEIRA MOREIRA**

Dissertation submitted for partial completion of the requirements in the degree of  
**MASTER IN CIVIL ENGINEERING — SPECIALIZATION IN GEOTECHNICS**

---

Supervisor: Cristiana Maria da Fonseca Ferreira

JUNE, 2015

## **INTEGRATED MASTERS IN CIVIL ENGINEERING 2014/2015**

DEPARTMENT OF CIVIL ENGINEERING

Tel. +351-22-508 1901

Fax +351-22-508 1446

✉ [miec@fe.up.pt](mailto:miec@fe.up.pt)

*Edited by*

FACULDADE DE ENGENHARIA DA UNIVERSIDADE DO PORTO

Rua Dr. Roberto Frias

4200-465 PORTO

Portugal

Tel. +351-22-508 1400

Fax +351-22-508 1440

✉ [feup@fe.up.pt](mailto:feup@fe.up.pt)

🌐 <http://www.fe.up.pt>

Partial reproductions of this document are authorized as long as its Author is mentioned and the referenced as *Integrated Masters in Civil Engineering – 2014/2015 – Department of Civil Engineering, Faculdade de Engenharia da Universidade do Porto, Porto, Portugal, 2015.*

The opinions and informations included in this document represent the point of view of its Author, the Editor cannot accept any responsibility of any kind regarding eventual errors or omissions.

This document was produced from the electronic version provided by its Author.

To blood, toil, tears and sweat

*It is paradoxical, yet true, to say that the more we know the more ignorant we become in the absolute sense, for it is only through enlightenment that we become conscious of our limitations*

*Nikola Tesla*



## **ACKNOWLEDGEMENTS**

I would like to thank everyone who was involved directly or indirectly in the successful development of this dissertation, without whom it would have been impossible:

- Professor Cristiana Ferreira for all the guidance, helpful insight and knowledge passed down during the past months;
- The team of the FEUP's Geotechnics Laboratory team, specially to Daniela and Catarina for the warm welcome and advising;
- My fellow colleagues who also prepared dissertations in FEUP's Geotechnics Laboratory Lília, Joana and Sara Teixeira for both complicity and support;
- All my colleagues who were present in my academic path, specially to Francisco, Pedro Teles, Rafael, João Barbosa and João Mora, for the countless nights of good times and study company;
- My fellow geotechnics colleagues, specially Bernardo and Gabriel, for the endless nights of geotechnical modeling;
- The older colleagues I had the chance to meet thanks to academic tradition, specially Vânia and André;
- My hometown friends who still accompany me, Edite, Vítor, Duarte, Pinto, João and Carlos;
- My family for the unconditional love and support, specially to my mother;
- Sara Pinto, for always being present whether needed or not.



## **ABSTRACT**

Soil damping evaluation is an important tool in geotechnical engineering projects. Given that various different sources can generate seismic waves that affect engineering structures, its impact can be decisive in design considerations and implementation of different solutions.

Bender elements have been successfully used in the last years to determine soil damping in triaxial cells. This equipment is relatively easy to implement, its tests are fast and do not need additional heavy/specific equipment in order to obtain test results. As such, the use of bender elements is a competitive method to obtain soil damping, in addition to other dynamic soil properties. However, no methodologies exist for bench testing with bender elements.

The present dissertation studies the possibility of soil damping determination by bench tests using bender elements. All tests were conducted in LabGeo, the Geotechnical Laboratory of the Faculty of Engineering of the University of Porto. A residual soil sample, from Porto granite, was tested for this effect. This soil is characterized by standard laboratory procedures and compared with typical values for residual soil from Porto granite. Afterwards, the bender element testing began using a conventional setup for seismic wave data acquisition. For data acquisition and treatment, an UCL developed software, ABETS, was implemented. This software was successfully used in the past by Ferreira (2003; 2009) in researching dynamic soil properties.

In order to evaluate the possibility of new software to calculate soil damping based on bender element test results, several original scripts were written using Matlab, based on methodologies used by some authors: logarithmic decay method, half-power bandwidth method and circle-fit method (Ewins, 1984; Brocanelli and Rinaldi, 1998; Karl, 2003, 2005). It was concluded that Matlab could be a more reliable and flexible tool than ABETS to calculate soil damping.

Previous damping results were provided by Ferreira (2009). These results were obtained using the standardized resonant column test, which is a reliable method to determine soil damping. The data from Ferreira's tests was treated by the aforementioned Matlab scripts, and its results compared with the resonant column tests.

The comparison between the tested methodologies, as well as resonant column tests, enabled to make some considerations on the accuracy, applicability and conformity of these methodologies. Unfortunately, the circle-fit decay method could not be implemented due to limitations associated with the available equipment.

The logarithmic decay method provided overall poor results, given that it is very sensitive to the shape and quality of the wave received by the bender element. As such, its results were eventually discarded. The half-power bandwidth method was found to be the preferable method to obtain damping ratio using bender elements, but its results were discrepant from the resonant column tests. A study was made in order to identify the reason for the difference in test results, but it was inconclusive. Further studies that can possibly justify this difference are exposed, based on other authors' findings.

**KEYWORDS:** DAMPING, SEISMIC WAVES, RESIDUAL SOIL, BENDER ELEMENTS, RESONANT COLUMN TEST.





## **RESUMO**

A avaliação do amortecimento de solos é uma ferramenta importante em projetos de engenharia geotécnica. Dado que várias fontes diferentes podem gerar ondas sísmicas que afectem estruturas de engenharia, o seu impacto pode ser decisivo nas considerações tomadas no dimensionamento, bem como na implementação de soluções construtivas.

Os bender elements têm sido utilizados com sucesso nos últimos anos na determinação do amortecimento de solo em câmaras triaxiais. Este equipamento é relativamente fácil de implementar, os seus ensaios são rápidos e não necessitam de equipamentos adicionais pesados/específicos para obter resultados. Como tal, o uso de bender elements é um método competitivo na obtenção do amortecimento de solos, para além de outras propriedades dinâmicas dos solos. Contudo, não existem metodologias para ensaios de bancada com recurso a bender elements.

A presente dissertação estuda a possibilidade da determinação do amortecimento de solo por ensaios de bancada com bender elements. Todos os ensaios foram realizados no LabGeo, o Laboratório de Geotecnia da Faculdade de Engenharia da Universidade do Porto. Uma amostra de solo residual, do granito do Porto, foi testada para este efeito. Este solo foi caracterizado por procedimentos laboratoriais normalizados e comparado com valores típicos para o solo residual do granito do Porto. Depois, os testes com bender elements começaram utilizando um setup convencional para aquisição de dados por ensaios de ondas sísmicas. Para aquisição e tratamento de dados, um software desenvolvido pela UCL, ABETS, foi implementado. Este software foi utilizado no passado por Ferreira (2003; 2009) na pesquisa de propriedades dinâmicas de solos.

Com a finalidade de avaliar a possibilidade de novos softwares para calcular o amortecimento de solos através de ensaios de bender elements, vários scripts originais foram escritos em Matlab, com base em metodologias utilizadas por alguns autores: método de decaimento logarítmico, método de largura de banda de meia potência e método de ajustamento a círculo (Ewins, 1984; Brocanelli and Rinaldi, 1998; Karl, 2003, 2005). Concluiu-se que o Matlab pode ser uma ferramenta mais confiável e flexível do que o ABETS para calcular o amortecimento de solos.

Resultados de amortecimento anteriores foram fornecidos por Ferreira (2009). Estes resultados foram obtidos através do ensaio, normalizado, de coluna ressonante, que é um método confiável para a determinação de amortecimento de solos. Os dados destes testes foram tratados pelos scripts de Matlab supracitados, e os seus resultados comparados com os do ensaio de coluna ressonante.

A comparação entre as metodologias testadas, bem como com o ensaio de coluna ressonante, possibilitaram algumas considerações sobre a precisão, aplicabilidade e conformidade destas metodologias. Infelizmente, o método de ajustamento a círculo não pode ser implementado devido a limitações associadas ao equipamento disponível.

O método de decaimento logarítmico forneceu resultados fracos, uma vez que este método é muito sensível à forma e qualidade da onda recebida pelo bender element. Como tal, os seus resultados foram eventualmente descartados. O método de largura de banda de meia potência foi o método preferido para a obtenção do amortecimento com recurso a bender elements, mas os seus resultados foram discrepantes dos obtidos pela coluna ressonante. Um estudo foi feito para identificar a razão para a diferença nos resultados, mas foi inconclusivo. Assim, são apresentadas algumas propostas de desenvolvimentos futuros que possam justificar esta diferença, baseadas em trabalhos anteriores.

**PALAVRAS-CHAVE:** AMORTECIMENTO, ONDAS SÍSMICAS, SOLO RESIDUAL, BENDER ELEMENTS, ENSAIO DE COLUNA RESSONANTE.



## GENERAL INDEX

<b>ACKNOWLEDGEMENTS</b> .....	i
<b>ABSTRACT</b> .....	iii
<b>RESUMO</b> .....	v
<b>1. INTRODUCTION</b> .....	1
1.1. MOTIVATION .....	1
1.2. OBJECTIVES .....	2
1.3. OUTLINE OF THE DISSERTATION.....	2
<b>2. STATE-OF-THE-ART</b> .....	3
2.1. INTRODUCTION .....	3
2.2. WAVE THEORY: BRIEF EXPLANATION ON WAVES .....	3
2.3. DYNAMIC SOIL PROPERTIES .....	5
2.3.1. SHEAR MODULUS AND DAMPING COEFFICIENT .....	5
2.3.2. BULK MODULUS AND CONSTRAINT MODULUS .....	7
2.4. SEISMIC WAVES .....	7
2.4.1. SEISMIC WAVES IN SOILS .....	10
2.4.1.1. Particle contact behavior .....	11
2.4.1.2. Water effect in soils .....	14
2.4.1.3. Relative scales and dispersion .....	20
2.5. DAMPING: DEFINITION AND OVERVIEW .....	22
2.5.1. DAMPING MECHANISMS .....	23
2.5.2. VISCOUS DAMPING .....	24
2.5.2.1. KELVIN-VOIGT MODEL .....	24
2.5.2.2. MAXWELL MODEL .....	26
2.5.2.3. STANDARD LINEAR SOLID MODEL .....	27
2.5.3. HYSTERETIC DAMPING .....	28
2.5.4. FRICTION DAMPING .....	30
2.6. EXPERIMENTAL DETERMINATION OF SHEAR MODULUS AND DAMPING RATIO .....	30
2.6.1. IN SITU TESTS .....	33
2.6.1.1. BOREHOLE METHODS: CROSSHOLE AND DOWNHOLE .....	34

2.6.1.2. SEISMIC CONE PENETROMETER TEST (SCPT).....	35
2.6.1.3. SPECTRAL ANALYSIS OF SURFACE WAVES (SASW).....	35
2.6.2. LABORATORY TESTS .....	37
2.6.2.1. BENDER ELEMENT TESTING .....	37
2.6.2.2. RESONANT COLUMN TEST .....	41
2.6.2.3. CYCLIC TRIAXIAL TEST.....	42
2.6.2.4. CYCLIC SIMPLE SHEAR TEST.....	43
2.6.2.5. TORSIONAL SHEAR TEST.....	43
2.6.3. SPECIFIC ISSUES REGARDING BENDER ELEMENT TESTING .....	44
<b>3. EXPERIMENTAL PROGRAM.....</b>	<b>47</b>
<b>3.1. INTRODUCTION.....</b>	<b>47</b>
<b>3.2. PROGRAM OVERVIEW.....</b>	<b>47</b>
<b>3.3. SOIL SAMPLE PREPARATION FOR BENDER ELEMENT TESTING.....</b>	<b>48</b>
<b>3.4. RESIDUAL SOIL FROM PORTO GRANITE .....</b>	<b>50</b>
<b>3.5. TESTED SOIL IDENTIFICATION AND CHARACTERIZATION .....</b>	<b>51</b>
<b>3.6. EXPERIMENTAL PROCEDURE.....</b>	<b>55</b>
3.6.1. LABORATORY EQUIPMENT.....	55
3.6.2. TEST SETUP .....	55
<b>3.7. DAMPING DETERMINATION .....</b>	<b>56</b>
3.7.1. LOGARITHMIC DECREMENT METHOD .....	58
3.7.2. HALF-POWER BANDWIDTH METHOD .....	59
3.7.3. CIRCLE-FIT METHOD .....	60
<b>4. EXPERIMENTAL RESULTS AND ANALYSIS.....</b>	<b>63</b>
<b>4.1. INTRODUCTION.....</b>	<b>63</b>
<b>4.2. TIME DOMAIN ANALYSIS USING TEKTRONIX TDS220 .....</b>	<b>63</b>
<b>4.3. FREQUENCY DOMAIN ANALYSIS USING PICO ADC-212 .....</b>	<b>67</b>
4.3.1. "CALIBRATION" SAMPLE P2 (150MM) .....	67
4.3.1.1. MATLAB SCRIPT HYPOTHESES .....	71
4.3.1.2. COMPARISON BETWEEN MATLAB AND ABETS RESULTS .....	74
4.3.1.3. CONSIDERATION ON THE COMPLETED WORK SO FAR .....	75

4.3.1.4. FURTHER SCRIPT DEVELOPMENTS: HALF-POWER BANDWIDTH AND CIRCLE-FIT METHODS .....	75
4.3.2. SCRIPT CAPABILITIES AND LIMITATIONS .....	79
4.3.3. FURTHER SAMPLE TESTING .....	81
4.3.4. RESULT ANALYSIS .....	83
<b>4.4. COMPARISON WITH RESONANT COLUMN TEST RESULTS.....</b>	<b>84</b>
4.4.1. SOIL 04 .....	85
4.4.2. SOIL 02 .....	86
4.4.3. SOIL 05 .....	88
4.4.4. RESULT ANALYSIS .....	88
<b>4.5. ADDITIONAL TEST SAMPLES .....</b>	<b>91</b>
4.5.1. SAMPLE P4 (100MM) .....	91
4.5.2. SAMPLE P5 (50MM) .....	92
4.5.3. SAMPLE P6 (50MM) .....	93
4.5.4. SAMPLE P7 (50MM) .....	94
4.5.5. RESULT ANALYSIS .....	95
<b>5. CONCLUDING REMARKS.....</b>	<b>97</b>
<b>5.1. INTRODUCTION.....</b>	<b>97</b>
<b>5.2. SUMMARY .....</b>	<b>97</b>
<b>5.3. FURTHER DEVELOPMENTS.....</b>	<b>97</b>
5.3.1. DATA ACQUISITION .....	97
5.3.2. BENDER ELEMENT INSTALLATION.....	98
5.3.3. SIGNAL PROCESSING .....	98
5.3.4. CONTINUATION OF THIS THESIS WORK.....	98
<b>REFERENCES .....</b>	<b>103</b>



**FIGURE INDEX**

Figure 2.1 – Elastic spring and undamped model (adapted from Crowel, 2002) ..... 3

Figure 2.2 –Typical representation of a sine wave ..... 4

Figure 2.3 – Hysteretic loop, shear modulus and damping (Park, 1998) ..... 6

Figure 2.4 – Schematic representation of P-waves and S-waves ..... 8

Figure 2.5 – Rayleigh’s wave particle motion ..... 9

Figure 2.6 – Schematic representation of Rayleigh and Love waves .....10

Figure 2.7 – Hertzian contact .....11

Figure 2.8 – Hertz’s theory nonlinear soil response .....12

Figure 2.9 – Mindlin’s non elastic contact behavior (adapted from Santamarina et al, 2001) .....13

Figure 2.10 – Mindlin’s hysteresis loop (adapted from Santamarina et al, 2001) .....13

Figure 2.11 – Contact meniscii according to Palmer and Traviolia model (Santamarina et al, 2001) ...14

Figure 2.12 – Threshold strain for menisci failure: experimental data and analytical prediction (Cho and Santamarina, 2001) .....15

Figure 2.13 – Stages of unsaturated conditions and their related phenomena (Santamarina et al, 2001).....16

Figure 2.14 – Degree of saturation versus frequency (Murphy, 1982).....17

Figure 2.15 – Shear wave velocity versus degree of saturation (Cho and Santamarina, 2001) .....18

Figure 2.16 – General equations from Biot’s theory (adapted from Santamarina et al, 2001) .....19

Figure 2.17 – Chain of springs and masses (adapted from Santamarina et al, 2001).....20

Figure 2.18 – Adjacent grains in opposite phase (adapted from Santamarina et al, 2001).....22

Figure 2.19 – Dependence of velocity on spatial scale (Santamarina et al, 2001).....22

Figure 2.20 – Damping in a SDOF system .....23

Figure 2.21 – Kelvin-Voigt model.....24

Figure 2.22 – Comparison of different damping conditions .....25

Figure 2.23 – Maxwell model.....26

Figure 2.24 – Standard linear solid model .....27

Figure 2.25 – Schematic presentation for definition of hysteretic damping ratio and secant shear modulus (adapted from Park, 1998) .....28

Figure 2.26 – Shear strain versus shear modulus (adapted from Ferreira, 2003).....30

Figure 2.27 – Expected shear strains in soils under different loading conditions (Park, 1998) .....31

Figure 2.28 – Overview of possible shear strain amplitudes (Studer and Koller, 1997) .....32

Figure 2.29 – Field tests for obtaining shear modulus and damping ratio (adapted from Campanella, 1994).....33

Figure 2.30 – Borehole methods: a) crosshole method; b) downhole method.....34

Figure 2.31 – Seismic cone penetrometer test (adapted from Stokoe and Santamarina, 2000) .....	35
Figure 2.32 – Spectral analysis of surface waves (Park, 1998) .....	36
Figure 2.33 – Surface wave method (Lopes et al, 2004) .....	36
Figure 2.34 – Bender element constitution (Dyvik and Madshus, 1985) .....	38
Figure 2.35 – Bender element functioning (adapted from Ferreira, 2003) .....	38
Figure 2.36 – Series connected a) and parallel connected b) bender elements (adapted from Dyvik and Madshus, 1985) .....	39
Figure 2.37 – Input wave suggestions (Ferreira, 2009) .....	39
Figure 2.38 – Bender element frequency domain analysis: a) input and output signals; b) coherence; c) wrapped phase angle; d) unwrapped phase angle .....	40
Figure 2.39 – Various setups for the resonant column test (adapted from Barros, 1996) .....	41
Figure 2.40 – Lissajous figures in an oscilloscope (adapted from Ferreira, 2009) .....	41
Figure 2.41 – Schematic representation of the cyclic triaxial test (adapted from Barros, 1996) .....	42
Figure 2.42 – Comparison of low amplitude shear moduli determined by cyclic triaxial and resonant column test (adapted from Ladd et al, 1989) .....	42
Figure 2.43 – Schematic representation of the cyclic simple shear test (adapted from Barros, 1996) .	43
Figure 2.44 – Schematic representation of the torsional shear test (adapted from Barros, 1996) .....	44
Figure 3.1 – CEFEUP-Borehole S2 (after first sawing) .....	48
Figure 3.2 – Testing samples: P1, P2 and P3 .....	49
Figure 3.3 – Detailed view of the sampling liner crack .....	49
Figure 3.4 – Sawed surfaces: surface irregularity (left) and presence of finer mass (right) .....	50
Figure 3.5 – Test setup: schematic representation (left); close up photograph .....	51
Figure 4.1 – Grain size distribution curve for granitic residual soils from northwestern Portugal (adapted from Viana da Fonseca et al, 2006) .....	54
Figure 4.2 – Disturbed sample and its reconstitution .....	55
Figure 4.3 – Heating of soil sample with sodium hexametaphosphate (left), mixing of heated sample with a particle mixer (right) .....	55
Figure 4.4 – Beaker used for specific gravity determination (left), detail on deposited particles after 24h (right) .....	56
Figure 4.5 – Pycnometers prepared for heating .....	56
Figure 4.6 – Grain size distribution curve of the soil under study .....	57
Figure 4.7 – Grain size distribution curve of the soil under study (red) fit to Viana da Fonseca et al (2006) fuse .....	57
Figure 4.8 – Fourier transform: time domain data (red) into frequency domain data (blue) (Barbosa, 2013) .....	58
Figure 4.9 – Explanation on the use of the FFT for test data .....	58



Figure 4.10 – Generic frequency spectrum plot (Inmann, 2001) .....59

Figure 4.11 – Resonant curve for half-power bandwidth method (Richart et al, 1970) .....60

Figure 4.12 – Nyquist plot for determination of material damping (Karl, 2005) .....62

Figure 4.13 – Bender element fixation and testing .....63

Figure 4.14 – Time domain analysis for sample P1 (100mm): output wave for 1kHz, 2kHz, 4kHz and 10kHz .....63

Figure 4.15 – Signals with poor logarithmic decay envelope due to: a) similar successive peaks, b) misshapen peaks and c) irregular peaks .....64

Figure 4.16 – Sample P2 (150mm), sweep 1: ABETS input and output amplitude versus time .....67

Figure 4.17 - Sample P2 (150mm), sweep 1: ABETS coherence versus frequency .....68

Figure 4.18 – Sample P2 (150mm), sweep 1: ABETS wrapped phase angle versus frequency .....68

Figure 4.19 – Sample P2 (150mm), sweep 1: ABETS unwrapped phase angle versus frequency .....68

Figure 4.20 – Presence of noise in the first wave of sweep 1 .....70

Figure 4.21 – Matlab’s Signal Analysis Application (Matlab incorporated data for example) .....70

Figure 4.22 – Signal averaging for the first sweep .....71

Figure 4.23 – Sample P2 (150mm): missing data from the second (left) and third sweeps (right) .....72

Figure 4.24 – Comparison between Matlab (left) and ABETS (right) results: coherence .....73

Figure 4.25 – Comparison between Matlab (left) and ABETS (right) results: phase .....73

Figure 4.26 – Comparison between Matlab (left) and ABETS (right) results: unwrapped phase .....73

Figure 4.27 – Comparison between Matlab (left) and ABETS (right) results: frequency spectrum .....74

Figure 4.28 – Sample P2 (150mm), sweep1: detailed view on amplitude truncation .....75

Figure 4.29 – Sample P2 (150mm): frequency spectrum .....76

Figure 4.30 – Close up on sample P2 (150mm) resonant peak .....77

Figure 4.31 – Sample P2 (150mm): Nyquist plot of the resonant frequency (red) and surrounding data points .....78

Figure 4.32 – Example of f1 miscalculation: automated use of data (red), supposed use of data (green) .....79

Figure 4.33 – Difficulty of data acquisition using PicoScope .....80

Figure 4.34 – New bender element test methodology .....81

Figure 4.35 – Sample P1 (100mm): frequency spectrum .....81

Figure 4.36 – Sample P3 (50mm): frequency spectrum .....82

Figure 4.37 – Obtained damping results versus sample height .....83

Figure 4.38 - Half-power bandwidth method and resonant column test results .....88

Figure 4.39 – Half-power bandwidth method and resonant column test results versus effective isotropic stress .....88

Figure 4.40 – Half-power bandwidth method and resonant column test results versus strain .....	89
Figure 4.41 – Half-power bandwidth method and resonant column test results versus shear modulus	89
Figure 4.42 – Sample P4 (100mm): frequency spectrum.....	90
Figure 4.43 – Sample P5 (50mm): frequency spectrum .....	91
Figure 4.44 – Sample P6 (50mm): frequency spectrum .....	92
Figure 4.45 – Sample P7 (50mm): frequency spectrum .....	93
Figure 4.46 – Half-power bandwidth values versus sample height.....	94
Figure 5.1 – Negatives used for bender element installation.....	98

## TABLE INDEX

Table 2.1 – Symbology, nomenclature and relations used in wave analysis.....	4
Table 2.2 – Shear modulus and damping ratio: parametric analysis (Hardin and Drnevich, 1972) .....	6
Table 2.3 – Laboratory tests and relative qualities in parameter measurement (adapted from Park, 1998).....	37
Table 3.1 – Test sample geometry.....	48
Table 3.2 – Laboratory equipment used in the experimental procedure .....	50
Table 4.1 – Natural physical parameters for residual soil from Porto granite (Viana da Fonseca et al, 2003).....	53
Table 4.2 – Time domain test characteristics.....	63
Table 4.3 – Signal quality terminology .....	64
Table 4.4 – Sample P2 (150m) test results for the logarithmic decay method.....	64
Table 4.5 – Summary of damping values for the logarithmic decay method .....	65
Table 4.6 – Sample P2 (150mm) sweep wave definition.....	66
Table 4.7 – Sample P2 (150mm): half-power bandwidth method results.....	75
Table 4.8 – Used sweep wave characteristics .....	80
Table 4.9 – Sample P1 (100m): half-power bandwidth method results.....	81
Table 4.10 – Sample P3 (50mm): half-power bandwidth method results.....	81
Table 4.11 – Comparison between half-power bandwidth and logarithmic decay method results.....	81
Table 4.12 – Tested soil samples provided by Ferreira (2009) .....	82
Table 4.13 – Soil 04: sweep wave test information.....	83
Table 4.14 – Soil 04: resonant column test results .....	83
Table 4.15 – Sample 04: summary of results with logarithmic decay method .....	83
Table 4.16 – Soil 04: comparison between damping values based on different methods .....	84
Table 4.17 – Soil 02: sweep wave test information.....	84
Table 4.18 – Soil 02: resonant column test results .....	85
Table 4.19 – Sample 02: summary of results with logarithmic decay method .....	85
Table 4.20 – Soil 02: comparison between damping values based on different methods .....	85
Table 4.21 – Soil 05: sweep wave test information.....	86
Table 4.22 – Summary on HPBM and RC damping ratios for Ferreira (2009) test results .....	86
Table 4.23 – Sample P4 (100mm): results for the half-power bandwidth method.....	89
Table 4.24 – Sample P5 (50mm): results for the half-power bandwidth method .....	90
Table 4.25 – Sample P6 (50mm): results for the half-power bandwidth method .....	91
Table 4.26 – Sample P7 (50mm): results for the half-power bandwidth method .....	92

Table 4.27 – Comparison between current research test results ..... 93

## **SYMBOLS AND ABBREVIATIONS**

ABETS – Automatic Bender Element Testing System

ASTM – American Society for Testing and Materials

BE – Bender Element

CEFEUP – FEUP's experimental camp

CFM – Circle-Fit Method

CPT – Cone Penetrometer Test

DFT – Discrete Fourier Transform

DLL – Dynamic Link Library

FEUP – Faculty of Engineering of the University of Porto

FFT – Fast Fourier Transform

HPBM – Half-Power Bandwidth Method

LabGeo – FEUP's Geotechnical Laboratory

OCR – Over Consolidation Ratio

PC – Personal Computer

PVC – Polyvinyl Chloride

RC – Resonant Column

SASW – Spectral Analysis of Surface Waves

SCPT – Seismic Cone Penetrometer Test

SDOF – Single Degree Of Freedom

SWM – Surface Wave Method

UCL – University College London

A – Amplitude

B – Bulk modulus

c – Viscous dashpot coefficient; damping ratio

$c_c$  – Critical damping coefficient

D – Damping; diameter

d – Distance;

E – Young's modulus; energy; exponent

e – Void ratio; Euler's number; exponent

F – Force

f – Frequency

- $f_s$  – Sampling frequency  
 $f_n$  – Natural frequency  
 $f_c$  – Biot's critical frequency  
 $G$  – Shear modulus  
 $G_0, G_{max}$  – Initial/maximum shear modulus  
 $G_g$  – Particle shear modulus  
 $g$  – Gravitational acceleration  
 $h$  – Height  
 $\text{Im}(X)$  – Imaginary part (of  $X$ )  
 $i$  – Imaginary constant  
 $J$  – Bessel function  
 $K$  – Volumetric deformability; wave number  
 $k$  – Stiffness  
 $k_{eq}$  – Equivalent stiffness  
 $l$  – Length  
 $l_b$  – Bender element length  
 $M$  – Constraint modulus  
 $\text{Mag}$  – Magnitude  
 $m$  – Mass  
 $N$  – Normal force; axial force  
 $N$  – Porosity  
 $Q$  – Quality factor  
 $p$  – Isotropic tension  
 $p'$  – Effective isotropic tension  
 $R_d$  – Ratio between distance and wavelength  
 $\text{Re}(X)$  – Real part (of  $X$ )  
 $r$  – Radius; distance from source, integration constant  
 $r_c$  – Hertzian contact radius  
 $S$  – Degree of saturation  
 $T$  – Tangential force, visco-dynamic operator  
 $t$  – Time  
 $u$  – Fluid pressure  
 $V$  – Velocity

$V_P$  – P-wave velocity

$V_S$  – S-wave velocity

$V_R$  – Rayleigh wave velocity

$V_g$  – Group velocity

$V_{ph}$  – Phase velocity

$x$  – Position

$\alpha$  – Angle; factor depending on spherical arrangement and elastic parameters; tortuosity factor

$\Gamma$  – Complex equation component

$\gamma$  – Shear strain

$\Delta$  - Variation

$\delta$  – Increment; decrement; logarithmic decrement; displacement

$\delta^*$  - Displacement at yield

$\delta_{tan}$  - Tangential displacement

$\varepsilon$  – Strain

$\lambda$  – Wavelength

$\nu$  - Poisson's coefficient

$\nu_g$  – Particle Poisson's coefficient

$\xi$  – Damping

$\pi$  – Pi number

$\rho$  – Medium density; mass density

$\rho_f$  – Mass density of the fluid phase

$\sigma$  – Normal tension; contact stress

$\tau$  - Tangential tension

$\omega$  – Angular frequency

$\omega_d$  – Damped angular frequency

$\omega_n$  – Natural angular frequency









# 1

## INTRODUCTION

### 1.1. MOTIVATION

Civil engineering works are subjected to various loading types. When accounting for specific geotechnical problems, Hardin and Black (1968) divided these into two groups, based on the loading and response of the soil. On the one hand, there is the group that involves large stress-strain relationships generated by a single application of loading and unloading. On the other hand, problems involving small amplitudes and repeated loading and unloading of soils for a certain number of cycles.

Seismic wave effects fall into this last group. The nomenclature for “seismic” waves suggests that this kind of waves is only caused by seismic activity, which is incorrect. Seismic waves are generated through seismic activity, in addition to equipment vibrations, road traffic, explosions and construction operations, to name a few.

The propagation medium of this type of waves is the material of the structure or, when it comes to geotechnical engineering, soil and rock. Contrary to current structural elements that are made of materials whose homogeneity control is somewhat guaranteed by their fabric processes, soil and rock materials do not have any kind of control and are therefore associated with higher levels of uncertainty and heterogeneity.

As such, the parameters of the medium and its characterization in geotechnical engineering is a difficult barrier to overcome, especially in the first stages of the geotechnical project. The number of tests used to obtain certain soil parameters is low, and these are based on empirical and semi-empirical models that are unable to consider all the aspects that influence the behavior of the medium. Not only for simplicity and ease, but also for uncertainty regarding the interaction of the parameters.

Note that certain characteristics, indispensable for geotechnical projects, can be obtained or estimated based on seismic wave propagation tests. Therefore, the study of this type of waves and associated tests is of high relevance.

With this in mind, the attenuation of vibrations, i.e., damping, is also of high relevance in order to evaluate its impact on engineering structures. These waves do not even need to have high amplitude in order to ruin structural elements, for their resonance can be enough to bring structures to failure (Tacoma Narrows Bridge, 1940). Therefore, the study and evaluation of seismic wave damping has become an important tool in geotechnical engineering projects, namely in high-speed railways. As such, the development of new and improved methods to obtain, study and characterize soil damping is of great importance in geotechnical engineering.

## **1.2. OBJECTIVES**

The main objective of the present dissertation is the determination of soil damping of the residual soil from Porto granite, using bench testing with bender elements.

In order to do so, various methodologies of damping determination are tested and evaluated. This evaluation is made by result comparison from various tested methods, in addition to previous results from Ferreira (2009) by a standardized laboratory test.

Additionally, the writing of a program that implements the aforementioned methods for damping determination is approached, based on bender element testing applied to bench tests.

This research will also complement other author's works in the characterization of the residual soil from Porto granite.

## **1.3. OUTLINE OF THE DISSERTATION**

This dissertation is divided in five chapters. The present chapter identifies the motivation that originated the title of the dissertation, as well as its objectives and sequence.

Chapter 2 features the scientific background underlying the theories and their application necessary for the research of this dissertation. It begins with an explanation on wave theory applied to ideal media, covering the associated basic concepts, in order to progress into the specific issues regarding soil particulate, multiphase and inelastic media. Damping is also approached, with description on some models that allow its quantification. This chapter ends with an overview on various in situ and laboratory tests, with special relevance on the use of bender element tests and the resonant column test.

Chapter 3 the experimental program is presented. An analysis on its planning is established, along with the preparation of the soil samples. The various test equipment are described, along with the used test set up for bender element testing.

Chapter 4 regards the obtained experimental results based on the presented experimental plan, along with several considerations. It begins with a comparison between the tested soil sample and usual residual soil from Porto granite samples. Also, it explains three different testing methods for obtaining damping ratio, which are the ones used in the experimental program. The original test results are then compared with resonant column test results, in order to verify their accuracy.

Chapter 5 synthesizes the conclusions made throughout chapter 4, based on the obtained test results. In addition, it contains additional statements on further developments, which can originate further researches on the approached subjects.

# 2

## STATE-OF-THE-ART

### 2.1. INTRODUCTION

This chapter begins with a preliminary approach to the propagation of seismic waves in a medium, followed by a brief reference to relevant dynamic soil properties. Once the definition of basic concepts is complete, the following subchapters explain the soil particularities as a medium and how it differs from other media.

Afterwards, an overview of damping is made based on mechanisms and models established by several authors, followed by an analysis on the experimental determination of damping for both field and laboratory tests, according to the tests available for this effect. Emphasis is made on the resonant column and bender element tests, given that the author's experimental results using bender elements are compared with results from the resonant column test.

### 2.2. WAVE THEORY: BRIEF EXPLANATION ON WAVES

Consider a perfectly elastic spring fixed on one end and with a mass on the other. If a force is applied to this mass, in the direction of the spring, the spring will compress and extend, oscillating the mass. In addition, if there are no losses in the system, it will keep oscillating indefinitely with amplitude of motion proportional to the initial strain caused by the applied force.

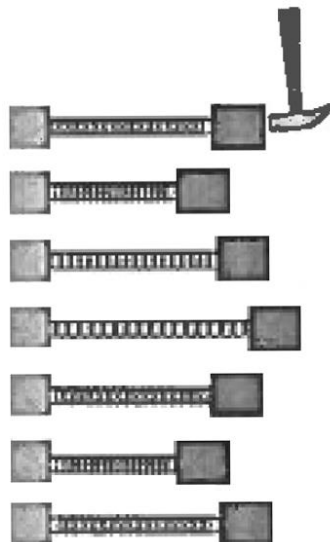


Figure 2.1 – Elastic spring and undamped model (adapted from Crowel, 2002)

If this system’s motion was measured in a position-time graph, it would have a perfect sinusoidal shape, as shown in Figure 2.2.

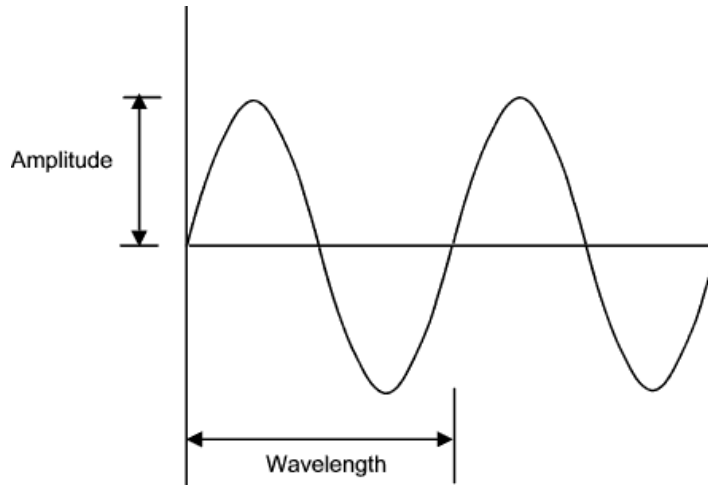


Figure 2.2 –Typical representation of a sine wave

Therefore, a periodic load in an infinite, perfectly elastic medium can be diminished to a sinusoidal load similar to the one in the previous figure. That is, it can be simplified to a seismic wave. This is the base knowledge that backs the theory of waves whose comprehension is necessary to understand damping in soils, which is the object of this dissertation.

Table 2.1 describes current sinusoidal wave analysis’ parameters symbology, nomenclatures and relations with one another. These terms will be present throughout the dissertation, so their early definition is made here.

Table 2.1 – Symbology, nomenclature and relations used in wave analysis

Symbology	Nomenclature	Relations	
A	Amplitude		
$\lambda$	Wavelength		
T	Period		
f	Frequency	$\frac{1}{T}$	
$\omega$	Angular frequency	$\frac{2\pi}{T}$	$2\pi f$
K	Wave number / Angular wave number	$\frac{1}{\lambda}$	$\frac{2\pi}{\lambda}$
$V_{ph}$	Phase velocity	$\frac{\lambda}{T}$	$\frac{\omega}{K}$
$V_g$	Group velocity		$\frac{d\omega}{dK}$

Consider the same spring and mass system as before. If the mass is hit with a force with another direction, the system will have a complex motion, unlike the previous simple oscillation. Note that a

vibrating system will pick out its resonant frequencies from a complex excitation and vibrate at frequencies close to those, removing other frequencies present in that excitation, which can be particularly useful in the elimination of background noise during tests (Nave, 2014).

### 2.3. DYNAMIC SOIL PROPERTIES

Dynamic properties are properties that, unlike static properties, are altered by inertia effects, i.e., change with strain rate. Such properties are fundamental for application in more advanced geotechnical models, and the phenomena that influence these properties are more complex. A realistic prediction of soil behavior and consequent structural displacements is only possible with sophisticated laboratory tests with high quality samples or with carefully executed in situ tests (Ferreira, 2003).

The most difficult part of a design evaluation is obtaining representative, solid values for critical soil properties, whose difficulty increases because of the strong dependence on many different parameters. Hardin and Drnevich (1972) stated that dynamic soil properties may vary by a factor of 10 in a soil deposit.

In the next subchapters follows an overview of some of the soil's dynamic properties, in order of importance to the present dissertation, as an introduction and explanation for the next chapter, regarding the actual propagation of seismic waves in soils.

#### 2.3.1. SHEAR MODULUS AND DAMPING RATIO

Shear modulus,  $G$ , is a reference parameter for these cases. Its characterization has a determinant influence in the definition of design values in geotechnical projects. It can be defined as the shear stress  $\tau$  required to cause unitary shear strain,  $\gamma$ .

$$G = \frac{\tau}{\gamma} \quad (1)$$

or, in terms of Young's modulus and Poisson's ratio,

$$G = \frac{E}{2(1+\nu)} \quad (2)$$

When a soil sample is loaded repeatedly, by propagation of a seismic wave, it experiences irreversible deformation and following loadings are different from the previous ones (Park, 1998). If a certain cycle of loading is repeated for several cycles, the stress-strain relationship becomes a closed, hysteretic loop. This loop can be defined by two parameters: the slope of the line that connects the loop's end points and the area enclosed by the loop. The slope of the line defines the shear modulus and the enclosed loop area has a relationship with damping, which will be further addressed in 2.5.3..

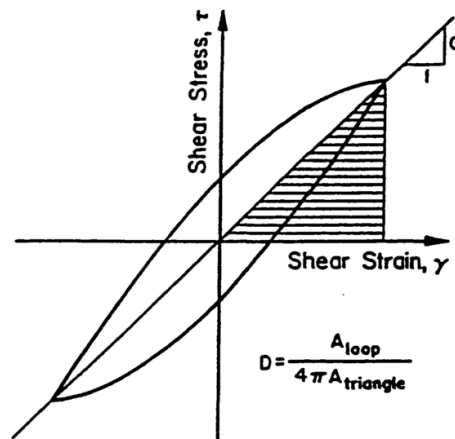


Figure 2.3 – Hysteretic loop, shear modulus and damping (Park, 1998)

The maximum shear modulus or initial shear modulus,  $G_{max}$  or  $G_0$ , is an important parameter for various geotechnical design considerations, associated with low (initial) shear strain levels of about  $10^{-5}$  and below. It can also be used as indirect indication of various soil parameters (Dyvik and Madshus, 1985).

The following table presents Hardin and Drnevich’s (1972) data from measurements of shear modulus and damping ratio for cleans sands and cohesive soils and represents how different soil properties, such as void ratio, saturation and over consolidation ratio (OCR), affect these two parameters.

Table 2.2 – Shear modulus and damping ratio: parametric analysis (Hardin and Drnevich, 1972)

Parameter	Importance to			
	Shear modulus		Damping ratio	
	Clean sand	Cohesive soil	Clean sand	Cohesive soil
Shear strain amplitude	V	V	V	V
Effective mean principal stress	V	V	V	V
Void ratio	V	V	V	V
Number of cycles of loading	R <sup>a</sup>	R	V	V
Degree of Saturation	R	V	L	V
OCR	R	L	R	L
Effective strength envelope	L	L	L	L
Octahedral shear stress	L	L	L	L
Frequency of loading (>0,1Hz)	R	R	R	L
Grain characteristics, size, shape gradation, mineralogy	R	R	R	R
Soil structure	R	R	R	R
Volume change due to shear strain (<0,5%)	U	R	U	R

V=very important; L=less important; R=relatively unimportant except as it may affect another parameter; U=relative importance is not clearly known

<sup>a</sup>=except for saturated clean sand, where it is a less important parameter



According to this data, shear strain amplitude, effective mean principal stress and void ratio are the most relevant parameters affecting shear modulus and damping ratio. OCR is somewhat important in cohesive soils and grain characteristics are unimportant, except for its effects on the other listed parameters.

### 2.3.2. BULK MODULUS AND CONSTRAINT MODULUS

While not as relevant as the previous two parameters, bulk modulus and constraint modulus have an impact on some phenomena relevant for describing soil behavior and, as such, are briefly explained.

Bulk modulus,  $B$ , is the ratio of change in an object's applied tension and the fractional volume compression. In other words, it describes the tendency of an object to deform three-dimensionally when loaded uniformly in all directions. As such, it can be written in terms of Poisson's ratio,  $\nu$ , and Young modulus,  $E$

$$B = \frac{E}{3(1-2\nu)} \quad (3)$$

Even though the compression of solids and liquids is relatively small when compared with gases, the bulk modulus has effects and implications detailed further ahead, especially regarding the effect of saturation in soils, addressed later in this chapter.

The constraint modulus,  $M$ , can be seen as Young's modulus accounted for the effects of the Poisson ratio, which translates in the following equation

$$M = \frac{E(1-\nu)}{(1+\nu)(1-2\nu)} \quad (4)$$

Or, in terms of  $B$  and  $G$ ,

$$M = B + \frac{4}{3}G \quad (5)$$

Note that for usual values of Poisson's ratio  $M$  and  $E$  are quite similar. Furthermore, when  $\nu = 0$ ,  $M = E$ .

Similar to bulk modulus, constraint modulus is briefly explained for better understanding of relevant phenomena in this dissertation, also addressed later in this chapter.

## 2.4. SEISMIC WAVES

A seismic wave is an acoustic wave that is able to travel through a medium, as a result of equipment vibration, road traffic, explosions or construction operations. Seismic waves can be broken down to simpler waves with distinct behaviors, velocity and modes of propagation, which helps their study and analysis.

Considering an infinite, isotropic, linear elastic continuum, two types of body waves are possible. The primary waves, also known as dilatation waves, pressure waves or simply as P-waves, have longitudinal propagation without rotation. As such, the motion of a particle in a medium affected by them is parallel to the direction of propagation. P-waves are able to travel through both solids and fluids, and are filtered in vacuum (Santamarina *et al*, 2001). These waves have the highest velocity and, therefore, are the first to be recorded.

The secondary waves, also known as shear waves, distortion waves or simply as S-waves, have pure distortional propagation and no volume variation. The particle motion is perpendicular to the direction of propagation. These waves require a medium with shear stiffness to propagate and, as such, are filtered in fluids. These waves have lower velocity than P-waves, hence their “secondary” nature. Note that differences in the propagation of P-waves and S-waves can be advantageously used to study particulate media (Santamarina *et al*, 2001).

Figure 2.4 shows a propagation schematic for both P-waves and S-waves.

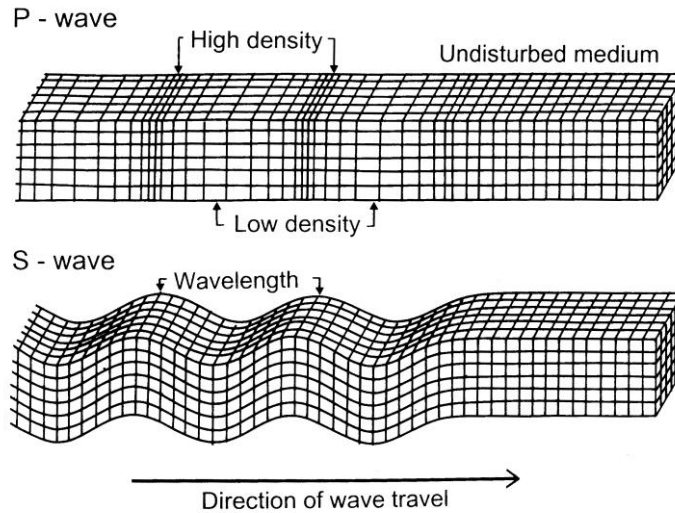


Figure 2.4 – Schematic representation of P-waves and S-waves

The velocity of P-waves and S-waves,  $V_P$  and  $V_S$  respectively, are connected to the medium’s characteristics. The following expressions are deduced from the general equations of movement, according to the theory of elasticity, and are the ones commonly used to characterize the propagating medium.

$$V_P = \sqrt{\frac{E}{\rho} \times \frac{1-\nu}{(1+\nu)(1-2\nu)}} = \sqrt{\frac{M}{\rho}} \quad (6)$$

$$V_S = \sqrt{\frac{E}{2\rho} \times \frac{1}{(1+\nu)}} = \sqrt{\frac{G}{\rho}} \quad (7)$$

where  $E$  is the Young's modulus,  $\rho$  the mass density,  $\nu$  the Poisson's ratio,  $M$  the constraint modulus and  $G$  the shear modulus.

Therefore, the determination of these wave velocities allows the evaluation of the medium's elastic parameters (Ferreira, 2003). It is possible to calculate both  $G$  and  $M$  from  $V_S$  and  $V_P$ , assuming that  $\rho$  is known. In addition, if both wave velocities are known,  $\nu$  can be calculated by combination of the last two equations

$$\nu = \frac{\left(\frac{V_P}{V_S}\right)^2 - 2}{2\left(\frac{V_P}{V_S}\right)^2 - 2} \quad (8)$$

The presence of boundaries or interfaces between different media affects the mode of propagation of waves near them. These new modes of propagation create new kinds of waves, such as Rayleigh waves and Love waves.

A Rayleigh wave is a surface wave that occurs in an elastic, limited medium (elastic half-space) near its borders' proximity. These waves describe a retrograde elliptic motion in the perpendicular plane to the wave propagation (Ferreira, 2003). The horizontal motion diminishes with depth faster than the vertical motion and has zero horizontal displacement at a depth of  $0.2\lambda$ , for a Poisson's ratio of  $\nu \approx 0.2\lambda$ . Therefore, while the particle motion at the surface is a retrograde ellipse, it changes into a prograde ellipse at that depth (Santamarina *et al*, 2001).

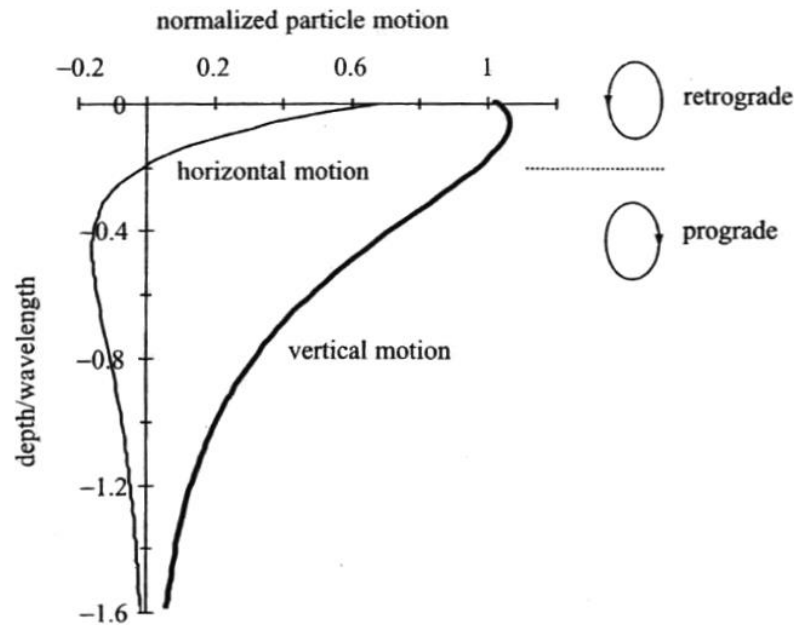


Figure 2.5 – Rayleigh's wave particle motion (Santamarina *et al*, 2001)

The velocity of Rayleigh waves,  $V_R$ , can be related to the velocities of P- and S-waves (Achenbach, 1975) by

$$\left(2 - \left(\frac{V_R}{V_S}\right)^2\right)^2 - 4\left(1 - \left(\frac{V_R}{V_P}\right)^2\right)^{1/2} \times \left(1 - \left(\frac{V_R}{V_S}\right)^2\right)^{1/2} = 0 \quad (9)$$

Love waves are horizontal waves and a result of the interference of S-waves, nearing the end of an elastic half-space, with perpendicular direction to the wave motion. Love waves are slower than P-waves and S-waves, but faster than Rayleigh waves.

Figure 2.6 illustrates the propagation of Rayleigh and Love waves.

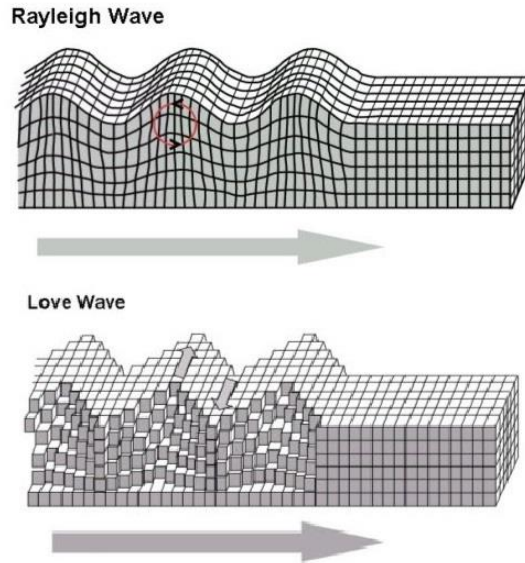


Figure 2.6 – Schematic representation of Rayleigh and Love waves

Contrary to the primary, volumetric waves that propagate along a spherical front, Rayleigh and Love surface waves propagate radially along a spherical front (Ferreira, 2003). The amplitude of volumetric waves decays in a  $1/r$  proportion, where  $r$  is the distance from the wave source, while superficial waves decay with a  $1/\sqrt{r}$  proportion.

More wave types exist, with different boundary conditions. For instance, Stoneley waves exist at the solid-solid interface, such as during borehole vertical seismic profiling (Stoneley, 1924). Additionally, Scholte waves occur at a solid-fluid interface, such as the bottom of the ocean (Scholte, 1947). Since their study is not relevant for the present dissertation, these waves are only mentioned.

#### 2.4.1. SEISMIC WAVES IN SOILS

So far, only the propagation of seismic waves in linear elastic, isotropic, homogenous and infinite (or semi-infinite, for Rayleigh and Love waves in half-spaces) mediums were discussed. This subchapter contains the specific aspects of soil particulate, multiphase medium and their effects on seismic wave propagation.

The large strain deformation behavior in soil is determined by fabric changes and rearrangement, while the small strain deformation behavior results from the deformation of particles. Since the area of particle contact is very small and the corresponding stresses are high, particle deformation takes place primarily at contacts (Santamarina *et al*, 2001). The study and modeling of these contacts motivated various authors to formulate different contact behavior theories.

### 2.4.1.1 Particle contact behavior

In order to better understand and characterize particle contact behavior, several authors postulated different contact behaviors, such as: normal force (Hertz, 1881), tangential force (Cattaneo, 1938; Mindlin, 1949), viscoplastic grain material (Lee and Radok, 1960), skeletal force and local van de Waals attraction force (Johnson *et al*, 1971), skeletal force and local capillary force, skeletal force and cementation and electrical force interactions. The first two models are enough proof of the nonlinear, inelastic behavior of soils and, as such, are the only ones discussed in this dissertation.

Hertz (1881) considered two spheres in contact made of a linear elastic material, whose initial contact area before loading is infinitesimal. When a small normal force  $N$  is applied, a large deformation is needed to mobilize the contact stress generated by that force. Successive increments of  $\Delta N$  encounter incrementally larger contact areas, which produce smaller incremental deformations.

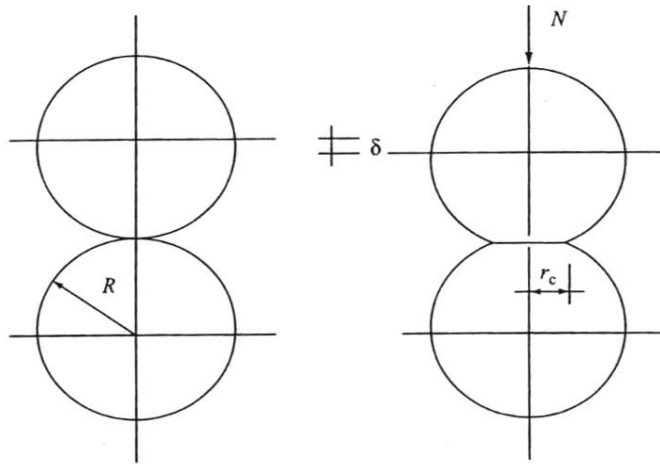


Figure 2.7 – Hertzian contact (adapted from Santamarina *et al*, 2001)

Therefore, large deformations take place at small contacts, while smaller deformations occur at higher contact forces. According to the following expression, the distribution of contact stress is parabolic.

$$\sigma_c(r') = \frac{3N}{2\pi r_c^2} \sqrt{1 - (r'/r_c)^2} \quad (10)$$

$$N = \int \sigma_c \, dA \quad (11)$$

where  $\sigma_c$  is the contact stress,  $r'$  the distance from the center of the contact,  $r_c$  the radius of the contact,  $N$  the normal force and  $A$  the contact area.

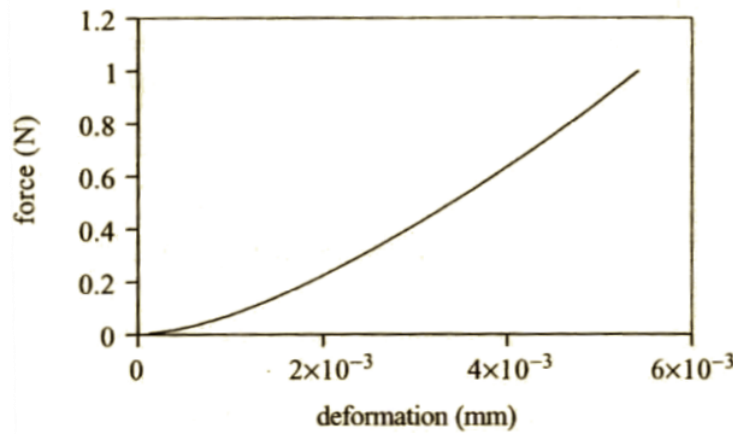


Figure 2.8 – Hertz's theory nonlinear soil response (Santamarina *et al*, 2001)

Therefore, the load-deformation response of a soil is nonlinear. This is highlighted by Biarez's (1962) work. Biarez assimilated Hertz's spherical medium to an elastic continuum. Based on Hertz's relations, the volumetric deformability,  $K$ , in order to the elastic parameters and isotropic applied tension is

$$K = \frac{3}{2}(1 - 2\nu)\alpha^{\frac{2}{3}}p^{\frac{1}{3}} \quad (12)$$

Where  $\alpha$  is a factor that depends on the sphere arrangement and elastic parameters, such as  $E$  and  $\nu$ , and  $p$  is the applied isotropic tension.

Equation (12) clearly shows that the volumetric deformability varies with tension, by a  $1/3$  exponent.

The Mindlin contact, also known as tangential force behavior, considers two spherical particles subjected to a normal contact force,  $N$ . Once the normal load is acting, a tangential force  $T$  is applied (note that the load history is accounted for in this contact, since it is not the same to load  $N$  followed by  $T$  or the reverse order). The applied tangential force is resisted by mobilized shear stress  $\tau$  at the contact, which tends to infinity at the contact edges. If a limiting interparticle friction coefficient,  $\mu$ , is considered, the maximum shear stress is given by

$$\tau_f = \sigma \times \mu \quad (13)$$

Slippage occurs at the contact edges where  $\tau > \tau_f$  and, afterwards, the distribution of contact stress in the central region, i.e., the non-slip region must change to maintain equilibrium in the contact direction. Note that the ring of slippage along the contact periphery causes energy losses. Further developments on energy losses, regarding hysteresis loops similar to Figure 2.10 will be addressed with more detail in chapter 2.4.

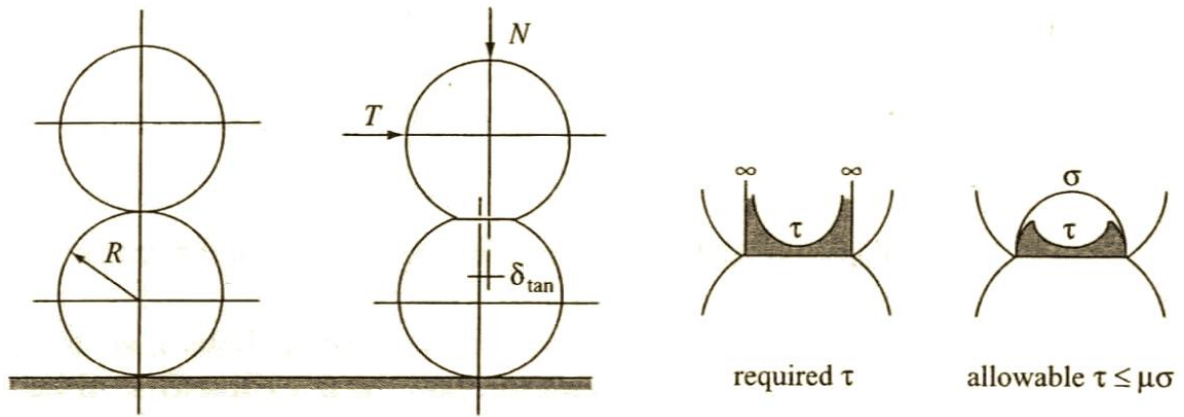


Figure 2.9 – Mindlin's non elastic contact behavior (adapted from Santamarina *et al*, 2001)

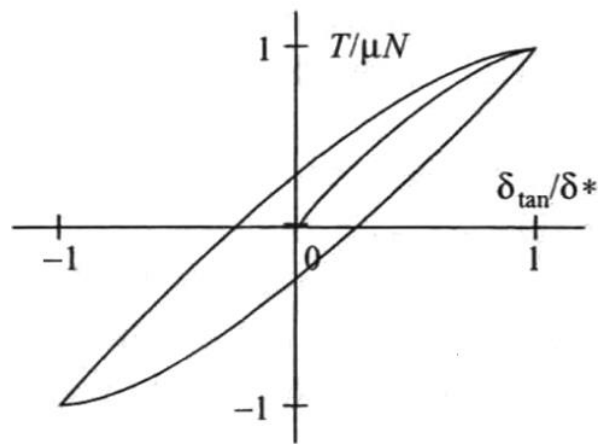


Figure 2.10 – Mindlin's hysteresis loop (adapted from Santamarina *et al*, 2001)

$\delta_{tan}$  is the tangential displacement and  $\delta^*$  is the displacement at yield. The displacement at yield is related to the tangential force, according several authors (Richart, *et al*, 1970; Dobry *et al*, 1982; Deresiewicz, 1973), by

$$\delta_{tan} = \left( 1 - \left( 1 - \frac{T}{\mu N} \right)^{2/3} \right) \delta^* \quad (14)$$

$$\delta^* = \frac{3}{8} (2 - \nu_g) \frac{\mu N}{G_g r_c} \quad (15)$$

where  $\nu_g$  and  $G_g$  are the Poisson's ratio and shear modulus of the particles, respectively. This non-elastic behavior due to slippage makes soil load-deformation behavior load-history dependent (Mindlin and Deresiewicz, 1953).

### 2.4.1.2. Water effect in soils

The multiphase nature of soils also has an impact in its load-deformation behavior and, therefore, also affects the propagation of waves in its medium. The coexistence of solid and fluid phases adds extra complexity and phenomena such as seepage, time-dependent pressure diffusion and effective skeletal stress.

For unsaturated soils, the menisci capillary forces are added to skeletal contact forces, increasing the stiffness of contacts and, in consequence, the skeleton itself. Palmer and Traviolia (1980) postulated that the relative movement of water menisci causes viscous damping.

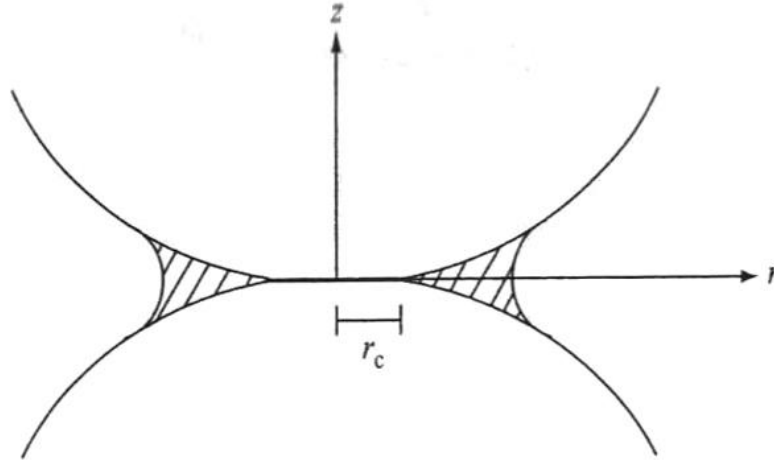


Figure 2.11 – Contact menisci according to Palmer and Traviolia model (Santamarina *et al*, 2001)

$$\frac{1}{Q} \approx \frac{75.5\eta\omega}{\sigma} \ln\left(\frac{r_c}{20\Delta r_c}\right) \quad (16)$$

Note that the relation  $1/Q$  is related to the amount of energy loss per a certain amount of cycles, and  $\eta$  is the fluid viscosity,  $\omega$  the angular frequency and  $\sigma$  the applied pressure,  $r_c$  the radius of the Hertzian contact and  $\Delta r_c$  the change in the radius contact caused by mechanical perturbation. So,  $1/Q$  is proportional to the fluid viscosity and angular frequency, independent of grain size and independent of saturation.

The compression of the gaseous phase in the fluid produces adiabatic heating of the gas (White, 1975; Kjartansson and Delinger, 1977), and the gas bubble motions themselves can dissipate energy. This mechanism, particularly relevant in the study of ocean bottom soils, explains the increase in damping with saturation. In addition, capillary forces enhance losses in P-wave propagation and decrease losses in S-wave propagation.

In addition, when the water content is less than 7%, menisci failure and regeneration can justify significant energy dissipation (Santamarina *et al*, 2001). Cho and Santamarina (2001) evaluated menisci failure, using glass beads. The analytical prediction is stated in equation (17), and Figure 2.12 show the similarity of the experimental data with that analytical prediction.

$$\varepsilon_a = \frac{\delta}{2R} \approx 0.53(\text{Se})^{1/3} = 0.53(G_s w)^{1/3} \quad (17)$$



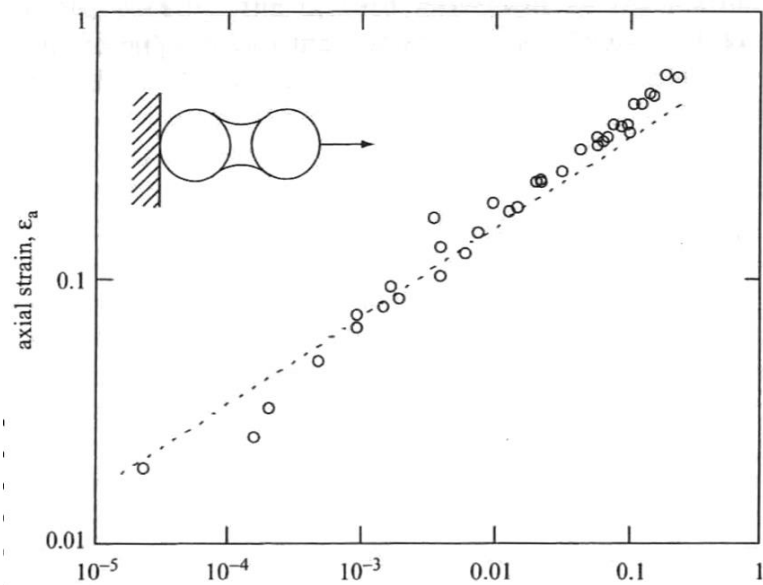


Figure 2.12 – Threshold strain for menisci failure: experimental data and analytical prediction (Cho and Santamarina, 2001)

However, these authors found that the threshold strain for menisci failure requires a very large strain level, larger than the threshold strain for contact loss in coarse grained soils.

Different degrees of saturation also impact differently the soil behavior. Cho and Santamarina (2001) also studied the effect of saturation for both shear modulus and shear wave velocity. Figure 2.13 describes the various stages of unsaturated soils and their relevant phenomena, and its explanation follows in the next paragraphs.

Consider a saturated soil sample, gradually drying over time. At the first stages of drying, the change in pore water pressure has an important global effect on the soil mass (Santamarina *et al*, 2001). When the air starts to break into the pore structure, its applied pressure is called the air entry value (or bubbling pressure, or threshold pressure (Aubertin *et al*, 1998)). This value depends on the pore size (finer particles have higher values of air entry). This phenomenon occurs at high degrees of saturation, between 90% and 100%.

Once the air starts to invade the sample, it becomes unsaturated. However, at this stage the water still forms a continuous phase, called the funicular stage. As drying continues to occur, the pore suction pressure increases, almost linearly with decreasing saturation. Note that eventual local changes in water pressure are rapidly homogenized by diffusion within the still continuous water phase.

When water becomes disconnected, the pendular stage is achieved. Water menisci forms around particle contacts with very small radiuses that cause a significant increase in suction pressure. Given that this is a contact level effect, due to the discontinuous water phase, an eventual change in suction is felt by other menisci through a corresponding change in pore vapor pressure. This is a slow homogenization process.

Finally, as the soil dries completely, fine material migrates to contacts, forming a kind of buttress that increases the stiffness of the skeleton. Eventually, salts dissolved in water start to crystalize, further increasing the stiffness of the skeleton. According to Rinaldi *et al* (1998) these phenomenon produces equivalent effects to those of cementation.

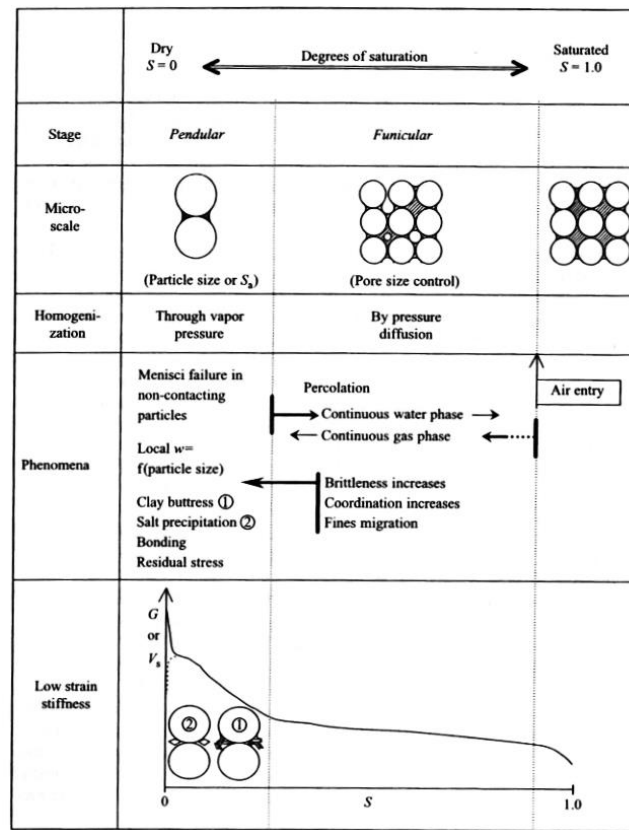


Figure 2.13 – Stages of unsaturated conditions and their related phenomena (Santamarina *et al*, 2001)

As stated earlier, the existence of both water and air content in soils adds extra complexity to their behavior. The velocity of both compression and shear waves in particle-fluid mixtures depend on bulk modulus, shear modulus and mass density of the mixture. Note that at low frequencies both fluid and solid actually move together.

The fluid phase, often consisting of water and air, presents a bulk modulus,  $B_f$  based on the change in the mixture's fluid pressure and its corresponding change in volume

$$B_f = \frac{\Delta u}{\varepsilon_v} = \frac{\Delta u}{\frac{\Delta V_w + \Delta V_a}{V_f}} \quad (18)$$

Rewriting the previous equation in terms of strains and degree of saturation, given by the relation  $S = V_w/V_f$ ,

$$B_f = \frac{1}{\frac{S}{B_w} + \frac{1-S}{B_a}} \quad (19)$$

For fluid filled particulate media, a change in confinement stress is distributed between the skeleton,  $\Delta\sigma'_0$ , and the fluid. The bulk modulus of the soil is given by

$$B_{soil} = \frac{\Delta\sigma'_0}{\varepsilon_v} + \frac{\Delta u}{\varepsilon_v} = B_{sk} + \frac{\Delta u}{\varepsilon_v} \quad (20)$$

Note that stress changes produce different effects: an increase in  $\Delta u$  decreases the volume of both grains and fluid, while an increase in  $\Delta\sigma'_0$  decreases the volume of grains. In addition, at low confinement due to effective stress are limited to contacts and can be disregarded (Santamarina *et al*, 2001). The pore fluid pressure becomes, when accounting for porosity,

$$\Delta u = -B_f \left[ \frac{1}{n} (1 + \varepsilon_v) - \frac{1-n}{n} \left( 1 + \frac{\Delta u}{B_g} \right) - 1 \right] \quad (21)$$

Substituting the previous equation in equation (20), the result is

$$B_{soil} = B_{sk} + \frac{1}{\frac{n}{B_f} + \frac{1-n}{B_g}} = B_{sk} + B_f \quad (22)$$

In a saturated soil, the P-wave velocity is primarily controlled by the bulk modulus of the fluid. Still, it is also affected by porosity and the bulk modulus of the grains' constituting material. Note that for soils with low degrees of saturation, the bulk modulus of the fluid approaches zero, which makes the P-wave velocity reflect the stiffness of the skeleton (and added capillary forces) by  $V_P = \sqrt{M_{sk}/\rho}$ .

Figure 2.14 shows the effects of the degree of saturation on attenuation, after Murphy's (1982) findings. The increase in attenuation with saturation can be explained by local flow, movement of droplets and compression of the gaseous phase (Santamarina *et al*, 2001).

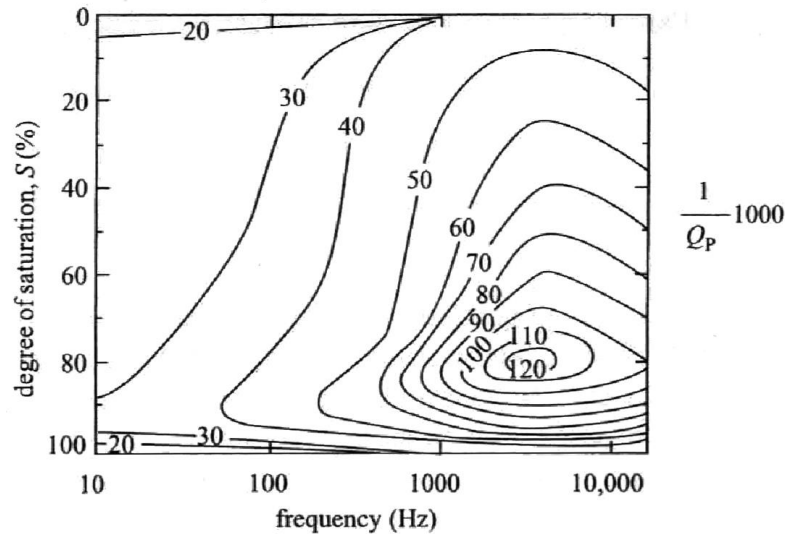


Figure 2.14 – Degree of saturation versus frequency (Murphy, 1982)

Even though S-waves do not propagate in fluids, its velocity is determined by the stiffness of the granular skeleton and the mass density of the soil, both affected by the degree of saturation. As stated before, even at constant effective confinement the soil skeleton stiffness increases with decreasing saturation due to contact level capillary forces, and eventually reaches its peak at dry conditions due to salt precipitation at contacts. Figure 2.15 shows the effect of degree of saturation on S-wave velocity for several soils.

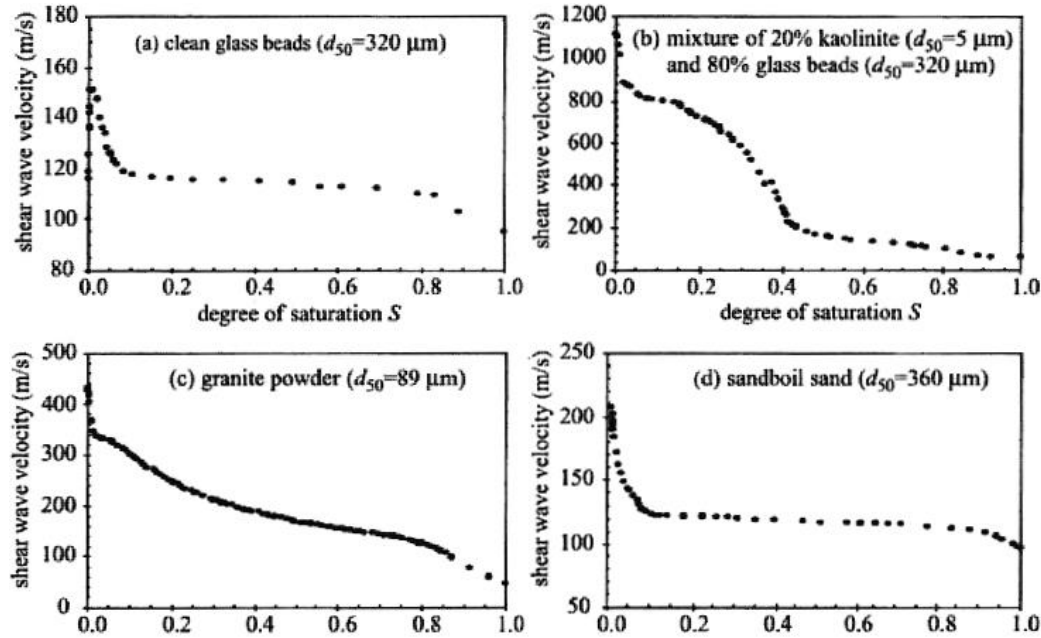


Figure 2.15 – Shear wave velocity versus degree of saturation (Cho and Santamarina, 2001)

Note that with increasing frequency differential inertial phenomenon causes relative displacement of the fluid phase with the skeleton. In this case, equation (22) loses validity. Biot (1956a, 1956b) postulated a general theory on dynamic poroelasticity based on the following assumptions, which manage to overcome the limitations of the equation:

- The medium is macroscopically homogenous and isotropic;
- All pores are interconnected and of uniform size;
- The wavelength is greater than the medium's particles,  $\lambda \gg d$ ;
- The mentioned relative motions satisfy Darcy's law;
- No chemical or electrical interactions exist between phases;
- Thermal effects can be disregarded.

The spectral response predicted by this theory is explained by a set of general equations exposed in the following figure.

<p style="text-align: center;"><i>Solve for P-wave velocity, <math>V_P</math></i></p> $\begin{vmatrix} \frac{H}{V_P^2} - \rho_{\text{mix}} & \rho_f - \frac{C}{V_P^2} \\ \frac{C}{V_P^2} - \rho_f & q - \frac{M}{V_P^2} \end{vmatrix} = 0$ <p style="text-align: center;"><i>Parameters</i></p> $H = B_{\text{sk}} + \frac{4}{3}G_{\text{sk}} + \frac{(B_g - B_{\text{sk}})^2}{D - B_{\text{sk}}}$ $M = \frac{B_g^2}{D - B_{\text{sk}}}$ $q = \frac{\alpha \rho_f}{n} - j \frac{\eta F}{\omega K}$ $\zeta = \sqrt{\frac{\omega a^2 \rho_f}{\eta}}$	<p style="text-align: center;"><i>Solve for S-wave Velocity, <math>V_S</math></i></p> $\begin{vmatrix} \rho_{\text{mix}} - \frac{G_{\text{sk}}}{V_S^2} & \rho_f \\ \rho_f & q \end{vmatrix} = 0$ $C = \frac{B_g - B_{\text{sk}}}{D - B_{\text{sk}}} B_g$ $D = B_g \left[ 1 + n \left( \frac{B_g}{B_f} - 1 \right) \right]$ $F = \frac{\zeta T}{4(1 + 2jT/\zeta)}$ $T = e^{j\zeta r} \cdot \frac{J_1(\zeta e^{-j\pi/4})}{J_0(\zeta e^{-j\pi/4})}$
--	--

 Figure 2.16 – General equations from Biot's theory (adapted from Santamarina *et al*, 2001)

$a$  is a pore size parameter,  $K$  the absolute hydraulic conductivity,  $\alpha$  a tortuosity factor,  $r$  an integration constant,  $\zeta$  a dimensionless factor,  $T$  a visco-dynamic operator and  $J_0$  and  $J_1$  are Bessel functions. The roots of the above equations predict a fast, standard P-wave, a S-wave and a slow, diffusional P-wave where fluid and skeleton actually move in opposite directions.

Biot's equations also involve a characteristic frequency, defined by

$$f_c = \frac{n \eta}{2\pi \rho_f K} \quad (23)$$

If Biot's theory is simplified for soils, some modifications and assumptions can be made. The equation for the characteristic frequency can be simplified to

$$f_c = \frac{n g}{2\pi k_h} \quad (24)$$

Consider a clayey soil with  $k_h = 10^{-9}$  m/s and a sandy soil with  $k_h = 10^{-4}$  m/s. For  $V_S = 200$  m/s, the critical frequencies and associated wavelengths are approximately  $10^9$  Hz –  $0.2 \mu\text{m}$  and  $10^4$  Hz –  $20$  mm, respectively. As such:

- The critical frequency approaches the used test frequencies in highly permeable soils. As permeability decreases with increasing fine materials, the characteristic frequency increases and the dispersion effects predicted by Biot lose relevance;
- When  $f$  tends to  $f_c$ , the wavelength for S-waves approaches the scale of the particle size. Therefore, S-wave propagation at high frequencies ( $f \gg f_c$ ) is more affected by grain scattering effects than by Biot's dispersion.

In addition, the ratio  $B_{sk} / B_g$  is  $< 10^{-2}$  for near-surface soils. In this range, this relation has the following effects on each propagation mode:

- The spectrum of the fast P-wave is virtually unaffected;
- The magnitude of  $V_S$  depends directly on  $B_{sk}$  throughout the spectrum;
- The maximum value of the slow P-wave occurs at high frequencies and depends on  $B_{sk}$ , while the low frequency limit for this wave is (still) zero.

The practical impact of Biot's theory is limited in most near-surface engineering applications and laboratory testing. At low frequencies  $V_P$  is governed by  $B_{fluid}$  and  $V_S$  by the skeleton stiffness. By the time the high frequency response applied ( $f \gg f_c$ ), the wavelength is on the order of magnitude of the internal scale of the material, and scattering gains relevance. As such, internal heterogeneities (layers, conglomerates) are more critical to velocity dispersion and attenuation than Biot related effects.

#### 2.4.1.3. Relative scales and dispersion

The seismic wave frequencies have two different effects regarding wave propagation in particulate media, both related to the associated with relative scales. The first one is related to the relative spatial scales (wavelength and grain size, layer thickness or conglomerate size, to name a few) and the second to the relative temporal scales (ratio between period and pore fluid dissipation, for example) (Santamarina *et al*, 2001). Only the relative spatial scales, more relevant to the objectives of the present dissertation, are addressed in this chapter.

Consider a chain of monosized masses separated by a certain distance,  $a$ , connected by springs, as represented in Figure 2.17. The distance between grains represents the spatial scale of the chain system, the masses represent grains (or layers/conglomerates) and the springs represent the stiffness between the grains.



Figure 2.17 – Chain of springs and masses (adapted from Santamarina *et al*, 2001)

Assuming an elastic behavior for the springs, according to Hooke's law, the equation of motion for a single grain is given by

$$m \frac{d^2 u_n}{dt^2} + k(u_n - u_{n-1}) + k(u_n - u_{n+1}) = 0 \quad (25)$$

where  $u$  is the motion of a certain grain. For  $N$  masses on the chain, it is possible to write  $N$  equations, plus boundary conditions. Assuming a particle motion, where the location  $x$  of a grain  $p$  is  $x = pa$  and  $K$  is the wave number, its equation is given by

$$u = Ae^{i(Kx-\omega t)} \quad (26)$$

and invoking the mathematical relations implied by Euler's identity, equation (26) becomes

$$-\omega^2 m + 2k - 2k \cos(Ka) = 0 \quad (27)$$

and, therefore,

$$\omega = 2\sqrt{\frac{k}{m}} \sin\left(\frac{Ka}{2}\right) \quad (28)$$

The relation  $\sqrt{k/m}$  is the resonant (or natural) frequency of vibration of a body with mass  $m$  connected to a spring with stiffness  $k$ . The resonant frequency is the frequency at which a body tends to resonate, i.e., to vibrate with greater amplitudes when this frequency is applied. Its effects on soil tests are properly addressed later in the current chapter.

From equation (28), the phase and group velocities are, respectively,

$$V_{ph} = \frac{\omega}{K} = \frac{2}{K} \sqrt{\frac{k}{m}} \sin\left(\frac{Ka}{2}\right) \quad (29)$$

$$V_g = \frac{d\omega}{dK} = a \sqrt{\frac{k}{m}} \cos\left(\frac{Ka}{2}\right) \quad (30)$$

Note that for  $Ka/2 = \pi/2$ ,  $V_g$  is null and energy is not transmitted through the chain. Therefore, the chain itself acts as a low-pass filter (Santamarina, 2001), i.e., a filter that passes a signal with lower frequency than a certain frequency (cutoff frequency) and attenuates the signal amplitude for frequencies higher than that frequency. As such, this chain allows waves with

$$\lambda \geq \lambda_{\min} = 2a \quad (31)$$

or

$$\omega < \omega_{\max} = 2\sqrt{\frac{k}{m}} \quad (32)$$

that is, only waves with wavelength superior or equal to double the grain distance or angular frequencies inferior to double the resonant frequency.

Note that when the wavelength approaches  $2a$ , neighboring grains are in opposite phase, as shown in Figure 2.18.



Figure 2.18 – Adjacent grains in opposite phase (adapted from Santamarina *et al*, 2001)

In addition, when group and phase velocity are plotted versus  $\lambda/a$  in order to demonstrate the geometric effect of wavelength to scale ratio, the wave propagates in the particular medium as if it were a continuum. That is, the effect of the relative spatial scale are not accountable when the wavelength is much larger than the internal scale of the medium, when  $\lambda \gg a$ . When the wavelength approaches the internal scale of the medium, the velocities start decaying until  $\lambda = 2a$ , where  $V_g = 0$ .

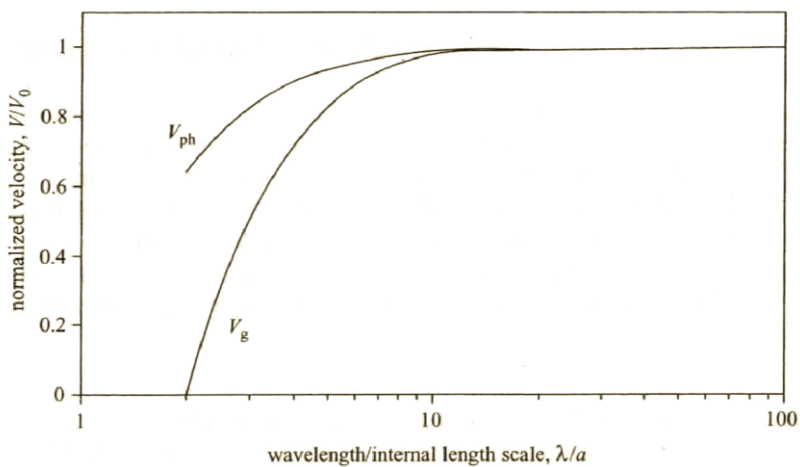


Figure 2.19 – Dependence of velocity on spatial scale (Santamarina *et al*, 2001)

## 2.5. DAMPING: DEFINITION AND OVERVIEW

The existence of frictional forces in a system constitutes a mechanism through which mechanical energy is transformed into other forms of energy, such as heat and sound. Damping is the term used to describe this energy transformation and dissipation (Park, 1998).

Figure 2.20 presents an ideal graph of damping, showing the amplitude of a wave exponentially decreasing over time, for a damped single degree of freedom system (SDOF).



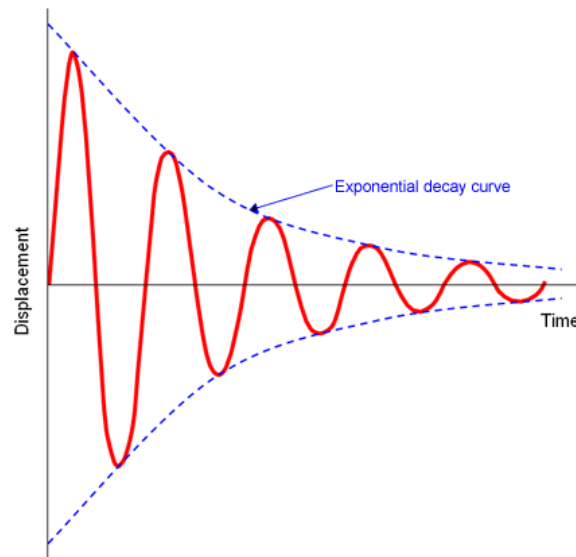


Figure 2.20 – Damping in a SDOF system

Damping is the general term to quantify the dissipation of energy during cyclic loading of an inelastic medium. As seen in the previous subchapter, soils are far from being ideal mediums and are to be treated as inelastic. So, damping is a parameter that needs to be accounted for more precise and realistic models, in order to accurately model soil response to cyclic loading (Park, 1998).

The dissipation of energy by wave propagation in a medium, also called radiation, dispersion or geometric damping, is the form of damping most easily understood. Still, part of the energy induced by the wave is absorbed into the medium itself, which is connected with deviations from Hooke's law and reflected by the hysteresis in the stress strain relationship (Venkatramaiah, 2006; Blanter *et al.*, 2007). As such, internal damping, material damping or hysteretic damping also occurs in nature. The hysteretic behavior of the soil will be approached later in the current chapter.

It is very important, and hard, to distinguish geometric and material damping, and this limitation makes damping measurement in the field less reliable (Park, 1998).

### 2.5.1. DAMPING MECHANISMS

Soil is a particulate media that consists of solid material, water and/or air. The particulate nature of soil contributes to the complexity on evaluating mechanisms for damping in soil (Dobry, 1970). The existence of other features, such as fractures and joints, add extra complexity. White (1983) and Stoll (1989) postulated two different mechanisms for internal soil damping: inelastic friction loss and fluid flow loss.

Inelastic friction loss occurs when soil is subjected to cyclic loading, in which the soil particles experience differential movement. This results in friction losses at the particle contacts, with inelastic, non-recoverable relative displacement between particles. This friction loss is a function of the normal force at the particle's interface and the friction of the contacting surfaces and, as such, it is hard to quantify (Park, 1998). At very small strains, the relative displacement can be very small may not even cause interparticle friction (Santamarina *et al.*, 2001). Inelastic friction loss is not dependent on the frequency of vibration (Spang and Wesley, 1995; Park, 1998).

The fluid flow loss mechanism is based on the principle that energy dissipation occurs by fluid flow drag due to the relative movement between soil particles and water, which results in shear forces at the soil-water interface. The application of this mechanism within a saturated soil medium is based on the work of Biot, already addressed in the previous subchapter. The losses of this mechanism are proportional to the velocity of motion and, therefore, to the frequency of vibration (Park, 1998). Permeability has a relevant impact on fluid flow loss, for higher permeability results in greater motion of water. However, the frequency at which contribution to damping from this effect is very high when compared with typical soil dynamics problems, which involve low frequencies (White, 1983).

Various authors have attempted to create models to account for the dissipation of energy in inelastic systems subjected to cyclic loading. These models, explained in the following topics, replace the damping mechanism for a model providing equivalent energy dissipation.

### 2.5.2. VISCOUS DAMPING

The response of a viscoelastic medium has, as the name implies, a viscous response in addition to an elastic response. As such, viscoelastic media resist shear flow and strain with time when stress is applied, in addition to being able to return to their original state once the stress is removed. The following statements translate the most important aspects of a viscoelastic medium:

- If strain is constant, stress decreases with time (relaxation);
- If stress is constant, strain increases with time (creep);
- If cyclic loading is applied, hysteresis occurs due to phase lag, which leads to dissipation of energy.

Several models have been suggested to represent geomaterials in the context of wave propagation, differing in the assumption regarding linearity, energy loss per cycle and velocity (Kjartansson, 1979).

#### 2.5.2.1. Kelvin-Voigt model

The most common assumption of a viscoelastic medium is a Kelvin-Voigt model (Santamarina *et al*, 2001). Figure 2.21 represents this model, which consists in a Newtonian dashpot and a Hookean spring in parallel.

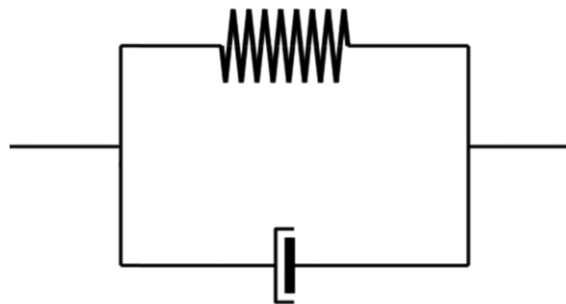


Figure 2.21 – Kelvin-Voigt model

This system's general equation of motion under free vibration is given by the following equation

$$x(t) = m \frac{d^2x}{dt^2} + c \frac{dx}{dt} + kx \quad (33)$$

where  $m$  is the mass of the system,  $c$  the viscous dashpot coefficient and  $k$  the spring constant. The first part is relative to the system's inertia, the second one to its viscous damping and the last one to its stiffness. The solution to the previous equation has three roots, which correspond to the overdamped, underdamped and critically damped conditions, illustrated in the following figure.

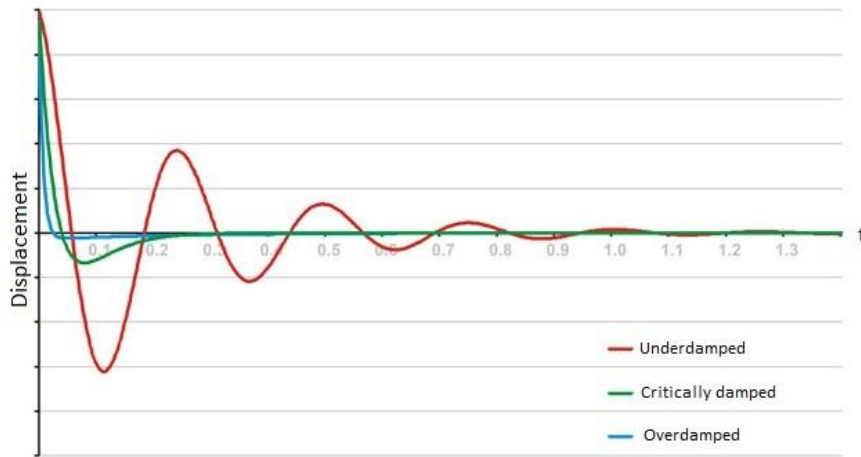


Figure 2.22 – Comparison of different damping conditions

In the overdamped condition the system returns to equilibrium without oscillating, an exponential decay and no cycles of motion, while in the underdamped condition the system oscillates with a gradual decrease in amplitude and multiple cycles of motion. A critically damped system returns to equilibrium without oscillating, during about one single cycle of motion.

For an underdamped system, the general equation of motion (33) becomes

$$x(t) = Ae^{-\xi\omega_n t} \sin(\omega_d t + \Phi) \quad (34)$$

Where  $A$  and  $\Phi$  are integration constants and  $\omega_d$  is the damped natural frequency, given by

$$\omega_d = \omega_n \sqrt{1 - \xi^2} \quad (35)$$

The deduction of equation (34) can be found in various authors' works. Since its grasp escapes this dissertation's objectives, only the resulting expression is presented. For a thorough deduction, see Inman (2001), section 1.3.

The critical damping coefficient is given by

$$c_c = 2\sqrt{km} \quad (36)$$

The viscous damping ratio is defined as the proportion of the system's viscous damping,  $c$  to the critical damping coefficient,  $c_c$ . As such, the final form for damping ratio based on this model is

$$\xi = \frac{c}{c_c} \quad (37)$$

At high frequencies, the Kelvin-Voigt model predicts velocities increasing indefinitely with frequency and energy arriving in zero travel time, which is physically impossible. However, damping effectively filters high frequency waves and this limitation has a small impact on practical problems (Santamarina *et al*, 2001). This model is good with modeling creep, but is much less accurate with regards to relaxation.

#### 2.5.2.2. Maxwell model

The Maxwell model is characterized by a Newtonian dashpot and a Hookean spring in series, as shown in Figure 2.23. The spring can be seen as the elastic component of the response while the dashpot represents the entropic component. In this model, the stress of each element is equal to the applied stress, while the total strain is the sum of the strain in both elements. The following equations demonstrate this model's behavior.



Figure 2.23 – Maxwell model

$$\sigma = \sigma_s = \sigma_d \quad (38)$$

$$\varepsilon = \varepsilon_s + \varepsilon_d \quad (39)$$

Note that the stress gradually relaxes when the system is under constant strain. When the system is subjected to constant stress, the strain has an elastic and viscous component. The elastic component occurs immediately (and disappears when the applied stress is nullified), while the viscous component grows with time while the stress is applied.

This model predicts a decay of stress with time, an aspect quite accurate for polymers. However, this model does not predict creep accurately: in constant stress conditions strain increases linearly with time.

### 2.5.2.3. Standard linear solid model

The standard linear solid model, linear solid model or Zener model, overcomes some of the limitations of the Kelvin-Voigt model. It consists of a spring in series with a Kelvin-Voigt model, as shown in Figure 2.24, somewhat combining the previous models' layout. Since it involves elements in parallel and in series, this model is more complex than the previous ones.

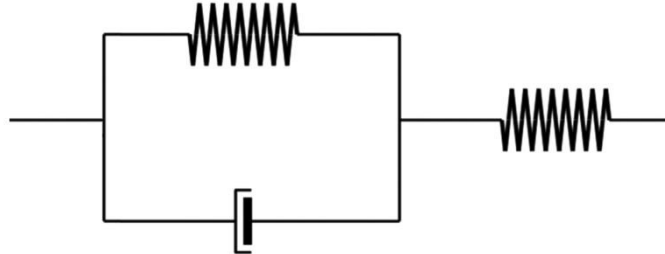


Figure 2.24 – Standard linear solid model

The equivalent stiffness of elements in parallel is the sum of the stiffnesses of the elements, while the stiffness of elements in series is the inverse of the sum of the inverse of the stiffnesses. So, according to the standard linear solid model, the equivalent stiffness,  $k_{eq}$ , is complex and equal to

$$k_{eq} = \left( \frac{1}{k_{spring\ 1}} + \frac{1}{k_{spring\ 2} + ic\omega} \right)^{-1} \quad (40)$$

The imaginary symbol indicates that the deformation lags behind the force with a 90° phase shift (Santamarina, 2001). Also, the system's stiffness varies with frequency. At very low frequencies, the dashpot effect is negligible and the stiffness is given by the stiffness of the springs in series. At very high frequencies, the dashpot does not allow the Kelvin-Voigt element to deform and the stiffness is given by the isolated spring.

Note that this model predicts identical behavior to the Kelvin-Voigt model at low frequencies, but at high frequencies the velocity in the standard linear solid model does not increase to infinity. Additionally, according to Santamarina (2001), this model reaches a maximum velocity for P-waves and S-waves equal to the equations exposed before,

$$V_P = \sqrt{\frac{M}{\rho}} \quad (41)$$

$$V_S = \sqrt{\frac{G}{\rho}} \quad (42)$$

### 2.5.3. HYSTERETIC DAMPING

Unlike elastic materials, viscoelastic materials dissipate energy when a load is applied and removed. If cyclic loading is applied, a phase lag occurs which leads to the mentioned dissipation of energy. Elastic materials have both stress and strain in phase, whereas in viscous materials strain lags stress by 90° phase lag. Therefore, viscoelastic materials demonstrate behavior in between these two types, exhibiting a lag in strain less than 90° (Meyers and Chawla, 2009). As a result, hysteresis is observed in the stress-strain curve, with the area of the loop equal to the energy lost during the loading cycle.

At the first stage of loading, the initial response of soil is governed by the maximum secant shear modulus,  $G_0$  or  $G_{max}$ . However, increasing the level of shear stress (or strain) causes a gradual decrease in shear modulus and nonlinear response (Park, 1998). Figure 2.25 represents the stress-strain curve of hysteretic damping.

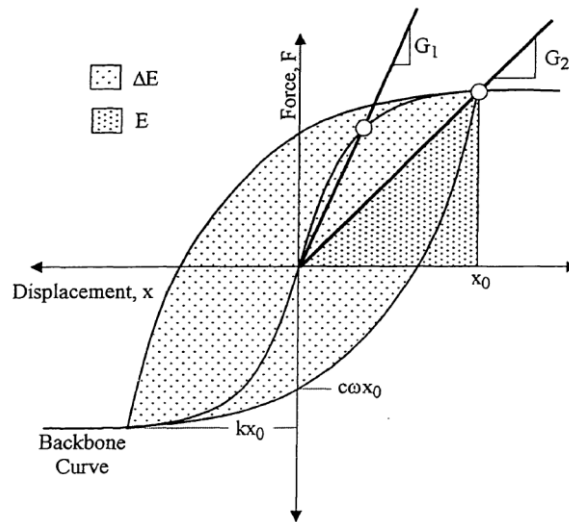


Figure 2.25 – Schematic presentation for definition of hysteretic damping ratio and secant shear modulus (adapted from Park, 1998)

Hysteretic damping ratio can be defined as the ratio of dissipation of energy in a load cycle to the maximum energy stored during it. The energy dissipated in a unit of displacement, function of the area of the hysteretic loop, is

$$\Delta E = F dx \quad (43)$$

where  $F$  is the damping force and  $dx$  the incremental displacement. Using the general equation for harmonic, forced vibrations in soils

$$x(t) = A \sin(\omega t) \quad (44)$$

The differential displacement with respect to time is given by the following equation

$$dx = \omega A \cos(\omega t) dt \quad (45)$$

Equation (44) can be solved by substituting the previous equation and  $F$

$$\Delta E = \omega^2 A^2 \cos^2(\omega t) \quad (46)$$

For a load cycle, this equation is integrated for a period of vibration

$$\Delta E = \int_0^{2\pi} \omega^2 A^2 \cos^2(\omega t) dt \quad (47)$$

The solution for  $\Delta E$  can be arranged in terms of  $c$ , which results in

$$c = \frac{\Delta E}{\pi A^2 \omega} \quad (48)$$

The maximum energy available in the spring during a cycle of constant amplitude loading can be expressed by

$$E = \frac{1}{2} k A^2 \quad (49)$$

where  $k$  is the soil stiffness at amplitude  $A$ . That is, it represents the area of a triangle in stress-strain plot. The natural frequency of soil is given by

$$\omega_n = \sqrt{\frac{k}{m}} \quad (50)$$

where  $m$  is the mass of the soil sample and  $k$  its soil stiffness. Combining the two last equations plus equation (36), results the following

$$c_c = \frac{4E}{A^2 \omega_n} \quad (51)$$

Using the values of  $c_c$  and  $c$  from the last equation and equation (48), respectively, equation (37) becomes

$$\xi = \frac{\Delta E}{4\pi E} \frac{\omega_n}{\omega} \quad (52)$$

The equivalent hysteretic damping ratio is obtained by multiplying the viscous damping ratio by  $\omega/\omega_n$ . This is done because the hysteretic damping ratio is independent of frequency (Roesset, 1991). Therefore, the damping ratio used to represent internal damping in soils is

$$\xi = \frac{\Delta E}{4\pi E} \tag{53}$$

This equation is used to measure the damping ratio from low frequency cyclic tests, by determining the area of the hysteretic loop.

#### 2.5.4. FRICTION DAMPING

Friction damping occurs when two particles in contact with each other experience relative movement and lose energy through heat or sound dissipation (Park, 1998). Since the normal force and coefficient of friction are considered constant over low to moderate velocities, it is assumed independent of frequency. Constant normal force and coefficient of friction result in a friction damping force that does not increase with amplitude. Since damping in soils increases with strain amplitude, a friction damping model is not adequate in geotechnical engineering. For further information on the topic, take a look at Park (1998), page 26.

### 2.6. EXPERIMENTAL DETERMINATION OF SHEAR MODULUS AND DAMPING RATIO

The previous subchapters stated, among other issues, the relevance of both shear modulus and damping ratio for the determination of soil's dynamic behavior. The present subchapter contains information on the various experimental procedures to obtain these parameters, in addition to factors that affect them.

There are both field and laboratory tests to determine shear modulus and damping ratio, and under these are various techniques available to do so, each with their own advantages and limitations. It is good practice to use techniques that reproduce the initial stress conditions and the expected cyclic loading conditions as closely as possible. Figure 2.26 highlights this aspect, by representing the degradation curve of soil stiffness with shear strain and relevant ranges for current geotechnical engineering structures and tests.

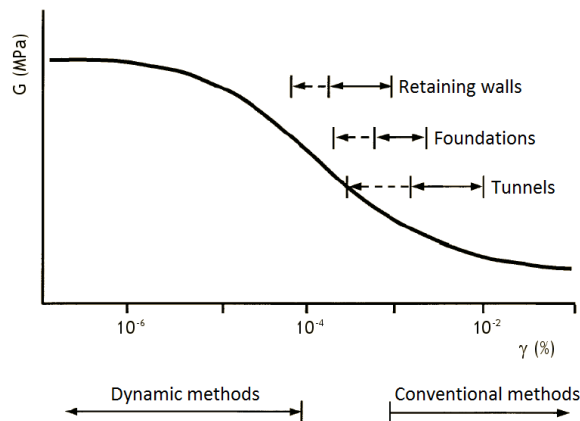


Figure 2.26 – Shear strain versus shear modulus (adapted from Ferreira, 2003)



In addition, the shear strains originated in dynamically tested soils are very different in magnitude, either at lower or higher strain levels. As such, the accurate measurement of shear modulus and damping ratio is one of the most important tasks in order to solve dynamic geotechnical engineering problems (Park, 1998), given that soils are very characteristic materials.

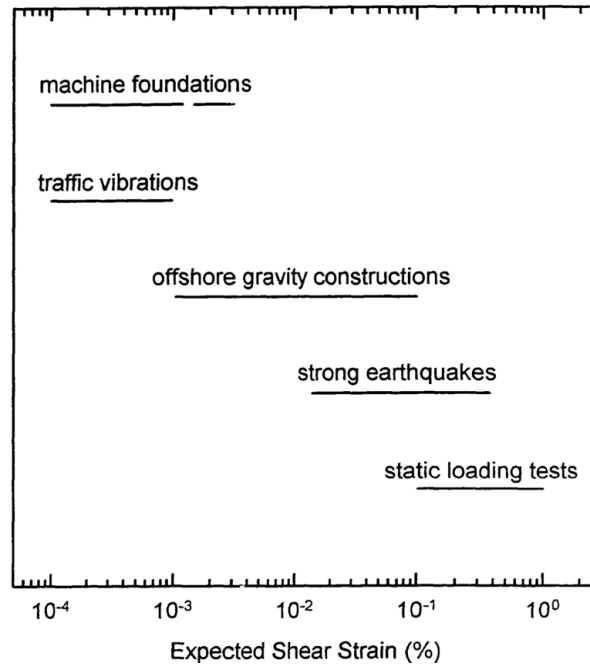


Figure 2.27 – Expected shear strains in soils under different loading conditions (Park, 1998)

Some errors in measuring the already mentioned parameters are unavoidable, for both field and laboratory tests. The variability of soils, anisotropy, sampling disturbance, testing errors, interpretation errors and limitations regarding the testing equipment are common sources of error. Careful collection, treatment and handling of soil samples must be assured in order to minimize the effects of sample disturbance, for example. All these sources of errors must be accounted for when evaluating test results, in order to improve their accuracy and veracity.

According to Karl (2005), testing procedures to determine dynamic soil parameters can be divided in low strain and high strain. The deformation in the first group can be regarded as elastic, while in the latter the deformations are influenced by plasticity. The following figure demonstrates the shear strain ranges for several tests in addition to the expected strain ranges for certain engineering problems.

Based on a brief analysis of the previous figure, low strain field tests use the propagation of seismic waves, by inducing vibrations in soil and measuring these with sensors. These tests include seismic reflection/refraction tests and boreholing techniques. High strain tests comprehend the conventional static tests, such as seismic penetrometer, pressuremeter and dilatometer tests. Note that these last tests imply an indirect method to obtain the damping ratio.

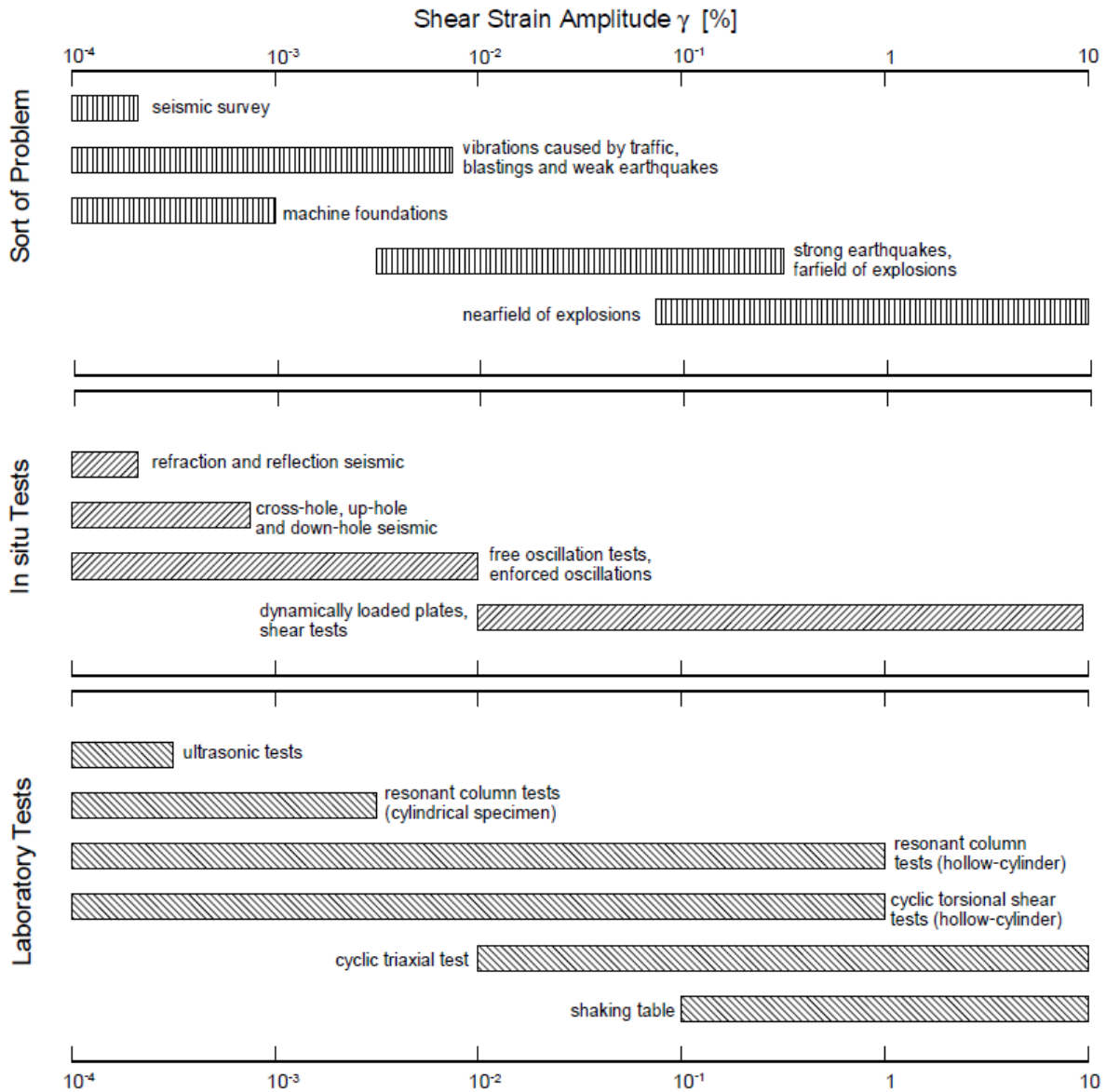


Figure 2.28 – Overview of possible shear strain amplitudes (Studer and Koller, 1997)

Low strain laboratory tests include both bender element and resonant column tests, which are approached with a special mention in this dissertation. High strain tests, such as simply/cyclic shear test and the cyclic triaxial test, are mainly used in the study of liquefaction behavior induced by earthquakes (Karl, 2005).

In order to determine damping, the seismic wave data must be treated after acquisition. Various methods exist, which are based either on a time domain or frequency domain analysis. A time domain analysis is simpler, since it involves the evaluation of the amplitude variation of the seismic wave signal with time. So far, the figures showed in this dissertation concerned only time domain analysis, given that their comprehension is easier at first.

Frequency domain analysis, as the name suggests, evaluates the seismic wave signal in respect of frequency, giving relevant information not available in a time domain analysis. It shows, for the duration of the test, the most prominent frequencies of response vibration, usually represented in a

spectrum. In order to convert a signal from time to frequency domain, a transform function must be applied to the test data. A detailed approach is made in 4.4., in a more suitable situation.

From here on, and until the end of the current chapter, various field and laboratory tests are addressed and detailed, with emphasis on the resonant column test and the use of bender elements, the latter being the principal study object on this dissertation's experimental program.

### 2.6.1. IN SITU TESTS

In situ tests manage to eliminate most of the problems associated with sample disturbance, but it is difficult to induce large strain amplitudes in natural soils. As such, the dynamic soil properties for field measurements can only be determined for small strain levels. Note that boreholing and insertion of probes for in situ tests still causes some local disturbance. Also, field testing preserves the effects of fabric and aging on the properties, in addition to its natural stress conditions.

The only method to test "truly" undisturbed samples is by testing soil in situ. Some procedures can be implemented to reduce sample disturbance for laboratory tests, such as freezing sampling techniques, but these can be very costly or even impossible for some soil types, such as weakly cemented sands and fractured soft rocks (Park, 1998).

Since laboratory tests are usually performed on intact specimens, field tests are more reliable in determining dynamic properties of soils with discontinuities (Tani, 1994).

Unfortunately, in many field test procedures both shear modulus and damping ratio are not directly measured, and must be determined by theoretical analysis or empirical correlations. Figure 2.29 shows in situ test techniques to obtain shear modulus and damping ratio.

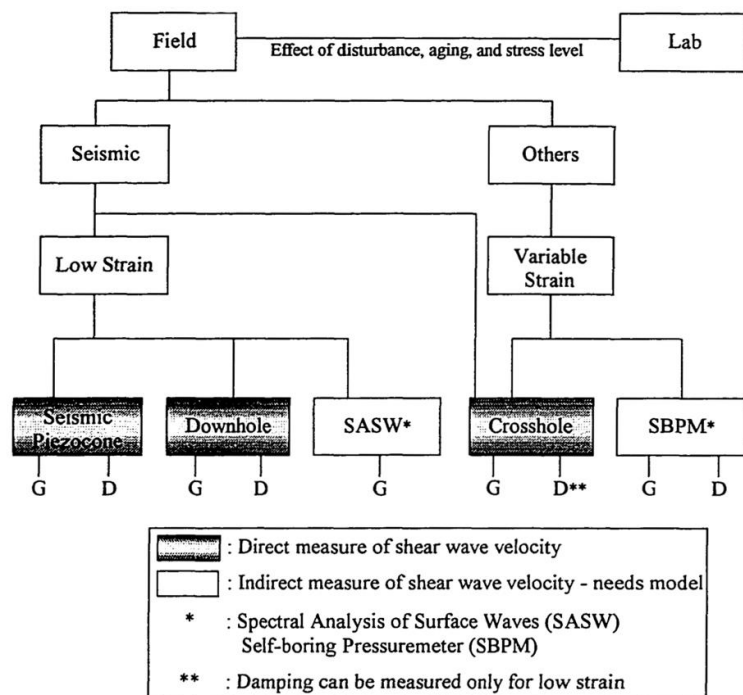


Figure 2.29 – Field tests for obtaining shear modulus and damping ratio (adapted from Campanella, 1994)

In addition, in situ tests only allow, of course, in situ conditions to be tested, so it is not possible to implement parametric studies. Note that time domain techniques for these tests are characterized by small display windows, which complicates obtaining clear and complete representations of the whole, damped wave (Park, 1998).

#### 2.6.1.1. Borehole methods: crosshole and downhole

Conventional borehole geophysics has been used in various industries for decades. The implementation of instruments in open boreholes is a method that allows in situ soil characterization, with the added vantage of providing the borehole log as a test sample for laboratory tests (Park, 1998). Using these borehole methodologies, shear and compression waves can be determined by measuring the travel time between a source and one (or more) receivers.

The crosshole test uses a source at a certain depth of a borehole and registers the travel time using receivers at the same depth, in adjacent boreholes. As such, shear wave velocity is determined by dividing the borehole spacings by the correspondent travel time (Ferreira, 2009). The test is the repeated at various depths in order to establish a profile of wave velocity with depth.

This method is considered as the most reliable among in situ borehole methods (Park, 1998). Both source and receivers are placed near the evaluated material, which enhances result resolution. Also, measurements can be gathered along inclined paths, which can be used to render tomographic images (Menke, 1989; Santamarina and Fratta, 1998). However, it is costly and time consuming, since it requires at least two boreholes, and good contact between the source and the soil may be hard to achieve (Larson and Mulabdic, 1991)

The downhole test is similar to the crosshole: the source is applied at the surface instead. As such, only one borehole is required, making this borehole method cheaper when accounting for boreholing expenses. Travel distances are usually based on the assumption that travel paths are straight between the source and the receivers, although analysis may sometimes account for refracted travel paths (Ferreira, 2009).

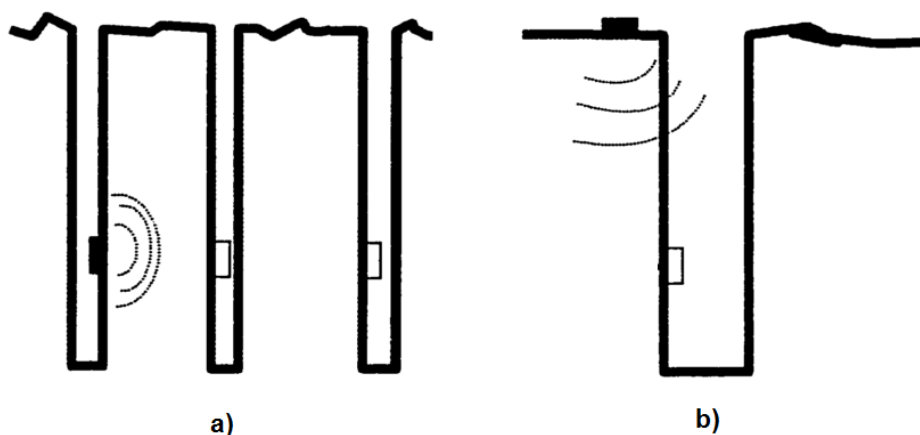


Figure 2.30 – Borehole methods: a) crosshole method; b) downhole method

### 2.6.1.2. Seismic cone penetrometer test (SCPT)

The SCPT is a modification of the standard cone penetration test (CPT) which allows measurement of shear wave velocities. It is a well-established tool for characterization of soil properties, by measuring tip and side resistances on a probe pushed into the soil (Lunne *et al*, 1997). In order to generate horizontally polarized waves, a horizontal impact on an embedded anvil is used. Travel time of shear wave is measured at one or more locations above the cone tip of the probe. After testing at a given depth, the probe penetrates further and the test is repeated.

One of the benefits of this test is that the seismic data can be combined with cone resistance values in order to characterize the soil in terms of strength and stiffness, which is an excellent example of the use of multiple techniques in site investigation (Stokoe and Santamarina, 2000). Also, it is a fast and relatively accurate method to determine soil stratigraphy (Park, 1998).

This method does not allow the obtainment of soil samples. Furthermore, probe penetration can be difficult for certain cemented soils and gravels.

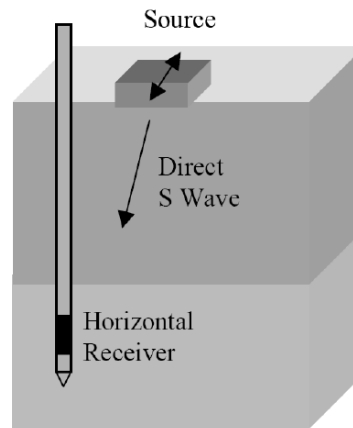


Figure 2.31 – Seismic cone penetrometer test (adapted from Stokoe and Santamarina, 2000)

### 2.6.1.3. Spectral analysis of surface waves (SASW)

The use of surface waves for geotechnical engineering applications was introduced with the spectral analysis of surface waves method (SASW method), by Nazarian and Stokoe in 1984. Surface wave testing can involve Rayleigh and Love waves, and testing has been conducted both on land and offshore (Stokoe *et al*, 1994; Stoll *et al*, 1994; Tokimatsu, 1995).

The SASW method involves the excitation of Rayleigh waves at one point and measuring the resultant vertical surface motions at various receiver points, placed along a linear array on the soil surface. It is based on the dispersive characteristic of Rayleigh waves when propagating in a layered system (Ferreira, 2009). As a result of the varying stiffness of these layers, waves with different wavelengths travel at different phase velocities, allowing the determination of a surface wave dispersion curve (variation of phase velocity with wavelength or frequency). Using this curve, it is possible to determine the shear wave velocity profile with depth.

This method provides an effective method for in situ characterization without boreholes, which makes it a non-intrusive, non-destructive and relatively cheap methodology (Park, 1998).

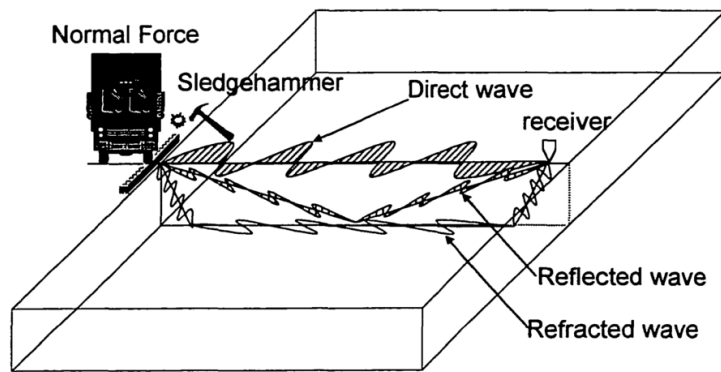


Figure 2.32 – Spectral analysis of surface waves (Park, 1998)

An acquisition scheme with multiple receivers has recently been introduced (Ferreira, 2009), which has a faster field procedure and more accurate results, due to higher spectral integrity of the acquired data (Gabriels *et al*, 1987; Park *et al*, 1999; Foti, 2000; Strobina, 2003; Lopes *et al*, 2004). This method is known as the surface wave method (SWM), represented by the following figure.

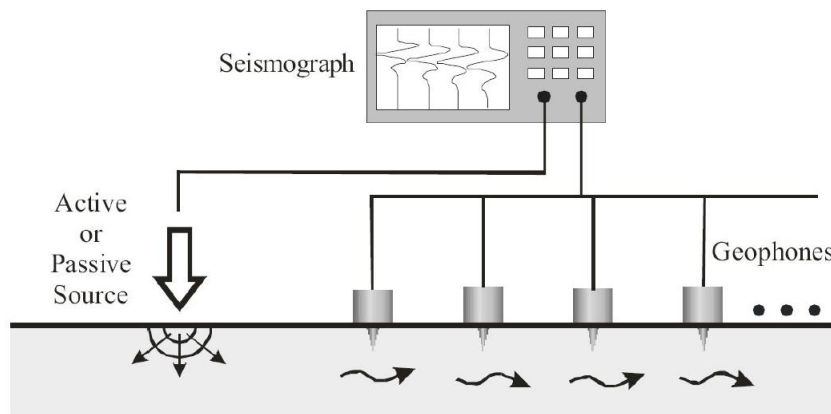


Figure 2.33 – Surface wave method (Lopes *et al*, 2004)

## 2.6.2. LABORATORY TESTS

In laboratory tests soil samples can be tested under a wide range of strains (as stated previously in the current chapter), but soil properties are inevitably influenced by the effects of sample disturbance. As a result, the measured dynamic properties of soils tend to differ from laboratory tests to field tests.

Some authors (Seed and Idriss, 1970; Yasuda and Yamaguchi (1984)) found that the shear moduli determined by laboratory tests were significantly lower than those determined by in situ measurements, when testing San Francisco bay mud and sands. Yasuda and Yamaguchi (1984) concluded that for in situ shear moduli greater than a certain threshold the laboratory test results were lower, and that for in situ shear moduli lower than that threshold the laboratory test results were higher.

Shear modulus and damping ratio are both influenced by factors that are hard to simulate in laboratory conditions, such as soil fabric and structure, age, stress history and cementation (Park, 1998). These effects are primarily important at low strain levels, high quality samples must be obtained for an accurate representation of the tested soil.

However, parametric studies are possible in laboratory testing, in contrast with field tests. This is an important factor when it comes to understanding dynamic soil behavior. In addition, different procedures exist for different strain ranges, from  $10^{-6}$  to  $10^{-2}$ .

Table 2.3 shows the accuracy for some laboratory tests in measuring dynamic parameters, in addition to Young's modulus.

Table 2.3 – Laboratory tests and relative qualities in parameter measurement (adapted from Park, 1998)

Laboratory test	Shear modulus	Damping ratio	Young's modulus
Resonant column	Good	Good	Good
Ultrasonic pulse	Fair	-	Fair
Cyclic triaxial	-	Good	Good
Cyclic simple shear	Good	Good	-
Cyclic torsional shear	Good	Good	-

#### 2.6.2.1. Bender element testing

In order to characterize soils dynamically, piezoceramic elements have been used in the past years. During early stages, piezoceramics were mainly used to generate and transmit compression waves, which provided only little information about the soil structure. Piezoceramics have been combined in different forms in order to generate and receive shear waves. Notably, one of these forms causes a bending motion in the piezoceramic elements. Such elements are called piezoceramic bender elements (BE) (Karl, 2005).

BE are particularly preferable piezoceramic elements given that they have the capacity of great deformation for low electrical voltages (Ferreira, 2009). Also, the characteristic impedance of these piezoceramic elements is closely matched with the characteristic impedance of the soil, which originates a closer relation between movement and applied force for both piezoceramic element and propagating medium (Shirley and Hampton, 1978).

A BE is an electro-mechanical transducer capable of converting electrical energy in mechanical energy (or vice versa). It consists of two thin piezoceramic plates rigidly bonded together with conducting faces between them and on the outsides. The polarization of these ceramic materials in each plate is such that when a driving voltage is applied, one plate elongates and the other one shortens, resulting in a bending motion. On the other hand, when a BE is forced to bend, one layer goes in tension and the other in compression, resulting in an electrical signal (Dyvik and Madshus, 1985).

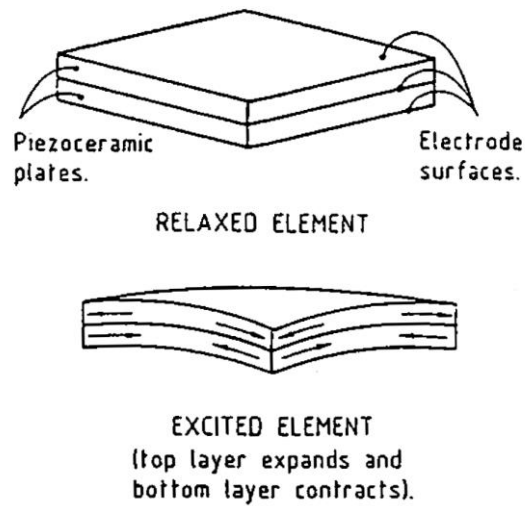


Figure 2.34 – Bender element constitution (Dyvik and Madshus, 1985)

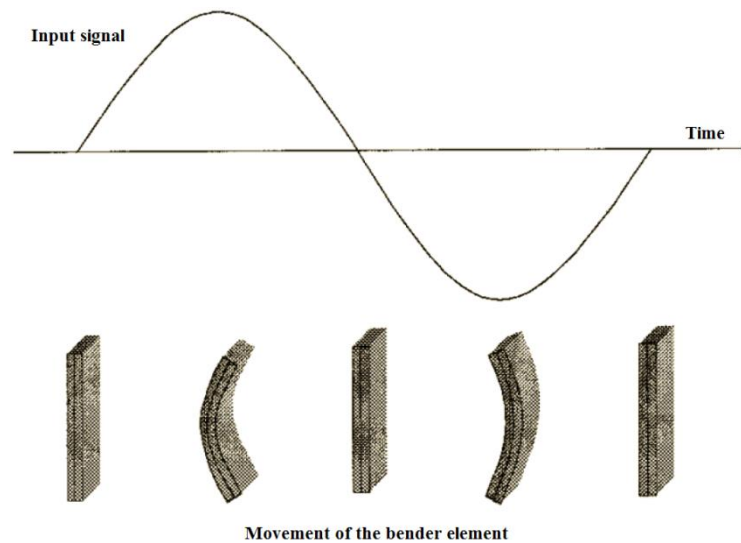


Figure 2.35 – Bender element functioning (adapted from Ferreira, 2003)

There are two possible connection setups for these elements: series connected and parallel connected. For a series connection the polarization of the ceramic material is oriented in opposite directions for each plate, while for a parallel connection the polarization is in the same direction for both plates.

Note that any of these connection setups can be used for both transmitter and receiver elements. However, a series connection produces double the energy than parallel connection for the same voltage: a parallel connected element is twice as effective as a series connected element when used as a transmitter. (Dyvik and Olsen, 1989) As such, a parallel connected element is used as the transmitter BE ( $BE_T$ ) and a series connected element as the receiver ( $BE_R$ ). Note that the maximum input energy must be limited in order to prevent depolarization of the piezoceramic material. Ferreira (2003) advised a  $\pm 20V$  voltage for this effect.



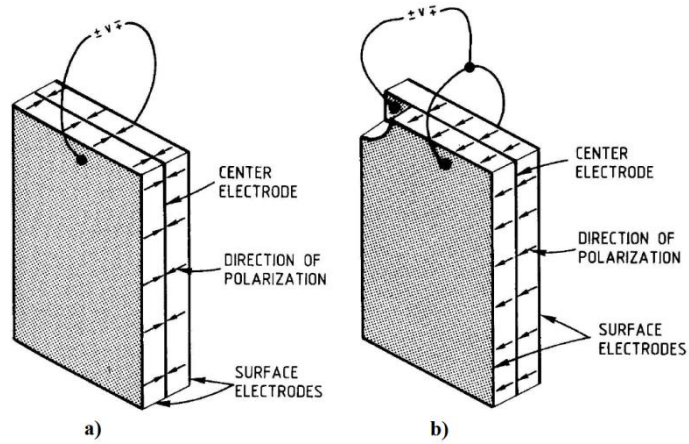


Figure 2.36 – Series connected a) and parallel connected b) bender elements (adapted from Dyvik and Madshus, 1985)

BE based methodologies are attractive given that they are apparently simple to use and can be placed in various testing devices, such as oedometer, simple shear test devices, conventional triaxial devices or resonant columns (Karl, 2005). In addition, measurement and calculation of  $G_{max}$  is much faster and easier than in the usual resonant column test (Dyvik and Olsen, 1989). However, several authors have dealt with difficulties in interpreting test results (Leong *et al.*, 2005; Greening and Nash, 2004; Arulnathan *et al.*, 1998; Jovicic *et al.*, 1996; Brignoli *et al.*, 1996; Viggiani and Atkinson, 1995), which makes the interpretation subjective and requiring some degree of judgment, since there is no ideal method of interpretation established (Ferreira, 2009).

Figure 2.37 shows the input wave shape suggested by different authors.






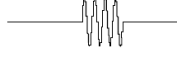
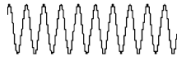

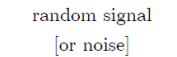
Input wave shape	Reference
 Square or step signal	Dyvik and Madshus (1985); Fam and Santamarina (1995)
 Impulse signal	Lee and Santamarina (2005)
 Sine wave	Viggiani and Atkinson (1995); Brignoli <i>et al.</i> (1996)
 Sine pulse [90° phase shift]	Pennington <i>et al.</i> (2001)
 Distorted sine wave [typically 30° phase shift]	Jovicic <i>et al.</i> (1996)
 Forced oscillation [sine wave cycles at resonance frequency]	Jovicic <i>et al.</i> (1996)
 Continuous sine wave of constant frequency	Greening and Nash (2004)
 Sine sweep of frequencies [typically 100 Hz to 20 kHz]	Greening and Nash (2004); Ferreira <i>et al.</i> (2007)
 random signal [or noise]	Roesler (1979); Santos <i>et al.</i> (2007)

Figure 2.37 – Input wave suggestions (Ferreira, 2009)

The selected input wave shape for this dissertation’s experimental program was a sweep sine signal. This non-harmonic sinusoidal continuous signal (Greening *et al*, 2003; Greening and Nash, 2004) enables the acquisition of a continuous phase angle *versus* frequency relationship. Ferreira (2009) considered that a sweep sine signal input with a 100Hz to 20kHz bandwidth is suitable for natural soil testing.

Figure 2.38 shows a BE example test using a sweep sine signal wave input, in order to exemplify a BE test analysis.

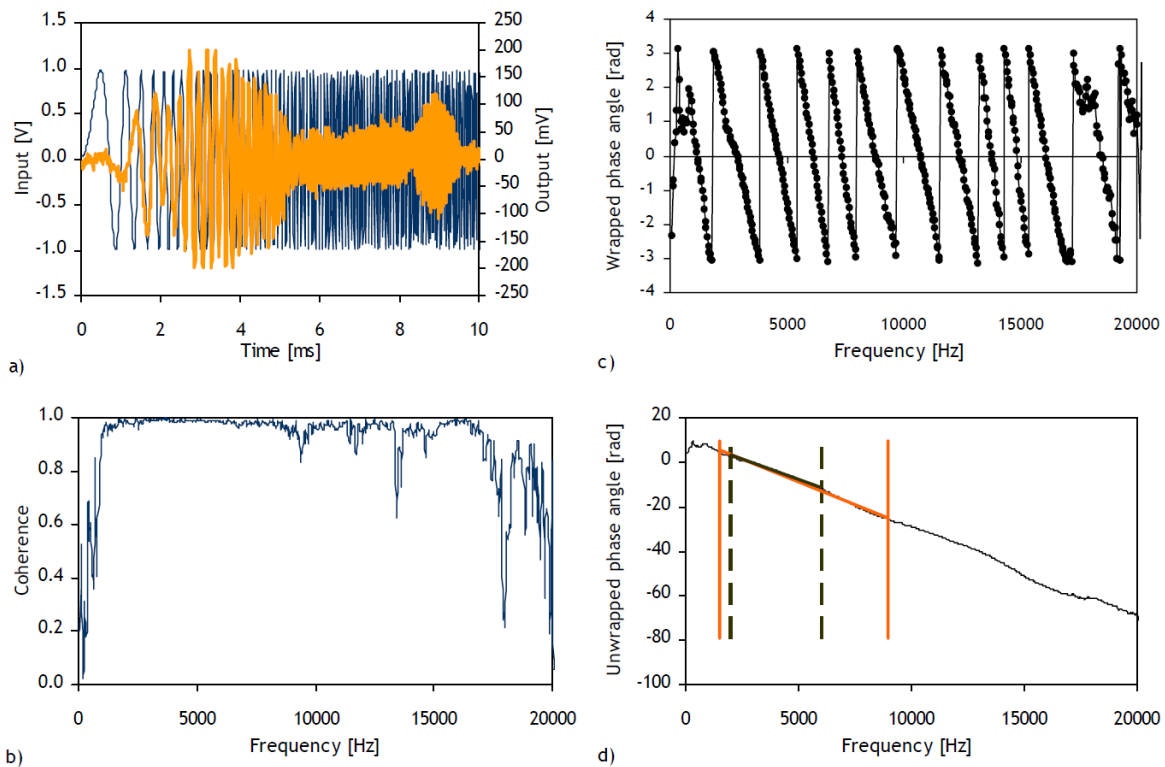


Figure 2.38 – Bender element frequency domain analysis: a) input and output signals; b) coherence; c) wrapped phase angle; d) unwrapped phase angle

The coherence between input and output (i.e., signal and received wave) *versus* input frequency serves as an indication of how well correlated are these signals. This coherence function indicates how much of the output signal’s energy is caused by the input signal (Hoffman *et al*, 2006).

The phase angle *versus* frequency can be displayed as wrapped or unwrapped, that is, ranging from  $[-\pi; +\pi]$  or starting at zero and increasing continuously. It illustrates the phase difference between the input and output signals. As such, its use is relevant when determining the travel time, since it derived directly from the slope of the best-fit straight line in the unwrapped phase plot (Ferreira, 2009).

### 2.6.2.2. Resonant column test

The resonant column test (RC) is the most widely used laboratory test to measure soil dynamic parameters for low to moderate strain, from  $10^{-6}$  to  $10^{-2}$ . This test consists on the application of a sinusoidal compression or torsion vibration to a cylindrical sample, either solid or hollow, inside a triaxial cell. Confining pressure is ensured and controlled by the triaxial cell. By varying the vibration frequency it is possible to determine the system's resonant frequency and, based on the theory of wave propagation, Young's modulus and shear modulus (Barros, 1996).

Depending on the equipment set up, the applied vibration can be either compressive or torsional, or even both. Each set up has its own associated methodology and interpretation.

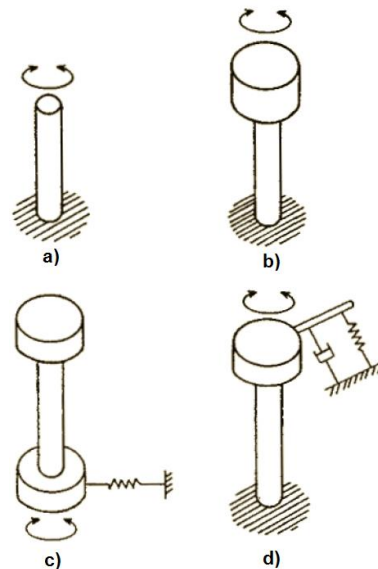


Figure 2.39 – Various setups for the resonant column test (adapted from Barros, 1996)

The most widely used set up is the fixed-free torsional resonant column, where the vibration is applied on the top of the sample, as well the response reading. Note that for this set up the top has no restraints and the base is considered fixed.

The signals from the torsional moment and acceleration are connected to an oscilloscope. When the torsional moment is applied, the phase of both signals is determined by the Lissajous figure in the oscilloscope display, which can be used to verify the system's resonance by varying the applied frequency (Ferreira, 2003). After resonance is achieved, the tangential acceleration and frequency are registered in order to calculate shear modulus and distortion.

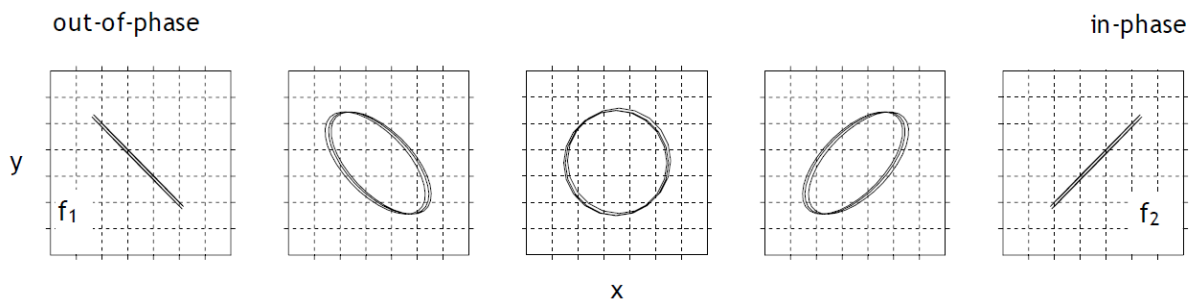


Figure 2.40 – Lissajous figures in an oscilloscope (adapted from Ferreira, 2009)

### 2.6.2.3. Cyclic triaxial test

The cyclic triaxial test has been one of the most commonly used tests for measurement of dynamic soil properties at high strain levels. In this test, a deviator stress is applied cyclically at a frequency of about 1 Hz in either stress or strain controlled conditions. Similar to the conventional triaxial test, it can be performed under isotropic or anisotropic conditions. The first is commonly used to represent level-ground sites where no initial shear stress exists. The latter is used to model conditions in and beneath slopes where initial static shear stress exists.

Figure 2.41 shows a schematic representation of the tensions in play during this test under isotropic conditions.

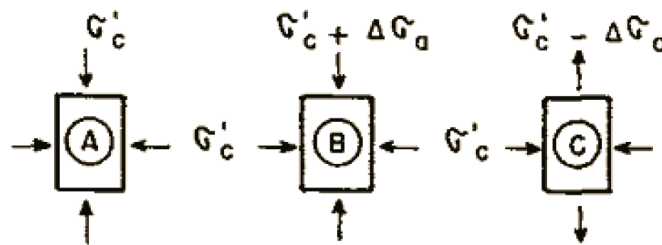


Figure 2.41 – Schematic representation of the cyclic triaxial test (adapted from Barros, 1996)

Ladd *et al* (1989) compared  $G_{max}$  obtained from cyclic triaxial and resonant column tests for Monterey sand and found that these results are reasonably comparable.

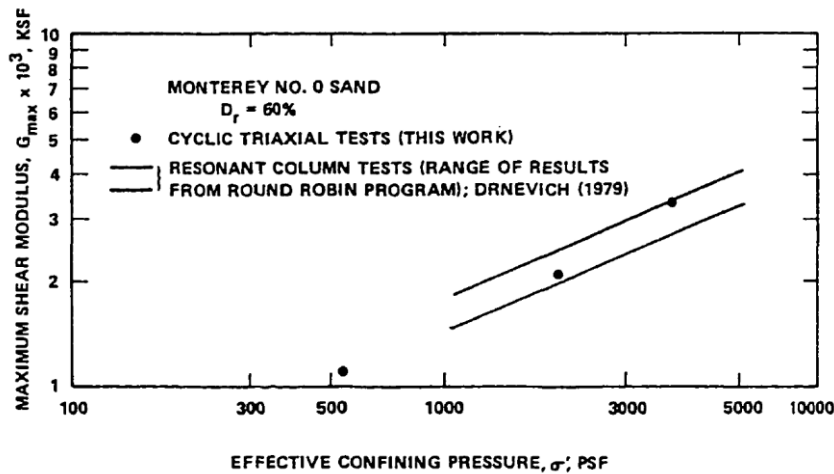


Figure 2.42 – Comparison of low amplitude shear moduli determined by cyclic triaxial and resonant column test (adapted from Ladd *et al*, 1989)

The strains and stresses measured in the cyclic triaxial test are used to determine both shear modulus and damping ratio. Both  $G_{max}$  and  $\zeta$  can be determined using the resulting hysteresis loop, as explained before in 2.4.3..

The cyclic triaxial test is unable to model stress conditions that exist in most seismic wave propagation problems (Park, 1998). Also, the soil specimen needs to be wrapped in a membrane which can be penetrated when testing coarse grained soils. In addition, Woods (1978) stated the following regarding this type of test:

- Shear strain measurements below  $10^{-4}$  are difficult to achieve;
- Since compression and extension phases of each cycle produce different results, hysteresis loops are not symmetric in strain-controlled tests;
- Void ratio redistribution occurs.

#### 2.6.2.4. Cyclic simple shear test

The cyclic simple shear test is capable of simulating earthquake stress conditions more accurately than the cyclic triaxial test (Alarcon *et al*, 1986; Park, 1998). It consists on the application of a cyclic horizontal shear stress at either top or bottom of the test sample, subjecting it to vertically propagating S-waves, as represented in Figure 2.43. Shear modulus and damping ratio are determined by the resulting hysteresis loop, as in other cyclic tests.

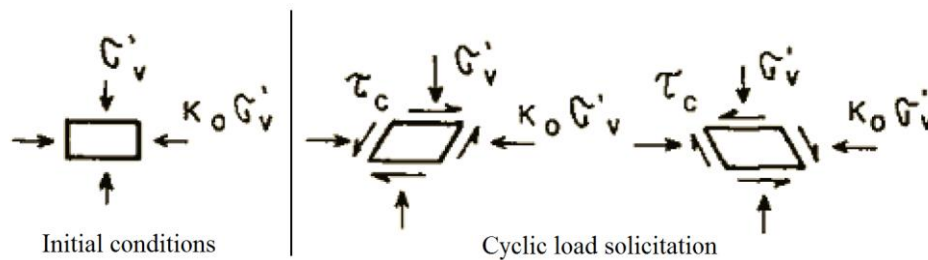


Figure 2.43 – Schematic representation of the cyclic simple shear test (adapted from Barros, 1996)

Various equipment exist for the cyclic triaxial test, differing on how the lateral boundary type. Cambridge-type equipment restrains the sample against lateral expansion using rigid boundary platens; SGI-type equipment uses a series of stacked rings; NGI-type equipment uses a wire reinforced membrane.

The shear apparatus applies shear stress only on the top or bottom surfaces of the soil sample. In situ, a soil specimen is subjected to complimentary shear stresses along its side when subjected to seismic horizontal loading. Since no corresponding shear stresses are imposed on the lateral sides, the moment caused by the horizontal stresses are not balanced by the distributed shear and normal stresses. This causes specimens to fail at lower applied stresses than those required in the field. In addition, most simple shear apparatus cannot control lateral confining pressure during cyclic loading, making it very difficult to study precise the effects of general anisotropic consolidation. Still, direct simple shear tests have been useful in studying cyclic shear phenomena (Park, 1998).

#### 2.6.2.5. Torsional shear test

Several difficulties associated with the cyclic triaxial and cyclic simple shear test can be avoided by loading cylindrical soil samples in torsion. In addition, this test is capable of measuring shear modulus and damping over a relatively wide range of strain, either under isotropic or anisotropic initial stress conditions (Park, 1998).

This test can be controlled either by stress (torque) or strain (rotation), where either of these is cycled to simulate earthquake loadings. Shear modulus and damping ratio are determined from the usual hysteretic loop.

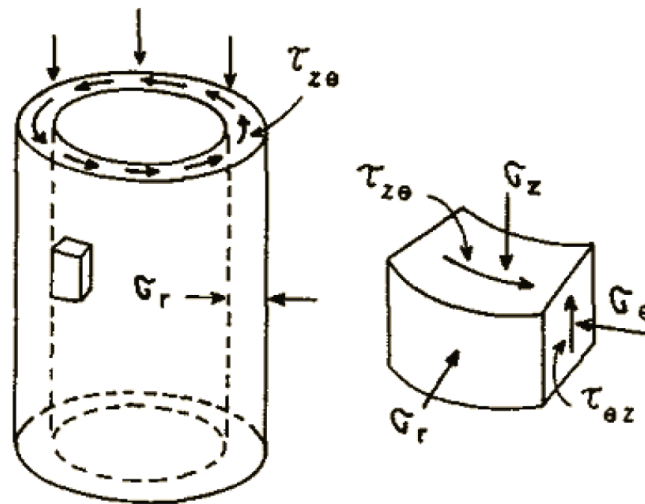


Figure 2.44 – Schematic representation of the torsional shear test (adapted from Barros, 1996)

Torsional testing of solid samples produces varying shear strains that range from zero along the axis of the specimen to a maximum value at the outer edges. In order to increase shear strain radial uniformity, Drnevich (1967; 1972) developed hollow cylinder cyclic torsional shear equipment. These hollow samples have many advantages besides the uniformity of this effect, including ease of testing with anisotropic stress conditions, accurate measurement of complete state of stress and minimized effects of end plates (Park, 1998). However, specimen preparation can be difficult and the equipment is not widely available. In addition, hollow specimens are more susceptible to membrane penetration due to its increased membrane area (about five times that of a solid cylindrical specimen).

### 2.6.3. SPECIFIC ISSUES REGARDING BENDER ELEMENT TESTING

Various authors (Sanchez-Salinero *et al* (1986); Viggiani and Atkinson (1995); Jovicic *et al* (1996; Arulnathan *et al* (1998)) demonstrated, both analytically and numerically, that there are various marginal effects associated with propagation of seismic waves that overlap the original wave. In addition, bender elements have the capacity to operate at a wide range of frequencies and, apart from the original seismic wave, also measure frequencies related to reflected waves in the soil container and background noise, for example. The combination of these factors, among others, the test duration and the relevant tridimensional anisotropy of the tested medium complicate wave analysis.

Sanchez-Salinero *et al* (1986) were the first to accomplish developments on these matters. After studying the propagation of a transversal sinusoidal wave, these authors established the following equation for the shear motion

$$S = \frac{\Gamma}{4\pi\rho V_S^2} \quad (54)$$

where  $\rho$  is the medium's density and  $\Gamma$  given by the following equation

$$\Gamma = \frac{1}{d} e^{-i\omega d/v_S} + \left( \frac{1}{i\frac{\omega d^2}{v_P}} - \frac{1}{\frac{\omega^2 d^3}{v_P^2}} \right) e^{-i\omega d/v_S} - \left( \frac{v_S}{v_P} \right)^2 \left( \frac{1}{i\frac{\omega d^2}{v_P}} - \frac{1}{\frac{\omega^2 d^3}{v_P^2}} \right) e^{-i\omega d/v_P} \quad (55)$$

Note that these velocities are complex, and have a component related to hysteretic damping. Also, the equation for  $\Gamma$  can be divided into three parts according to

$$\Gamma = \Gamma_1 + \Gamma_2 - \Gamma_3 \quad (56)$$

where each component is equal to its equivalent part in equation (55). As a result, it is possible to understand that a transversal sinusoidal wave has a different mode of propagation than the considered shear wave, propagating longitudinally and polarized transversally (Ferreira, 2003). Each component corresponds, in fact, to shear movements, but move at different velocities. The first two components are related to the velocity of the shear wave, while the last component is associated with the velocity of the compression wave.

Also, each component has its own damping coefficients, which results in a faster decay for the last two components and creates the so-called near field effect. In addition, in a time domain analysis, the “actual” shear wave, corresponding to  $\Gamma_1$ , appears last.

The near field effect is a recurrent source of error in seismic wave testing, characterized for an interference of the initial response wave due to single wave reflection. In an attempt to evaluate the wave configuration due to this effect, Sanchez-Salinero *et al* (1986) adopt the parameter  $R_d$  given by

$$R_d = \frac{d}{\lambda} \quad (57)$$

which is the ration of the number of wavelengths  $\lambda$  that occupy a certain distance  $d$ . These authors found that for values of  $R_d < 2$  the combination of the three components  $\Gamma_1$ ,  $\Gamma_2$  and  $\Gamma_3$  is clear and also that there is an initial wave deflection. This near field effect amplifies if  $R_d$  is increased, i.e., the test frequency is increased. This created a generalized opinion that signal acquisition with bender elements is improved by measuring shear and compression waves in separate, using specific bender elements associated to each wave (Brignoli *et al*, 1996).

Jovicic *et al* (1996) also evaluated the influence of boundary conditions and the near field effect on analytical solutions in bender element tests, in triaxial chambers. They found that for low values of  $R_d$  the near field effect is confirmed, and that it disappears for values higher than 8.1.

Besides the near field effect, there are other issues that affect the test quality, some of which are connected to the equipment itself. Arulnathan *et al* (1998) stated that the near field effect in bender element tests is more complex than the common triaxial cell test and three reasons that justify it:

- The used interpretation methods have a null value of  $R_d$ , which can imply that the near field effect are much more relevant than the one considered;
- The waves generated by the transmitter bender element have spherical diffusion and can, therefore, be reflected on the sample boundary and propagate between the bender and the sample;

- The transmitted bender element creates waves along the its surfaces, i.e., is not a point source.

Additionally, these authors also analyzed unidimensional propagation of waves, using bender elements, to evaluate the effect of reflected waves in the sample's rigid boundaries, i.e., the soil sampler or the walls of the chamber. Using a parameter similar to  $R_d$ , comprising wavelength and the bender element's length ( $\lambda/l_b$ ), they found that not considering the wave reflection can lead to significant deviations when calculating the propagation time, relevant to obtaining the wave speed. Also similar to  $R_d$ , this the propagation time is overrated when the stated relation ( $\lambda/l_b$ ) increases.

Note that Jovicic *et al* (1996) and Arulnathan *et al* (1998) findings both regard relative (spatial) scales, already mentioned in 2.3.1.3., and their effect in bender element tests.

Another issue to account for is the bender element's resonance. When the benders are excited with a frequency close to their resonant frequency (or natural frequency), they will oscillate with increased amplitude, not corresponding to the expected amplitudes. Viggani and Atkinson (1995) evaluated the resonant frequency of bender elements in triaxial cells and found that it comprises values from  $f_n = 2kHz$  to  $f_n \geq 10kHz$ . Ferreira (2003) found some irregularities in the response signal due to the bender element's resonance in some tests.

Electrical noise, or pink noise, can also be seen in the response wave, due to the bender element's frequency range. This can be mitigated by carefully assembling the test equipment and assuring good cable insulation conditions, for example. In addition, some testing equipment can effectively filter the characteristic signal of the electrical current, with a frequency of 50Hz (Ferreira, 2003).

Even though all the above issues can be mitigated, their added effects can contribute to somewhat significant deviations from the expected results. As such, and as stated before, they should be taken in consideration when evaluating both methodologies and test results alike.



# 3

## EXPERIMENTAL PROGRAM

### 3.1. INTRODUCTION

The present chapter begins by giving an explanation on the established planning of the experimental program, briefly stating its considerations, objectives and sequence.

The preparation of the tested soil samples follows, with indications and justification of some assumptions made throughout this stage of the experimental program, such as sample size, sample liner conditions and residual soil variability.

The used laboratory equipment are described, with relevant information on their use. The test set up is also approached, accompanied by figures and photographs of the conducted experimental procedures.

### 3.2. PROGRAM OVERVIEW

This research was based on tests on three soil samples from residual soil from Porto granite. These samples were tested using the available bender elements, to measure seismic waves generated by a function generator and acquired by means of an oscilloscope. The visualization of the test results was possible using a PC and proper software, available in the oscilloscope manufacturer's websites.

The primary focus of the experimental program was to establish considerations on bender element testing for damping determination, as well as the implementation of different methodologies for determining damping ratio. Also, an evaluation on the accuracy and applicability of these methodologies was also achieved, by comparison with one another and with resonant column test results. The comparison with resonant test results was pertinent, given that this method is normalized and standardized, establishing a reference value for damping ratio.

### 3.3. SOIL SAMPLE PREPARATION FOR BENDER ELEMENT TESTING

A soil sample from CEFEUP experimental site was provided by Geotechnical Laboratory, LabGeo for use in this research. The cylindrical bored sample was stored in the laboratory’s humid chamber and labeled “CEFEUP-Borehole S2”, collected at a depth of 9-9.5m.



Figure 3.1 – CEFEUP-Borehole S2 (after first sawing)

This soil sample was divided into three smaller specimens for testing, which geometry is displayed in the following table. These measurements were obtained using a caliper rule and a conventional scale. Note that both diameter and weight include the PVC sampling liner.

Table 3.1 –Test sample geometry

Test sample: CEFEUP-BoreholeS2 (9-9,5m depth)						Preparation date: 01/04/2015					
Sample 1 - P1				Sample 2 - P2				Sample 3 - P3			
h [cm]		D [cm]		h [cm]		D [cm]		h [cm]		D [cm]	
10,33		7,50		15,16		7,61		4,92		7,63	
10,29	10,29	7,45		15,11	15,14	7,64		5,00	4,96	7,67	
10,24		7,45		15,16		7,63		4,96		7,60	
		7,55				7,63				7,60	
		7,55				7,68				7,58	
		7,55				7,60				7,68	
Vol [cm <sup>3</sup> ]	454,45	γ [kN/m <sup>3</sup> ]	19,79	Vol [cm <sup>3</sup> ]	688,78	γ [kN/m <sup>3</sup> ]	19,48	Vol [cm <sup>3</sup> ]	226,79	γ [kN/m <sup>3</sup> ]	19,51
Weight [g]	917			Weight [g]	1368			Weight [g]	451		



Figure 3.2 – Testing samples: P1, P2 and P3

As such, the three test samples P1, P2 and P3 were defined as having a height of 100mm, 150mm and 50mm, respectively. The different heights of the samples were intentional, in order to evaluate its effect on test results. The considered soil volumetric weight was established using the average of each sample's values, at  $\gamma = 19.60 \text{ kN/m}^3$ .

The slight variation of diameter is due to the sampler's conditions. As seen in Figure 3.2, and Figure 3.3 in detail, it was cracked top to bottom, and the crack opening was wider in the region used for sample P1 (100mm).



Figure 3.3 – Detailed view of the sampling liner crack

Typical residual soil characteristics were visible right from the sample preparation stage. The resulting sawed surfaces were highly irregular, since some larger grains were sawed off and fell when the cut

was complete. Also, when sawing samples P1 (100mm) and P3 (50mm) a big mass of clayey material was found, a clear evidence of the high variability and heterogeneity, typical of this residual soil.



Figure 3.4 – Sawed surfaces: surface irregularity (left) and presence of finer mass (right)

### 3.4. RESIDUAL SOIL FROM PORTO GRANITE

The tested residual soil, originated from Porto granite rock, presents several characteristics that make it unique. Its chemical and mineralogical constitution varies greatly, resulting in a fairly heterogeneous mass (Ferreira, 2009) composed by weathered alkaline rock with medium to coarse grains and micas (Costa and Teixeira, 1957).

This residual soil, characteristic of the northwestern zone of Portugal, generally has a small clay fraction with low activity minerals. As such, the residual soil from Porto granite present low to none plasticity (Matos Fernandes, 2006). The following figure shows various grain sized distribution curves of this type of soil. Note that the dotted fuse corresponds to more than 100 curves.

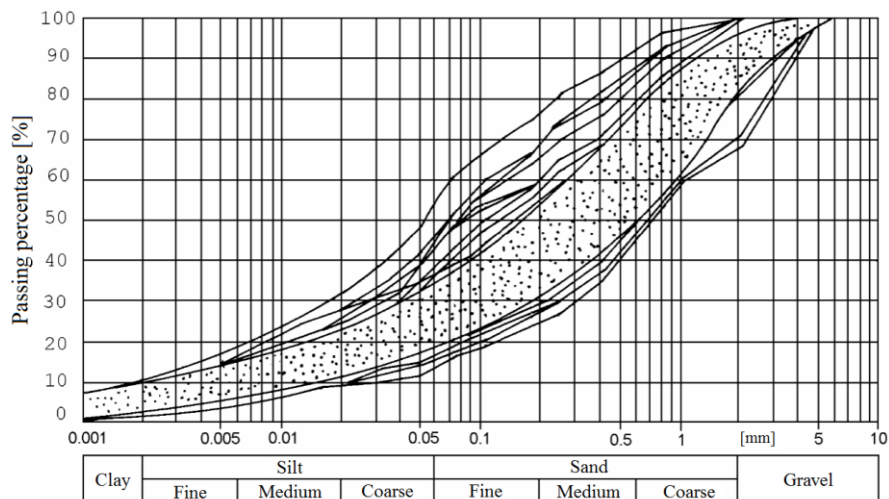


Figure 3.5 – Grain size distribution curve for granitic residual soils from northwestern Portugal (adapted from Viana da Fonseca *et al*, 2006)

The main weathering factors of granite rocks act at the discontinuities level (number, spacing, orientation and continuity of joints) and at the proximity of various geological events that, eventually, may increase water flow on the already mentioned discontinuities. As such, Viana da Fonseca *et al* (2003), found that the following weathering factors were prevalent

- Location;
- Topography, in particular natural slopes;
- Mass joint and composition of the parent rock;
- Climate factors, such as rain intensity, temperature gradients and humidity;
- Hydrologic factors, such as water level and percolation;
- Presence of vegetation.

According to ASTM D2487-85, residual soil from Porto granite can be classified as silty (SM) or well graded (SW) sand, and more uncommonly as clayey sand (SC).

Usual ranges for some physical parameters are presented in Table 3.2.

Table 3.2 – Natural physical parameters for residual soil from Porto granite (Viana da Fonseca *et al*, 2003)

$\gamma_s$ [kN/m <sup>3</sup> ]	w [%]	$\gamma_d$ [kN/m <sup>3</sup> ]	$S_r$ [%]	e	k [m/s]
25,7 - 26,5	15 - 25	15,0 - 18,5	80 - 100	0,40 - 0,70	$10^{-6}$ - $10^{-5}$

Several studies have been made in the past several years, by various authors from the University of Porto, in an attempt to characterize this particular residual soil for design purposes (Silva Cardoso, 1986; Viana da Fonseca, 1988, 1996; Begonha, 1989; Viana da Fonseca *et al*, 1994, 2006; Ferreira, 2003, 2009; among others). The present dissertation's purpose also involves the characterization, and validation, of dynamic properties of this soil, in particular on damping parameters.

### 3.5. TESTED SOIL IDENTIFICATION AND CHARACTERIZATION

In order to characterize the tested soil, a disturbed sample collected at 3m of depth from FEUP's experimental site, CEFEUP, labeled "CEFEUP-Plat.2-Field4", was submitted to grain size distribution analysis according to CEN ISO/TS 17894, as well as water content and specific gravity, according to CEN ISO/TS 17892-1 and CEN ISO/TS 17892-4, respectively. The equivalent ASTM standards are ASTM D 6913-04, ASTM D2216-98 and ASTM D2937-94, respectively.

Given that these experimental procedures are normalized and can be reviewed in the aforementioned standards, these are not further detailed in this dissertation. Photographs of these identification tests carried out in this research are presented in the following figures 3.7 to 3.10..



Figure 3.6 – Disturbed sample and its reconstitution



Figure 3.7 – Heating of soil sample with sodium hexametaphosphate (left), mixing of heated sample with a particle mixer (right)



Figure 3.8 – Beaker used for specific gravity determination (left), detail on deposited particles after 24h (right)



Figure 3.9 – Pycnometers prepared for heating

The tested soil was found to have a water content of 31.6%. The specific gravity for the whole sample was  $20.8\text{kN/m}^3$ , while the specific gravity for the passing of sieve #10 was  $26.4\text{kN/m}^3$ . The resulting grain size distribution curve is shown in the following Figure 3.10. Note that the complete test results are included in the appendix.

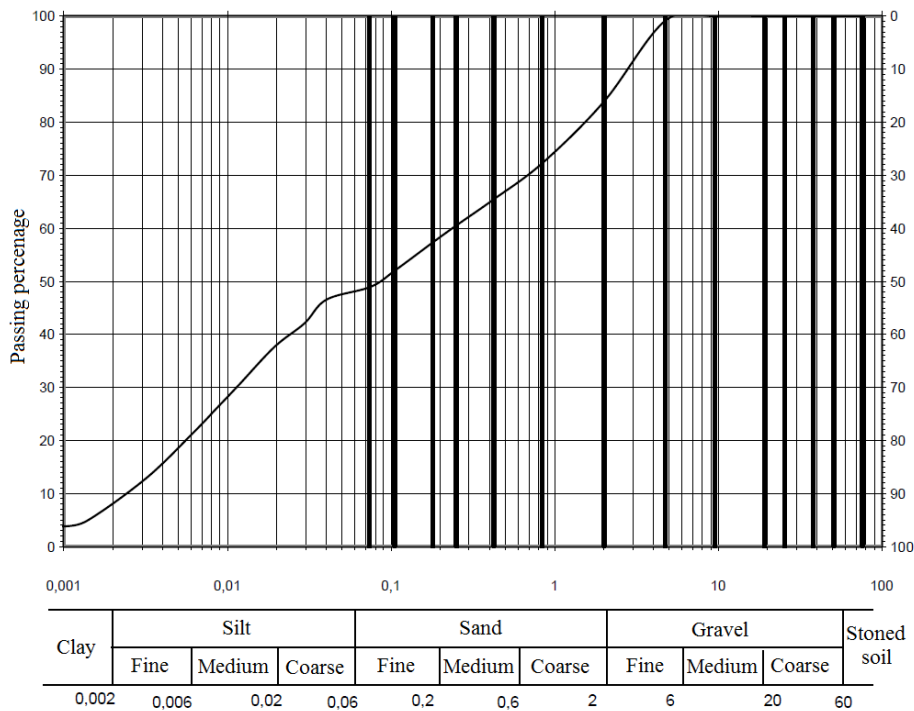


Figure 3.10 – Grain size distribution curve of the soil under study

The following figure shows the conformity between the tested soil’s granulometry and the fuse proposed by Viana da Fonseca *et al* (2006).

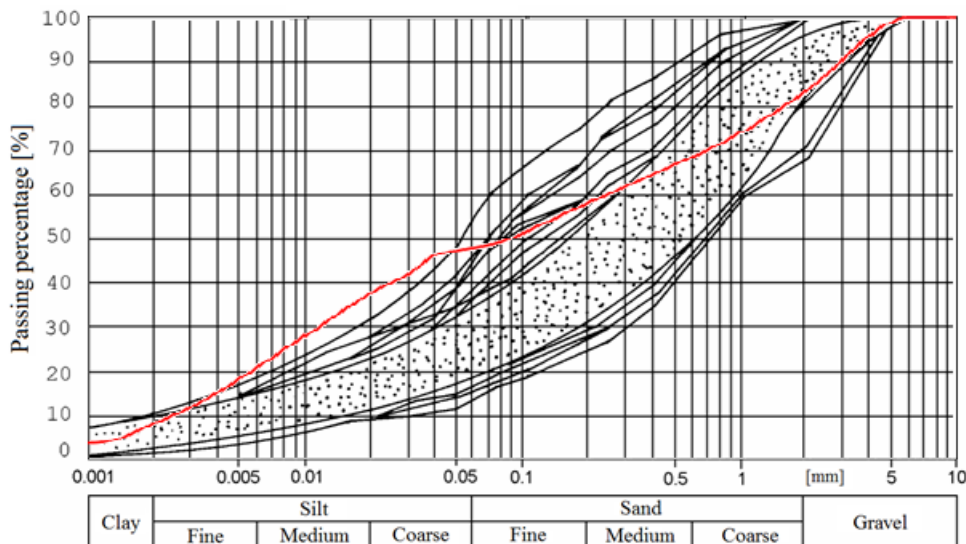


Figure 3.11 – Grain size distribution curve of the soil under study (red) fit to Viana da Fonseca *et al* (2006) fuse

The tested soil is a silty sand (SM) with gravel, according to ASTM D2487-85. In addition, it presents slightly more silt than the more usual residual soil from Porto granite, proof of the high natural variability of this soil.



### 3.6. EXPERIMENTAL PROCEDURE






The experimental program was conducted in the Geotechnical Laboratory (LabGeo) of the Faculty of Engineering of the University of Porto (FEUP). It provided all the necessary equipment in order to successfully complete the laboratory tests. Furthermore, the tested soil samples were also stored in LabGeo’s humid chamber.

The used laboratory equipment, methodologies, test samples are described in this subchapter, which also presents some discussion on test results and data analysis. Note that only relevant data for discussion is presented here, given that full presentation of the test data would be too lengthy to include here. As such, all the laboratory test results are included in the appendix.

#### 3.6.1. LABORATORY EQUIPMENT

The following table presents the used laboratory equipment, accompanied by a brief description. These were collected from their respective manuals or manufacturer’s websites, when applicable.

Table 3.3 – Laboratory equipment used in the experimental procedure

	Equipment	Description
Bender elements		--- These bender elements were manufactured in LabGeo. With dimensions of approximately 2.0x0.4x0.2cm, these were successfully used previously in other author’s researches (Ferreira, 2009) .
Function generator		TTI TG1010 A programmable function generator with frequency range of 0.1mHz to 10Mhz, capable of creating and saving various signal configurations (sinusoidal, square, ramp and arbitrary, in continuous or triggered mode).
Oscilloscopes		Tektronix TDS220 An oscilloscope capable of a record length of 2500 points per channel. Various acquisition modes are possible with this equipment, such as whole sample, average sample and peak detection.
		PICO ADC-212 A low cost oscilloscope capable and FFT-based spectrum analyser. Dual-channel, 16bit resolution and 333kS/s sampling rate. This analyzer digitizes the signal using an analog-to-digital converter and the stored values are then processed using a FFT algorithm.
Amplifier		--- A two-channel amplifier developed by ISMES-Enel.Hydro manufacturer. Capable of amplifying input and output signals by up to 10x.

#### 3.6.2. TEST SETUP

The bender element test setup used in this research is shown in Figure 3.12. The bender elements were installed at the top and bottom ends of each sample, and the signal to drive the transmitter bender element was generated by two different function generators. The transmitter bender element was connected directly to the generator and an oscilloscope, and the receiving bender element was

connected to the signal analyzer. A signal amplifier was also used in order to improve the signal readability.

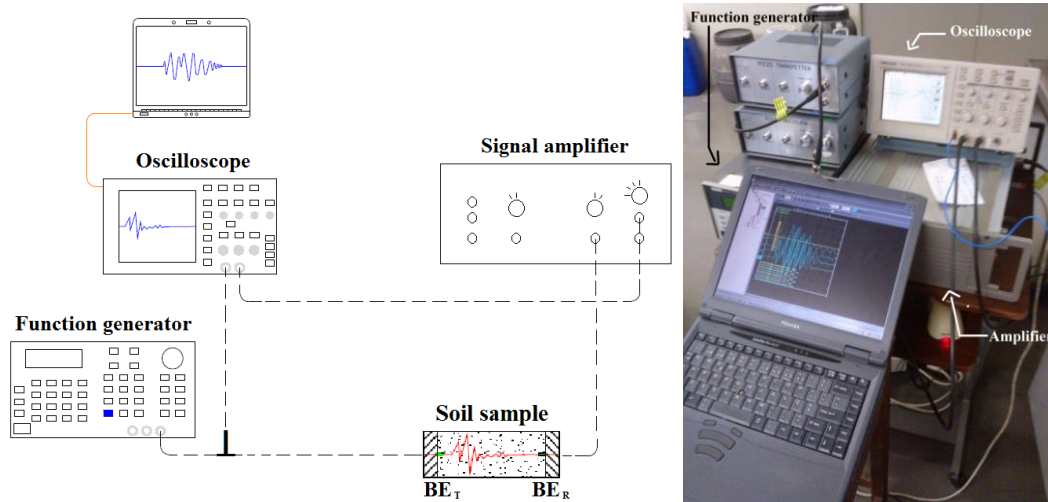


Figure 3.12 – Test setup: schematic representation (left); close up photograph

### 3.7. DAMPING DETERMINATION

As stated before in chapter 2, damping determination can be achieved by either a time domain or frequency domain analysis. This subchapter gives a more thorough explanation on the frequency domain method and also exposes some methods based on these two types of analysis.

A frequency domain analysis involves the transformation of data with respect to time into frequency; while a time domain graph illustrates how amplitude changes with time, a frequency domain graph (i.e., a frequency spectrum or simply spectrum) illustrates how much of the signal has a certain frequency.

In order to transform time domain data into frequency domain data (and *vice versa*), a transform function must be applied to the data. The most commonly used transform function is the Fourier transform, which follows Fourier’s analysis theory. This theory states that complex functions (seismic waves, in this case) can be broken down into the sum of simpler sinusoidal functions, each with its own frequency component (Fourier, 1822) Figure 3.13 demonstrates the transformation of time domain data into a frequency spectrum, by breaking down a complex wave into a sum of waves with different frequencies.

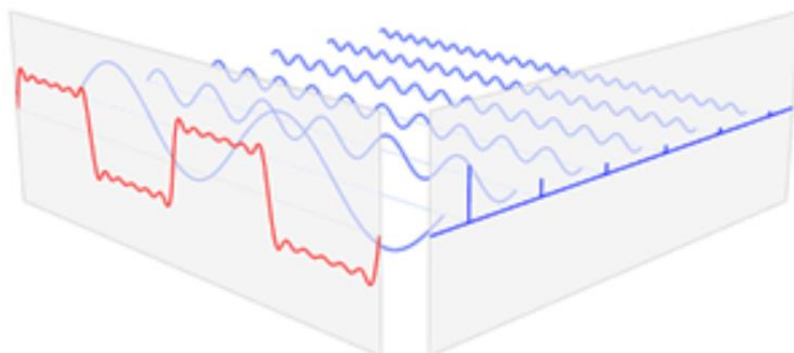


Figure 3.13 – Fourier transform: time domain data (red) into frequency domain data (blue) (Barbosa, 2013)

The present dissertation uses the fast Fourier transform, FFT, which is a fast computation algorithm for the discrete Fourier transform, DFT. The FFT, or DFT for that matter, transforms an array of  $N$  real values of sample data, with intervals corresponding to the sampling interval (inverse of the sampling frequency); into  $N$  complex values of transformed, dimensionless sample data, with equally spaced intervals that do not correspond to neither time nor frequency. In order to match the dimensionless data, or bins, to its corresponding frequency range, the sampling frequency,  $f_s$ , is used to establish this connection. These complex values hold information on magnitude and phase of the signal, each related to the real and imaginary parts of the transformed data, respectively.

Figure 3.14 illustrates the basic concept of the FFT.

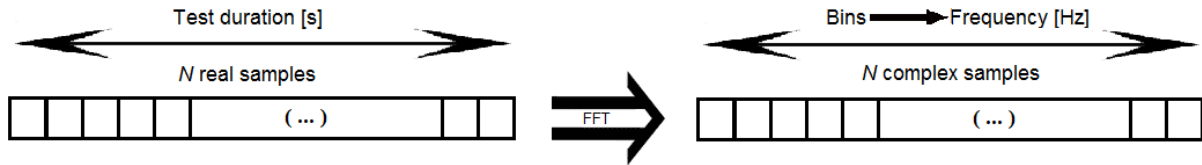


Figure 3.14 – Explanation on the use of the FFT for test data

Note that the spectrum calculated using the FFT is symmetric and, as such, the second half of the data is redundant. This is why most frequency spectra, such as the ones presented in this dissertation, only show its first half (single-side spectrum).

One of the grey areas in this type of modal testing is deciding the number of degrees of freedom to assign to the test subject (Inmann, 2001). The easiest method to use on this type of data is the SDOF method. In this method the spectrum is sectioned in ranges containing each resonant peak. Then, each peak is analyzed individually, assuming that that the frequency associated with maximum magnitude is the response frequency of that mode of vibration. As such, this method assumes that in the vicinity of the resonance the frequency response is dominated by that mode.

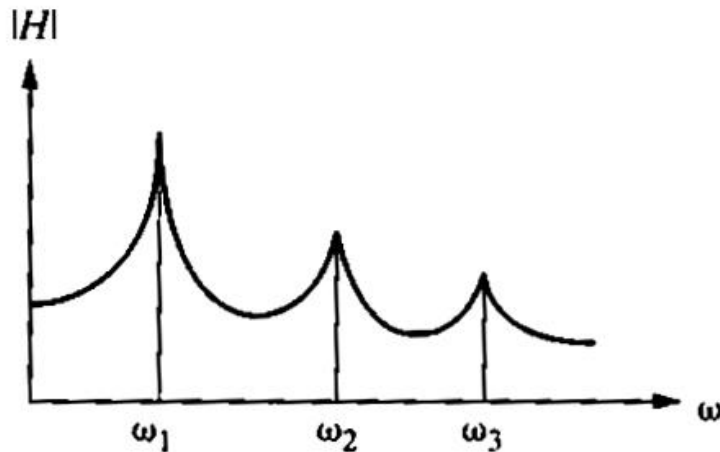


Figure 3.15 – Generic frequency spectrum plot (Inmann, 2001)

In addition, for the frequency range around the first resonant peak it is assumed that the plot is due to a harmonic input at, or near, the first natural frequency (Inmann, 2001).

### 3.7.1. LOGARITHMIC DECREMENT METHOD

Observing an underdamped system response, an envelope can be determined to express its decay in amplitude. For such system, this decay envelope presents a logarithmic shape, as already shown in Figure 2.20.

The peaks of the response data can be curve fit to the decay envelope, by using a logarithmic decrement method, and so the system's damping can be calculated based on a time domain analysis.

The logarithmic decrement, which can be interpreted as the energy loss per cycle (Santamarina *et al*, 2001), is defined by the following equation

$$\delta = \ln \left( \frac{x(t)}{x(t+T)} \right) \quad (58)$$

Substituting the analytical form of the underdamped equation of motion (equation (34)) equation (58) becomes

$$\delta = \ln \left( \frac{Ae^{-\xi\omega_n t} \sin(\omega_d t + \Phi)}{Ae^{-\xi\omega_n(t+T)} \sin(\omega_d t + \omega_d T + \Phi)} \right) \quad (59)$$

where  $\omega_n$  and  $\omega_d$  are the angular natural frequency and the damped angular natural frequency, respectively. Given that  $T = 2\pi/\omega_d$  for low damping (Inman, 2001), the previous equation becomes, when solving for the damping coefficient,

$$\xi = \frac{\delta}{\sqrt{4\pi^2 + \delta^2}} \quad (60)$$

Note that this method can be applied to any two positive successive peaks. To improve the accuracy of  $\delta$ , equation (59) can be modified in order to account for various successive peaks (Inman, 2001)

$$\delta = 1/n \ln \left( \frac{x(t)}{x(t+nT)} \right) \quad (61)$$

Where  $n$  is the number of peaks after the maximum peak.

### 3.7.2. HALF-POWER BANDWIDTH METHOD

The most common method of measuring damping uses the relative width of the response spectrum and the resonant frequency. Using the quantities indicated on Figure 3.16, the logarithmic decrement can be calculated, according to Richart *et al* (1970), by

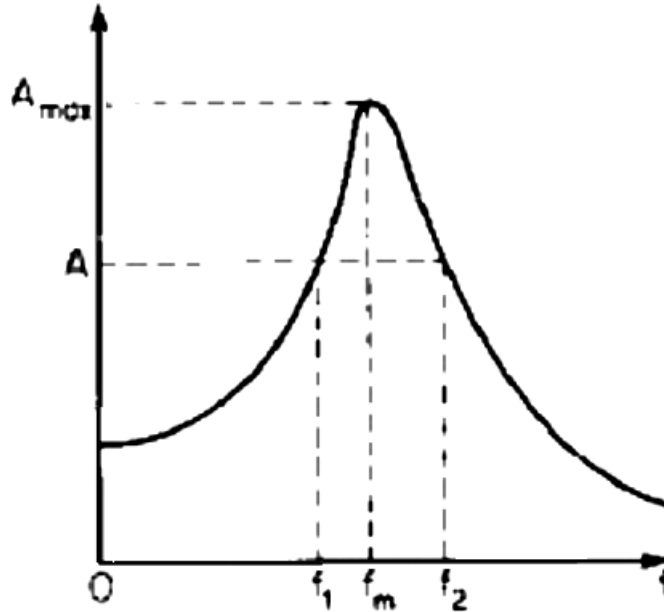


Figure 3.16 – Resonant curve for half-power bandwidth method (Richart *et al*, 1970)

$$\delta = \frac{\pi}{2} \frac{f_2^2 - f_1^2}{f_m^2} \sqrt{\frac{A^2}{A_{max}^2 - A^2}} \frac{\sqrt{1 - 2\xi^2}}{1 - \xi^2} \quad (62)$$

where  $A_{max}$  is the maximum amplitude,  $f_m$  its resonant frequency and  $f_1$  and  $f_2$  the frequencies at each side of  $f_m$ , for a certain value of amplitude,  $A$ .

For the case of low damping ratio, the previous equation can be simplified to (Brocanelli and Rinaldi, 1998)

$$\xi = A \frac{f_2^2 - f_1^2}{\sqrt{A^2 f_2^4 - 2A^2 f_2^2 f_1^2 + A^2 f_1^4 + 16f_m^4 (A_{max}^2 - A^2)}} \quad (63)$$

Furthermore, if  $A$  is chosen equal to  $A_{max}/\sqrt{2}$ , equation (62) becomes (Karl, 2005)

$$\xi = \frac{f_2^2 - f_1^2}{4f_m^2} \quad (64)$$

The half-power bandwidth method (HPBM) needs a large number of data points in order to accurately define the resonant curve/spectrum, which makes damping calculation experimentally difficult with standard oscilloscopes and signal generators (Brocanelli and Rinaldi, 1998).

### 3.7.3. CIRCLE-FIT METHOD

If the real part of the frequency response is plotted versus its imaginary part, the resulting figure is a circle. These planes are commonly called Nyquist plots, or Argand plane plots (Inman, 2001). Ewins (1984) proposed an alternative approach to the determination of material damping based on these Nyquist plots, where the resulting circles are fitted in order to determine the natural frequency and estimate the system's damping.

Considering a SDOF system with viscous damping, the dynamic mobility is given by

$$Y(\omega) = \frac{i\omega}{(k - \omega^2 m) + i(\omega c)} \quad (65)$$

or, in terms of its complex components, by

$$\left(Re(Y) - \frac{1}{2c}\right)^2 + (Im(Y))^2 = \left(\frac{1}{2c}\right)^2 \quad (66)$$

where

$$Re(Y) = \frac{\omega^2 c}{(k - \omega^2 m)^2 + (\omega c)^2} \quad (67)$$

$$Im(Y) = \frac{i\omega(k - \omega^2 m)}{(k - \omega^2 m)^2 + (\omega c)^2} \quad (68)$$

The plot from the resulting equation (66) plots in the Nyquist plane according to Figure 4.12.

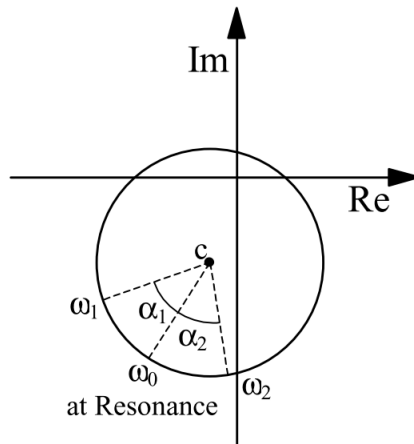


Figure 3.17 – Nyquist plot for determination of material damping (Karl, 2005)

Damping can then be calculated, based on the following equation (Ewins, 1984)

$$\xi = \frac{\omega_2^2 - \omega_1^2}{2\omega_0(\omega_2 \tan(\alpha_2/2) + \omega_1 \tan(\alpha_1/2))} \quad (69)$$

where  $\omega_0$  is the angular frequency corresponding to the natural frequency,  $\omega_1$  and  $\omega_2$  are the angular frequencies corresponding to the points at each side of  $\omega_0$  and  $\alpha_1$  and  $\alpha_2$  their corresponding angles.

Contrary to the half-power bandwidth method, the circle-fit method's (CFM) circle plot can be defined with fewer data points that do not necessarily need to include the ones corresponding to the natural frequency. Still, note that the half-power bandwidth method allows the analysis of close peaks and other resonant nodes in the proximity of the resonant node under study, which can distort the shape of the plot in the Nyquist plane, while this effect can be imperceptible in the circle-fit method (Brocanelli and Rinaldi, 1998).





# 4

## EXPERIMENTAL RESULTS AND ANALYSIS

### 4.1. INTRODUCTION

In this chapter the performed experimental procedures using bender elements are detailed. The first test results refer to time domain analysis, where its experimental procedure and results are described. The same is also done for the frequency domain tests. Note that the first approach based on frequency domain analysis was performed by trial and error, where different methods of test implementation, data acquisition and treatment were tested. As such, the first “calibration” sample presents a more thorough experimental procedure, where these issues were tested and discussed. After data treatment, the tests and analyses of the subsequent samples were performed in a more efficient and focused manner.

These results from the tested samples are then compared with results obtained by Ferreira (2009) when testing the same soil using the resonant column test. Given that this test is normalized and has a well-defined procedure and analysis methodology, it was possible to assess, evaluate and calibrate the author’s tests accuracy and applicability.

### 4.2. TIME DOMAIN ANALYSIS USING TEKTRONIX TDS220

On a first analysis, all three samples were tested using the Tektronix TDS220 oscilloscope, with each test data imported to PC. These tests were performed with a series of continuous, sinusoidal wave function with various frequencies, in order to implement the logarithmic decay method. The used frequency range was from 1kHz to 10kHz, and the used frequencies were chosen based on the quality of the received wave.

Given that no normalized equipment or procedure exists for damping determination in bender element testing, some considerations were made for their installation:

- The bender elements were installed by direct penetration of the sample. This installation had to be done carefully, in order to not disturb significantly the initial conditions in the vicinity of the BE and to prevent damage to them;
- In normal testing conditions, the gap between the sample end the bulkier part of the BE is usually filled with an impermeable flexible material, such as silicone rubber (Rio, 2006). However, no such material was available and, as such, the BE penetrated the soil sample until the bulkier part was in contact with the soil sample;
- The fixation of the BE to the sample was assured by two styrofoam molds. Later, a weight was used to keep the top styrofoam mold in place, as depicted in Figure 4.1;

- The use of these molds to keep the BE in place was also useful to secure the grounding wiring in place, in order to reduce background and electrical noise;
- Since this test was a bench test, it was found that when some laboratory equipment were running (specially LabGeo's air compressor) the background noise was very significant. As such, BE testing regarding bench tests must be carefully isolated in order to minimize noise.

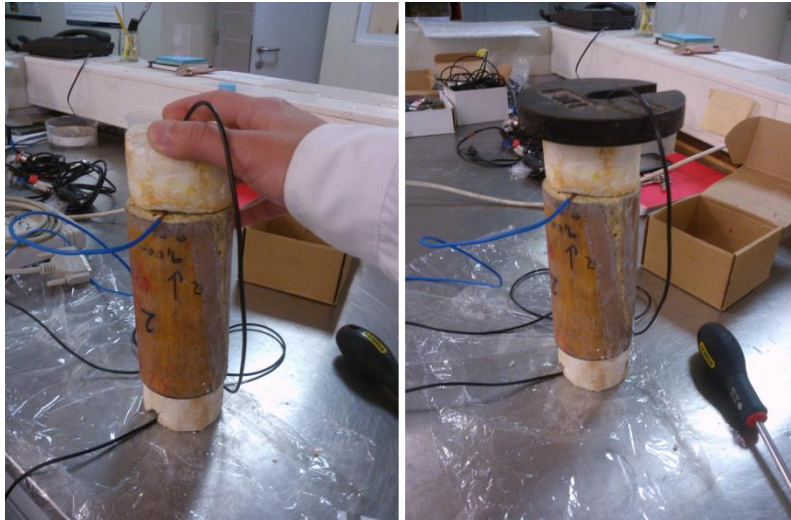


Figure 4.1 – Bender element fixation and testing

The test data was displayed using the manufacturer's software WaveStar (version 2.4), which presented a time domain plot for analysis. Figure 4.2 shows some experimental results for sample P1 (100mm), where the received wave for 8kHz was excluded to improve readability. The remaining test results are included in the appendix and are mentioned when relevant. In addition, Table 4.1 displays information on data acquisition and test characteristics.

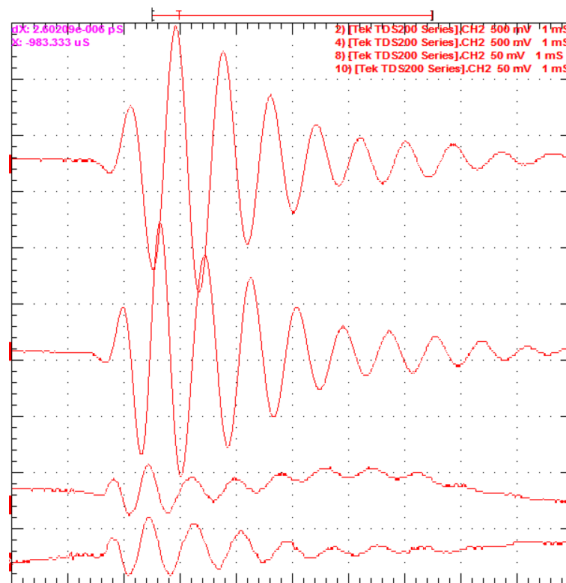


Figure 4.2 – Time domain analysis for sample P1 (100mm): output wave for 1kHz, 2kHz, 4kHz and 10kHz

Table 4.1 – Time domain test characteristics

Test sample	Window resolution		Tested signal frequencies					
	Input	Output	1kHz	2kHz	4kHz	6kHz	8kHz	10kHz
P1 (100mm)	5V ; 1ms	500mV ; 1ms 50mV ; 1ms	X	X	X		X	X
P2 (150mm)			X	X	X	X		
P3 (50mm)			X	X	X		X	

Given that the entire (relevant) peak data was available, it was possible to calculate damping based on various numbers of successive peaks. While the accuracy of this method is improved with a higher use of number of successive peaks (Inman, 2001), it was found that some signals were significantly noisy, disturbed or presented successive peaks with very similar amplitudes (Figure 4.15).

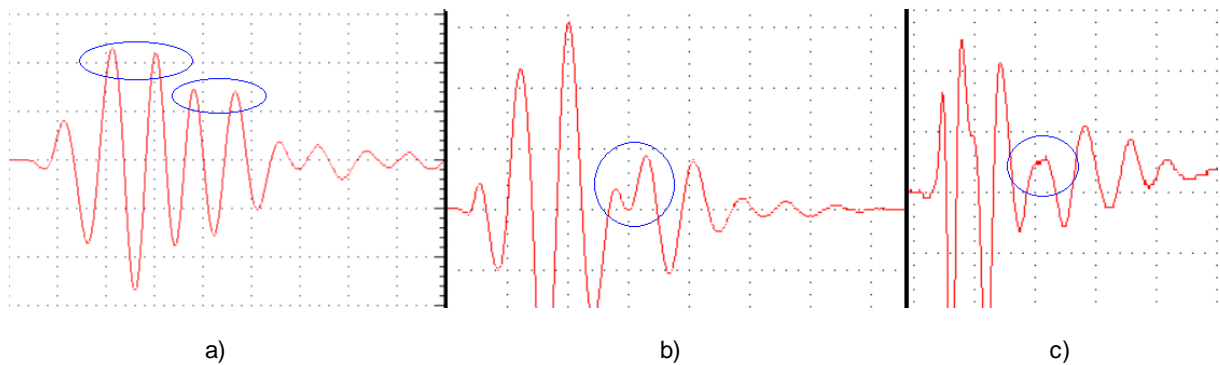
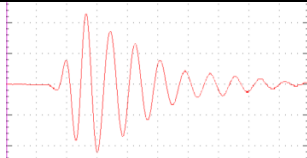
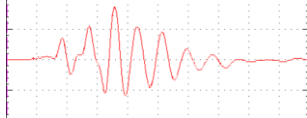
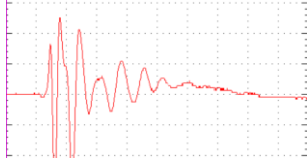
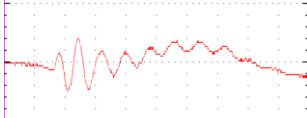


Figure 4.3 – Signals with poor logarithmic decay envelope due to: a) similar successive peaks, b) misshapen peaks and c) irregular peaks

As such, while implementing this method, an evaluation parameter was created and designated “signal quality”. This parameter attempts to qualify the received signal in terms of data quality, as the name suggests, in order to evaluate the method’s applicability. The signals were classified by having very low, low, high or very high quality. Unfortunately, this qualification is subjective and based on the observation of the received wave trace. Table 4.2 explains the attribution of this nomenclature in order to minimize the subjectivity of this classification.

Table 4.2 – Signal quality terminology

Signal quality		Description
Very high		Signal with near-perfect decay envelope
High		Signal with small but noticeable effects, such as slightly misshapen peaks, successive peaks with similar amplitude and/or noise, affecting slightly the decay envelope
Low		Signal with aggravated effects of misshapen peaks, successive peaks with very similar amplitude, peaks with irregular amplitude and/or noise, affecting significantly the decay envelope
Very low		Signal heavily affected by misshapen peaks, successive peaks with very similar amplitude, peaks with irregular amplitude and/or noise, justifying its disposal due to low applicability of the method

In order to implement the logarithmic decay method, the test data was imported from WaveStar to Excel in order to have the information regarding amplitude (voltage) of the received waves. With the various values from peak amplitudes, the logarithmic decrement was calculated as stated before in 4.4.1..

Given that the results are extensive, only the ones regarding sample P2 (150mm) are presented, in Table 4.3. In addition, Table 4.4 shows the various damping values for each test sample, regarding each tested frequency. The remaining test results are presented in the appendix.

Table 4.3 – Sample P2 (150m) test results for the logarithmic decay method

	Voltage [mV]			
	1kHz	2kHz	4kHz	6kHz
Max peak	1220	1600	332	100
Following peaks	1180	1060	224	68
	800	960	208	60
	780	500	108	30
	260	340	80	22
	-	160	-	-
Signal quality	Low	High	High	High
Nr. of successive peaks	Logarithmic decrement, $\delta$			
	1kHz	2kHz	4kHz	6kHz
2	0,0333	0,4117	0,3935	0,3857
3	0,2110	0,2554	0,2338	0,2554
4	0,1491	0,3877	0,3743	0,4013
5	0,3865	0,3872	0,3558	0,3785
6	-	0,4605	-	-

Nr. of successive peaks	Damping [%]			
	1kHz	2kHz	4kHz	6kHz
2	0,5	6,5	6,3	6,1
3	3,4	4,1	3,7	4,1
4	2,4	6,2	5,9	6,4
5	6,1	6,2	5,7	6,0
6	-	7,3	-	-

red value = peak value similar to the previous one

Table 4.4 – Summary of damping values for the logarithmic decay method

Sample	Damping [%]					
	1kHz	2kHz	4kHz	6kHz	8kHz	10kHz
P1 (100mm)	7,1	6,5	7,5	-	X	X
P2 (150mm)	4,8	6,0	6,0	6,2	-	-
P3 (50mm)	7,5	3,7*	5,8	-	X	-

X = discarded result due to very low signal quality; red value = low quality test result; - = untested frequency; \* = test with low amplitude variability

The damping values determined by the logarithmic decrement method depend greatly on the signal wave quality. This method relies on the assumption that the wave configuration can be fit to a logarithmic decay envelope, which is hard to achieve during testing. Furthermore, higher frequency signals caused lower quality test results due to the amount of noise present in the received wave.

Given that these factors were unknown at the time of the test, damping determination based on the logarithmic decay method provided overall poor results.

### 4.3. FREQUENCY DOMAIN ANALYSIS USING PICO ADC-212

In order to obtain data to implement both half-power bandwidth and circle-fit methods, the Tektronix TDS220 oscilloscope was substituted by a PICO ADC-212. This change was made based on an attempt to have a higher sampling frequency, given that frequency domain methods require a large number of data points in order to properly define the frequency spectrum (Brocanelli and Rinaldi, 1998).

The chosen input wave was a sine sweep signal, which was successfully used by several authors successfully in the past (Greening and Nash, 2004; Rio, 2006; Ferreira, 2009). By varying the frequency of the input signal, it is possible to obtain information regarding the sample's resonance modes for that frequency range.

As stated before, the first test sample was used to determine preferred ways to acquire data and to define a treatment method using an original, author-written Matlab script, as well as compare the results of this script with previously tested software, namely ABETS (Ferreira, 2003; 2009). Some considerations are described along with the used methodology, both for test execution and script writing.

4.3.1. “CALIBRATION” SAMPLE P2 (150MM)

The first test data was acquired using ABETS software. ABETS (Automatic Bender Element Testing System) is a programmed Excel file, developed by Paul Greening, from UCL Department of Civil and Environmental Engineering, capable of reading and treating BE test data. Its use has demonstrated satisfactory results for analysis (Greening and Nash, 2004; Ferreira, 2003; 2009).

Three different sweep waves were used for this sample. The description of these input waves is presented in Table 4.5.

Table 4.5 – Sample P2 (150mm) sweep wave definition

	Starting frequency	Stopping frequency	Input scale	Output scale	Sampling frequency
Sweep 1	200 Hz	5 kHz	10 V	2 V	200 kHz
Sweep 2	800 Hz	5 kHz	10 V	5 V	
Sweep 3	1 kHz	4 kHz	10 V	5 V	

ABETS also allows the treatment of the test data, in addition to its acquisition. It is capable of displaying the test plot in time domain, as well as calculating the associated frequency vector, magnitude, coherence and both wrapped and unwrapped phase. It also automatically plots the frequency spectrum and wrapped/unwrapped phases. Unfortunately, this software is not capable of damping calculation. However, its results can be used to its calculation, thus justifying its use.

An example of the plots provided as outputs of ABETS are presented in the following figures. The complete test results are available in the appendix.

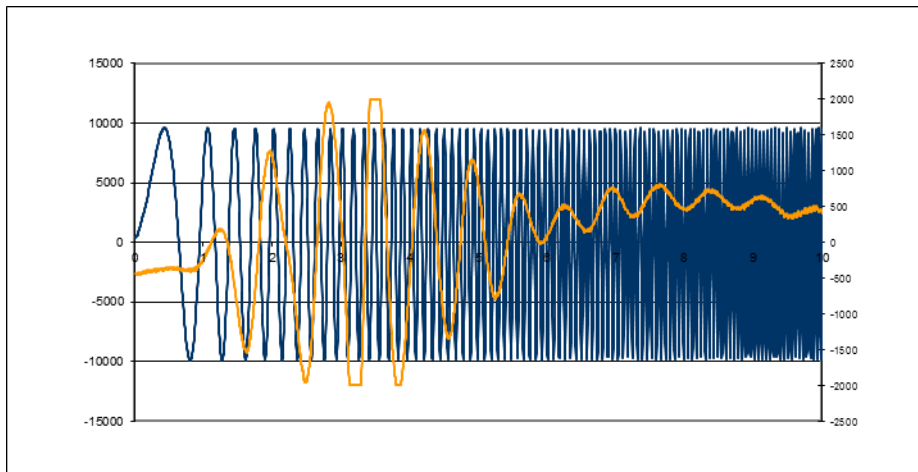


Figure 4.4 – Sample P2 (150mm), sweep 1: ABETS input and output amplitude versus time

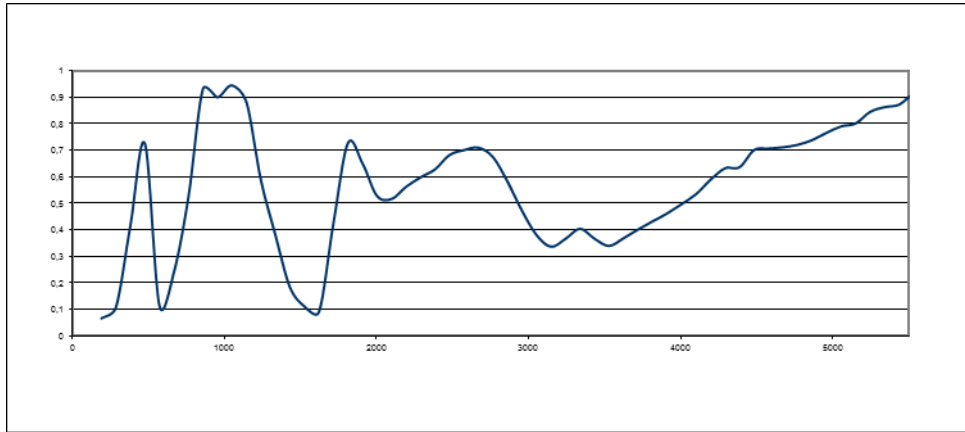


Figure 4.5 - Sample P2 (150mm), sweep 1: ABETS coherence *versus* frequency

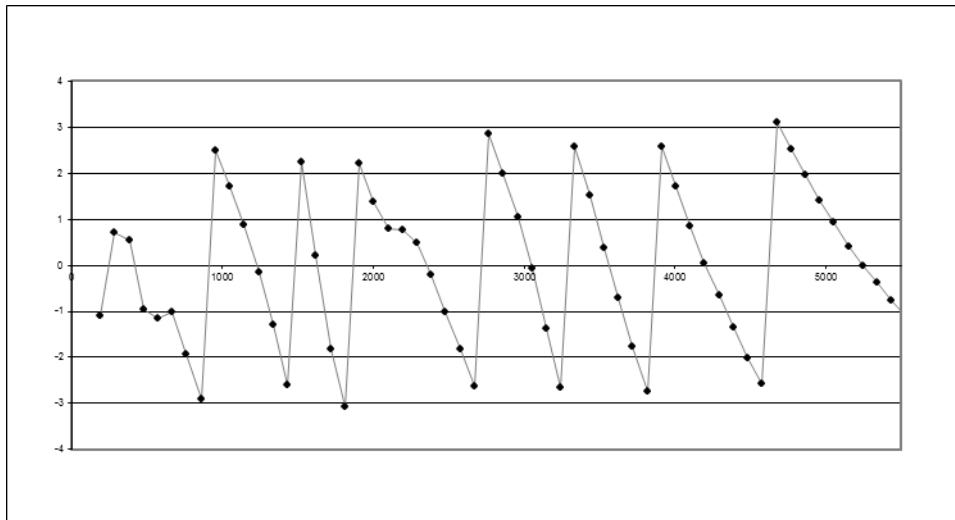


Figure 4.6 – Sample P2 (150mm), sweep 1: ABETS wrapped phase angle *versus* frequency

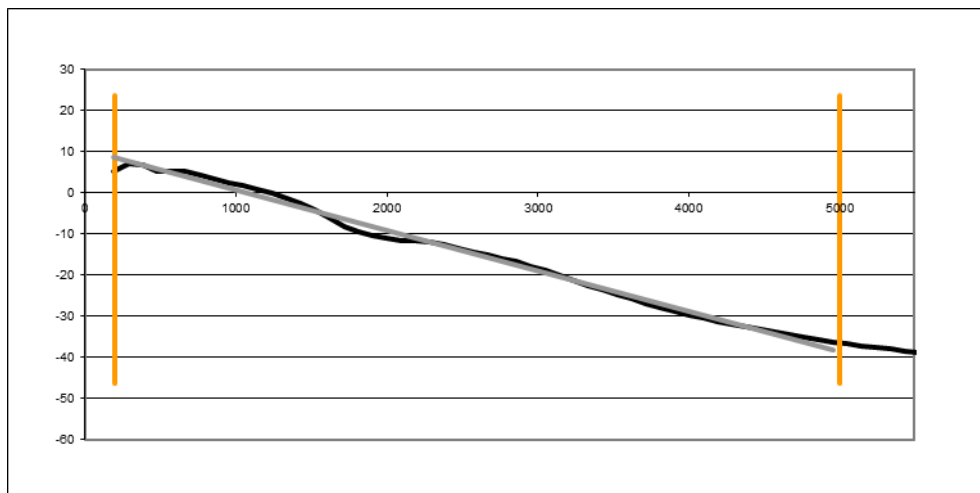


Figure 4.7 – Sample P2 (150mm), sweep 1: ABETS unwrapped phase angle *versus* frequency

After examining the first sweep test results, the following considerations were made:

- ABETS automatically defines a time and frequency domain range. The time domain range usually comprehends the first wave of the sweep, while the frequency domain comprehends the start and stop frequencies of the sweep;
- The received wave was truncated for certain values of voltage, resulting in some data inaccuracy for those data points. Even though care was taken in the definition of the window resolution, the chosen output scale was not enough. Hence, further consideration must be done when defining window resolution.

Unfortunately, the current ABETS code is invisible to the user. It uses multiple dynamic link libraries (DLL's) in order to analyze and treat data, many of which are actually Matlab DLLs. In order to better understand this software capacities and data treatment procedures, the possibility of using of Matlab was studied and applied.

Matlab is a powerful software interactive environment developed by MathWorks, widely used worldwide with innumerous capacities such as numeric computation, programming and algorithm development and data analysis (MathWorks, 2015).

The development of the Matlab script began at this time. Its first focus was the export of test data from the ABETS Excel file, for subsequent data treatment and representation similar to ABETS procedures. Comparison between ABETS and Matlab results was valuable in order to evaluate the script and the possibility of using Matlab for data analysis.

The first part of the script's algorithm imported the time domain test data and calculated its respective frequency vector, in order to plot the frequency domain figures. This frequency vector was calculated based on the sampling frequency of the signals, as already mentioned.

In order to calculate magnitude and phase information, Matlab provides a preset command to calculate its FFT. This command was used, and the magnitude and phase information were retrieved by calculating the real and imaginary parts of the FFT, respectively. It also has a preset command to evaluate coherence, which was used in the same manner.

The first issue regarding this script was the noise in the signal (Figure 4.8), which was not present in the ABETS results. This noise significantly affected the frequency spectrum and, therefore, would affect damping determination using the aforementioned methods. Note that the data used for ABETS and this script was exactly the same, which means that ABETS was removing this noise in some manner.



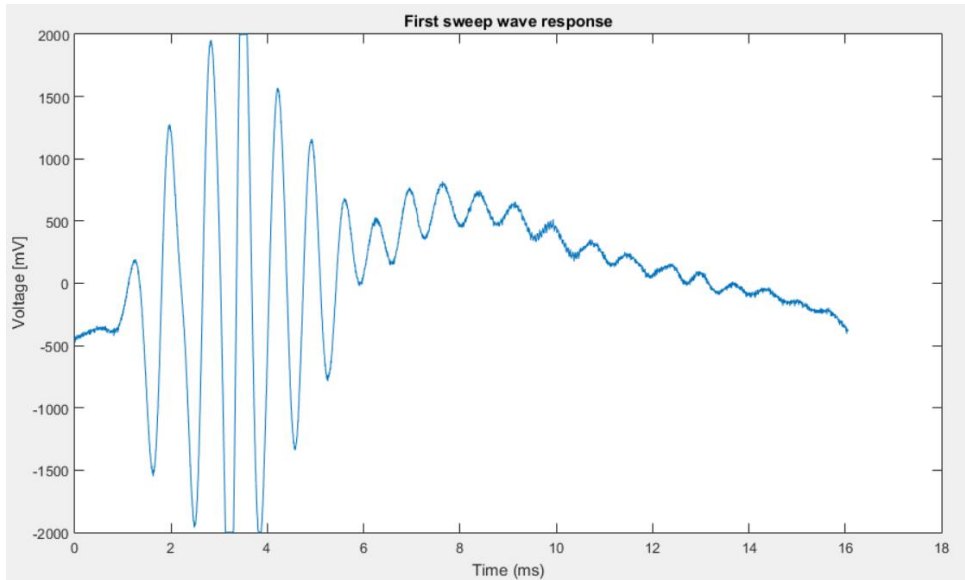


Figure 4.8 – Presence of noise in the first wave of sweep 1

In order to remove the noise to improve test data, in a similar fashion as ABETS, some methods were tested. These methods are described below and include an evaluation of their effect on data analysis and results. Not all of the tested methods were actually implemented, but the ones which were used are identified accordingly.

#### 4.3.1.1. Matlab script hypotheses

Matlab includes a signal analysis tool, which was taken into consideration for data analysis. This “Signal Analysis Application” has the capacity of representing and providing some analysis on signals and spectra, as well as defining filters.

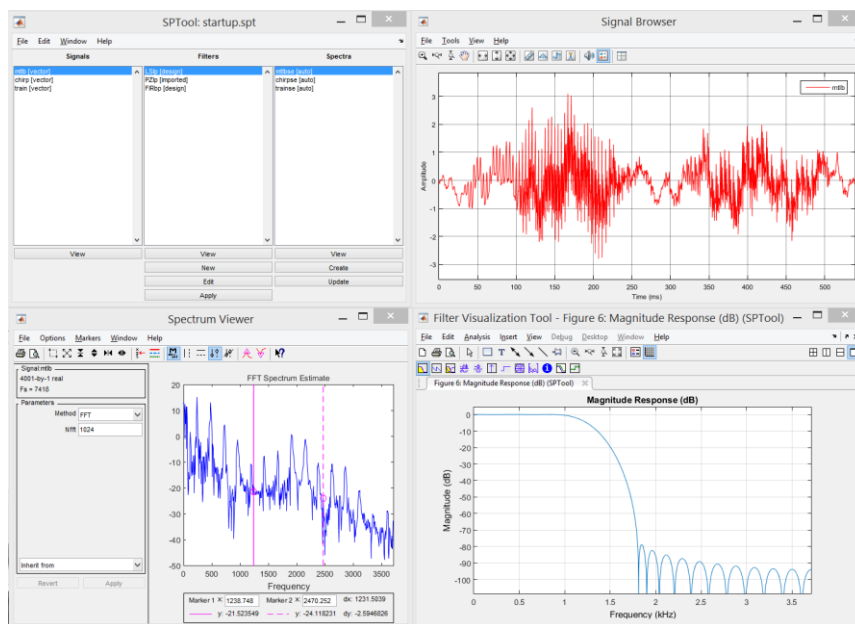


Figure 4.9 – Matlab’s Signal Analysis Application (Matlab incorporated data for example)

However, the use of this tool proved to be very limited in terms of data definition and treatment. In addition, only the information presented in Figure 4.9 was available for visualization, which would difficult the comparison between Matlab and ABETS data. As such, it was decided to use the actual Matlab algorithm capabilities to develop a script to analyze and represent data in a more flexible and controlled manner.

The evaluation of the use of a filter followed. The use of Butterworth filters was proven successful by a previous author (Ferreira, 2009) and, as such its viability was tested. A Butterworth filter (Butterworth, 1930) is a low-pass filter and, therefore, only passes the part of the signal with frequency lower than the designated cutoff frequency and attenuates the part of the signal with higher frequency than the cutoff frequency (as mentioned before). Matlab also provides preset commands to define Butterworth filters and its application. This process slightly improved the signal quality, but it was still not enough to produce reliable test results.

The next step was to create a moving average filter, which would average the values of adjacent points (or groups of points), which would attenuate fast signal variations. Its implementation caused a displacement of the data vector due to the aggregation of values, i.e., a delay in time domain. This delay can be overcome by accounting for it in data representation. However, this method would significantly reduce the number of data points available, highly compromising the implementation of the half-power bandwidth and circle-fit methods. In addition, the magnitude values were highly altered by the moving average filter. Therefore, the use of moving average filter was discarded. Still, its algorithm is included in the final part of the script for reference.

Each sweep comprehended more than one sine sweep wave test. Using the average of the signals is a technique that could reduce noise in the treated signal. This technique assumes that, for an ideal situation, signal and noise are uncorrelated, the signal strength is the same for each repetition and that noise is random. As such, the more signals are included when averaging, the higher the signal-to-noise ratio, *signal/noise*, increases (Van Drongelen, 2006). Figure 4.10 shows the results regarding the direct signal averaging for the aforementioned sweep test. Each truncation represents one sine sweep wave response.

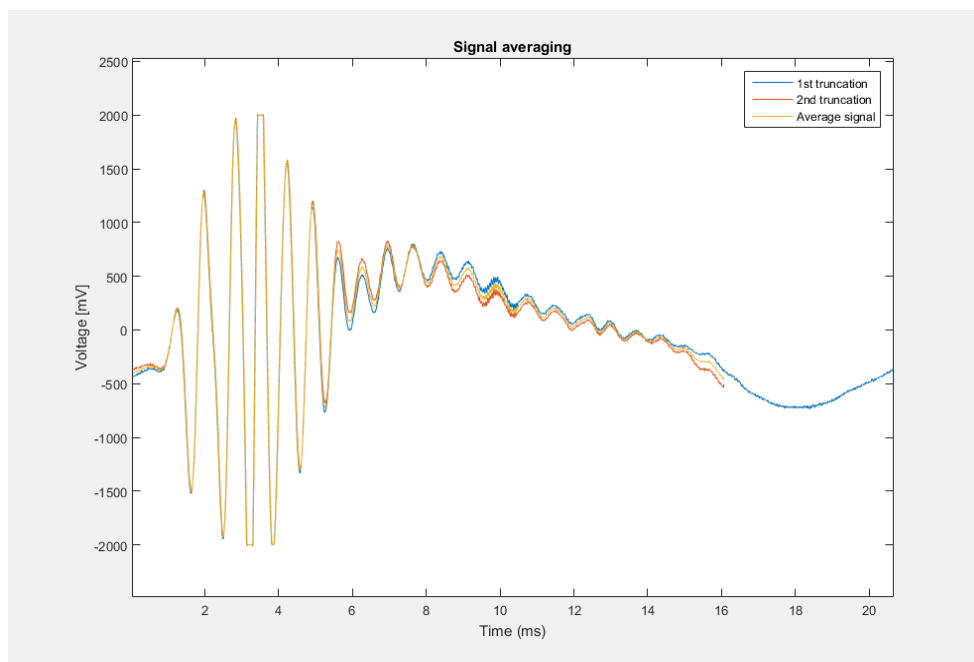


Figure 4.10 – Signal averaging for the first sweep

In addition to the direct averaging of the signals, averaging of the value of the FFT and averaging of the signal magnitudes were also experimented. However, the results obtained for these two methods were absurd.

Signal averaging proved to be an effective method to improve the quality of the test. This, in addition to the Butterworth filter, was enough to produce smoother signal and frequency spectra, enabling the implementation of the half-power bandwidth and circle-fit methods. The implemented script is presented in the appendix, with some indications along the algorithms that explain what it is doing and why. The script does the following steps:

- Given an Excel file name and after defining some vector ranges, it imports the vectors corresponding to the time vectors of the various truncations of the original signal;
- Calculates the sampling frequency of the signals;
- Imports the received wave corresponding to the time vectors previously determined;
- Averages the previous signals and applies a user-defined Butterworth filter, finalizing the received wave signal for spectral analysis;
- Calculates the signal's FFT, followed by coherence, phase and magnitude;
- Defines the frequency vector used for the spectral analysis, based on the sampling frequency and the number of unique points of the spectrum, in order to represent the single-side spectrum;
- Plots the following figures: time domain representation of the test signals; coherence between input and output signals; phase of the received signal; unwrapped phase of the received signal; frequency spectrum.

This script is not completely automated and requires some user-defined parameters to work successfully. More particular aspects and limitations are included in 4.6.2..

When the remaining sweep wave tests were to be treated with the Matlab script, it was noted that these two sweep tests, unlike the first one, presented different starting conditions. The first test data acquisition started when the first sweep wave started, which meant that it contained complete received wave data information. However, the second and third sweeps presented a random starting point, and for that reason, the tests did not contain all the information of the received wave.

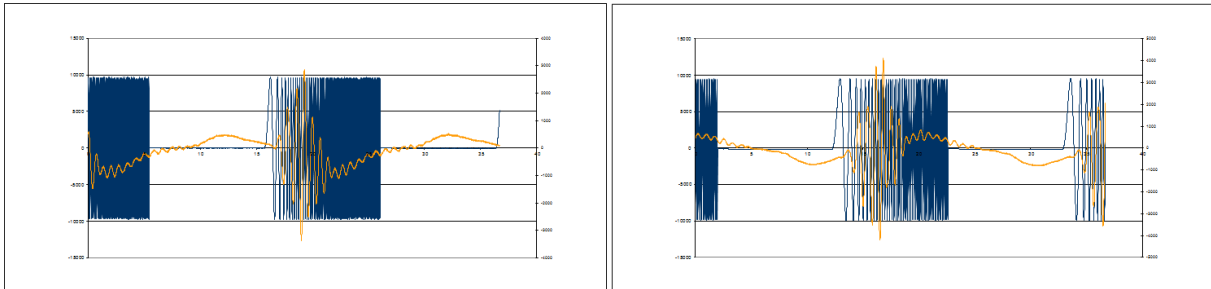


Figure 4.11 – Sample P2 (150mm): missing data from the second (left) and third sweeps (right)

After further analysis, it was found that ABETS acquired data at random intervals and the fact that the first sweep data acquisition began at the same time as the first sweep wave was just coincidence. Furthermore, given that these last two sweep tests did not provide the same information as the previous one, they were ultimately discarded.

### 4.3.1.2. Comparison between Matlab and ABETS results

Now that Matlab data processing results were ready for analysis, the same plots that were obtained by ABETS were also represented, in order to evaluate the similarity between results. The following figures show the Matlab treated data versus ABETS treated data.

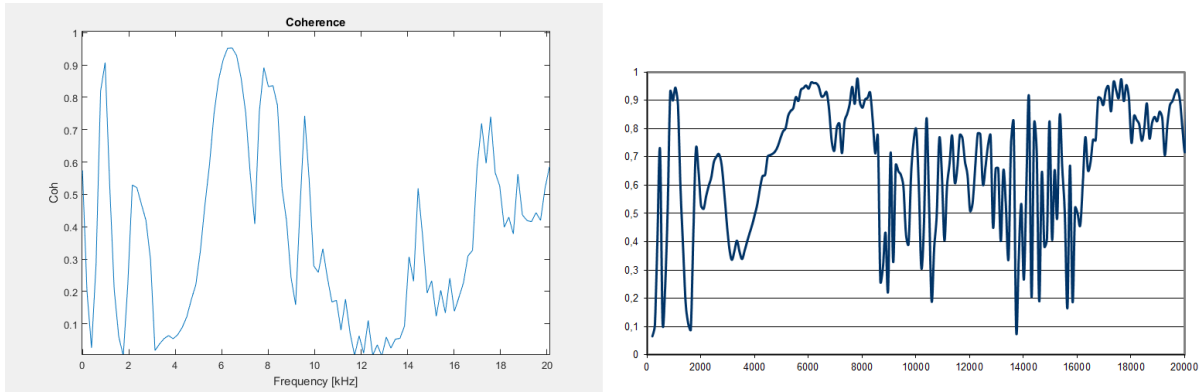


Figure 4.12 – Comparison between Matlab (left) and ABETS (right) results: coherence

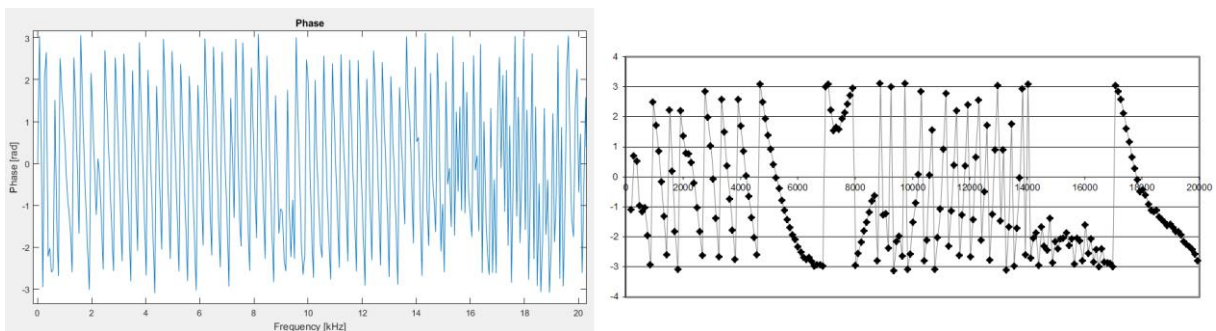


Figure 4.13 – Comparison between Matlab (left) and ABETS (right) results: phase

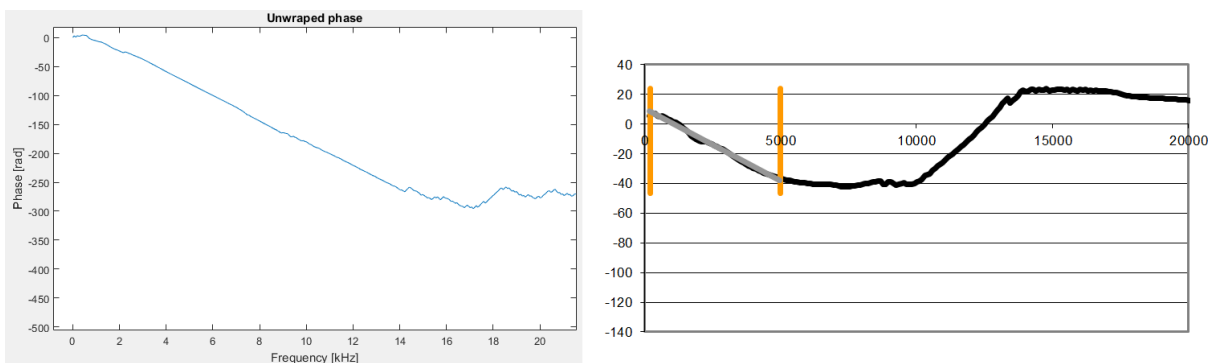


Figure 4.14 – Comparison between Matlab (left) and ABETS (right) results: unwrapped phase

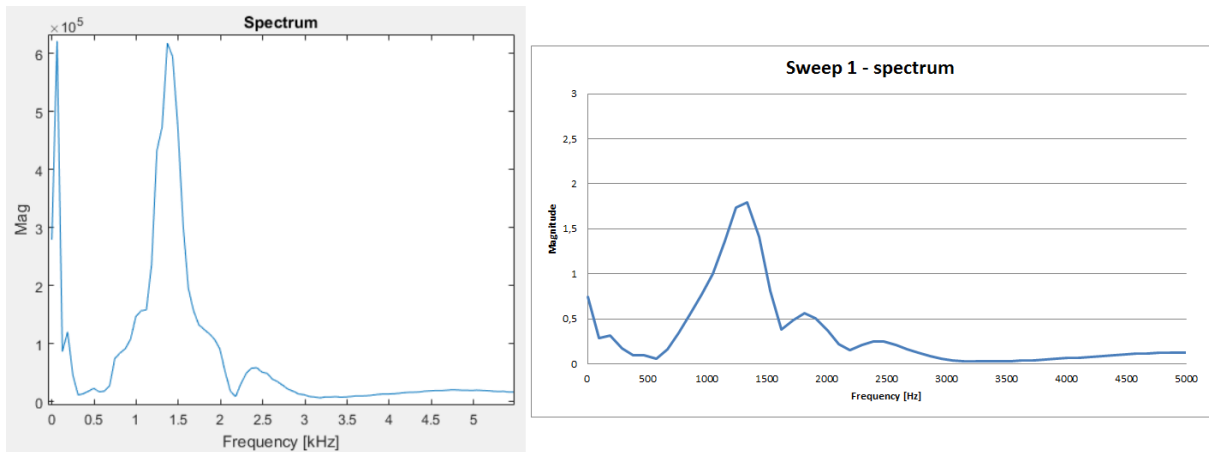


Figure 4.15 – Comparison between Matlab (left) and ABETS (right) results: frequency spectrum

A quick analysis on the above figures show that Matlab and ABETS data are not in agreement. Even though the coherences are similar up to 8kHz and the frequency spectrum has a similar shape, the results are significantly different. In addition, the order of magnitude of the frequency spectra are different, another proof that ABETS performs a signal treatment methodology that is not fully understood.

#### 4.3.1.3. Considerations on the completed work so far

The explained procedure enabled the formulation of the following considerations:

- The two truncations had a different number of data points (review Figure 4.10), due to the data acquisition from ABETS. ABETS acquires the correct length (duration) of the test, but does not synchronize acquisition with the beginning of the sweep wave input. As such, acquisition with ABETS may not include the whole sine wave responses, resulting in some data loss. It is important to acquire the results, in ABETS or any other software, that successfully gathers a well-chosen data range;
- Given that the second and third sweep tests had large missing portions of data (shown in Figure 4.11), it was not possible to average the input signal, which caused a received wave (and spectrum) with too much noise to implement the half-power bandwidth and circle-fit methods. Therefore, these test results were eventually discarded;
- As already mentioned, the display window (and scale ranges) must be carefully selected in order to show the full extents of the signal, that is, to not truncate some peaks, which occurred in the first sweep (Figure 4.16). This leads to lower accuracy both in time domain amplitude analysis and in the spectrum definition in frequency domain analysis. The display window must be adapted to each sweep, independent of acquisition software;

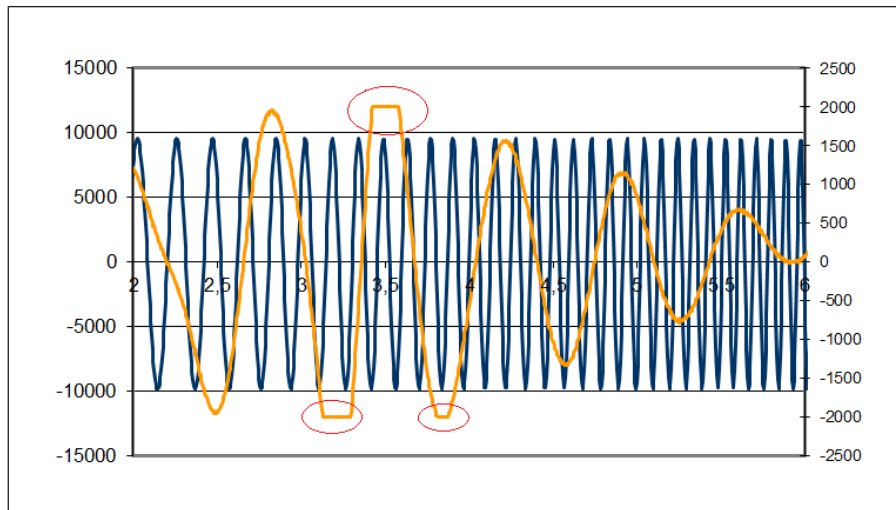


Figure 4.16 – Sample P2 (150mm), sweep1: detailed view on amplitude truncation

- ABETS automatically ignores the first data points, concerning the first sampling frequencies, given that these data are highly influenced by noise and, therefore, are unreliable. The Matlab script does not ignore these data entries, which are represented in its spectrum. Nevertheless, the peaks caused by this effect are ignored;
- The magnitude calculated by ABETS is normalized in some unknown way, different from the usual  $Mag/Max(Mag)$  ranging from  $[0; 1]$ , while the Matlab script calculates the “real” values of magnitude. Karl (2003, 2005) presented spectra with magnitude values similar to Matlab’s values, so the spectrum calculated by the Matlab script is admitted to be correct;
- After signal averaging, the improvement caused by the implementation of the Butterworth filter was lower than the improvement caused before averaging. This turned the use of the Butterworth filter somewhat obsolete, and so it was eventually removed from the script;
- Given that the Matlab results were in conformity with previous authors’ results (Karl, 2003, 2005; Brocanelli and Rinaldi, 1998) and that the analysis and processing procedure was known, spectral analysis using ABETS was discontinued.

#### 4.3.1.4. Further script developments: half-power bandwidth and circle-fit methods

In order to determine the tested soil damping, a new script was written, this time specialized in importing test data and determine damping using the half-power bandwidth method (HPBM). This script was also used to determine if the differences between Brocanelli and Rinaldi (1998) and Karl (2003, 2005) equations for damping determination. The resulting script is included in the appendix, with notes along the algorithms explaining its functioning. It does the following steps:

- Given an Excel file name and defining some vector ranges, imports vectors corresponding to the time vectors of the various truncations of the original signal;
- Calculates the sampling frequency of the test;
- Defines the frequency vector used for the spectral analysis, based on the sampling frequency and the number of unique points of the spectrum;
- Plots the various truncations of the signal and the resulting averaged signal;

- Calculates the signal’s FFT and magnitude;
- Plots the resulting frequency spectrum;
- Calculates the magnitude,  $A_m$ , and frequency,  $f_m$ , associated with the maximum magnitude (excluding the first peaks at low frequencies)
- Calculates the “notable” value of  $A = A_m/\sqrt{2} = A_{not}$ ;
- For the left side of the spectrum, defines the two data points that include  $A_{not}$ , checks their frequency and interpolates the frequency  $f_1$ ;
- The same procedure, for the right side of the spectrum in order to determine  $f_2$ ;
- Determines damping using Brocanelli and Rinaldi (1998) and Karl (2005) formulations, exposed in 4.4.2. as equation (63) and (64), respectively.

Similar to the previous script, this one also possesses some particularities and limitations, also exposed in 4.6.2..

The following figure and table present the script’s results, in addition to the damping values according to the aforementioned authors, for the resulting frequency spectrum.

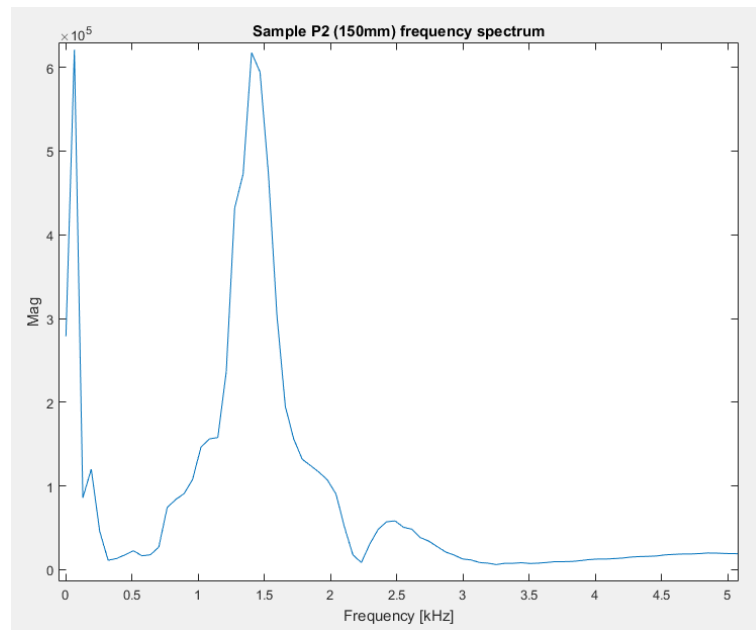


Figure 4.17 – Sample P2 (150mm): frequency spectrum

Table 4.6 – Sample P2 (150mm): half-power bandwidth method results

$A_m$	$f_m$ [kHz]	$A_{not}$	$f_1$ [kHz]	$f_2$ [kHz]	$\xi_{BR}$	$\xi_K$
6.1751e+05	1.40	4.3665e+05	1.28	1.54	9.39%	9.35%

The damping values obtained for Brocanelli and Rinaldi (1998) and Karl (2003; 2005) equations were  $\xi_{BR} = 9.39\%$  and  $\xi_K = 9.35\%$ , respectively. As expected, the damping values are very similar, resulting in a final average damping value of  $\xi = 9.4\%$ . Either equation is plausible for determining low damping values in soils.

In order to implement the circle-fit method (CFM) and evaluate its conformity with the HPBM, a circle-fitting algorithm had to be used in order to plot a circle that fits the data points around the resonant peak. Since the information on the resonant peak was already obtained using the half-power

bandwidth method, this new script would take the real and imaginary parts of these data points, plot them in the Nyquist plane and determine the best-fitting circle for the data.

A circle-fitting algorithm was needed in order to fit the test data. The algorithm proposed by Pratt (1987), based on direct least squares fitting, was found online already adapted in Matlab readable language. This script is also available in the appendix.

A preliminary analysis of the resonant peak, obtained using the HPBM script, showed signs of data inadequacy for the CFM. Even though this method can be defined with fewer data points than the HPBM, the resonant peak presents very few data points, which could compromise this method's applicability.

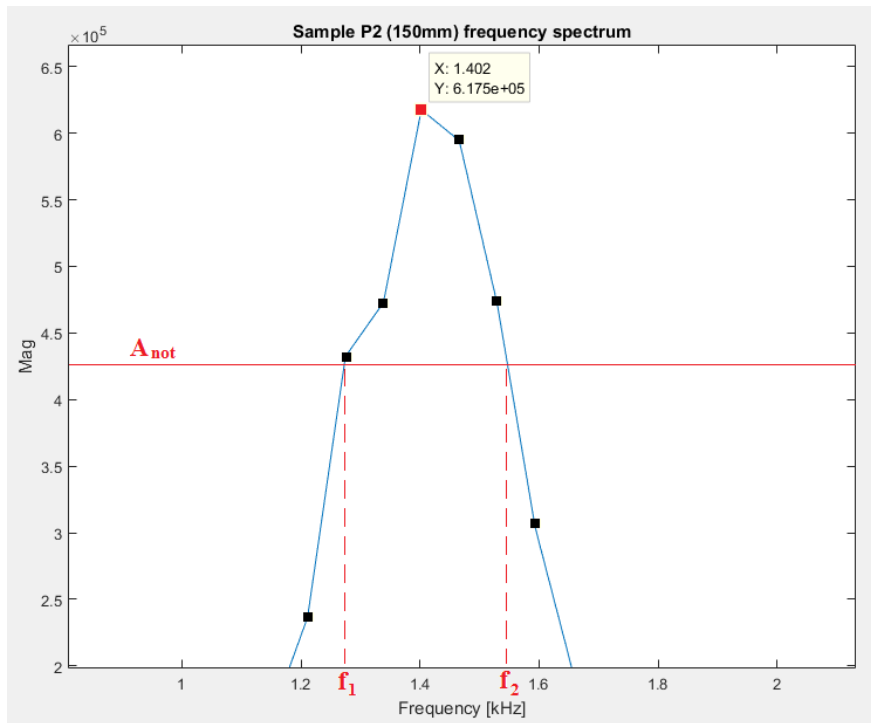


Figure 4.18 – Close up on sample P2 (150mm) resonant peak

The first step to evaluate the applicability of the circle-fit method for the obtained test data consisted of representing several points of the resonant peak in the Nyquist plane. Figure 4.19 shows this representation for seven data points of the resonant peak: the resonant frequency and three points on either side.



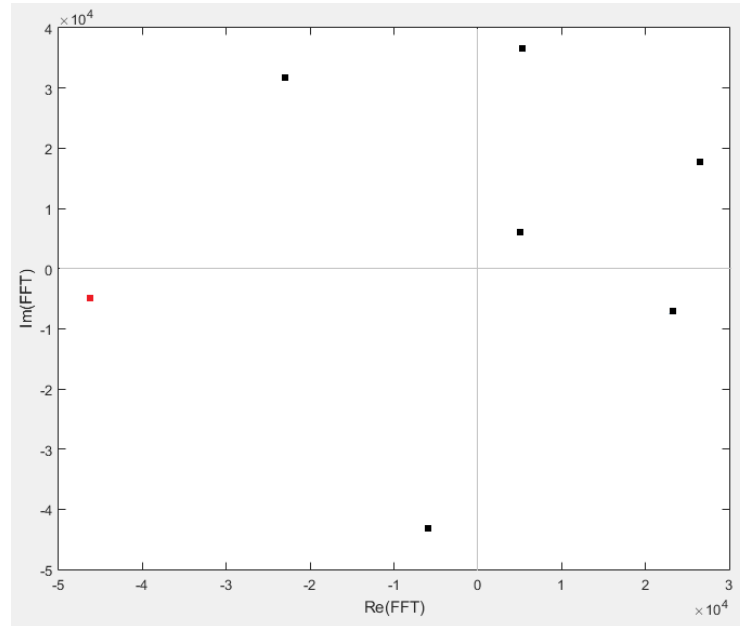


Figure 4.19 – Sample P2 (150mm): Nyquist plot of the resonant frequency (red) and surrounding data points

The use of more points around the resonant peak, which would theoretically improve the circle-fitting suitability, provided even more discrepant points for circle-fitting, which would result in lower correlation coefficients. The presented data range is lower when compared with other authors results (Karl, 2003, 2005; Brocanelli and Rinaldi, 1998, which used 12 and 8 points, respectively) and with inferior correlation than those. In addition, a quick examination of the previous figure shows that the circle fit to those data points would not have a favorable correlation coefficient. Therefore, the results from the circle-fit method for the current test would be inconclusive.

To increase the number of data points around each peak, and in order to improve the applicability of the circle-fit method (and accuracy of the half-power bandwidth method), a higher sampling frequency would have to be used. Unfortunately, the used oscilloscope already provided the best sampling frequency available in LabGeo. For this reason, the circle-fit method was not implemented.

#### 4.3.2. SCRIPT CAPABILITIES AND LIMITATIONS

The elaborated script manages to successfully determine damping ratio of soil samples tested using bender elements, using the half-power bandwidth method. It uses two different formulas for this effect, the one proposed by Brocanelli and Rinaldi (1998) and the other by Karl (2003; 2005), which provide very similar results for low damping ratios.

The script is capable of importing test data from an Excel file, averaging various sweep signal response waves in order to reduce noise and calculating the resulting FFT and spectrum. In addition, it shows several figures with information on the sweep tests, resulting averaged signal and spectra.

However, this script is not directly applicable to all tests data. The presented script included in the appendix is only automated for the following conditions:

- The time data must be included in column B;
- The input wave data must be included in column C;

- The output wave data must be included in column F;
- The above data must start in line 4;
- The test must have 1788 data points and 4 sweep waves.

For other types of tests, with different sampling frequency ( $f_s$ ) and duration (hence, different number of data points) or different number of sweep waves (hence, different number of test waves to be averaged), the script must be updated accordingly. As such, it may have to be adapted to other test conditions, which can easily be done by anyone with basic Matlab algorithm knowledge. In addition, the Excel format stated above can also be adapted in the same fashion.

In addition, the auxiliary variables regarding the number of data points at each side of the maximum amplitude used to determine  $f_1$  and  $f_2$  may need to be modified for each test, in the following cases:

- If there are peaks close to the maximum peaks with data points closer to  $A_m$  than the ones included in the maximum peak (the script will calculate  $f_1$  or  $f_2$  with the data points of the adjacent peak);
- If the maximum peak presents a low value of  $f_m$ , the number of points accounted for to the left of the peak can exceed the number of data points available, resulting in an error.

Also, if the spectrum presents high variability near  $A_m$ , the corresponding frequency value can be miscalculated, as shown in Figure 4.20.

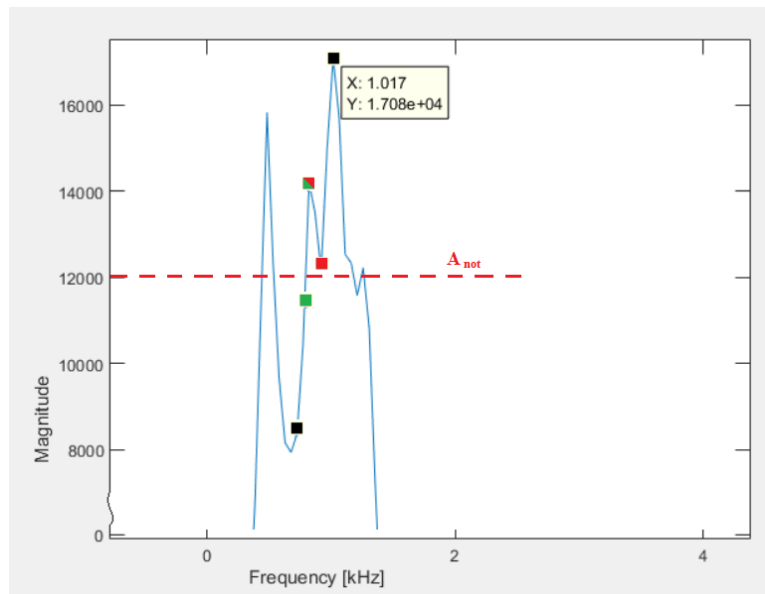


Figure 4.20 – Example of  $f_1$  miscalculation: automated use of data (red), supposed use of data (green)

In sum, a careful analysis of the spectrum should be done, in order to identify and correct this problem. This can be done by manually selecting the points corresponding to the correct interpolation.

All the Matlab scripts used in the present dissertation are included in the appendix. If these are copied to the Matlab editor they can be run and applied to other tests data, as long as some small adaptations are made. These scripts also include notes that explain how and what they are doing along the algorithms. Note that the script used to compare ABETS and Matlab results is a simplified version of the original script. The original one includes many other signal treatments and plots, as discussed in 4.6.1., and its complete list of algorithms would be too lengthy for presentation purposes. A shorter version is listed here, with the final list of algorithms used for the final comparison between ABETS

and Matlab results. Also, given that the number of variables of the completed script was very high, the remaining variable names are quite long in order to better understand which information they actually contain.

#### 4.3.3. FURTHER SAMPLE TESTING

Based on the previous assumptions and conclusions, the other two samples were tested. This time, some of the issues encountered for the previous test were mitigated, with special attention to the display window resolution (to prevent signal truncation) and the test length (to assure full data acquisition).

Since the use of ABETS was discontinued, a new method of acquiring data was implemented. The data acquisition was assured by PICO ADC-212 manufacturer's software, PicoScope. This software is capable of amplifying the test signal with good resolution, so the use of an amplifier was unnecessary. In addition, it also allows signal averaging, which further improves test results.

However, the test results must be manually taken by the user. The test is continuous and a "snapshot" of the results must be taken, which corresponds to the test readings. This proved to be a troublesome method to gather test results, due to the fast change of the receiver signal. On average, for each good acquisition over 7 poor ones were taken.

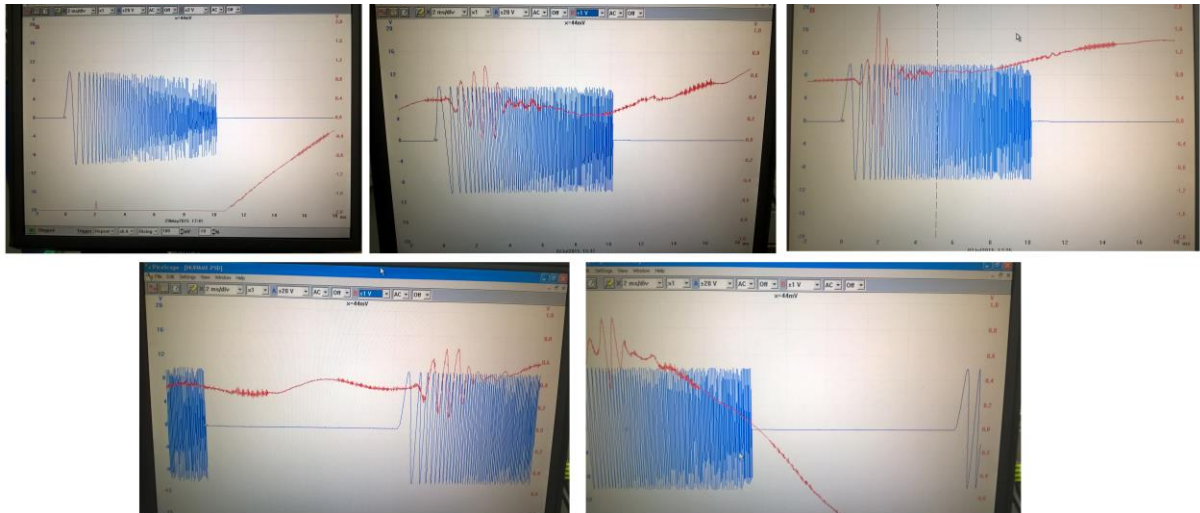


Figure 4.21 – Difficulty of data acquisition using PicoScope

Bender element fixation with the previously used styrofoam molds proved unsuccessful this time, since that it was not possible to adequately maintain contact between the BE and the new samples. Instead, the fixation was assured by hand, which provided better test results. Also, a sponge base was also used to help support the sample and reduce bench vibrations. The following figure shows the new test method.



Figure 4.22 – New bender element test methodology

The signal averaging technique tested in previous tests proved to be a very effective method to reduce background noise and to improve test data. In order to take advantage of this effect, the remaining samples were tested with an averaging of four different sweep sine waves.

Each sweep wave test used the same sweep wave, with the characteristics stated in the following table.

Table 4.7 – Used sweep wave characteristics

Starting frequency [kHz]	Stopping frequency [kHz]	Sampling frequency [kHz]
2	10	100

In addition, the used time domain was shifted by -2s, so the display window range was [-2;18] seconds. This was used in order to eliminate initial data loss.

The test results were then converted to a notepad file, which was later imported to Excel. After data arrangement in the Excel file, the results were imported to Matlab and treated with the completed script.

The results for damping determination with the half-power bandwidth method are presented below for the three tested samples. More complete test results are included in the appendix.

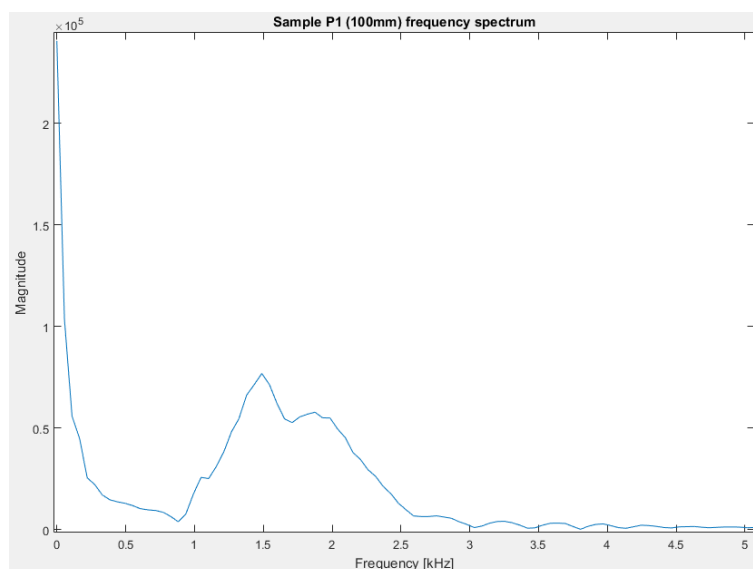


Figure 4.23 – Sample P1 (100mm): frequency spectrum

Table 4.8 – Sample P1 (100m): half-power bandwidth method results

$A_m$	$f_m$ [kHz]	$A_{not}$	$f_1$ [kHz]	$f_2$ [kHz]	$\xi_{BR}$	$\xi_K$
7.6874e+04	1.49	5.4358e+04	1.32	1.66	11.31	11.38

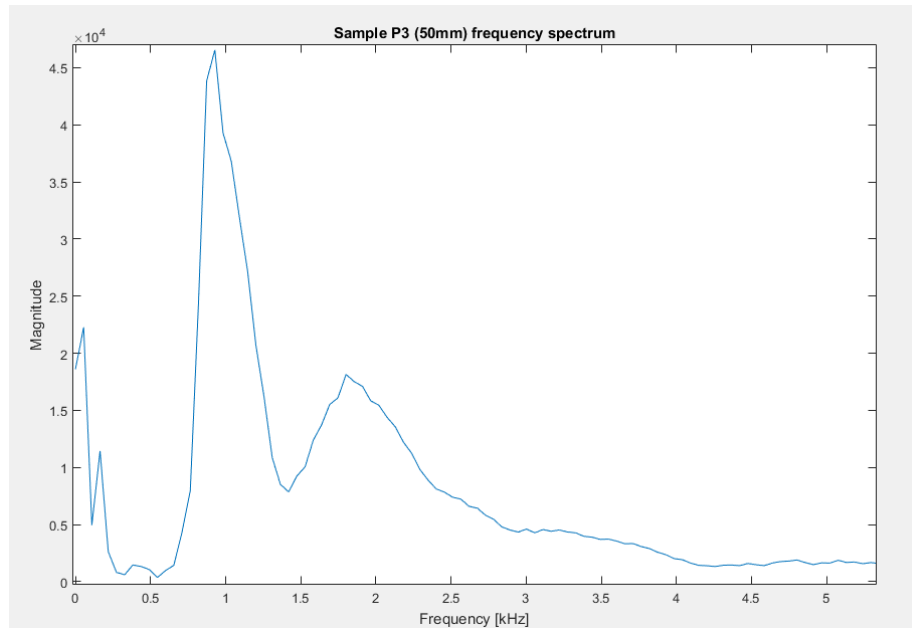


Figure 4.24 – Sample P3 (50mm): frequency spectrum

Table 4.9 – Sample P3 (50mm): half-power bandwidth method results

$A_m$	$f_m$ [kHz]	$A_{not}$	$f_1$ [kHz]	$f_2$ [kHz]	$\xi_{BR}$	$\xi_K$
4.6556e+04	0.93	3.2920e+04	0.84	1.08	13,14	13,26

#### 4.3.4. RESULT ANALYSIS

The following table summarizes the obtained results for the HPBM and LDM.

Table 4.10 – Comparison between half-power bandwidth and logarithmic decay method results

	Damping [%]	
	HPBM	LDM
P2 (150mm)	9,4	6,1
P1 (100mm)	11,4	7,0
P3 (50mm)	13,2	5,8

The logarithmic decay envelope for the LDM is very difficult to determine, since the measured signals differ greatly from the theoretical signal shape. As such, these results are unreliable. Hall and Bodare (2000) found that this amplitude decay is “very difficult to obtain as the signals are corrupted by inhomogeneous effects in the soils through which the ground motions travel”. In addition, sample geometry and BE-related phenomena play an important part in the performance of the BE, in particular spatial and boundary conditions, BE alignment, wave reflections, coupling, near-field effects and overshooting at high frequencies (Rio, 2006; Ferreira, 2009).

Given that the tested soil was the same, the damping results should be fairly close to each other. A quick analysis on the results obtained by the HPBM suggest a relation between damping and the sample height, illustrated in the following figure.

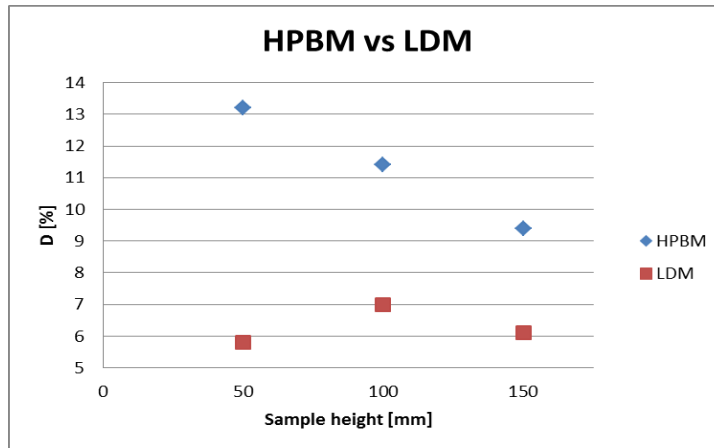


Figure 4.25 – Obtained damping results *versus* sample height

The above relation is highly unlikely, given that the frequency input was the same for each test sample. The following reasons were established, that could (unlikely) explain these results:

- Since the tested samples contained residual soil, high anisotropy and soil variability could explain the disparity in results;
- Given that damping was higher for smaller samples, the boundary reflection could potentially be more impactful, altering the shape of the receiving wave;
- Shorter samples could have, by chance, higher number/bigger conglomerates, which could alter the shape of the receiving wave in a similar fashion.

#### 4.4. COMPARISON WITH RESONANT COLUMN TEST RESULTS

As stated before, bender element testing is not yet standardized, and there are no results for residual soil from Porto granite tested by bench testing with BE. In order to compare the accuracy and applicability of the tested methods, resonant column (RC) test results were provided by Ferreira, (2009). These new results provided more testing data for treatment with the elaborated script, in addition to damping values determined by this normalized laboratory test for comparison.

The soil samples were also residual soil samples from Porto granite, collected in CICCOPN’s experimental sites at a depth of 2m. These were transferred for testing in LabGeo. The main characteristics of each soil sample are exposed in the following table.

Table 4.11 – Tested soil samples provided by Ferreira (2009)

	Sample height [mm]	Diameter [mm]	$\gamma_s$ [kN/m <sup>3</sup> ]
Soil 04	104,7	71,0	26,2
Soil 02	99,4	70,5	26,2
Soil 05	102,4	72,3	26,3

Note that the used nomenclature is the same as Ferreira’s, so that both authors’ works could be easily comparable.

#### 4.4.1. SOIL 04

Fifteen tests were done with a sample designated “soil 04”, which included sweep wave tests for frequency domain analysis and continuous sine signal waves for time domain analysis. Given that data treatment of all these sweeps would be too time consuming, only seven were actually treated. The selection of these tests was based on different received wave configurations and quality. In addition, a time domain analysis was made for four of these seven tests.

Each test comprehended a sweep wave analysis and various continuous, sinusoidal wave functions with various frequencies. As such, it was possible to determine damping using both LDM and HPBM and compare these with RC test results. The following table presents the relevant information on the used sweep wave tests. In addition, each sweep test had four different sweep waves, which were used for signal averaging.

Table 4.12 – Soil 04: sweep wave test information

Sweep test	Starting frequency [kHz]	Stopping frequency [kHz]	$f_s$ [kHz]	Test duration [s]
03	3,50	4,70	80	86
04	7,00	16,00		
10	1,25	1,60		
11	6,00	18,00		

Only a summary of this test results are stated here. The full test details are included in the appendix.

Table 4.13 – Soil 04: resonant column test results

Sweep test	$\gamma$	G [MPa]	$e$	Damping [%]
01	4,29E-06	35,8	0,62	7,0
03	4,06E-06	87,2	0,57	3,1
04	3,84E-06	124,2	0,55	2,0
07	4,29E-06	173,0	0,51	1,7
08	4,29E-06	176,5	0,51	1,9
10	4,51E-06	181,4	0,51	1,8
11	4,29E-06	182,6	0,51	1,4

Table 4.14 – Sample 04: summary of results with logarithmic decay method

Sweep	Damping [%]					
	2kHz	4kHz	8kHz	10kHz	15kHz	20kHz
03	5,6	X	X	X	X	-
04	5,4	5,6*	X	X	3,7	X
10	-	9,9	-	18,8	21,2	18,2
11	-	5,8*	-	14,4	17,0	18,9

X = discarded result due to very low signal quality; red value = low quality test result; - = untested frequency; \* = test with high variation on damping value

Table 4.15 – Soil 04: comparison between damping values based on different methods

Sweep test	Damping [%]		
	LDM	HPBM	RC
01	-	7,0	7,0
03	5,6	6,2	3,1
04	5,4	6,7	2,0
07	-	6,9	1,7
08	-	9,0	1,8
10	6,6	7,5	1,8
11	14,0	7,9	1,4

Most of the waves available presented overall poor quality and, as consequence, the reliability of the LDM is very low. Once again the results obtained using this method were found to be poor. In addition, and as expected, LDM results differed significantly with damping values obtained using the RC test.

Similar to previous testing, LDM and HPBM results differ significantly due to the already mentioned aspects. Only for the first sweep test the HPBM and RC results converge.

#### 4.4.2. SOIL 02

Soil 02 was tested with seven different tests, each comprising both frequency and time domain analysis. Therefore, LDM and HPBM were applied in this testing series.

The following table presents information of the various used sweep waves, which are similar to the ones used for testing soil 04. Each sweep test also contained four sweep waves, which were used for signal averaging.

Table 4.16 – Soil 02: sweep wave test information

Sweep test	Starting frequency [kHz]	Stopping frequency [kHz]	$f_s$ [kHz]	Test duration [s]
00	1,0	6,0	80	86
01	1,0	6,0		
02	1,5	6,0		
03	2,0	8,0		
04	2,0	10,0		
05	1,5	5,0		
06	2,0	5,0		
07	1,5	5,0		



Similar to the data presentation used for soil 04, only a summary of the test results are stated here. The full test details are included in the appendix.

Table 4.17 – Soil 02: resonant column test results

Sweep test	$\gamma$	G [MPa]	$e$	$p'$ [MPa]	Damping [%]
00	3,78E-06	13,5	0,59	0	4,3
01	3,31E-06	28,9	0,58	13,1	4,0
02	4,02E-06	37,2	0,57	26,5	3,6
03	3,78E-06	58,2	0,55	53,1	2,4
04	3,31E-06	77,3	0,53	80,0	2,1
05	2,84E-06	48,2	0,54	26,3	2,8
06	2,60E-06	56,5	0,53	40,3	2,6
07	-	-	-	-	-

Table 4.18 – Sample 02: summary of results with logarithmic decay method

Sweep	Damping [%]					
	0,5kHz	1kHz	2kHz	4kHz	6kHz	8kHz
00	-	6,2*	7,3	X	-	-
01	8,5*	14,6*	33,2	X	X	X
02	-	9,8	7,6	X	X	-
03	-	3,6	8,7	8,4	X	-
04	-	X	3,8	17,1	X	X
05	-	8,5	6,7	X	X	X
06	-	9,7*	9,4*	X	-	X
07	-	-	X	13,2	-	X

X = discarded result due to very low signal quality; red value = low quality test result; - = untested frequency; \* = test with high variation on damping value

Table 4.19 – Soil 02: comparison between damping values based on different methods

Sweep test	Damping [%]		
	LDM	HPBM	RC
00	6,8	5,9	4,3
01	18,8	17,8	4,0
02	8,7	5,3	3,6
03	6,9	6,3	2,0
04	10,4	7,0	2,1
05	7,6	6,1	2,8
06	9,6	6,7	2,6
07	13,2	13,6	-

#### 4.4.3. SOIL 05

Soil 05 was tested using a single sweep wave test. As such, there was not enough data available for a time domain analysis using the logarithmic decay method.

The used sweep wave is similar to the one used in the previously presented soil tests.

Table 4.20 – Soil 05: sweep wave test information

	Starting frequency [kHz]	Stopping frequency [kHz]	$f_s$ [kHz]	Test duration [s]
Sweep test	7,5	15,0	80	86

However, only three complete signals are available, since one is truncated and presents missing data. As such, signal averaging for soil 05 was done using three sweep wave results.

The test results are included in the appendix. The result for HPBM was 7.2%, and for the RC test 2.2%.

#### 4.4.4. RESULT ANALYSIS

Test results using the LDM were found, once again, to be unreliable. The time domain analysis tests elaborated by Ferreira (2009) were focused on the determination of the velocity of S-waves,  $V_s$ , a parameter that is not treated in this dissertation. As such, the test results only focused on having a clear representation of the beginning of the S-wave, disregarding the remaining shape of the received wave. The received waves have an overall poor logarithmic decay envelope (and signal quality), lower than the original test results, further discrediting this method.

The following table summarizes HPBM and RC test results, for easier comparison between one another.

Table 4.21 – Summary on HPBM and RC damping ratios for Ferreira (2009) test results

Damping [%]							
	Sweep	HPBM	RC		Sweep	HPBM	RC
Soil 04	01	7,0	7,0	Soil 02	00	5,9	4,3
	03	6,2	3,1		01	17,8	4,0
	04	6,7	2,0		02	5,3	3,6
	07	6,9	1,7		03	6,3	2,0
	08	9,0	1,8		04	7,0	2,1
	10	7,5	1,8		05	6,1	2,8
Soil 05	11	7,9	1,4	06	6,7	2,6	
	-	7,2	2,2	07	13,6	-	

A quick analysis of Table 4.21 shows that the results of these are divergent, with values from the HPBM more than double than the RC. Only the result from the HPBM of sweep 01 from soil 04 is coherent with the RC result, which is in fact the same.

A study was elaborated in order to evaluate and identify the differences between these two methods. Given that there was various data regarding soil 02 tests, such as strain, isotropic tension and shear modulus, these results were the ones that this study was based on.

Figure 4.26 illustrates the test results for HPBM and RC. Note that results from sweep 01 were excluded since they were very different and, for this reason, considered as an outlier. Also, results from RC for sweep 07 were unavailable and excluded as well.

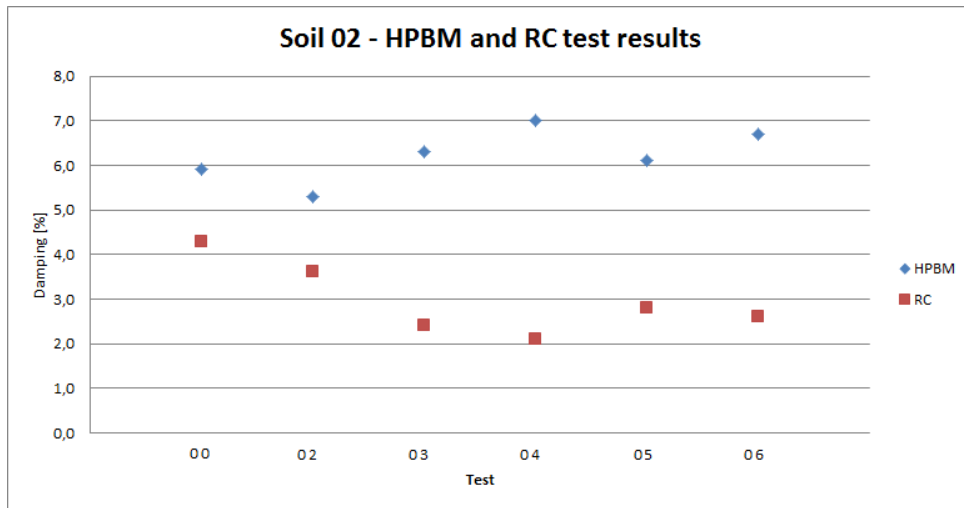


Figure 4.26 - Half-power bandwidth method and resonant column test results

A first analysis shows a curious reflection of damping values from sweeps 03 to 06 around 4.5% damping value.

Figures 4.39 to 4.41 shows HPBM and RC test results *versus* effective isotropic stress, strain and shear modulus, respectively.

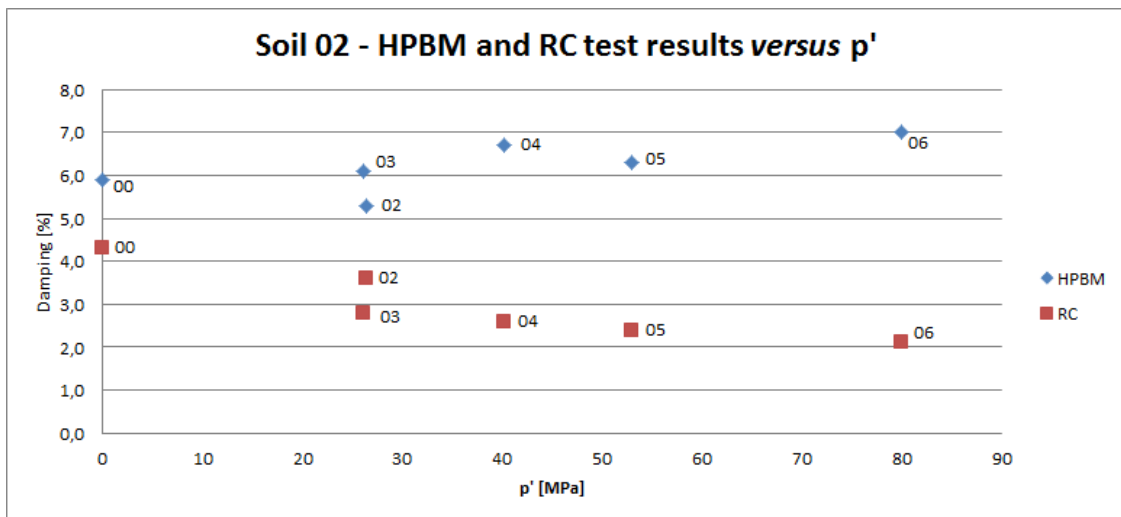


Figure 4.27 – Half-power bandwidth method and resonant column test results *versus* effective isotropic stress

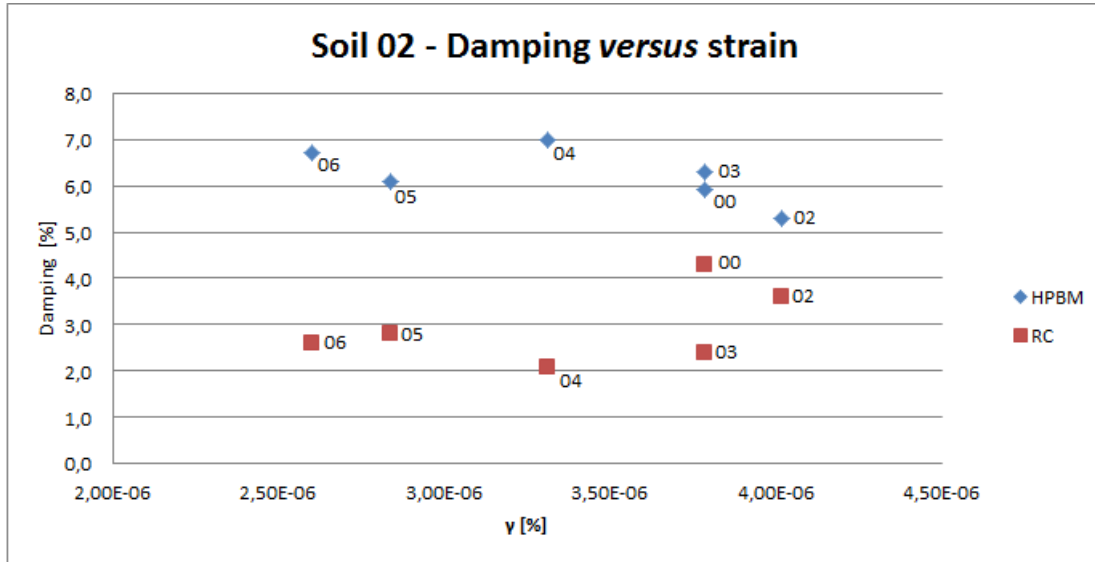


Figure 4.28 – Half-power bandwidth method and resonant column test results versus strain

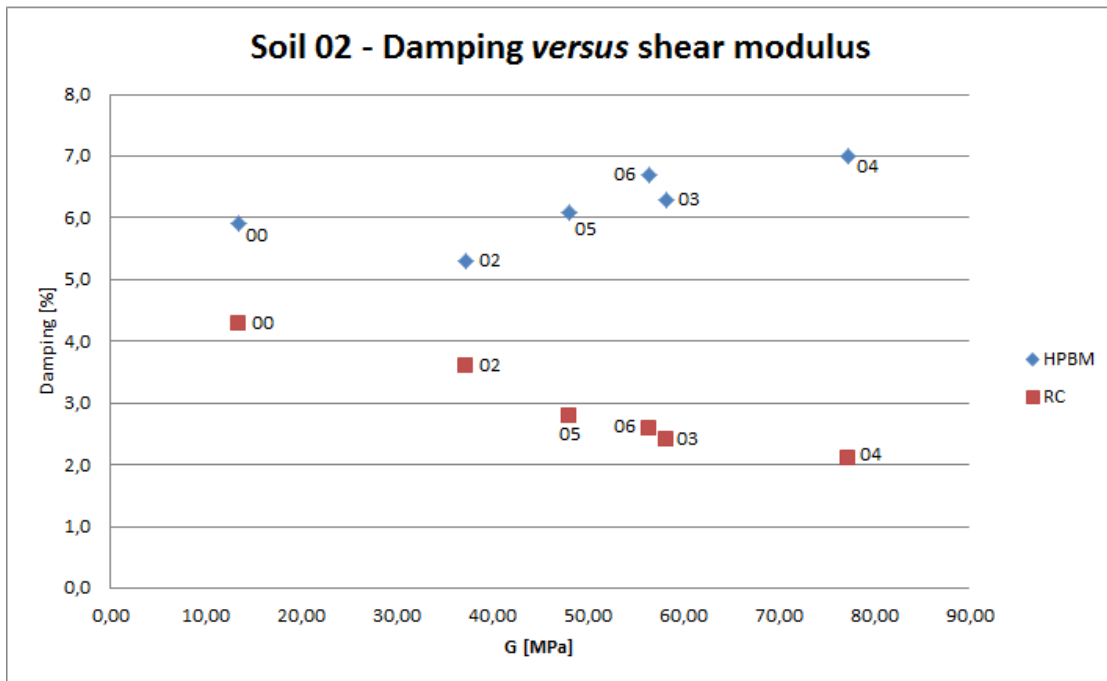


Figure 4.29 – Half-power bandwidth method and resonant column test results versus shear modulus

Similar reflections are found on all the considered relations. However, no cause for this effect was found. A possible analysis that could explain this behavior is explained in 5.3.4..

#### 4.5. ADDITIONAL TEST SAMPLES

Previous damping results were somewhat inconclusive, so further test analysis was required. Sample P2 (150mm) was sawed into samples P4 (100mm) and P5 (50mm). After testing, sample P4 (100m) was then sawed into samples P6 (50mm) and P7 (50mm). This provided an additional 100mm sample and three additional 50mm samples.

Only HPBM was used for these samples, given that LDM provided poor results so far and proved to be an ineffective method for damping calculation using BE.

##### 4.5.1. SAMPLE P4 (100MM)

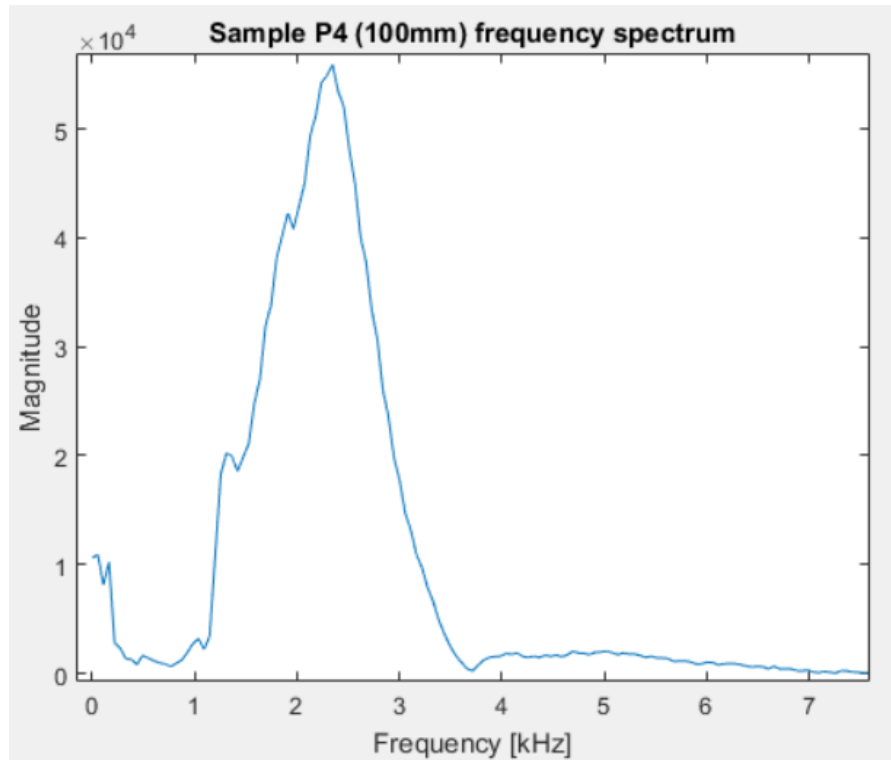


Figure 4.30 – Sample P4 (100mm): frequency spectrum

Table 4.22 – Sample P4 (100mm): results for the half-power bandwidth method

$A_m$	$f_m$ [kHz]	$A_{not}$	$f_1$ [kHz]	$f_2$ [kHz]	$\xi_{BR}$	$\xi_K$
5.5898e+04	2.35	3.9526e+04	1.84	2.63	15.96	16.17

4.5.2. SAMPLE P5 (50MM)

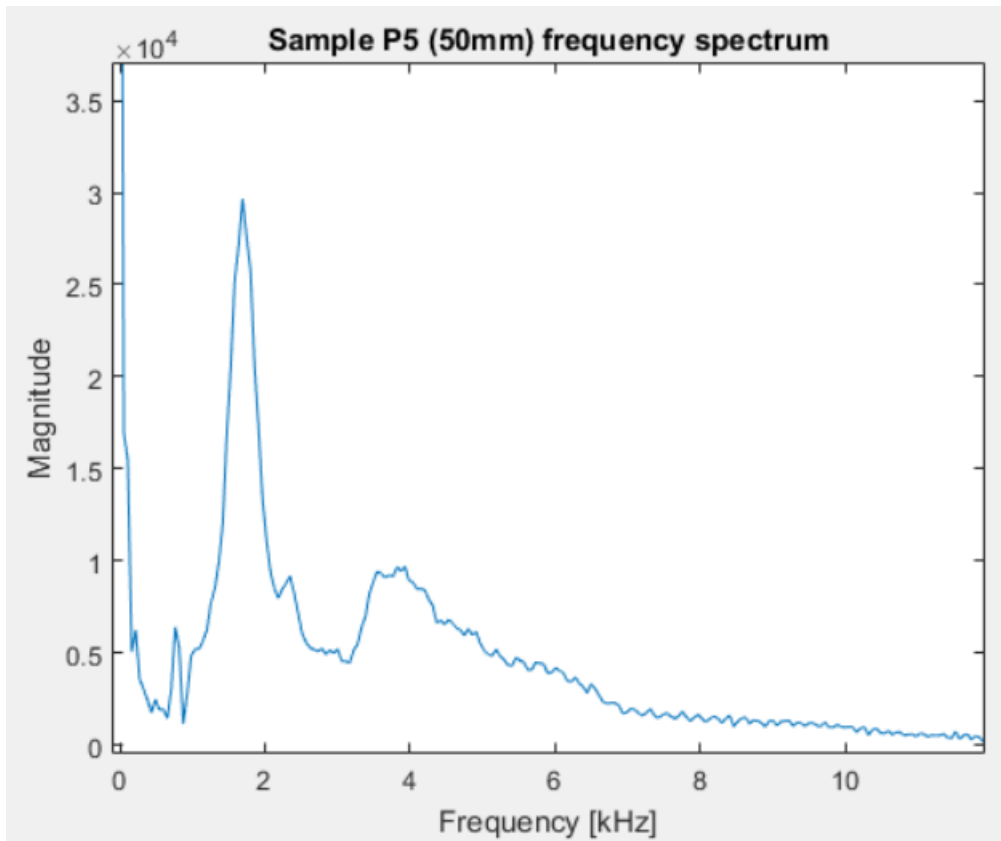


Figure 4.31 – Sample P5 (50mm): frequency spectrum

Table 4.23 – Sample P5 (50mm): results for the half-power bandwidth method

$A_m$	$f_m$ [kHz]	$A_{not}$	$f_1$ [kHz]	$f_2$ [kHz]	$\xi_{BR}$	$\xi_K$
2.9659e+04	1.69	2.0972e+04	1.53	1.85	9.37	9.41

4.5.3. SAMPLE P6 (50MM)

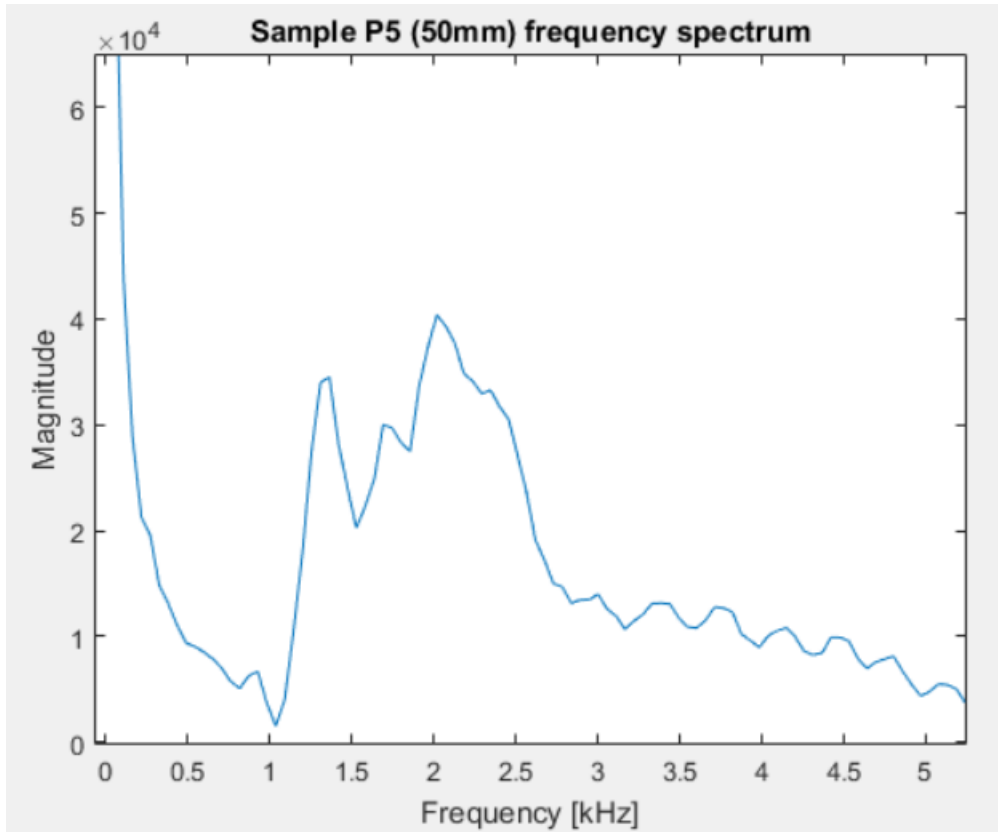


Figure 4.32 – Sample P6 (50mm): frequency spectrum

Table 4.24 – Sample P6 (50mm): results for the half-power bandwidth method

$A_m$	$f_m$ [kHz]	$A_{not}$	$f_1$ [kHz]	$f_2$ [kHz]	$\xi_{BR}$	$\xi_K$
4.0374e+04	2.02	2.8594e+4	1.78	2.49	18.14	18.45

4.5.4. SAMPLE P7 (50MM)

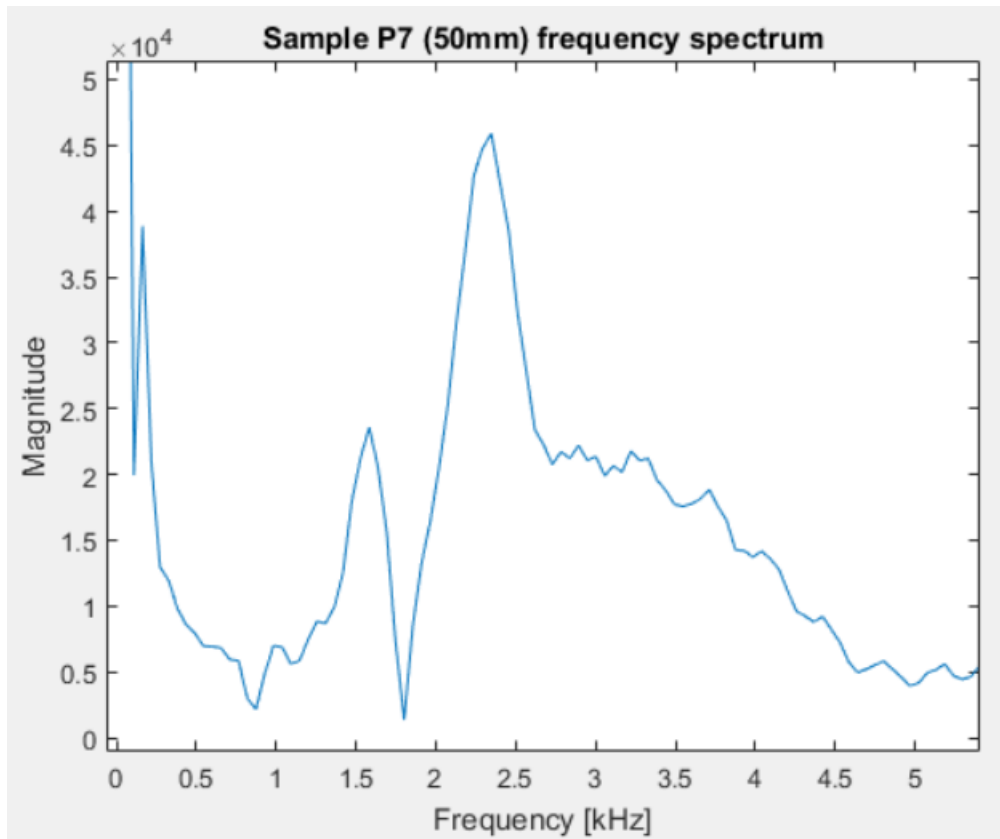


Figure 4.33 – Sample P7 (50mm): frequency spectrum

Table 4.25 – Sample P7 (50mm): results for the half-power bandwidth method

$A_m$	$f_m$ [kHz]	$A_{not}$	$f_1$ [kHz]	$f_2$ [kHz]	$\xi_{BR}$	$\xi_K$
4.5896e+04	2.35	3.2454e+04	2.14	2.51	7.82	7.85



4.5.5. RESULT ANALYSIS

The following table compares the damping values of the current research test results, in addition to their respective frequency values associated with the maximum magnitude,  $f_m$ , and the relation  $f_2^2 - f_1^2$ , used in the formulas for damping determination. These values are represented in order to evaluate their effect on damping value using the HPBM.

Table 4.26 – Comparison between current research test results

Soil sample	$f_m$ [kHz]	$f_2^2 - f_1^2$ [kHz]	Damping [%]	
			HPBM	LDM
P2 (150mm)	1,49	0,73	9,4	6,1
P1 (100mm)	1,40	1,01	11,4	7
P3 (50mm)	0,93	0,24	13,2	5,8
P4 (100mm)	2,35	0,79	16,1	-
P5 (50mm)	1,69	0,32	9,4	-
P6 (50mm)	2,02	0,71	18,2	-
P7 (50mm)	2,35	0,37	7,8	-

The obtained damping values are discrepant, which should not occur given that both the soil and solicitation (i.e., sweep wave input) was the same for each test. Additionally, no correlation was found between  $f_m$  or the aforementioned relation with the damping values obtained using the HPBM, so no conclusions can be taken based on them.

Figure 4.34 shows the damping values from the previous table plotted *versus* the sample heights.

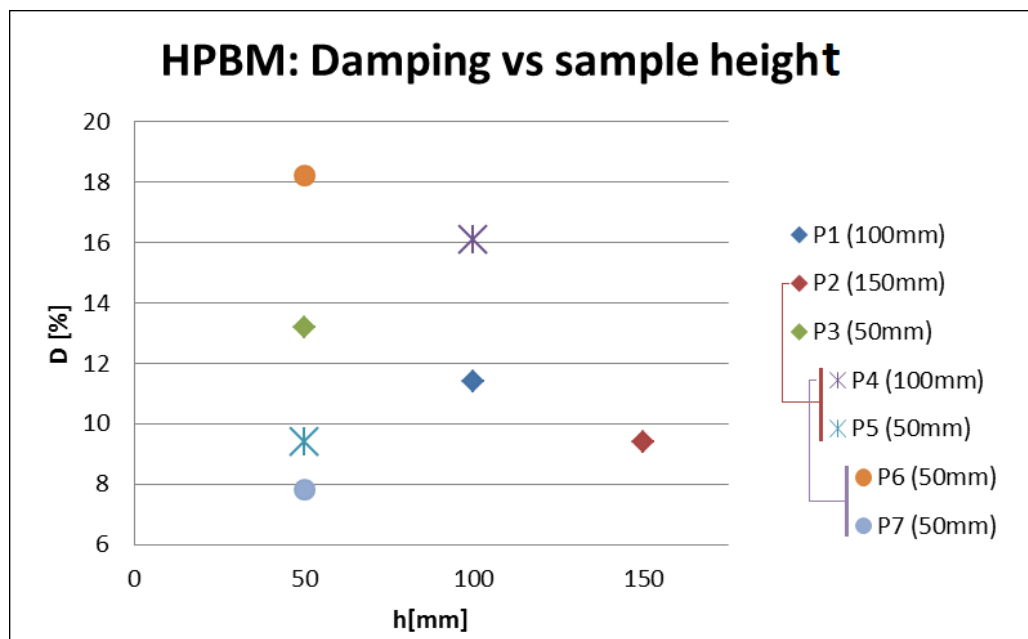


Figure 4.34 – Half-power bandwidth values *versus* sample height

The initial test results (P1, P2 and P3) presented a decrease in damping value with increasing sample height, as stated before in 4.6.4.. However, the new test results show now correlation whatsoever. Additionally, the damping values should all be fairly similar to each other given that the soil was the same for all samples.

Sample P2 (150mm) was divided into samples P4 (100mm) and P5 (50mm), with damping values of 9.4%, 16.1% and 9.4%, respectively. One of the samples has the same damping value from the originating sample. As seen right from the sample preparation stage, the tested soil presented considerable anisotropy and heterogeneity, typical from this soil. The discrepant value from sample P4 (100mm) could be explained by this, by issues regarding bender element implementation or a combination of both.

Sample P4 (100mm) was divided into samples P6 (50mm) and P7 (50mm), with damping values of 16.1%, 18.2% and 7.8%, respectively. Similarly with the previous case, this variability on damping value could be explained by the same reason.

# 5

## CONCLUDING REMARKS

### 5.1. INTRODUCTION

The present chapter synthesizes the considerations and conclusions from the research, disposed in chapter 4. It also contains directives and comments regarding future developments of BE techniques for soil damping determination, based on past and present findings. Several aspects are addressed, such as BE implementation and data acquisition.

### 5.2. SUMMARY

The logarithmic decay method is greatly affected by the shape of the decay envelope of the received wave, which justified the implementation of a parameter that managed to qualify it. This method was found to be poor for damping determination using bender elements, given its sensitivity to the decay envelope of the received wave and disparity of both half-power bandwidth method and resonant column test results.

Given that the tested soil was the same, the damping results from the half-power bandwidth method should be fairly close to each other, which was not the case. High anisotropy and heterogeneity, typical of the tested residual soil, could justify this effect. Additionally, after the second round of tests, which used samples that were obtained by division of the samples from the first round, it was found that one of the secondary samples had the same or close damping value from its originating soil sample.

When comparing fourteen results from the standardized resonant column test with the half-power bandwidth method, only one value was coherent between them. The remaining results presented significant discrepancy between these methods. Unfortunately, the elaborated study to determine the reason behind this was inconclusive. However, various symmetries were found throughout this study, which can imply a yet unknown relation between soil parameters and damping.

### 5.3. FURTHER DEVELOPMENTS

#### 5.3.1. DATA ACQUISITION

The methods to obtain damping ratio, either based on time or frequency domain (but specially the first group), are sensitive to the quality of the test data. As stated before, care with window resolution must be taken in order to not truncate the signal. Signal truncation loses valuable data for treatment, which can potentially invalidate test results.

In addition, only high quality waves should be used for analysis, with similar standards than those exposed in 4.5.. That is, their peaks should be well-developed, it should have the least amount of background noise possible and the whole representation of the wave must be assured.

There is no software available for specific use with BE, or at least with a suitable way of taking BE testing data. A software that managed to let the user choose the preferred display from a group would be ideal. For example, if this software could take several “snapshots” of the display and present them to the user, so that he/she could choose from the available displays which data to import, it would remove the frustration of attempting to get a good display snapshot with many attempts, as stated before in 4.6.3. In addition, it would greatly decrease testing time, since a considerable amount of time is wasted on trying to acquire good test results.

### 5.3.2. BENDER ELEMENT INSTALLATION

The viability of application or coating of the BE with materials that can enhance the signal or adherence in the BE-soil interface could be tested. Brocanelli and Rinaldi (1998) coated BE with a conductive silver painting, which improved the received signal. In addition, when they tested these BE in a low-noise environment, no averaging or filtering were necessary.

To help the bender element installation in medium to coarse soil samples, a negative of the BE can be used in order to “pre-penetrate” the soil sample in order to reduce the risk of damage to the BE.



Figure 5.1 – Negatives used for bender element installation

### 5.3.3. SIGNAL PROCESSING

Regarding signal processing and data treatment, the only suitable way found to improve signal quality was signal averaging. Some other methods were tested (Butterworth filter, moving average filter) but with little to no gain. Additional methods could be tested and implemented to further improve test quality and improve BE competitiveness with other tests.

### 5.3.4. CONTINUATION OF THIS THESIS WORK

A possible update for the script would be the implementation of dialog boxes, which would require the user to input information regarding the number of data points ( $f_s$  and test duration) and number of sweeps in each test. However, this would imply the use of dynamic variables in the script, which would complicate it by a reasonable amount.

The elaboration of a script, based on Pratt’s circle-fit method script presented in the appendix, that implements the circle-fit method to BE testing data is pertinent. Note that in order to successfully do so it required to have more data points from each test than the ones acquired for the present thesis, so that the circle fit to the data has good correlation with it.

After this development, an evaluation of its performance is pertinent, as well as comparison with results from the half-power bandwidth and logarithmic decay method. Then, it would be possible to further analyze the possibility of implementation of these of these methods for damping determination using BE, based on their accuracy. Further comparison with resonant column test results is also relevant.

These methodologies could also be compared with other authors' methods, such as the use of multiple shear wave arrivals, use of different travel paths (Karl, 2006) and the spectral-ratio method (Wang *et al.*, 2006).

The elaborated script was written by an author with basic knowledge of the used programming language. Refinement and empowerment of this script is also possible, regarding the already mentioned issues in 4.6.2.. There is room for improvement in the substitution of some variables, such as sweep signal wave lengths, by dynamic variables based on inputs by the user. This would greatly boost the script's ease of application to different testing methods (different sampling frequency and test duration, for instance) by users with low algorithmic knowledge. In addition, if this script could work in pair with the software described in 5.3.1., the use of Excel would become obsolete, which would improve velocity in terms of data treatment.

Given that BE testing procedures are not yet standardized, the development of a uniform methodology for BE testing in bench tests is important, in order to make the results more easily comparable. This methodology could include considerations regarding sample size (or ratio between the sample's  $D$  and  $h$ ), minimum number of sweeps for signal averaging and/or minimum value for  $f_s$ . Additionally, the development of a specific apparatus for BE testing could also be relevant in the same way.

The use of additional equipment as practical as BE that work in conjunction with these, such as accelerometers, can provide feedback of the BE performance, as well as providing additional data for treatment and evaluation on the use of this equipment. Ferreira *et al.* (2013) recently tested small strain stiffness on a stress-path chamber using both BE and accelerometers, and found that the obtained measurements showed good agreement between BE and accelerometer results.

Further analysis on the difference between HPBM and RC tests could be done, based on Santo (1999) research. He found that for strain values lower than a certain value, the volumetric threshold strain ( $\gamma_t^v$ ), the stiffness degradation and soil damping have low values due to the soil's initial elasticity. The volumetric threshold strain depends on the stress history and soil nature which can be, in a way, correlated to the plasticity index (higher plasticity index causes higher volumetric threshold strain). With this in mind, this author proposed that soil behavior should be compared using a normalized strain given by  $\gamma^* = \gamma / \gamma_t^v$ . A study based on this normalized strain could shed some light in these matters.









## REFERENCES

- Achenbach, JD - Wave propagation in elastic solids. Amsterdam: North-Holland, 1975.
- Alarcon, A; Chameau, JL; Leonards, GA - A new apparatus for investigating the stress-strain characteristics of sands. *ASTM geotechnical testing journal*. Vol. 9. n.º 4 (1986). p. 204-212. 0149-6115
- Arulnathan, R; Boulanger, RW; Riemer, MF - Analysis of bender element tests. *ASTM geotechnical testing journal*. Vol. 21. n.º 2 (1998). p. 120-131. 0149-6115
- Aubertin, M; Ricard, JF; Chapuis, RP - A predictive model for the water retention curve: application to tailings from hard-rock mines. *Canadian Geotechnical Journal*. Vol. 35. n.º 1 (1998). p. 55-69. 0008-3674
- Barbosa, LV - Fourier transform: time and frequency domains gif. 2013.
- Barros, JMC - Shear dynamic modulus of tropical soils. University of Sao Paulo, Brazil, 1996.
- Begonha, A - Alteração das Rochas Graníticas do Norte e Centro de Portugal. Uma Contribuição. Universidade Nova de Lisboa, 1989.
- Biazee, J - Contribution à l'étude des propriétés mécaniques des sols et des matériaux pulvérulents. 1962.
- Biot, MA - Theory of propagation of elastic waves in a fluid-saturated porous solid. I. Low-frequency range. *the Journal of the Acoustical Society of America*. Vol. 28. n.º 2 (1956a). p. 168-178. 0001-4966.
- Biot, MA - Theory of propagation of elastic waves in a fluid-saturated porous solid. II. Higher frequency range. *the Journal of the Acoustical Society of America*. Vol. 28. n.º 2 (1956b). p. 179-191. 0001-4966.
- Biot, MA - Mechanics of deformation and acoustic propagation in porous media. *Journal of Applied Physics*. Vol. 33. n.º 4 (1962). p. 1482-1498.
- Blanter, MS; Golovin, IS; Neuhäuser, H; Sinning, H-R - Internal Friction in Metallic Materials: A Handbook. *Springer Series in Materials Science* ((2007). 3540687572.
- Brignoli, EGM; Gotti, M; Stokoe, KH - Measurement of shear waves in laboratory specimens by means of piezoelectric transducers. *ASTM geotechnical testing journal*. Vol. 19. n.º 4 (1996). p. 384-397. 0149-6115.
- Brocanelli, D; Rinaldi, V - Measurement of low-strain material damping and wave velocity with bender elements in the frequency domain. *Canadian Geotechnical Journal*. Vol. 35. n.º 6 (1998). p. 1032-1040. 0008-3674.
- Butterworth, S - On the theory of filter amplifiers. *Wireless Engineer*. Vol. 7. n.º 6 (1930). p. 536-541.
- Campanella, RG - Field methods for dynamic geotechnical testing: Overview of capabilities and needs. 1994. 0803118775.
- Cattaneo, C - Sul contatto di due corpi elastici. *Accademia dei Lincei, Rendiconti*. (1938).
- Cho, GC; Santamarina, JC - Unsaturated particulate materials-particle-level studies. *Journal of geotechnical and geoenvironmental engineering*. Vol. 127. n.º 1 (2001). p. 84-96. 1090-0241
- Costa, JC; Teixeira, C - Nota explicativa da folha 9-C - Porto. 'Carta Geológica de Portugal' na escala 1:50000. *Serviços Geológicos de Portugal*. (1957).
- Crowell, Benjamin - Vibrations and waves. Light and Matter, 2002. 0970467036
- Deresiewicz, H - Bodies in contact with applications to granular media. *RD Mindlin and applied mechanics*. (2013). p. 105-147.
- Dobry, R - Damping in soils: its hysteretic nature and the linear approximation. MIT Department of Civil Engineering, Inter-American Program, 1970.
- Dobry, R - Prediction of pore water pressure buildup and liquefaction of sands during earthquakes by the cyclic strain method. US Department of Commerce, National Bureau of Standards, 1982.
- Drnevich, VP - Effect of Strain History on the Dynamic Properties of Sand. Ann Arbor, Michigan: The University of Michigan, 1967.
- Drnevich, VP - Undrained Cyclic Shear of Saturated Sand. *Journal of the soil mechanics and foundations division*. Vol. 98. n.º SM8 (1972).
- Dyvik, R; Madshus, C - Lab Measurements of Gmax Using Bender Elements. ASCE, 1985.

- Dyvik, R; Olsen, TS - Gmax measured in oedometer and DSS tests using bender elements. 1989.
- Ewins, DJ - Modal testing: theory and practice. *Hertfordshire: Research Studies Press Ltd.* (1984).
- Ferreira, C - Implementação e aplicação de transdutores piezoeléctricos na determinação de velocidades de ondas sísmicas em provetes Avaliação da qualidade de amostragem em solos residuais. Porto: FEUP, 2003.
- Ferreira, C - The use of seismic wave velocities in the measurement of stiffness of a residual soil. Porto: [s. n.], 2009.
- Ferreira, C; Martins, JP; Correia, AG - Determination of the Small-Strain Stiffness of Hard Soils by Means of Bender Elements and Accelerometers. (2013).
- Foti, S - Multistation methods for geotechnical characterization using surface waves. Politecnico di Torino, 2000.
- Fourier, BJB - Théorie Analytique de la Chaleur. Chez Firmim Didot, père et fils, 1822.
- Gabriels, P; Snieder, R; Nolet, G - In situ measurements of shear-wave velocity in sediments with higher-mode Rayleigh waves. *Geophysical prospecting*. Vol. 35. n.º 2 (1987). p. 187-196. 1365-2478
- Greening, PD; Nash, DFT - Frequency Domain Determination of  $G \sim 0$  Using Bender Elements. *Geotechnical Testing Journal*. Vol. 27. n.º 3 (2004). p. 288-294. 0149-6115
- Greening, PD; Nash, DFT; Benahmed, N; Ferreira, C; Viana da Fonseca, A - Comparison of shear wave velocity measurements in different materials using time and frequency domain techniques. 2003.
- Hardin, BO; Black, WL - Vibration modulus of normally consolidated clay. *Journal of Soil Mechanics & Foundations Div.* (1968).
- Hardin, BO; Drnevich, VP - Shear modulus and damping in soils: measurement and parameter effects (terzaghi lecture). *Journal of the soil mechanics and foundations division*. Vol. 98. n.º 6 (1972). p. 603-624. 0044-7994.
- Hertz, H - On the contact of elastic solids. *J. reine angew. Math.* Vol. 92. n.º 156-171 (1881). p. 110.
- Hoffman, K; Varuso, R; Fratta, D - he Use of Low-Cost MEMS Accelerometers in Near-Surface Travel-Time Tomography. Atlanta, GA: 2006.
- Inman, DJ - Engineering Vibration. Upper Saddle River: Pearson Prentice Hall, 2001. 978-0-13-228173-7.
- Johnson, KL; Kendall, K; Roberts, AD - Surface energy and the contact of elastic solids. The Royal Society, 1971. 0080-4630.
- Jovicic, V; Coop, MR; Simic, M - Objective criteria for determining Gmax from bender element tests. *Géotechnique*. Vol. 46. n.º 2 (1996).
- Karl, L - Dynamic soil properties out of SCPT and bender element tests with emphasis on material damping. Ghent University, 2005.
- Karl, L; Haegeman, W; Pyl, L; Degrande, G - Measurement of material damping with bender elements in triaxial cell. *Deformation Characteristics of Geomaterials/Comportement Des Sols Et Des Roches Tendres*. (2003). p. 3. 0415889200.
- Kjartansson, E - Constant Q-wave propagation and attenuation. *Journal of Geophysical Research: Solid Earth (1978–2012)*. Vol. 84. n.º B9 (1979). p. 4737-4748. 2156-2202.
- Kjartansson, E; Denlinger, R - Seismic wave attenuation due to thermal relaxation in porous media. 1977.
- Ladd, RS; Dobry, R; Dutko, P; Yokel, FY; Chung, RM - Pore-water pressure buildup in clean sands because of cyclic straining. *ASTM Geotechnical Testing Journal*. Vol. 12. n.º 1 (1989). 0149-6115.
- Larsson, R; Mulabdic, M - Shear moduli in Scandinavian clays; measurements of initial shear modulus with seismic cones; empirical correlations for the initial shear modulus in clay. (1991).
- Lee, EH; Radok, JRM - The contact problem for viscoelastic bodies. *Journal of Applied Mechanics*. Vol. 27. n.º 3 (1960). p. 438-444. 0021-8936.
- Leong, EC; Yeo, H; Rahardjo, H - Measuring shear wave velocity using bender elements. *Geotechnical Testing Journal*. Vol. 28. n.º 5 (2005). p. 488. 0149-6115

- Lopes, I; Strobbia, C; Almeida, I; Teves-Costa, P; Deidda, GP; Mendes, M; Santos, JA - Joint acquisition of SWM and other seismic techniques in the ISC'2 experimental site. Porto: Milpress, 2004.
- Lunne, T; Berre, T; Strandvik, S - Sample disturbance effects in soft low plastic Norwegian clay. 1997. 9054108851.
- MathWorks - <http://www.mathworks.com/products/matlab/>. 2015. Access date: 1st June 2015
- Matos Fernandes, M - Mecânica dos solos: conceitos e princípios fundamentais. FEUP edições, 2006. 9727520863
- Mayne, PW - Unexpected but foreseeable mat settlements of Piedmont residuum. *Int. Conf. Geoengr Case Histories*. Vol. 1. n.º 1 (2005). p. 7-8.
- Menke, W - Geophysical data analysis: discrete inverse theory. Academic press, 2012. 0123971608
- Meyers, MA; Chawla, KK - Mechanical behavior of materials. Cambridge university press Cambridge, 2009.
- Mindlin, RD - Compliance of Elastic Bodies in Contact. *J. of Appl. Mech.* Vol. 16. (1949).
- Mindlin, RD; Deresiewicz, H - Elastic spheres in contact under varying oblique forces. *J. of Appl. Mech.* Vol. 20. (1953).
- Murphy III, William F - Effects of partial water saturation on attenuation in Massillon sandstone and Vycor porous glass. *The Journal of the Acoustical Society of America*. Vol. 71. n.º 6 (1982). p. 1458-1468. 0001-4966.
- Nave, CR - HyperPhysics. Georgia State University, 2015.
- Nazarian, S; Stokoe, KH - In situ shear wave velocities from spectral analysis of surface waves. 1984.
- Palmer, ID; Traviolia, ML - Attenuation by squirt flow in undersaturated gas sands. *Geophysics*. Vol. 45. n.º 12 (1980). p. 1780-1792. 0016-8033.
- Park, CB; Miller, RD; Xia, J - Multichannel analysis of surface waves. *Geophysics*. Vol. 64. n.º 3 (1999). p. 800-808. 0016-8033.
- Park, D - Evaluation of dynamic soil properties: Strain amplitude effects on shear modulus and damping ratio. Ann Arbor: Cornell University, 1998.
- Pratt, V - Direct least-squares fitting of algebraic surfaces. *ACM SIGGRAPH computer graphics*. Vol. 21. n.º 4 (1987). p. 145-152. 0897912276
- Richart, FE; Hall, JR; Woods, RD - Vibrations of soils and foundations. (1970).
- Rinaldi, VA; Redolfi, ER; Santamarina, JC; Robertson, PK; Mayne, PW - Characterization of collapsible soils with combined geophysical and penetration testing. *Robertson and Mayne Eds., Geotechnical Site Characterization, Balkema. Rotterdam*. Vol. 1. (1998). p. 581-588.
- Rio, J - Advances in laboratory geophysics using bender elements. University of London, 2006.
- Roesler, SK - Anisotropic shear modulus due to stress anisotropy. *Journal of the Geotechnical Engineering Division*. Vol. 105. n.º 7 (1979). p. 871-880. 0093-6405
- Roesset, JM - Energy Dissipation. 1991.
- Roylance, D - Engineering viscoelasticity. *Department of Materials Science and Engineering- Massachusetts Institute of Technology, Cambridge MA*. Vol. 2139. (2001). p. 1-37.
- Sanchez-Salineró, I; Roesset, JM; Stokoe, II; Kenneth, H - Analytical studies of body wave propagation and attenuation. DTIC Document, 1986.
- Santamarina, JC; Fratta, D - Introduction to discrete signals and inverse problems in civil engineering. ASCE, 1998. 0784403112
- Santamarina, JC; Klein, KA; Fam, MA - Soils and waves: particulate materials behavior, characterization and process monitoring. *England: John Wiley and Sons Ltd*. (2001).
- Santos, JA - Caracterização de solos através de ensaios dinâmicos e cíclicos de torção Aplicação ao estudo do comportamento de estacas sob acções horizontais estáticas e dinâmicas. Universidade Técnica de Lisboa: 1999.
- Santos, JA; Camacho-Tauta, J; Parodi, M; Viana Da Fonseca, A; Ferreira, C - Use of random vibrations to measure stiffness of soils. *Experimental Vibration Analysis for Civil Engineering Structures (EVACES'07), Porto*. (2007). p. 1169-78.
- Scholte, JG - The range of existence of Rayleigh and Stoneley waves. *Geophysical Journal International*. Vol. 5. n.º s5 (1947). p. 120-126. 1365-246X

- Seed, HB; Idriss, IM - Soil moduli and damping factors for dynamic response analyses. (1970).
- Shirley, DJ; Hampton, LD - Shear-wave measurements in laboratory sediments. *The Journal of the Acoustical Society of America*. Vol. 63. n.º 2 (1978). p. 607-613. 0001-4966
- Silva Cardoso, A - Ensaaios triaxiais dos solos residuais da cidade do Porto. *Geotecnia*. Vol. nº 47. (1986).
- Spang; Wesley - In situ measurements of damping ratio using surface waves. (1995).
- Stokoe, KH; Santamarina, JC - Seismic-wave-based testing in geotechnical engineering. International Society for Rock Mechanics, 2000.
- Stokoe, KH; Wright, SG; Bay, JA; Roesset, JM - Characterization of geotechnical sites by SASW method. *Geophysical characterization of sites*. (1994). p. 15-25.
- Stoll, RD - Sediment Acoustics. *Lecture Notes in Earth Sciences, Berlin Springer Verlag*. Vol. 26. (1989).
- Stoll, RD; Bryan, GM; Bautista, EO - Measuring lateral variability of sediment geoaoustic properties. *The Journal of the Acoustical Society of America*. Vol. 96. n.º 1 (1994). p. 427-438. 0001-4966
- Stoneley, R - Elastic waves at the surface of separation of two solids. *Proceedings of the Royal Society of London. Series A, Containing Papers of a Mathematical and Physical Character*. (1924). p. 416-428. 0950-1207
- Strobbia, C - Surface wave methods: acquisition, processing and inversion. *Torino: Politecnico di Torino*. (2003).
- Studer, JA; Koller, MG - Bodendynamik. Grundlagen, Kennziffern, Probleme. (1997).
- Tani, K - General Report: Measurement of Shear Deformation of Geomaterials - Field Tests. 1994.
- Tokimatsu, K; Kōgakkai, J - Geotechnical site characterization using surface waves. publisher not identified, 1995.
- Van Dronghen, W - Signal processing for neuroscientists: an introduction to the analysis of physiological signals. Academic Press, 2006. 008046775X
- Venkatramiah, C - Geotechnical engineering. New Age International, 2006. 8122417930
- Viana da Fonseca, A - Caracterização geotécnica de um solo residual do granito da região do Porto. FEUP, Porto, 1988.
- Viana da Fonseca, A; Carvalho, J; Ferreira, C; Santos, JA; Almeida, F; Pereira, E; Feliciano, J; Grade, J; Oliveira, A - Characterization of a profile of residual soil from granite combining geological, geophysical and mechanical testing techniques. *Geotechnical and Geological Engineering*. Vol. 24. (2006).
- Viana da Fonseca, A; Matos Fernandes, M; Silva Cardoso, A; Barreiros Martins, J - Portuguese experience on geotechnical characterization of residual soils from granite. New Delhi, 1994: Oxford IBH Publishing CO PVT. Ltd, 1994.
- Viana da Fonseca, A; Vieira de Sousa, J; Ferreira, C - Deriving Stiffness Parameters from "Simple" in Situ Tests and Relating them with Reference Values on Saprolitic Soils from Granite. MIT, Cambridge, USA: 2003.
- Viggiani, G; Atkinson, JH - Interpretation of bender element tests. 1995. 0148-9062
- Wang, Yu; Yan, W; Lo, K - Damping-ratio measurements by the spectral-ratio method. *Canadian Geotechnical Journal*. Vol. 43. n.º 11 (2006). p. 1180-1194. 0008-3674
- White, JE - Seismic waves: radiation, transmission and attenuation in rocks with partial gas saturation. *Geophysics*. n.º 40 (1975).
- White, JE - Underground sound: Application of seismic waves. Elsevier Amsterdam, 1983.
- Woods, RD - Measurement of dynamic soil properties. 1978.
- Yasuda, S; Yamaguchi, I - Dynamic Shear Moduli Measured in the Laboratory and the Field. Tokyo: Japanese Society of Soil Mechanics and Foundation Engineering, 1984.

# A

## APPENDIX

### A.1. SCRIPTS

#### A.1.1. SCRIPT USED TO COMPARE ABETS AND MATLAB RESULTS

```
%Data import from Excel.
    %Note that all the sweep's data was in a single file, each sweep in a
    %different sheet with a normalized format. Also, *t1 stands for the
    %first truncation and *t2 stands for the second one.

filename='S2-9m-P2-150mm - sweeps.xlsx'

s_time=xlsread(filename, 'Sweep1', 'A8:A7175');
    s_time_t1=xlsread(filename, 'Sweep1', 'A8:A4038');
    s_time_t2=xlsread(filename, 'Sweep1', 'A4038:A7175');
    s_time_t2=s_time_t2-xlsread(filename, 'Sweep1', 'A4038'); %Shift in the
                                                                %2nd truncation
                                                                %time vector,
                                                                %so it starts
                                                                %at t=0.

fs=xlsread(filename, 'Sweep1', 'Q2');    %Sampling frequency as the inverse
                                                                %of the cell corresponding to the
                                                                %second time acquisition (the first
                                                                %corresponds to t=0).

s1_signal=xlsread(filename, 'Sweep1', 'C8:C7175');
s1_receptor=xlsread(filename, 'Sweep1', 'E8:E7175');
    s1_receptor_t1=xlsread(filename, 'Sweep1', 'E8:E4038');
    s1_receptor_t2=xlsread(filename, 'Sweep1', 'E4038:E7175');
    s1_receptor_tm=(s1_receptor_t1(1:3138)+s1_receptor_t2)/2;

display('Data imported!')

%Definition of the Butterworth filter and signal filtering. Note that the
%variable cutoff is not equivalent to an actual value of frequency, but is
%instead a parameter with range [0;1]. n1 and n2 are related with the
%filter's order, which are the same for previous works of Ferreira.
cutoff=0.5;
n1=4;
n2=10;

[b1, a1]=butter(n1, cutoff);
[b2, a2]=butter(n2, cutoff);

s1_receptor_f=filtfilt(b2, a2, s1_receptor);
    s1_receptor_t1_f=filtfilt(b2, a2, s1_receptor_t1);
    s1_receptor_t2_f=filtfilt(b2, a2, s1_receptor_t2);
```

```

s1_receptor_tm_f=filtfilt(b2,a2,s1_receptor_tm);

clear n* b* a*

%FFT calculation
%It's not required to create a new variable to save the
%FFT values, since this step could be included inside other
%algorithms that use the FFT values. However, the script is
%presented this way for easier comprehension.
FFT_s1_receptor_tm_f=fft(s1_receptor_tm_f);

display('FFTs complete!')

%Coherence calculation
[coh_s1_tm_f , F_tm]=mscohere(s1_signal_t2,s1_receptor_tm_f,[],[],[],fs);

display('Coherencies calculated!')

%Phase calculation
phase_s1_receptor_tm_f=angle(FFT_s1_receptor_tm_f);

display('Phases calculated!')

%Magnitude dos FFT's
mag_s1_receptor_tm_f=abs(FFT_s1_receptor_tm_f);

display('Magnitudes calculated!')

%Auxiliary variable corresponding to the number of points of the
%first half of the spectrum, in order to eliminate mirror redundancy.
NrUniqPts=ceil((length(s_time)+1)/2);
NrUniqPts_t=ceil((length(s1_receptor_t1)+1)/2);
%Determination of the frequency vectors.
s_freq=(0:NrUniqPts-1)*fs/length(s_time);
s_freq_t=(0:NrUniqPts_t-1)*fs/length(s1_receptor_t1);

%Figures 11 and 12: signal plots
figure(1)
plot(s_time,s1_signal,s_time,s1_receptor_f);
title('Sweep1 - Time domain test result');
xlabel('Time (ms)');
ylabel('Voltage [mV]');
legend('Signal wave','Filtered received wave');

figure(12)
plot(s_time_t1,s1_receptor_t1_f, s_time_t2,s1_receptor_t2_f,
s_time_t2,s1_receptor_tm_f);
title('Signal averaging');
xlabel('Time (ms)');
ylabel('Voltage [mV]');
legend('1st truncation','2nd truncation','Average signal');

%Figura 2: Coherence
figure(2)
plot(F_tm,coh_s1_tm_f);
title('Coherence');
xlabel('Frequency [kHz]');
ylabel('Coh');

```

```

%Figura 3: phase plot
figure(3)
plot(s_freq_t,phase_s1_receptor_tm_f(1:NrUniqPts_t));
    title('Phase');
    xlabel('Frequency [kHz]');
    ylabel('Phase [rad]');

%Figura 4: unwrapped phase plot
figure(4)
plot(s_freq_t,unwrap(phase_s1_receptor_tm_f(1:NrUniqPts_t)));
    title('Unwrapped phase');
    xlabel('Frequency [kHz]');
    ylabel('Phase [rad]');

%Figure 5: Frequency spectrum
figure(5)
plot(s_freq_t,mag_s1_receptor_tm_f(1:NrUniqPts_t));
    title('Spectrum');
    xlabel('Frequency [kHz]');
    ylabel('Mag');

%Moving average filter -> Unused
%aglom=3; -> Nr of points to average
%coeffs=ones(1, aglom)/aglom;

%maf=filter(coeffs, 1, mag_s1_receptor_f);
%mafdelay=(length(coeffs)-1)/2;

```

## A.1.2. HALF-POWER BANDWIDTH METHOD

```
%1) Data import from Excel.
    %Note that all the sweep's data was in a single file, each sweep in a
    %different sheet with a normalized format.

filename='BE-P3-50mm-sweeps.xlsx'

time=xlsread(filename, 'Sweep1', 'B4:B1792');
signal=xlsread(filename, 'Sweep1', 'C4:C1792');
receptor1=xlsread(filename, 'Sweep1', 'F4:F1792');
receptor2=xlsread(filename, 'Sweep2', 'F4:F1792');
receptor3=xlsread(filename, 'Sweep3', 'F4:F1792');
receptor4=xlsread(filename, 'Sweep4', 'F4:F1792');
    receptor_m=(receptor1+receptor2+receptor3+receptor4)/4;
fs=1/xlsread(filename, 'Sweep1', 'B5'); %Sampling frequency as the inverse
    %of the cell value corresponding to
    %the second time acquisition (the
    %first corresponds to t=0).

NrUniqPts=ceil((length(receptor_m)+1)/2); %auxiliary variable corresponding
    %to the number of points of the
    %first half of the spectrum, in
    %order to eliminate mirror
    %redundancy.
freq=(0:NrUniqPts-1)*fs/length(receptor_m); %Frequency vector
    %determination.

figure(1)
subplot(2,2,1);
    plotyy(time, signal, time, receptor1);
    title('1st sweep');
    xlabel('Time (ms)');
    ylabel('Voltage [mV]');
    legend('Signal wave', 'Receiver wave');
subplot(2,2,2);
    plotyy(time, signal, time, receptor2);
    title('2nd sweep');
    xlabel('Time (ms)');
    ylabel('Voltage [mV]');
    legend('Signal wave', 'Receiver wave');
subplot(2,2,3);
    plotyy(time, signal, time, receptor3);
    title('3rd sweep');
    xlabel('Time (ms)');
    ylabel('Voltage [mV]');
    legend('Signal wave', 'Receiver wave');
subplot(2,2,4);
    plotyy(time, signal, time, receptor4);
    title('4th sweep');
    xlabel('Time (ms)');
    ylabel('Voltage [mV]');
    legend('Signal wave', 'Receiver wave');

figure(2)
plotyy(time, signal, time, receptor_m);
    title('Sample P3 (50mm) averaged receiver wave');
    xlabel('Time (ms)');
    ylabel('Voltage [mV]');
    legend('Signal wave', 'Receiver wave');
```



```

%2) FFT and magnitude.
    %It's not required to create a new variable to save the
    %magnitude values, as abs(fft( ... )) does the same. The script is
    %presented this way for easier comprehension.

FFT_receptor_m=fft(receptor_m);
mag=abs(FFT_receptor_m);

%3) Damping determination by half-power bandwidth method.
    %Explanation and variable nomenclature as stated before.

aux=5; %Auxiliary variable used to ignore the first (five) points of the
    %spectrum, associated to test noise.

figure(3)
    plot(freq,mag(1:NrUniqPts))
    title('Sample P3 (50mm) frequency spectrum')
    xlabel('Frequency [kHz]')
    ylabel('Magnitude')

Am=max(mag(aux:NrUniqPts));
Anot=Am/2^0.5; %Notable value of A for determination of f1 and f2, with
    %the relation already stated.

indexm=find(mag(aux:NrUniqPts)==Am)+aux-1
fm=freq(indexm)

clear aux

%3.1) 1st truncation interpolation
    aux2=indexm-10 %Auxiliary variable to determine the range of data
    %points (10 data points in this case) at the left of fm
    %for interpolation
[c index1]=min(abs(mag(aux2:indexm)-Anot))
clear c;
    index1=index1+aux2-1;
closestvalue1=mag(index1)

if closestvalue1>Anot
    index1t1=index1-1
    index2t1=index1
else
    index1t1=index1
    index2t1=index1+1
end

clear aux2

f1=freq(index1t1)+(((Anot-mag(index1t1))/(mag(index2t1)-
mag(index1t1)))*(freq(index2t1)-freq(index1t1)))%Interpolation to calculate
    %the value of f1

%3.2) 2nd truncation interpolation
    aux3=indexm+10; %Same as aux2.

[c index2]=min(abs(mag(indexm:aux3)-Anot))
clear c;
    index2=index2+indexm-1

```

```

closestvalue2=mag(index2)

if closestvalue2>Anot
    index1t2=index2
    index2t2=index2+1
else
    index1t2=index2-1
    index2t2=index2
end

clear aux3

f2=freq(index1t2)+(((Anot-mag(index1t2))/(mag(index2t2)-
mag(index1t2)))*(freq(index2t2)-freq(index1t2))))

%4) Damping determination

D_BR=Anot*((f2^2-f1^2)/(Anot^2*f2^4-
2*Anot^2*f2^2*f1^2+Anot^2*f1^4+16*fm^4*(Am^2-Anot^2))^0.5)*100
    %Damping according to Brocanelli and Rinaldi (1998)

D_LK=(f2^2-f1^2)/(4*fm^2)*100
    %Damping according to Lutz Karl (2005)

```

### A.1.3. PRATT'S CIRCLE-FIT METHOD

```
function Par = CircleFitByPratt(XY)

%-----
%
%   Circle fit by Pratt
%   V. Pratt, "Direct least-squares fitting of algebraic surfaces",
%   Computer Graphics, Vol. 21, pages 145-152 (1987)
%
%   Input:  XY(n,2) is the array of coordinates of n points x(i)=XY(i,1),
%           y(i)=XY(i,2)
%
%   Output: Par = [a b R] is the fitting circle:
%           center (a,b) and radius R
%
%   Note: this fit does not use built-in matrix functions (except
%   "mean"),
%           so it can be easily programmed in any programming language
%-----

n = size(XY,1);      %Number of data points

centroid = mean(XY); %The centroid of the data set

%Computing moments (note: all moments will be normed, i.e. divided by n)

Mxx=0; Myy=0; Mxy=0; Mxz=0; Myz=0; Mzz=0;

for i=1:n
    Xi = XY(i,1) - centroid(1); % centering data
    Yi = XY(i,2) - centroid(2); % centering data
    Zi = Xi*Xi + Yi*Yi;
    Mxy = Mxy + Xi*Yi;
    Mxx = Mxx + Xi*Xi;
    Myy = Myy + Yi*Yi;
    Mxz = Mxz + Xi*Zi;
    Myz = Myz + Yi*Zi;
    Mzz = Mzz + Zi*Zi;
end

Mxx = Mxx/n;
Myy = Myy/n;
Mxy = Mxy/n;
Mxz = Mxz/n;
Myz = Myz/n;
Mzz = Mzz/n;

%Computing the coefficients of the characteristic polynomial

Mz = Mxx + Myy;
Cov_xy = Mxx*Myy - Mxy*Mxy;
Mxz2 = Mxz*Mxz;
Myz2 = Myz*Myz;

A2 = 4*Cov_xy - 3*Mz*Mz - Mzz;
A1 = Mzz*Mz + 4*Cov_xy*Mz - Mxz2 - Myz2 - Mz*Mz*Mz;
A0 = Mxz2*Myy + Myz2*Mxx - Mzz*Cov_xy - 2*Mxz*Myz*Mxy + Mz*Mz*Cov_xy;
```

```

A22 = A2 + A2;

epsilon=1e-12;
ynew=1e+20;
IterMax=20;
xnew = -10;

%Newton's method starting at x=0

for iter=1:IterMax
    yold = ynew;
    ynew = A0 + xnew*(A1 + xnew*(A2 + 4.*xnew*xnew));
    if (abs(ynew)>abs(yold))
        disp('Newton-Pratt goes wrong direction: |ynew| > |yold|');
        xnew = 0;
        break;
    end
    Dy = A1 + xnew*(A22 + 16*xnew*xnew);
    xold = xnew;
    xnew = xold - ynew/Dy;
    if (abs((xnew-xold)/xnew) < epsilon), break, end
    if (iter >= IterMax)
        disp('Newton-Pratt will not converge');
        xnew = 0;
    end
    if (xnew<0.)
        fprintf(1,'Newton-Pratt negative root: x=%f\n',xnew);
        xnew = 0;
    end
end
end

%Computing the circle parameters

DET = xnew*xnew - xnew*Mz + Cov_xy;
Center = [Mxz*(Myy-xnew)-Myz*Mxy , Myz*(Mxx-xnew)-Mxz*Mxy]/DET/2;

Par = [Center+centroid , sqrt(Center*Center'+Mz+2*xnew)];

end

```

**A.2. ORIGINAL TEST RESULTS**

A.2.1. TIME DOMAIN

A.2.1.1. Sample P1 (100mm)

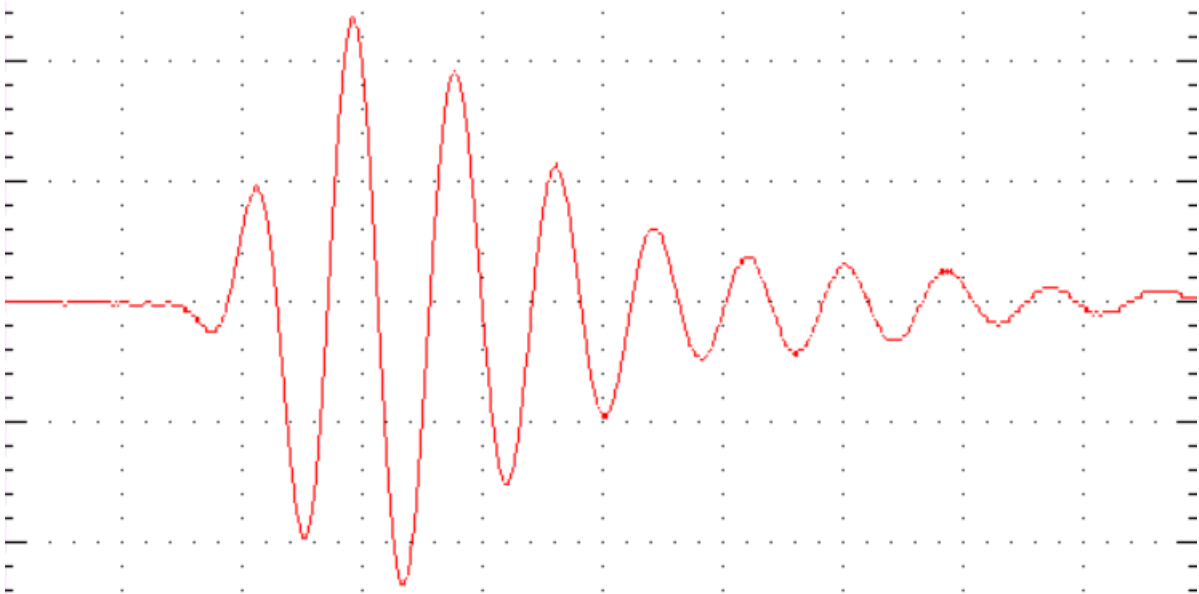


Figure A.1 – Sample P1 (100mm): output wave, 1kHz

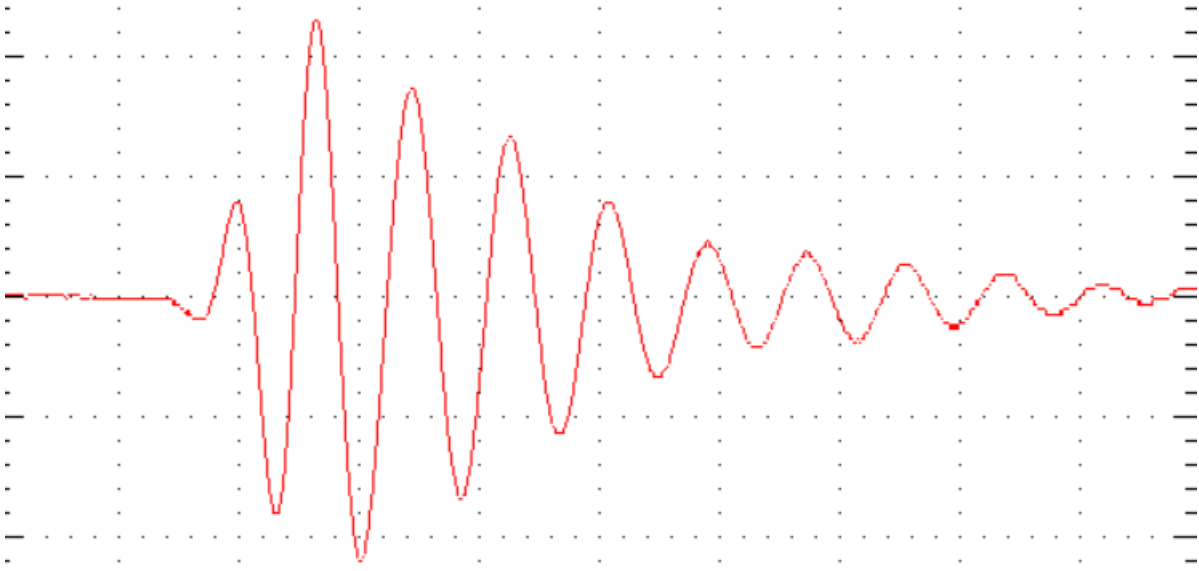


Figure A.2 – Sample P1 (100mm): output wave, 2kHz

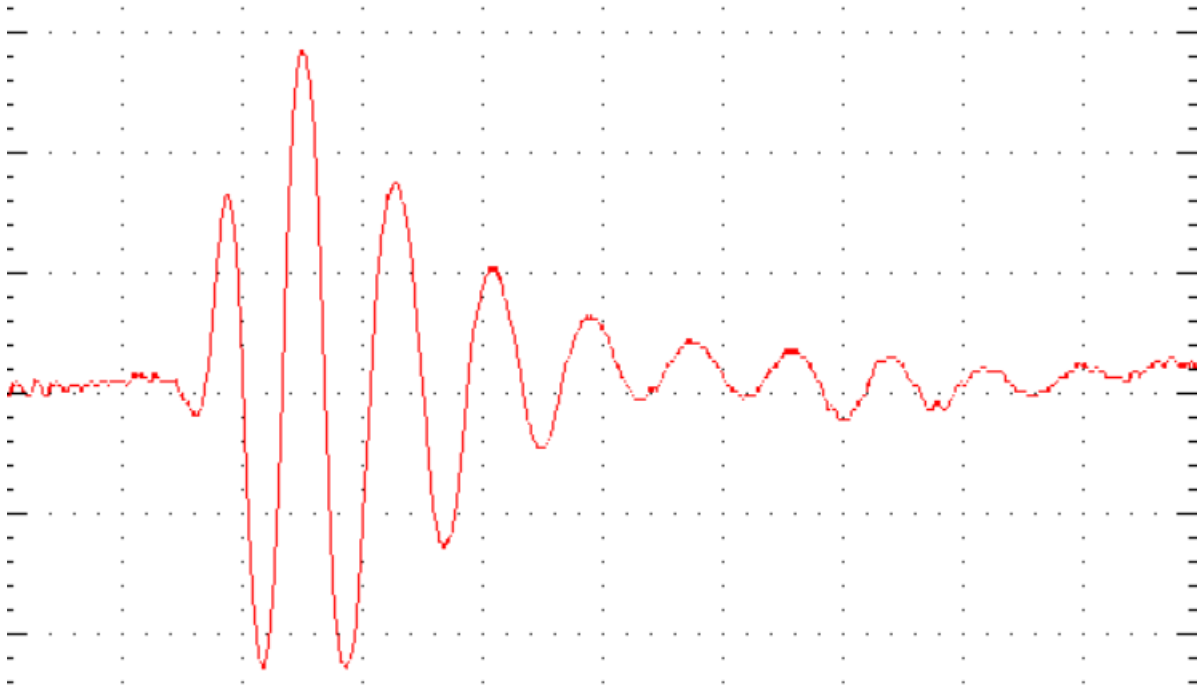


Figure A.3 – Sample P1 (100mm): output wave, 4kHz

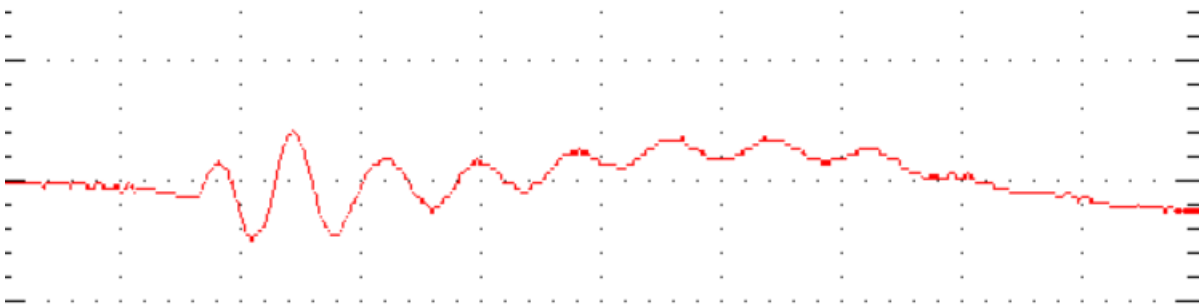


Figure A.4 – Sample P1 (100m): output wave, 8kHz

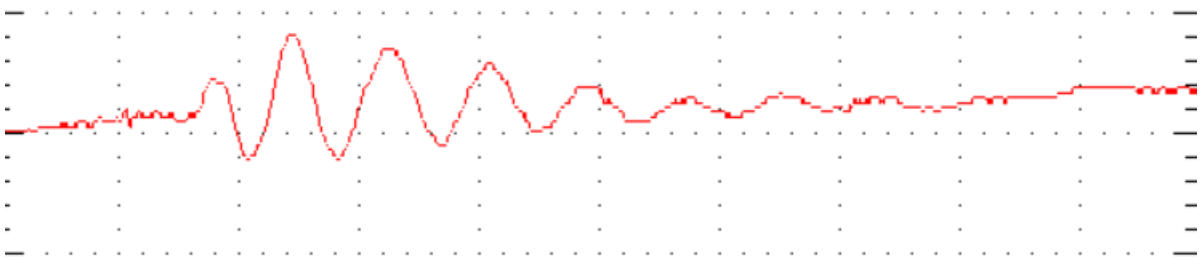


Figure A.5 – Sample P1 (100mm): output wave, 10kHz

Table A.1.1 – Sample P1 (100mm): logarithmic decay method

P1-s1-1-2-4-6kHz-1ms				100mm	
	Voltage [mV]				
	1kHz	2kHz	4kHz	8kHz	10kHz
Max peak	1200	1140	146		
Following peaks	980	840	90		
	600	640	56		
	320	380	34		
	200	200	24		
	180	160			
	160	100			
	80	60			
Signal Quality	Very high	Very high	High	Very low	Very low
Nr. of successive peaks	Logarithmic decrement, $\delta$				
	1kHz	2kHz	4kHz	8kHz	10kHz
2	0,2025	0,3054	0,4838		
3	0,3466	0,2887	0,4791		
4	0,4406	0,3662	0,4857		
5	0,4479	0,4351	0,4514		
6	0,3794	0,3927			
7	0,3358	0,4056			
8	0,3869	0,4206			
Nr. of successive peaks	Damping [%]				
	1kHz	2kHz	4kHz	8kHz	10kHz
2	3,2	4,9	7,7		
3	5,5	4,6	7,6		
4	7,0	5,8	7,7		
5	7,1	6,9	7,2		
6	6,0	6,2			
7	5,3	6,4			
8	6,1	6,7			

red value = peak value similar to the previous one

A.2.1.2. "Calibration" sample P2 (150mm)

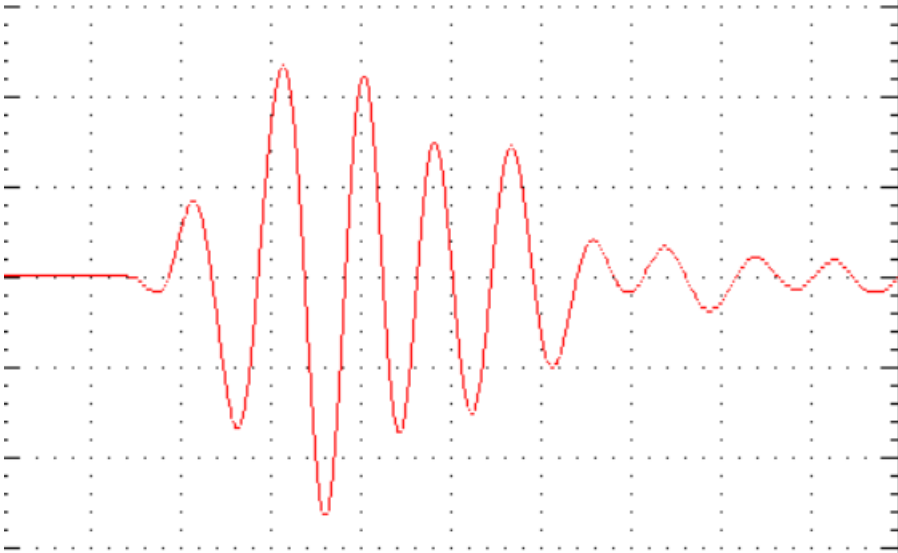


Figure A.6 – Sample P2 (150mm): output wave, 1kHz

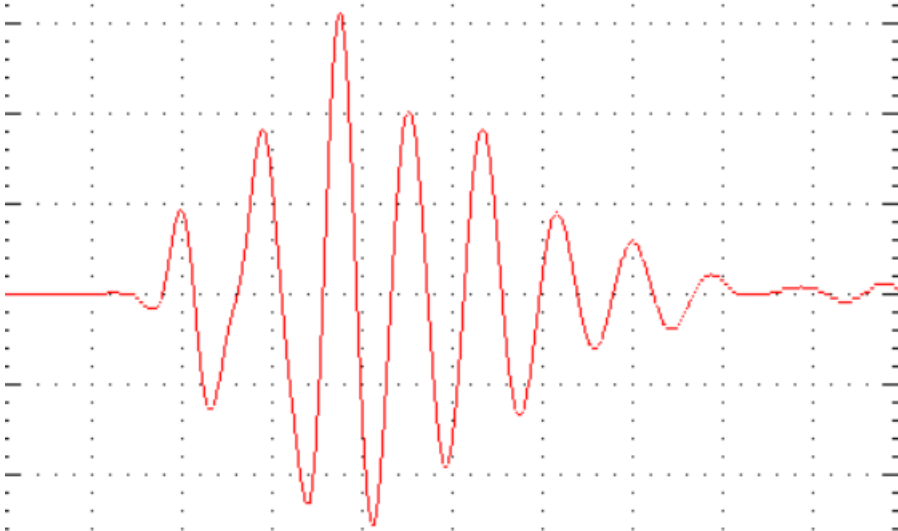


Figure A.7 – Sample P2 (150mm): output wave, 2kHz



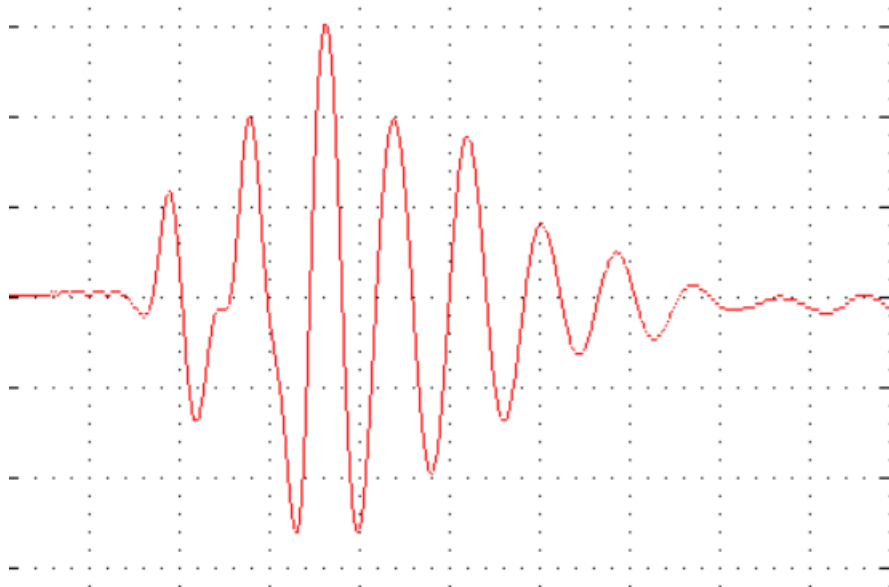


Figure A.8 – Sample P2 (150mm): output wave, 4kHz

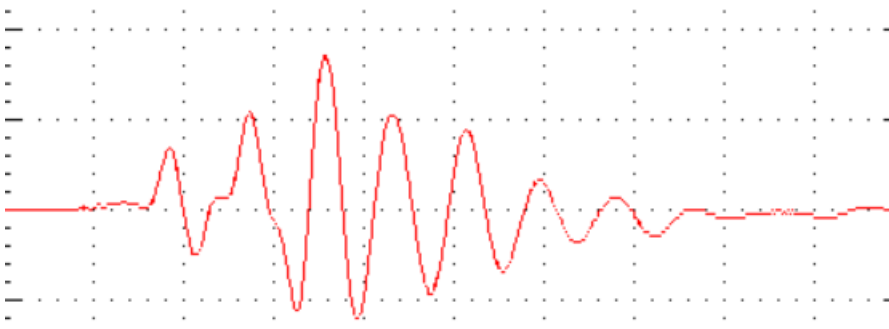


Figure A.9 – Sample P2 (150mm) output wave, 6Khz

Table A.1.2 – Sample P2 (150mm): logarithmic decay method

P2-s1-1-2-4-6kHz-1ms		150mm			
		Voltage [mV]			
		1kHz	2kHz	4kHz	6kHz
Max peak		1220	1600	332	100
		1180	1060	224	68
		800	960	208	60
Following peaks		780	500	108	30
		260	340	80	22
		160			
Signal quality		Low	High	High	High
		Logarithmic decrement, $\delta$			
	Nr. of successive peaks	1kHz	2kHz	4kHz	6kHz
	2	0,0333	0,4117	0,3935	0,3857
	3	0,2110	0,2554	0,2338	0,2554
	4	0,1491	0,3877	0,3743	0,4013
	5	0,3865	0,3872	0,3558	0,3785
	6	0,4605			
		Damping [%]			
	Nr. of successive peaks	1kHz	2kHz	4kHz	6kHz
	2	0,5	6,5	6,3	6,1
	3	3,4	4,1	3,7	4,1
	4	2,4	6,2	5,9	6,4
	5	6,1	6,2	5,7	6,0
	6	7,3			

red value = peak value similar to the previous one

A.2.1.3. Sample P3 (50mm)



Figure A.10 – Sample P3 (50mm): output wave, 1kHz

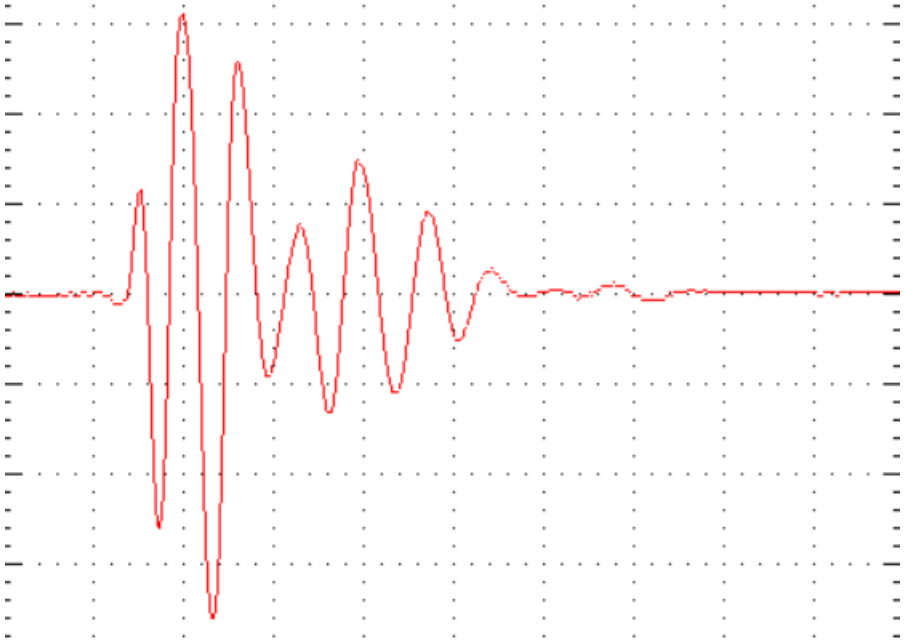


Figure A.11 – Sample P3 (50mm): output wave, 2kHz

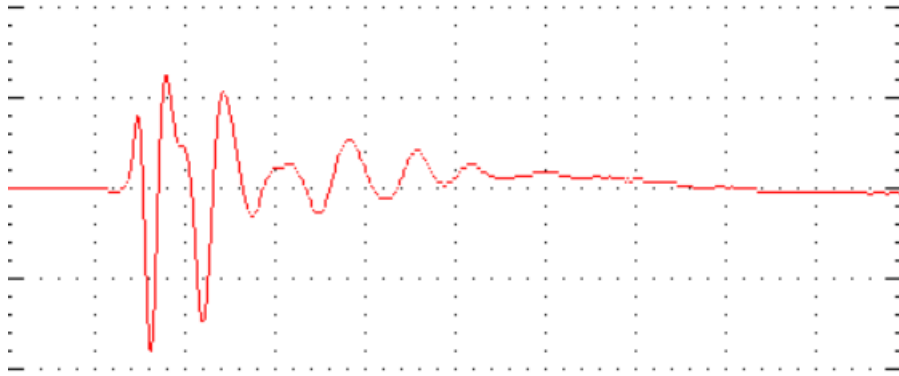


Figure A.12 – Sample P3 (50mm): output wave, 4kHz

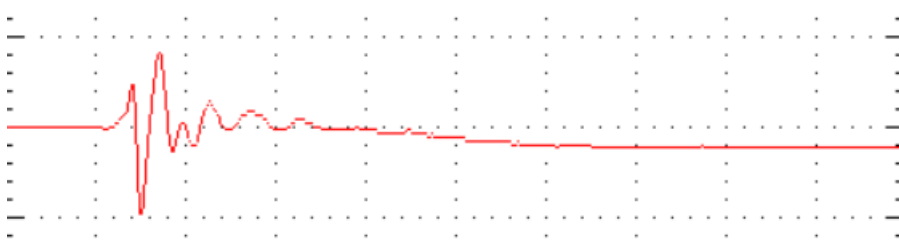


Figure A.13 – Sample P3 (50mm): output wave, 8kHz

Table A.1.3 – Sample P3 (50mm): logarithmic decay method

P3-s1-1-2-4-8kHz-1ms				50mm
	Voltage [mV]			
	1kHz	2kHz	4kHz	8kHz
Max peak	1600	648	152	
	200	536	132	
	480	168	56	
Following peaks	440	320	80	
	140	216	68	
	120			
Signal Quality	High	High	Low	Very low
	Logarithmic decrement, $\delta$			
Nr. of successive peaks	1kHz	2kHz	4kHz	8kHz
2	2,079442	0,189757	0,141079	
3	0,601986	0,674963	0,499264	
4	0,430328	0,23519	0,320927	
5	0,609029	0,274653	0,402186	
6	0,518053			
	Damping [%]			
Nr. of successive peaks	1kHz	2kHz	4kHz	8kHz
2	31,4	3,0	2,2	
3	9,5	10,7	7,9	
4	6,8	3,7	5,1	
5	9,6	4,4	6,4	
6	8,2			

red value = peak value similar to the previous one

## A.2.2. FREQUENCY DOMAIN

### A.2.2.1. Sample P1 (100mm)

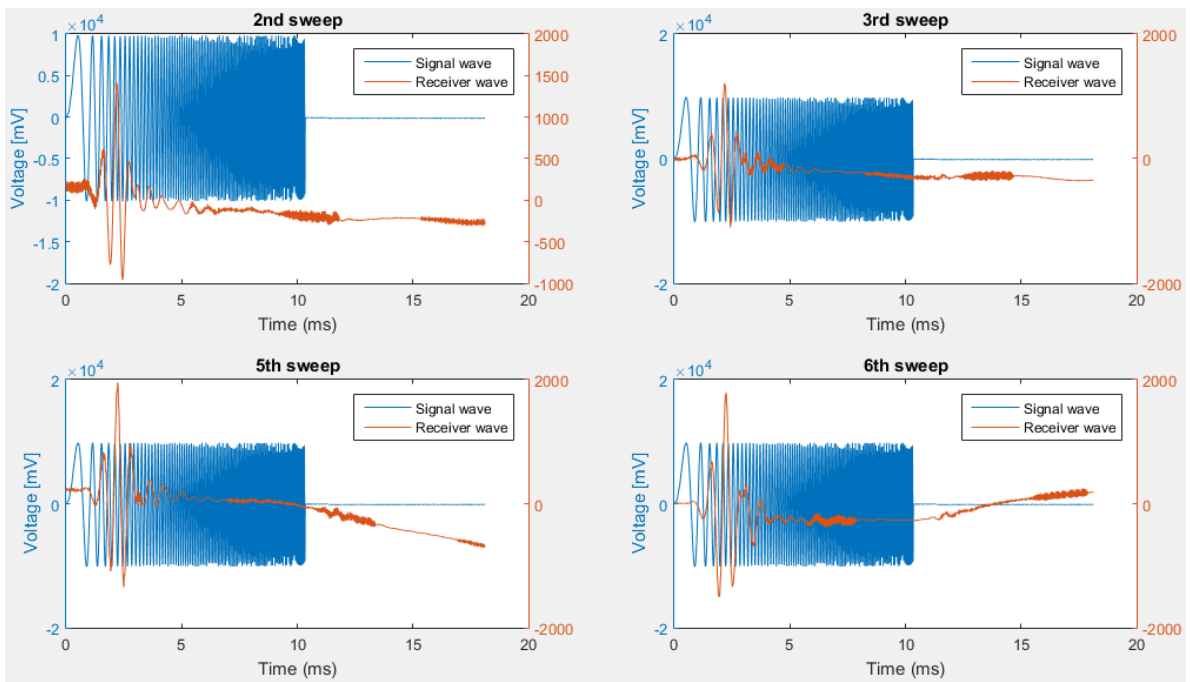


Figure A.14 – Sample P1 (100mm): chosen sweep tests

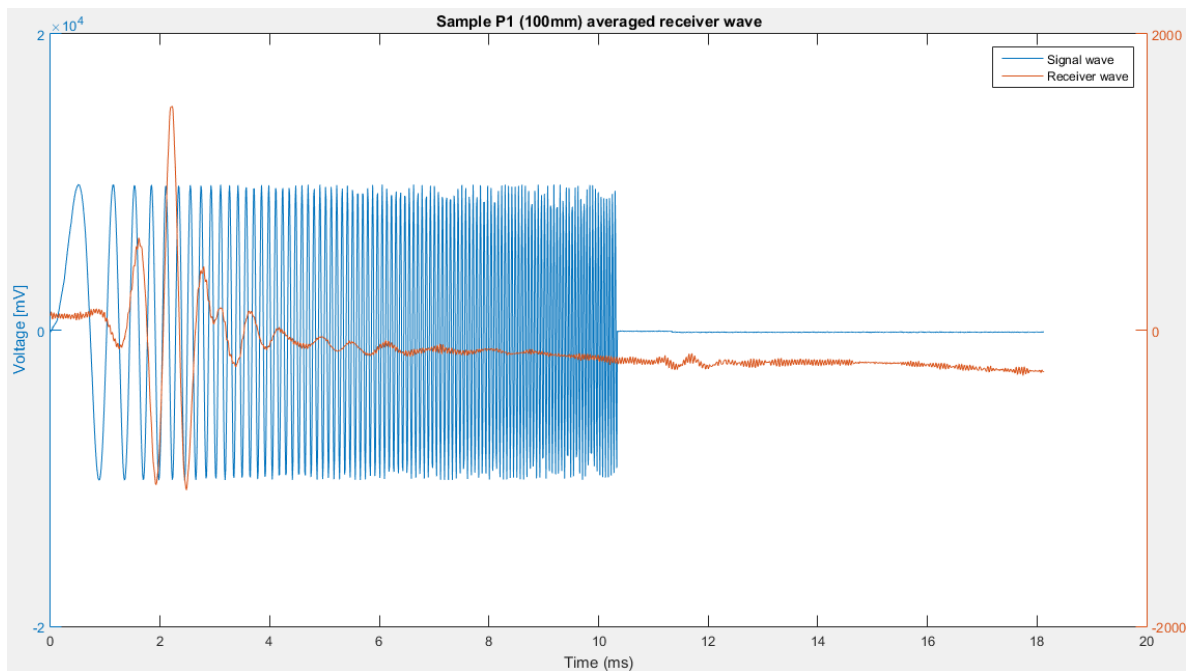


Figure A.15 – Sample P1 (100mm): averaged signal

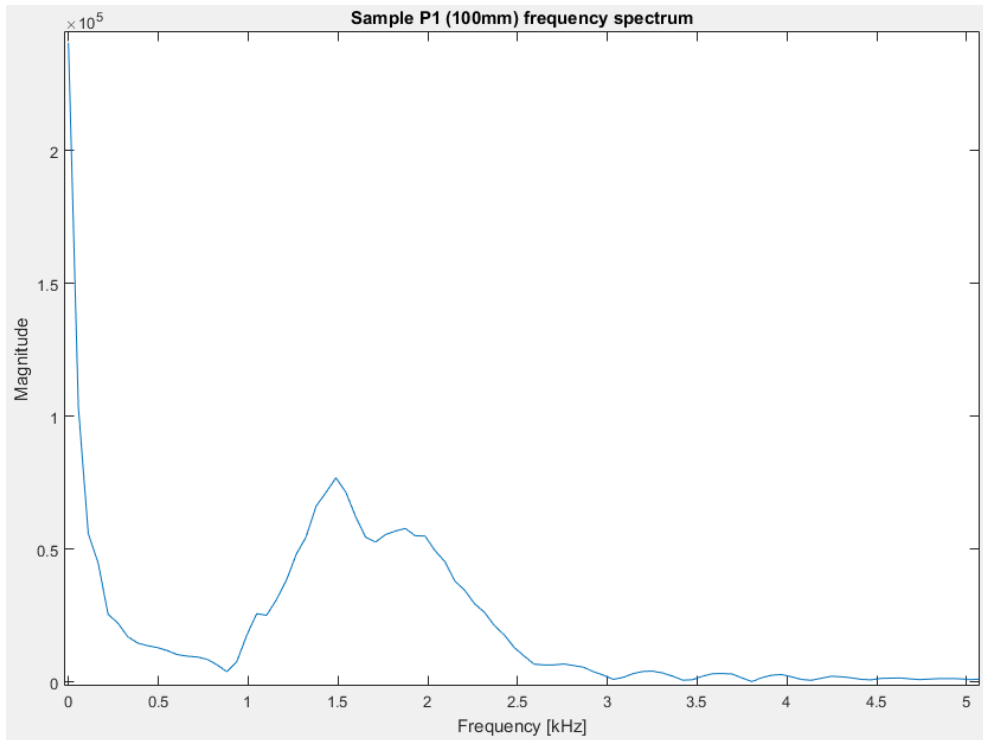


Figure A.16 – Sample P1 (100mm): frequency spectrum

Table A.1.4 – Sample P1 (100mm): results for the half-power bandwidth method

$A_m$	$f_m$ [kHz]	$A_{not}$	$f_1$ [kHz]	$f_2$ [kHz]	$\xi_{BR}$	$\xi_K$
7.6874e+04	1.49	5.4358e+04	1.32	1.66	11.31	11.38

A.2.2.2. "Calibration" sample P2 (150mm)

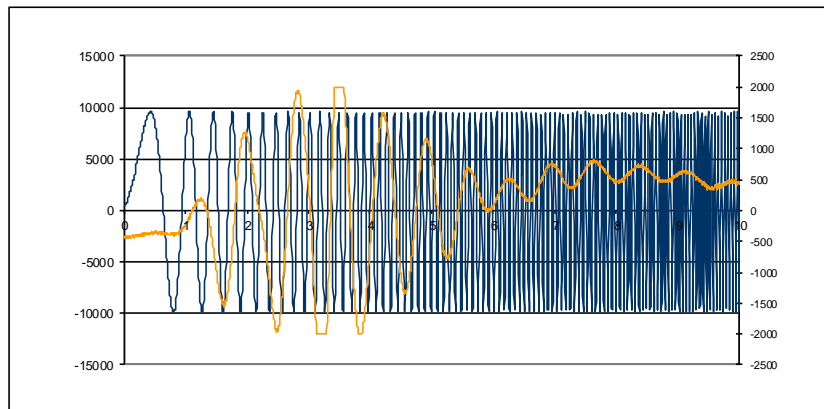


Figure A.17 – Sample P2 (150mm), sweep 1: ABETS' test display

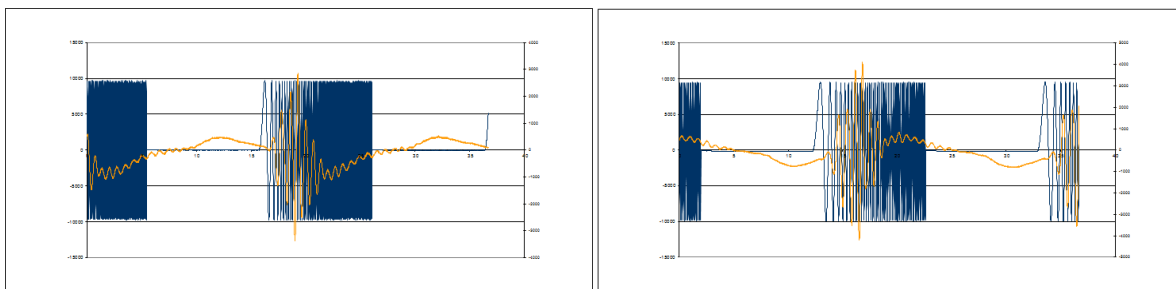


Figure A.18 – Sample P2 (150mm), sweep 2 (left) and sweep 3 (right): ABETS' test display

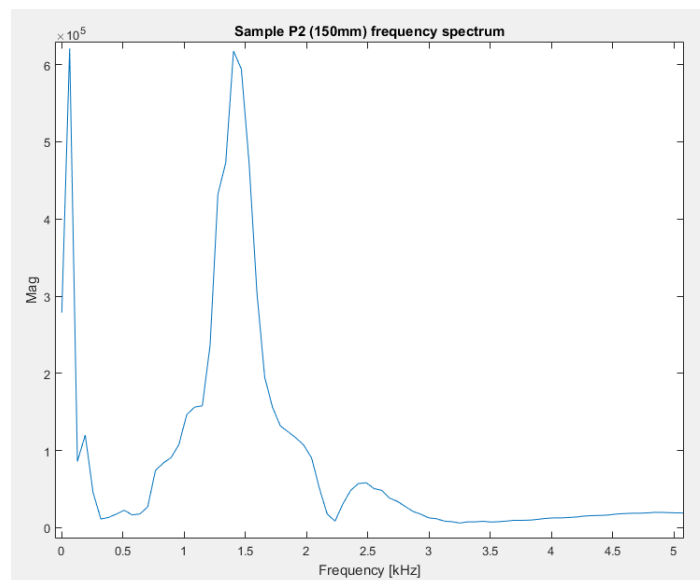


Figure A.19 – Sample P2 (150mm): frequency spectrum

Table A.1.5 – Sample P2 (150mm): half-power bandwidth method results

$A_m$	$f_m$ [kHz]	$A_{not}$	$f_1$ [kHz]	$f_2$ [kHz]	$\xi_{BR}$	$\xi_K$
6.1751e+05	1.40	4.3665e+05	1.28	1.54	9.39%	9.35%



### A.2.2.3. Sample P3 (50mm)

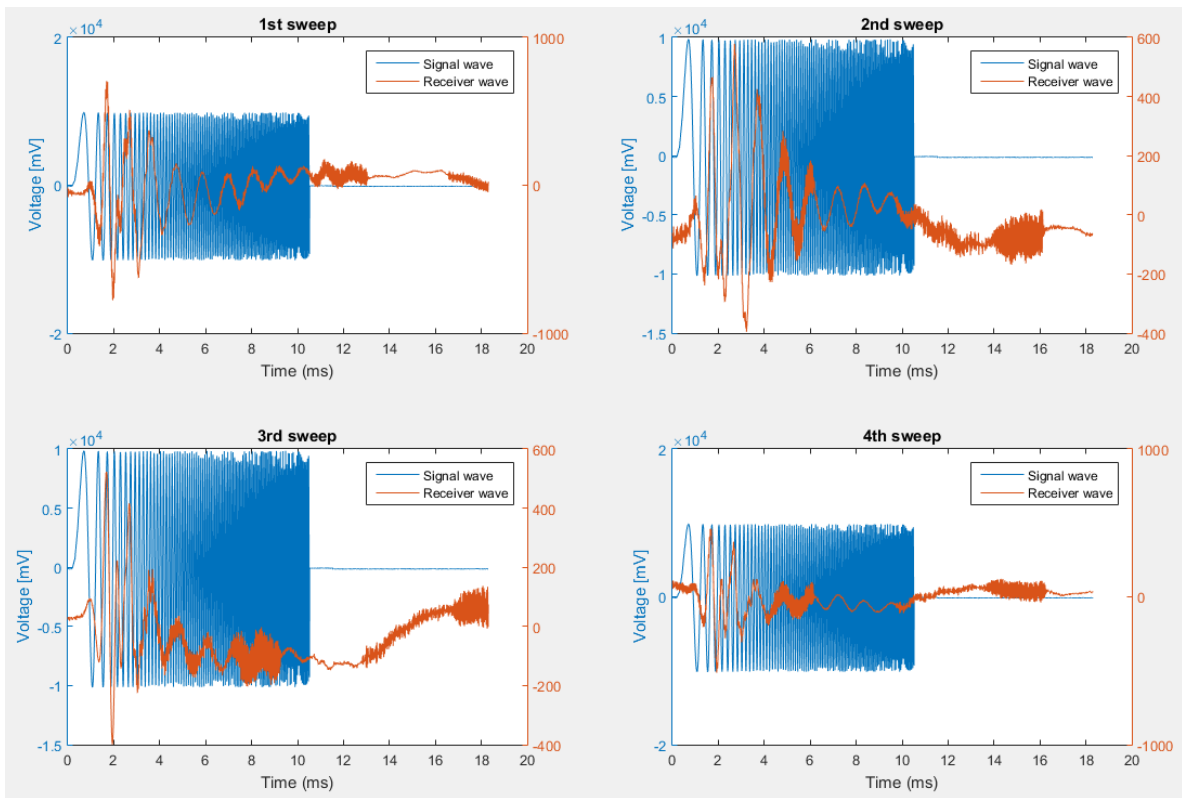


Figure A.20 – Sample P3 (50mm): chosen sweep signals

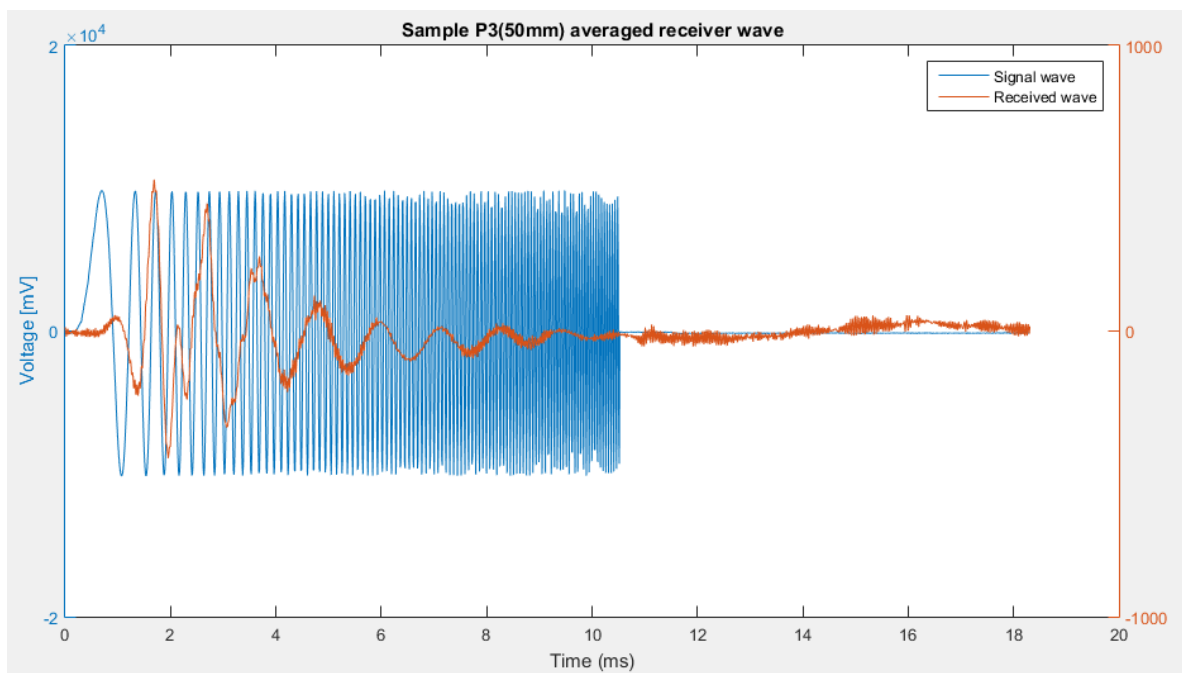


Figure A.21 – Sample P3 (50mm): averaged signal

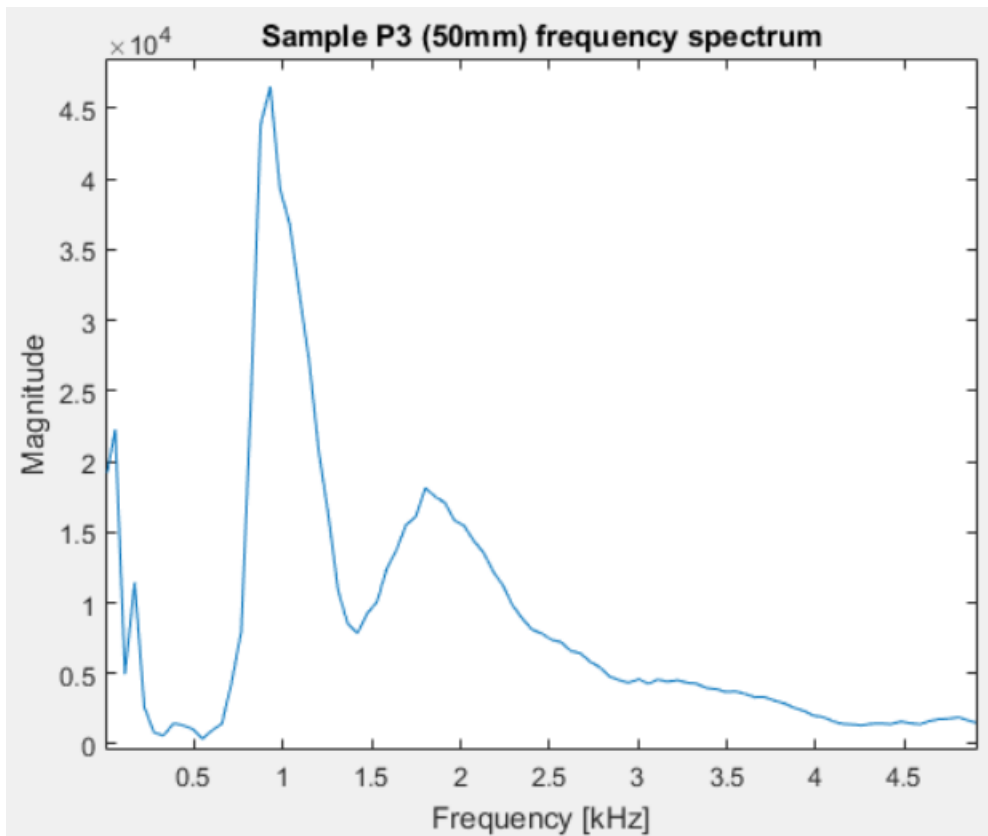


Figure A.22 – Sample P3 (50mm): frequency spectrum

Table A.1.6 – Sample P3 (50mm): results for half-power bandwidth method

$A_m$	$f_m$ [kHz]	$A_{not}$	$f_1$ [kHz]	$f_2$ [kHz]	$\xi_{BR}$	$\xi_K$
4.6556e+04	0.93	3.2920e+04	0.84	1.08	13,14	13,26

A.2.2.4. Sample P4 (100mm)

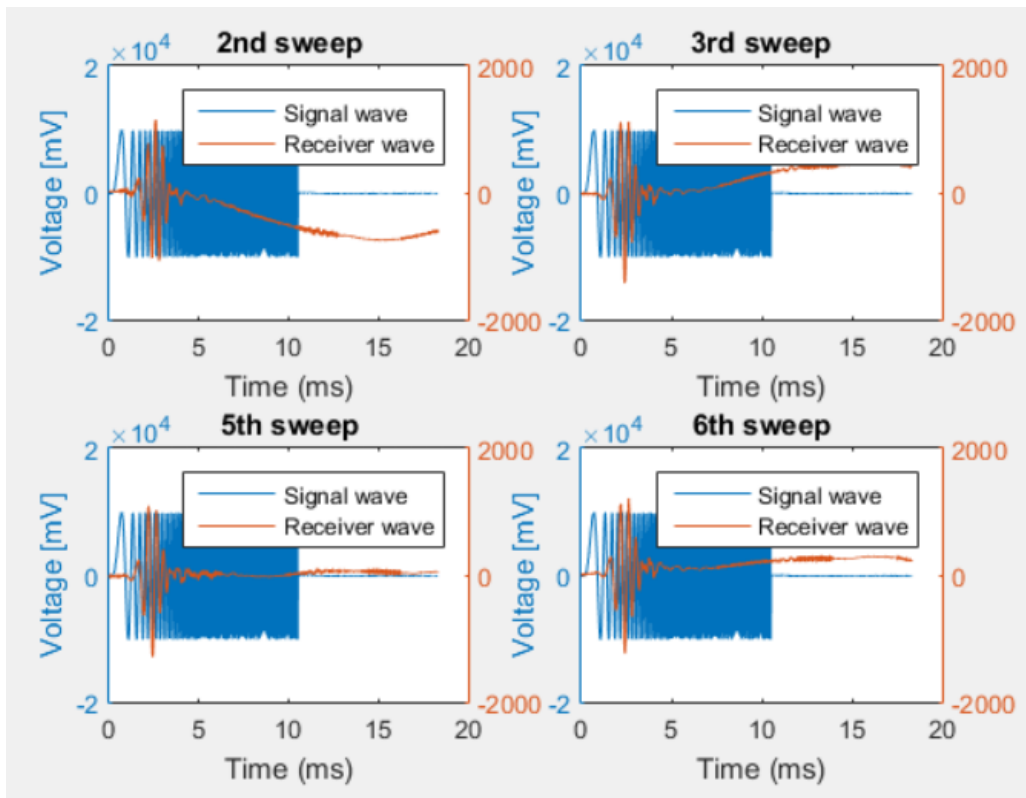


Figure A.23 – Sample P4 (100mm): chosen sweep tests

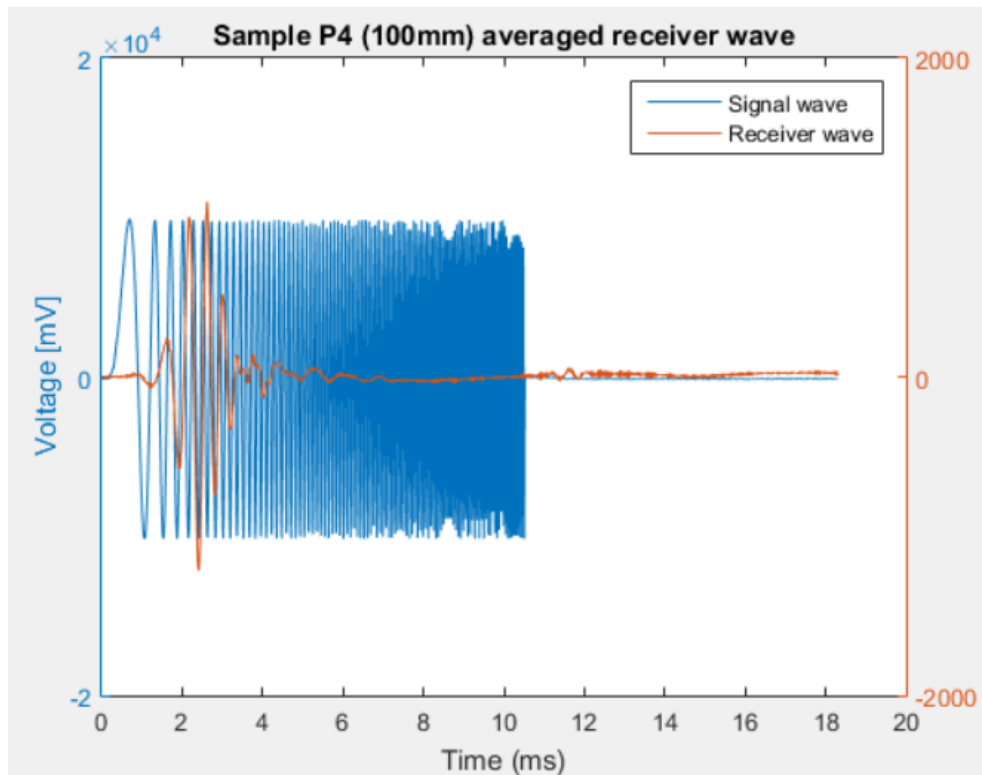


Figure A.24 – Sample P4 (100mm): averaged signal

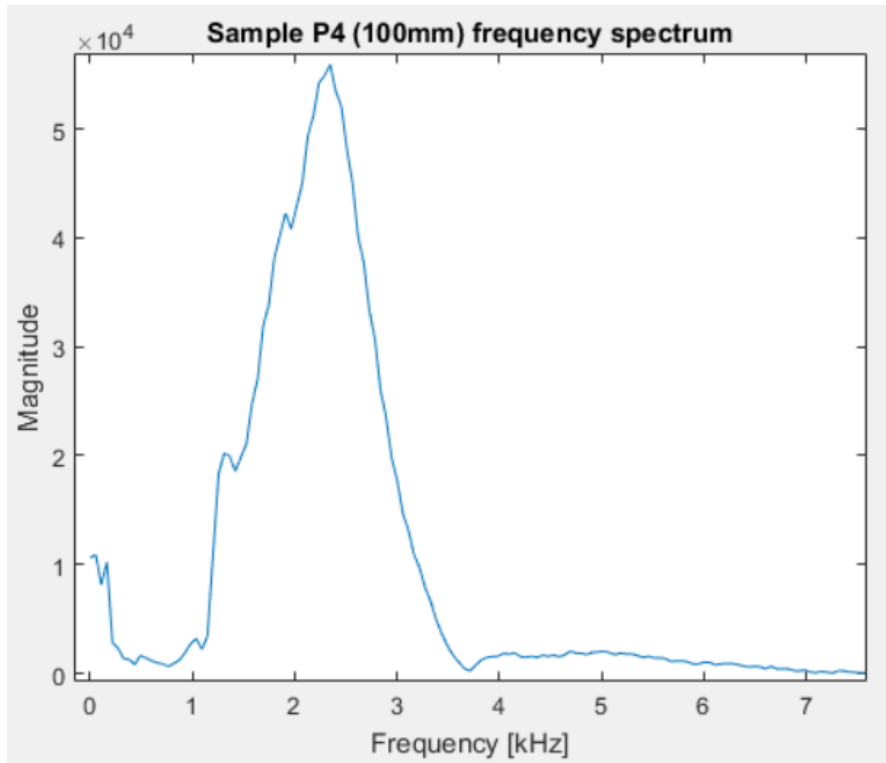


Figure A.25 – Sample P4 (100mm): frequency spectrum

Table A.1.7 – Sample P4 (100mm): results for the half-power bandwidth method

$A_m$	$f_m$ [kHz]	$A_{not}$	$f_1$ [kHz]	$f_2$ [kHz]	$\xi_{BR}$	$\xi_K$
5.5898e+04	2.35	3.9526e+04	1.84	2.63	15.96	16.17

A.2.2.5. Sample P5 (50mm)

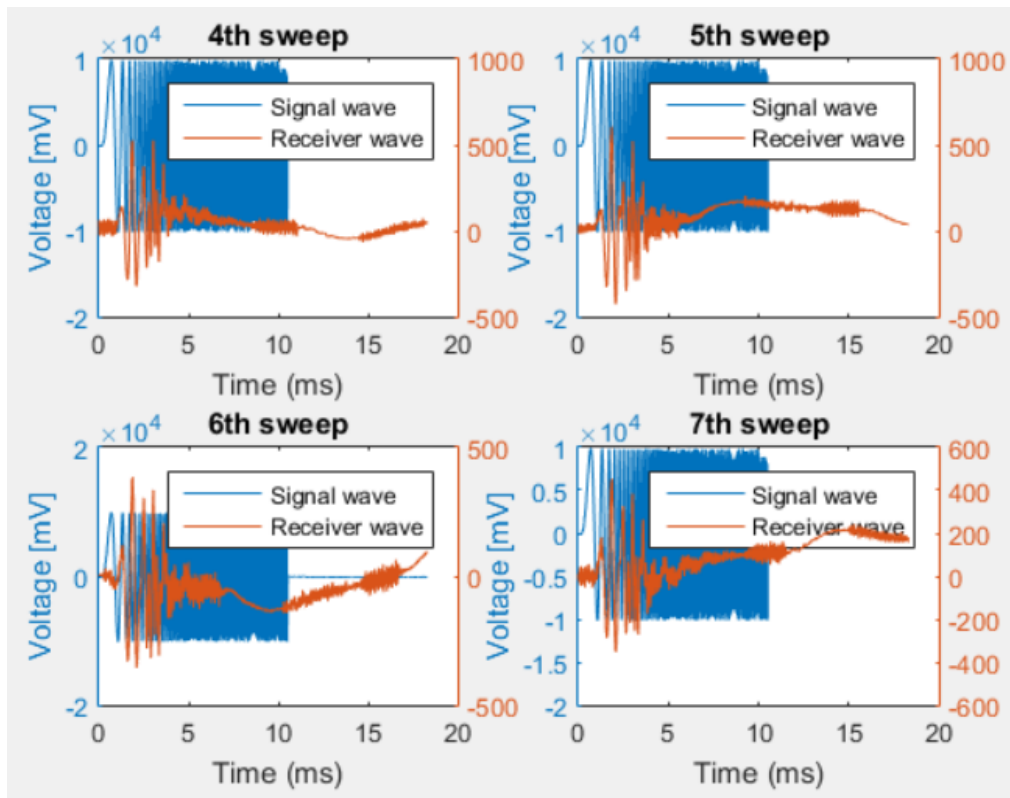


Figure A.26 – Sample P5 (50mm): chosen sweep tests

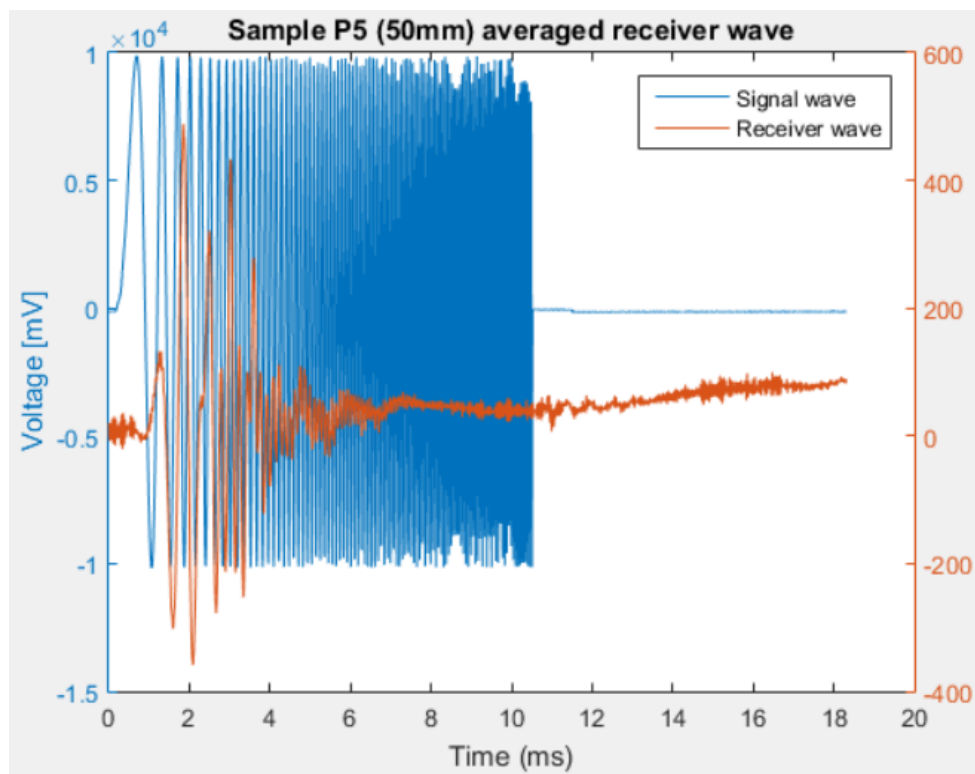


Figure A.27 – Sample P5 (50mm): averaged signal

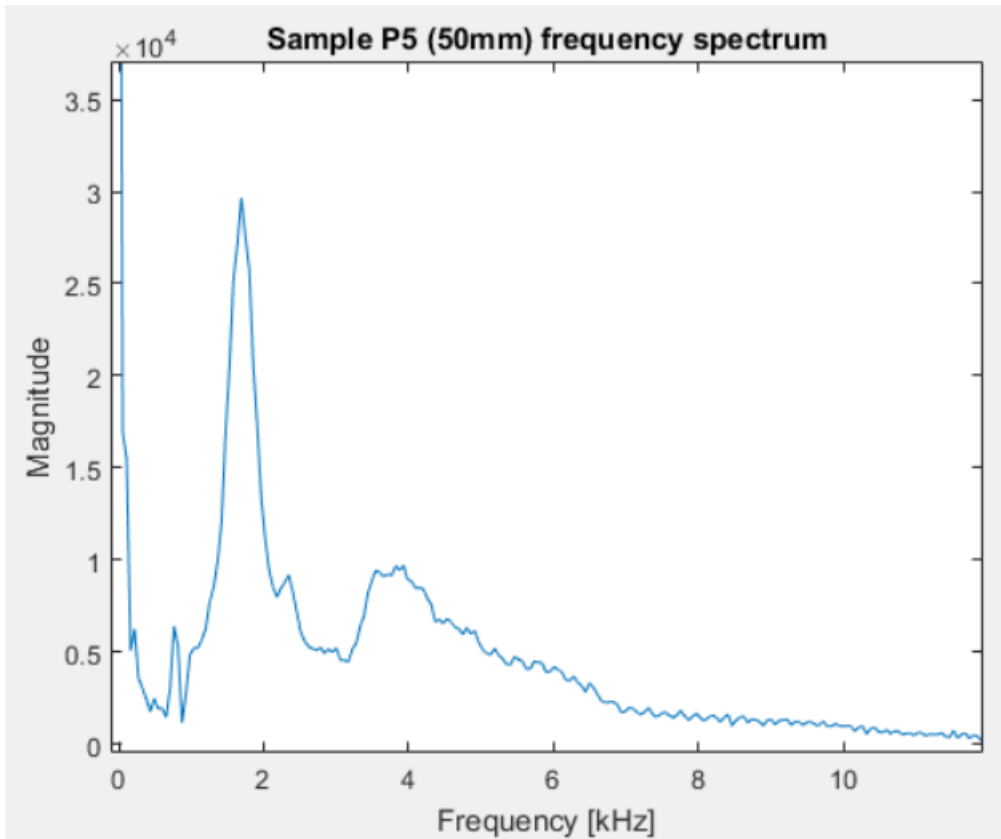


Figure A.28 – Sample P5 (50mm): frequency spectrum

Table A.1.8 – Sample P5 (50mm): results for the half-power bandwidth method

$A_m$	$f_m$ [kHz]	$A_{not}$	$f_1$ [kHz]	$f_2$ [kHz]	$\xi_{BR}$	$\xi_K$
2.9659e+04	1.69	2.0972e+04	1.53	1.85	9.37	9.41

A.2.2.6. Sample P6 (50mm)

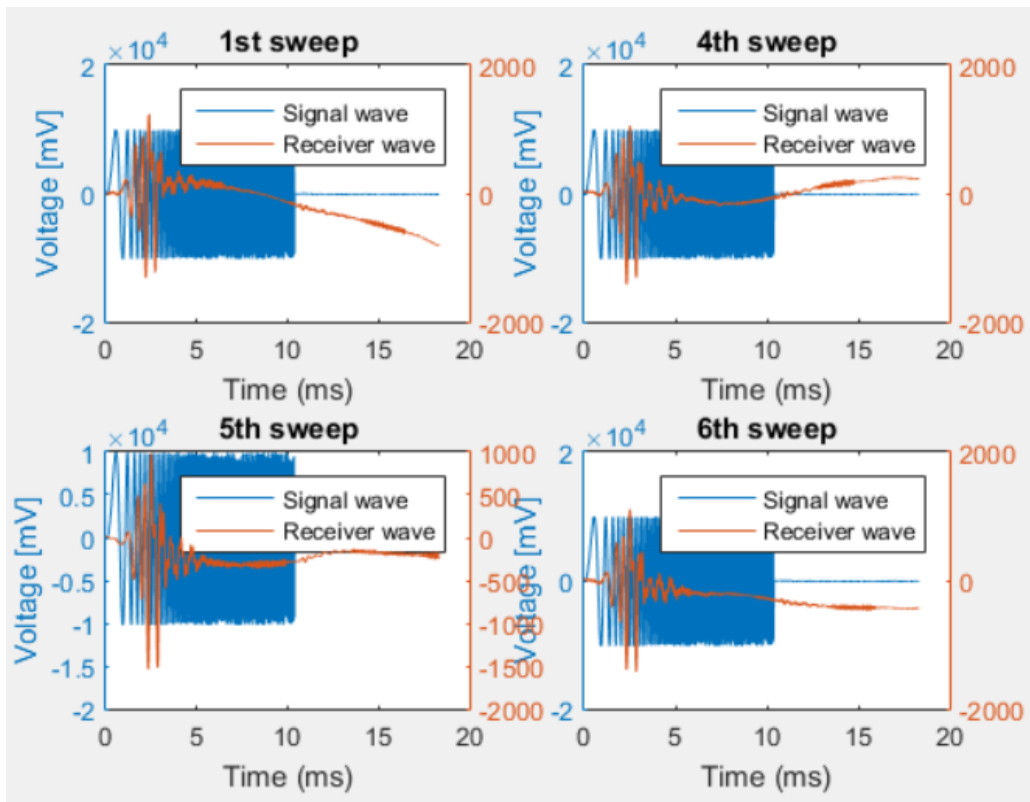


Figure A.29 – Sample P7 (50mm): chosen sweep tests

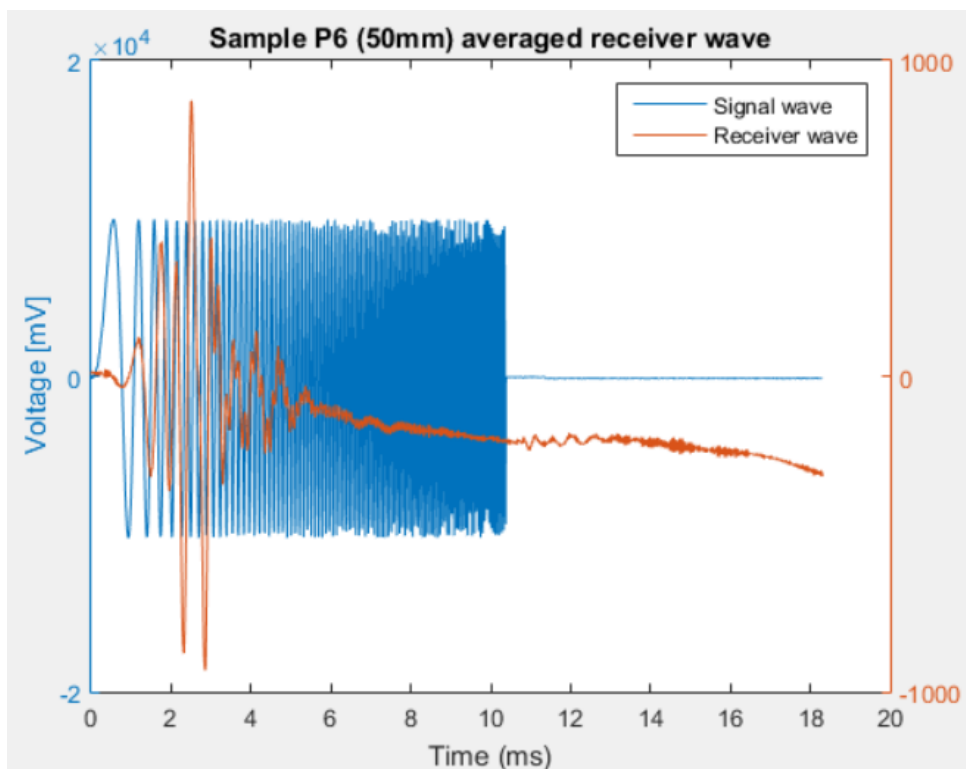


Figure A.30 – Sample P6 (50mm): averaged signal

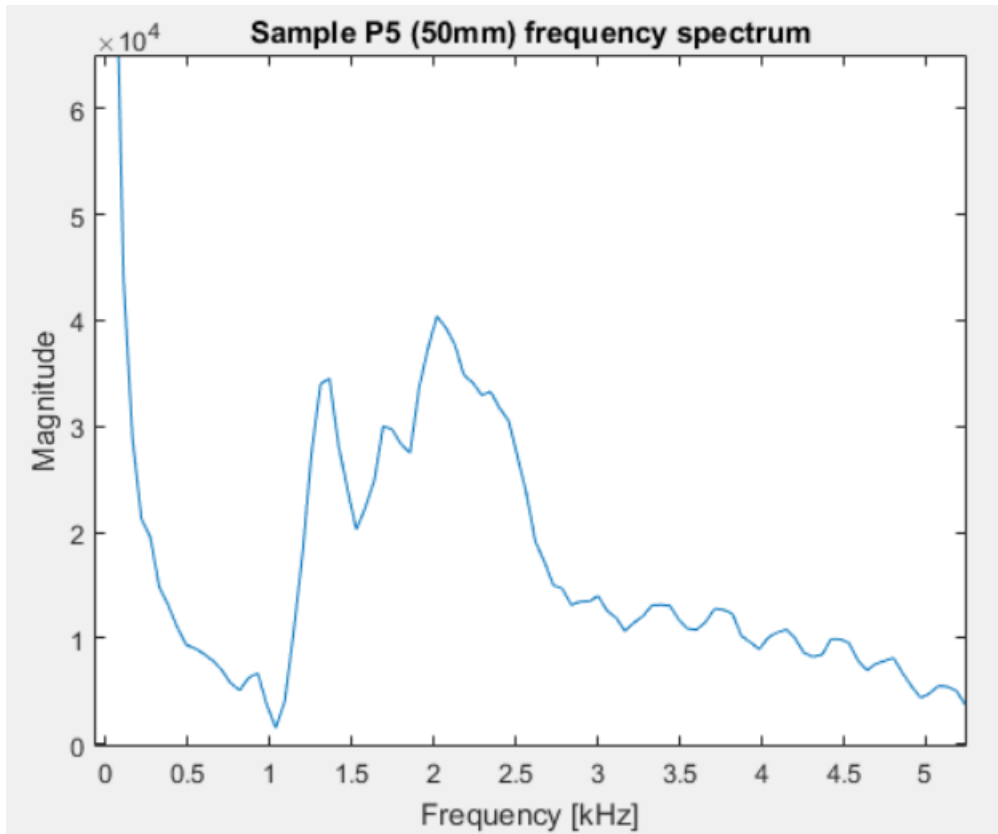


Figure A.31 – Sample P6 (50mm): frequency spectrum

Table A.1.9 – Sample P6 (50mm): results for the half-power bandwidth method

$A_m$	$f_m$ [kHz]	$A_{not}$	$f_1$ [kHz]	$f_2$ [kHz]	$\xi_{BR}$	$\xi_K$
4.0374e+04	2.02	2.8594e+4	1.78	2.49	18.14	18.45



A.2.2.7. Sample P7 (50mm)

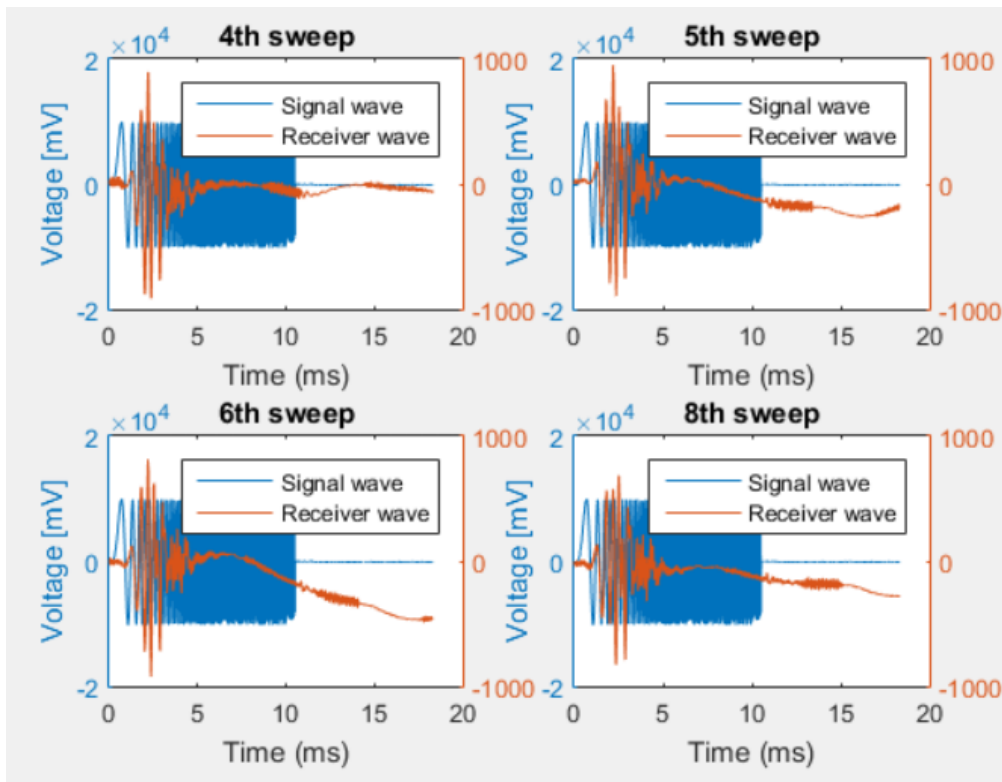


Figure A.32 – Sample P7 (50mm): chosen sweep tests

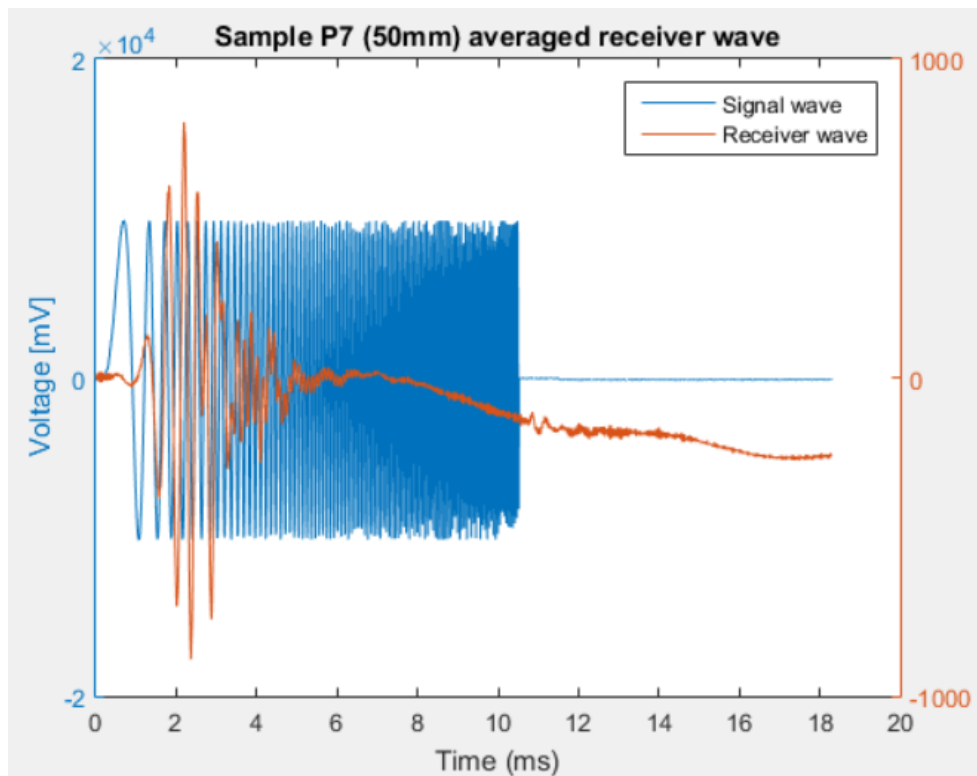


Figure A.33 – Sample P7 (50mm): averaged signal

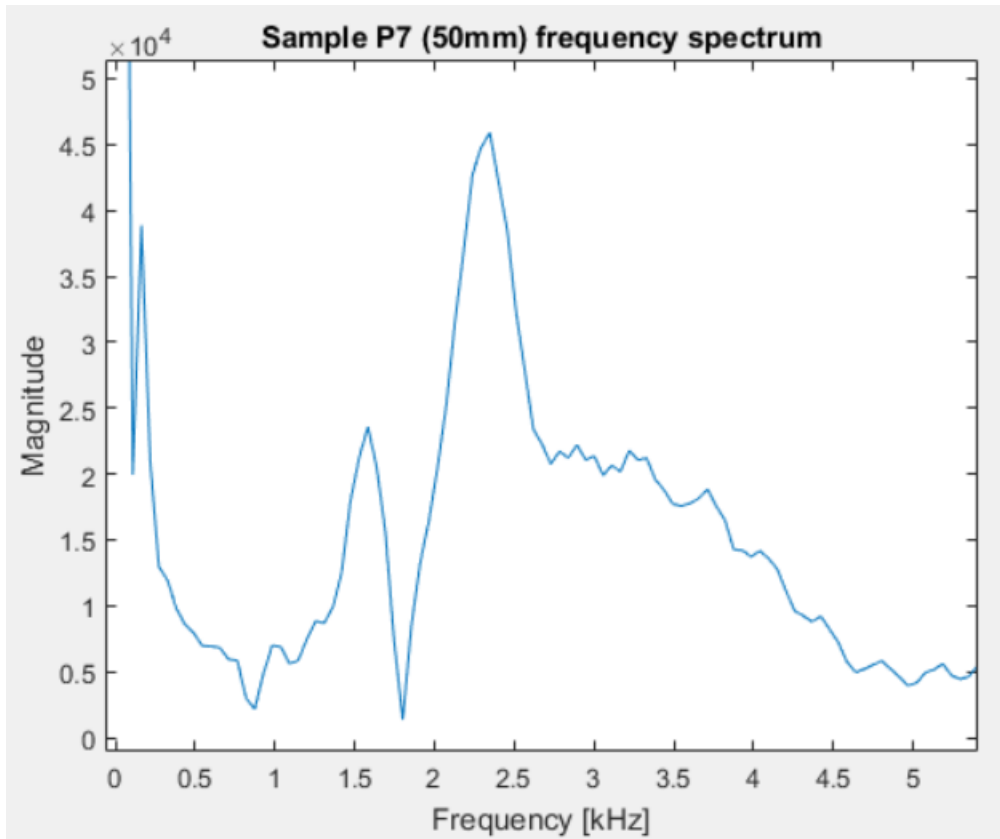


Figure A.34 – Sample P7 (50mm): frequency spectrum

Table A.1.10 – Sample P7 (50mm): results for the half-power bandwidth method

$A_m$	$f_m$ [kHz]	$A_{not}$	$f_1$ [kHz]	$f_2$ [kHz]	$\xi_{BR}$	$\xi_K$
4.5896e+04	2.35	3.2454e+04	2.14	2.51	7.82	7.85

### A.3. FERREIRA'S TEST RESULTS

#### A.3.1. TIME DOMAIN

##### A.3.1.1. Sample 04

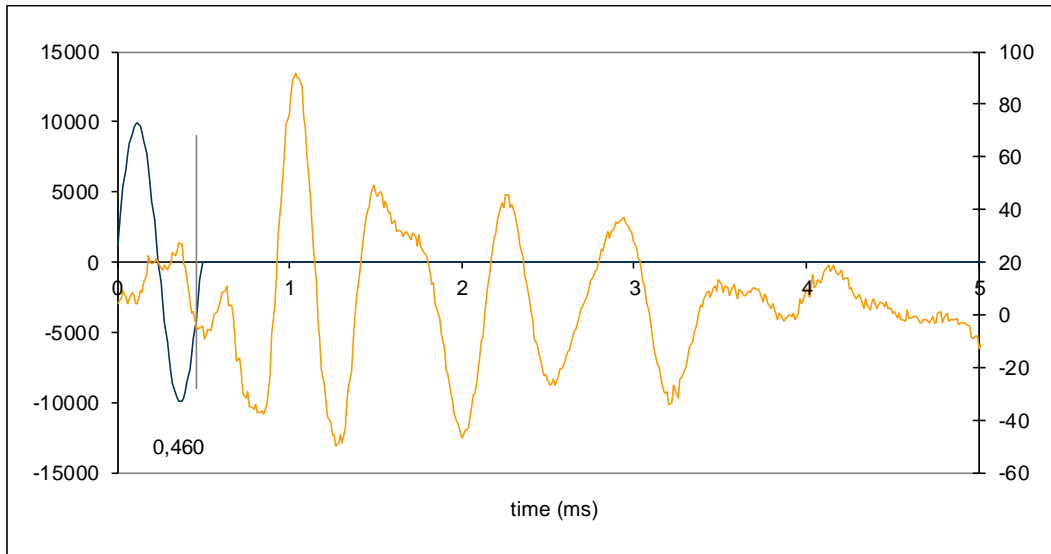


Figure A.35 – Sample 04: sweep 03, 2kHz

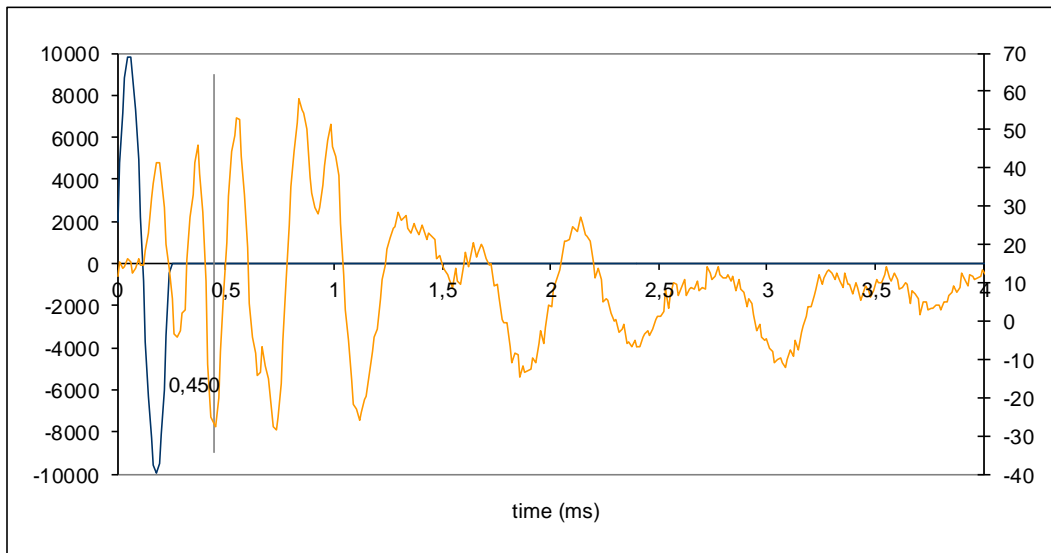


Figure A.36 – Sample 04: sweep 03, 4kHz

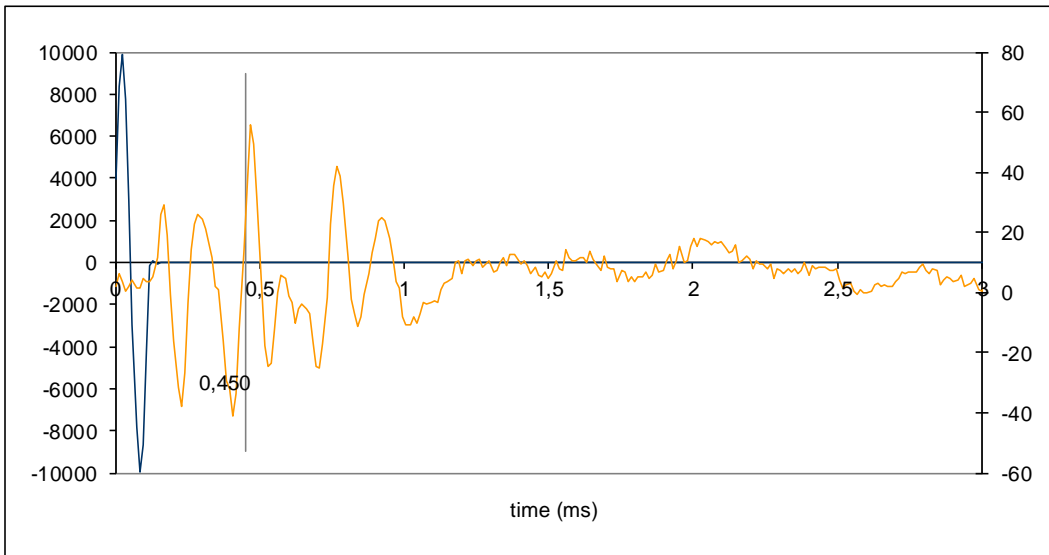


Figure A.37 – Sample 04: sweep 03, 8kHz

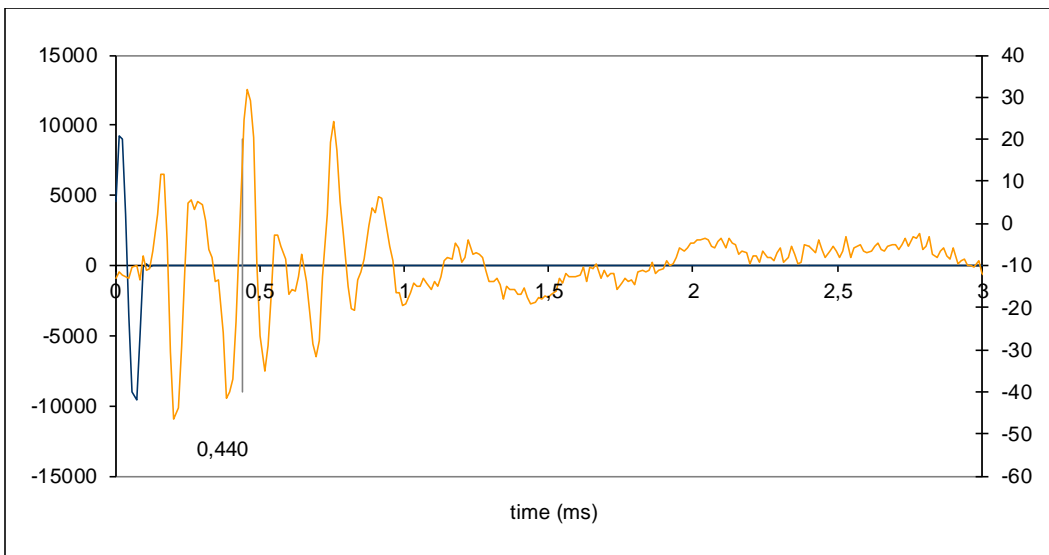


Figure A.38 – Sample 04: sweep03, 10kHz

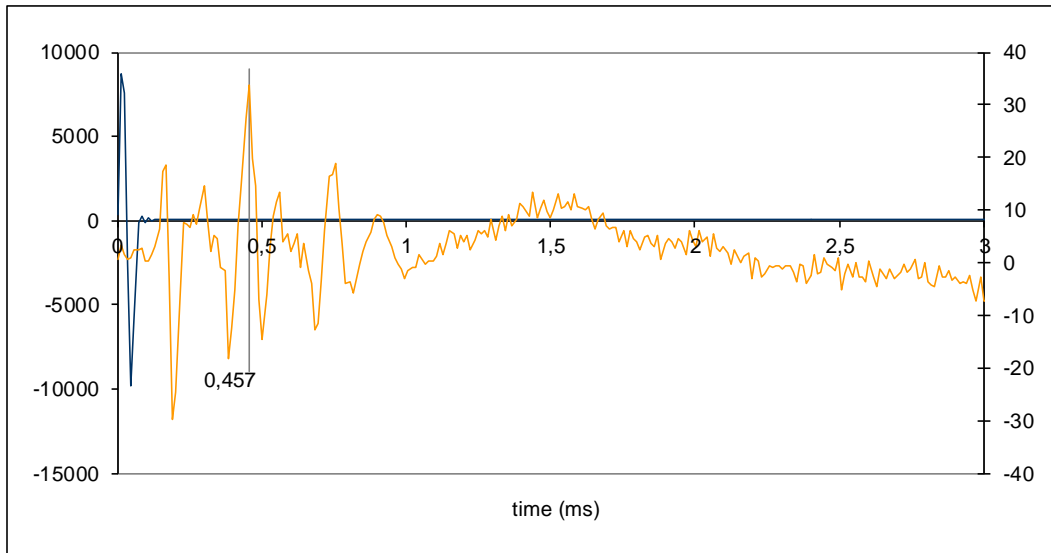


Figure A.39 – Sample 04: sweep 03, 15kHz

Table A.1.11 – Sample 04: logarithmic decrement method for sweep 03

04-CRBE-s03-1-1						
	Voltage [mV]					
	2kHz	4kHz	8kHz	10kHz	15kHz	20kHz
Max peak	88,861					
Following peaks	46,466					
	42,645					
	32,77					
Signal Quality	Low	Very low	Very low	Very low	Very low	-
Logarithmic decrement, $\delta$						
Nr. of successive peaks	2kHz	4kHz	8kHz	10kHz	15kHz	20kHz
2	0,648352					
3	0,367082					
4	0,33252					
Damping [%]						
Nr. of successive peaks	2kHz	4kHz	8kHz	10kHz	15kHz	20kHz
2	10,3					
3	5,8					
4	5,3					

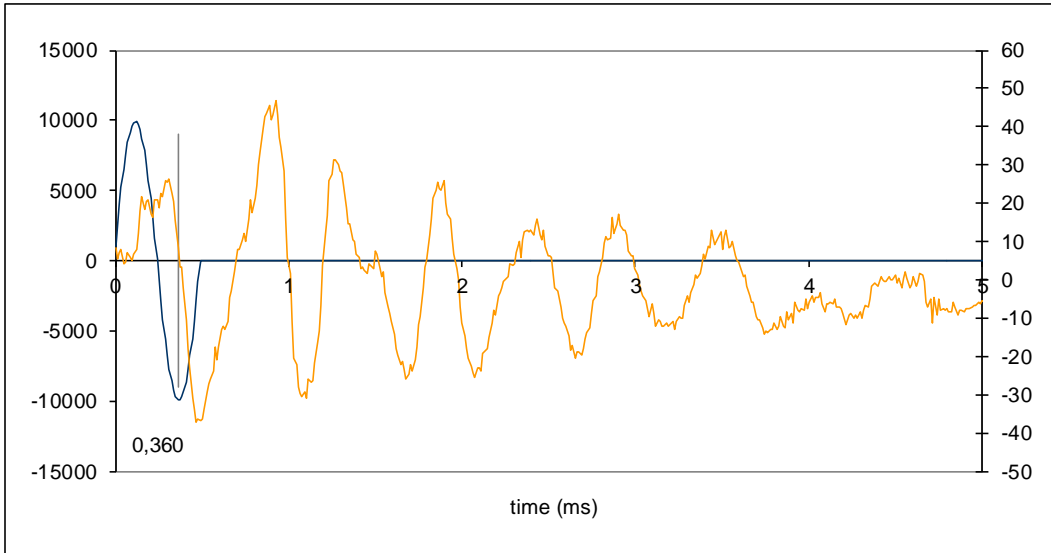


Figure A.40 – Sample 04: sweep 04, 2kHz

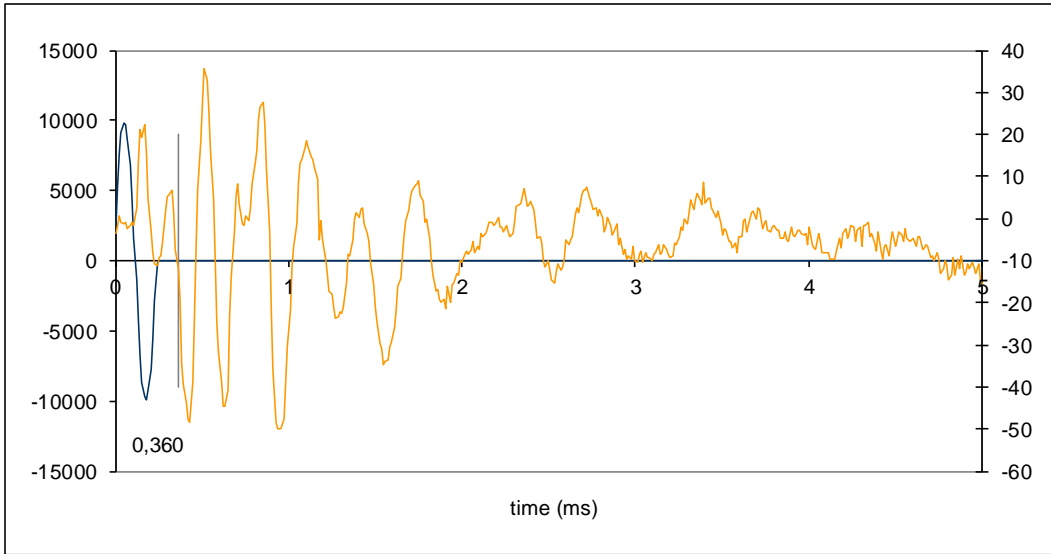


Figure A.41 – Sample 04: sweep 04, 4kHz

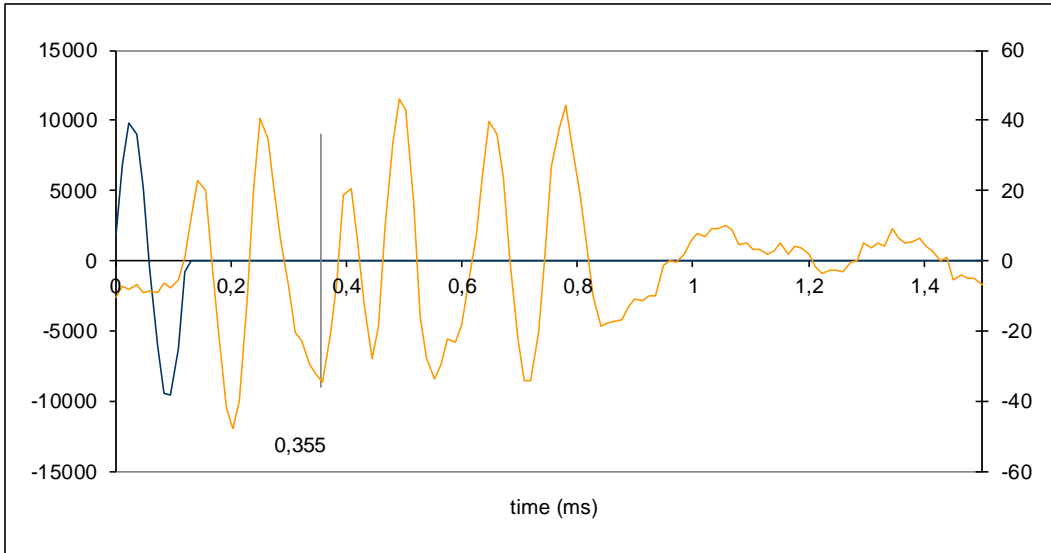


Figure A.42 – Sample 04: sweep 04, 8kHz

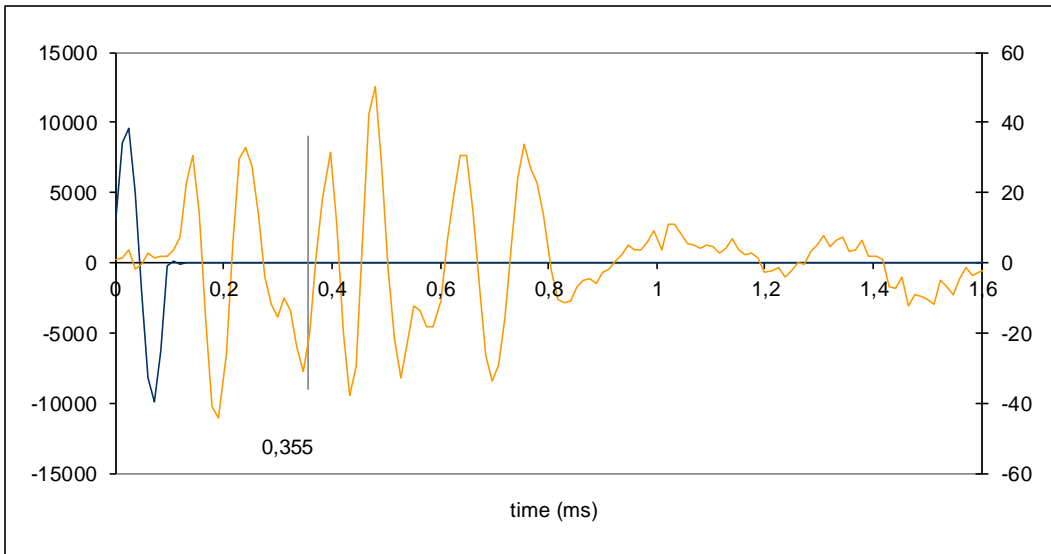


Figure A.43 – Sample 04: sweep 04, 10kHz

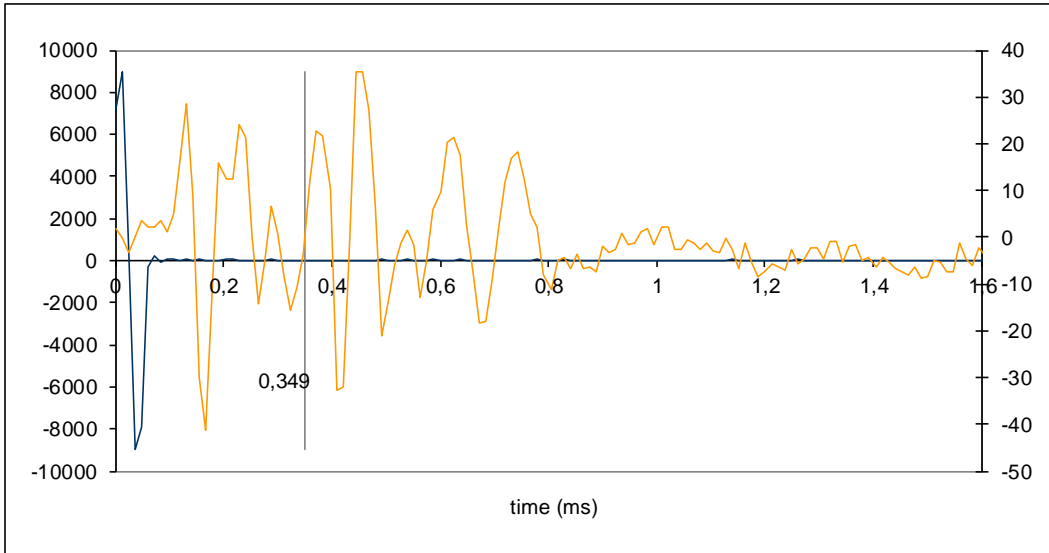


Figure A.44 – Sample 04: sweep 04, 15kHz

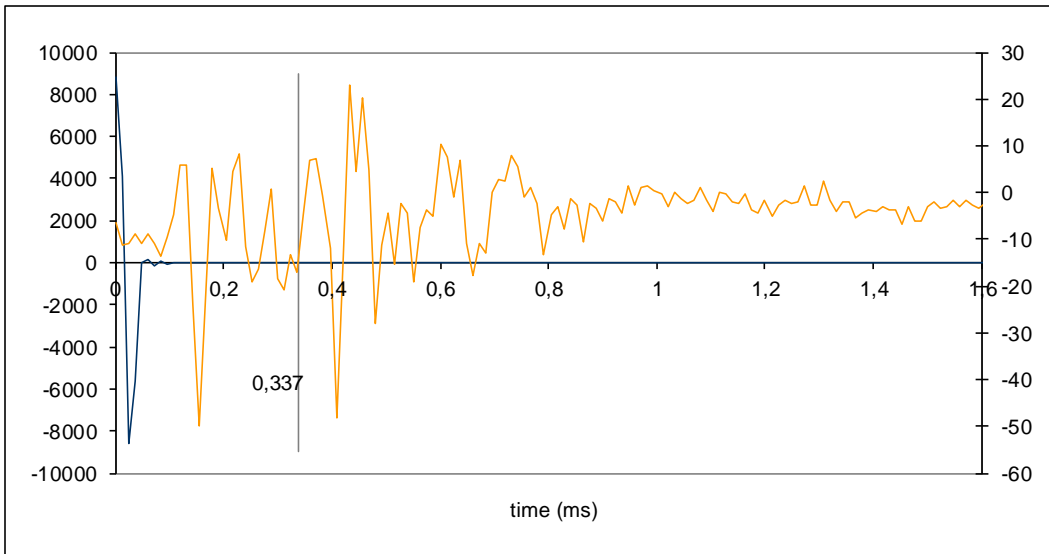


Figure A.45 – Sample 04: sweep 04, 20kHz



Table A.1.12 – Sample 04: logarithmic decrement method for sweep 04

04-CRBE-s04-1-1						
	Voltage [mV]					
	2kHz	4kHz	8kHz	10kHz	15kHz	20kHz
Max peak	45,575	35,751			35,331	
Following peaks	31,235	26,636			1,631	
	23,59	16,563			20,312	
	14,357	1,279			16,783	
	16	8,001				
Signal Quality	High	Low	Very low	Very low	Low	Very low

Nr. of successive peaks	Logarithmic decrement, $\delta$					
	2kHz	4kHz	8kHz	10kHz	15kHz	20kHz
2	0,37782	0,294315			3,075567	
3	0,329268	0,384703			0,276774	
4	0,385041	1,110167			0,184516	
5	0,261693	0,374253				

Nr. of successive peaks	Damping [%]					
	2kHz	4kHz	8kHz	10kHz	15kHz	20kHz
2	6,0	4,7			44,0	
3	5,2	6,1			4,4	
4	6,1	17,4			2,9	
5	4,2	5,9				

red value = peak value similar to the previous one

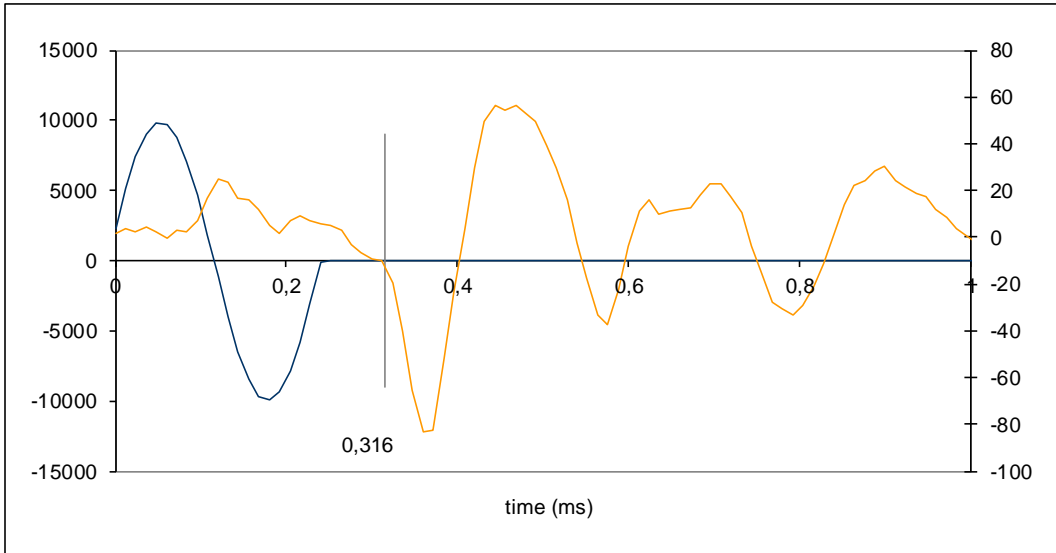


Figure A.46 – Sample 04: sweep 10, 4kHz

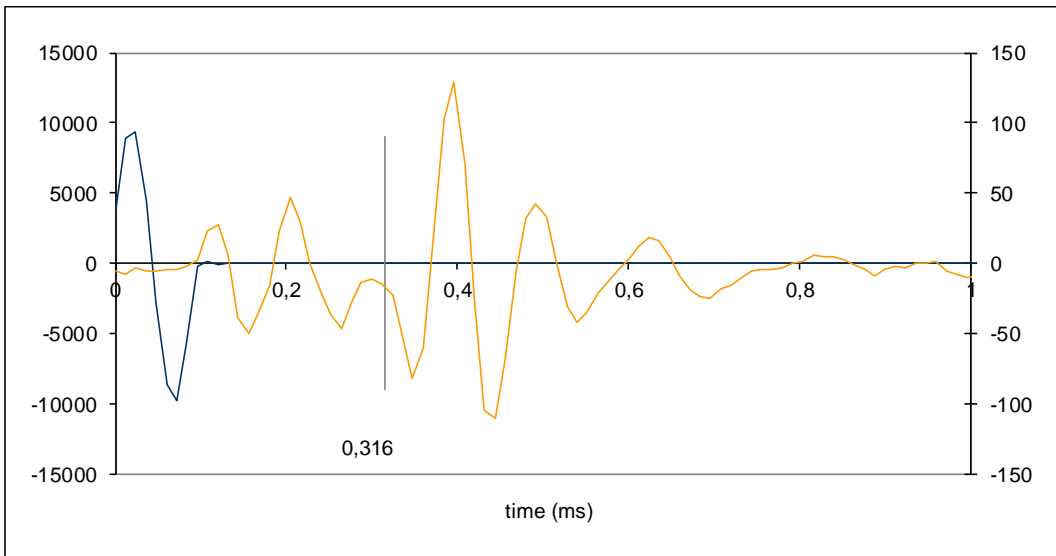


Figure A.47 – Sample 04: sweep 10, 10kHz

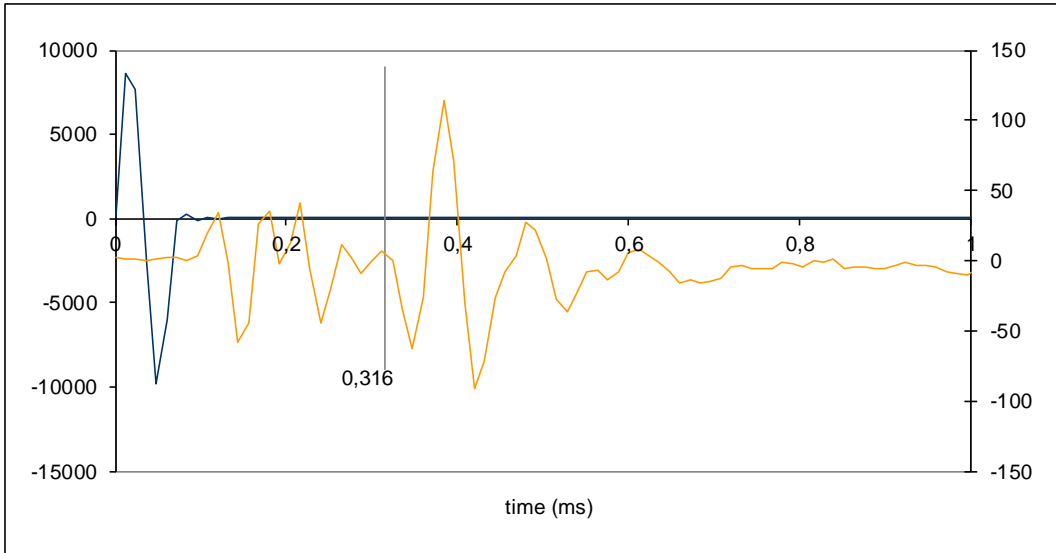


Figure A.48 – Sample 04: sweep 10, 15kHz

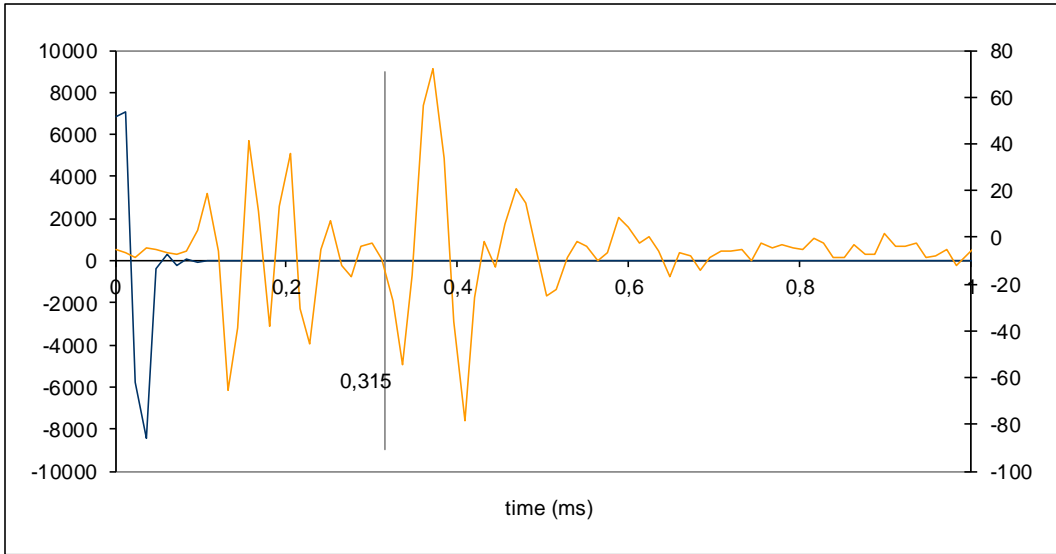


Figure A.49 – Sample 04: sweep 10, 20kHz

Table A.1.13 – Sample 04: logarithmic decrement method for sweep 10

04-CRBE-s10-1-1						
	Voltage [mV]					
	2kHz	4kHz	8kHz	10kHz	15kHz	20kHz
Max peak		56,11		129,456	114,039	72,327
		18,274		42,48	27,466	20,996
Following peaks		28,334		12,909	8,46	8,237
		17,7				
		18,22				
Signal Quality	-	Low	-	Low	Low	Low

Nr. of successive peaks	Logarithmic decrement, $\delta$					
	2kHz	4kHz	8kHz	10kHz	15kHz	20kHz
2		1,121835		1,114308	1,423592	1,236866
3		0,341626		1,152708	1,300596	1,086281
4		0,384583				
5		0,281199				

Nr. of successive peaks	Damping [%]					
	2kHz	4kHz	8kHz	10kHz	15kHz	20kHz
2		17,6		17,5	22,1	19,3
3		5,4		18,0	20,3	17,0
4		6,1				
5		4,5				

red value = peak value similar to the previous one

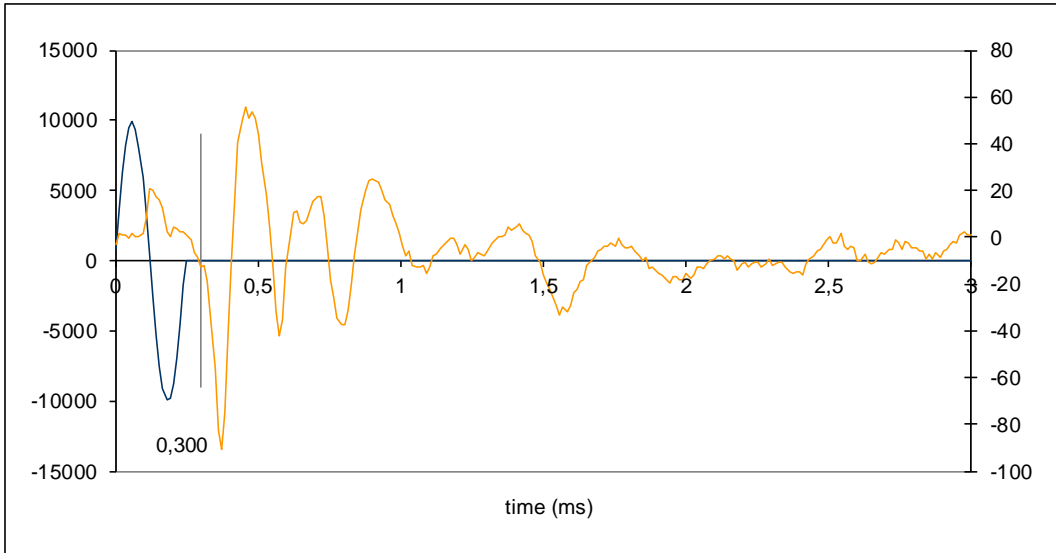


Figure A.50 – Sample 04: sweep 11, 4kHz

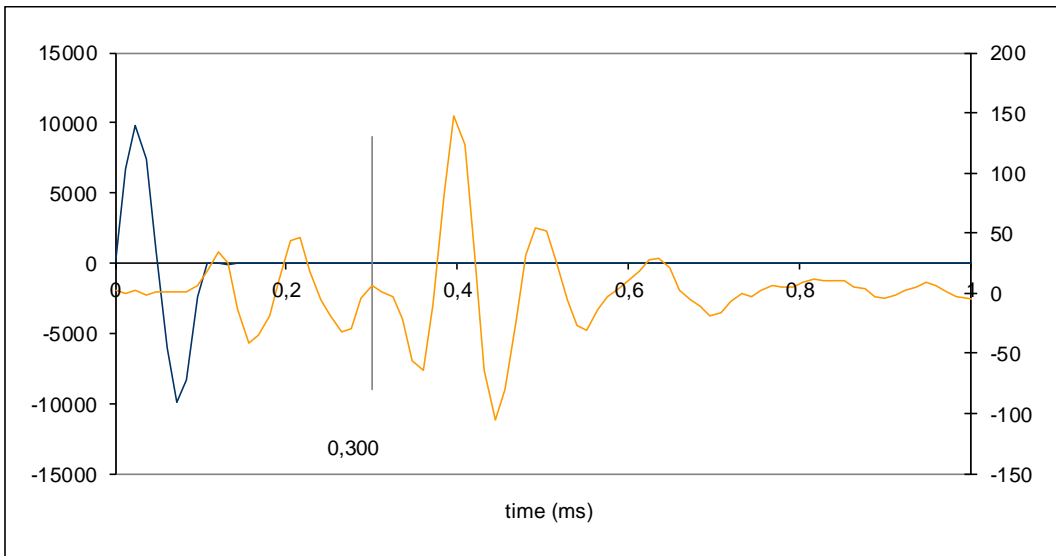


Figure A.51 – Sample 04: sweep 11, 10kHz

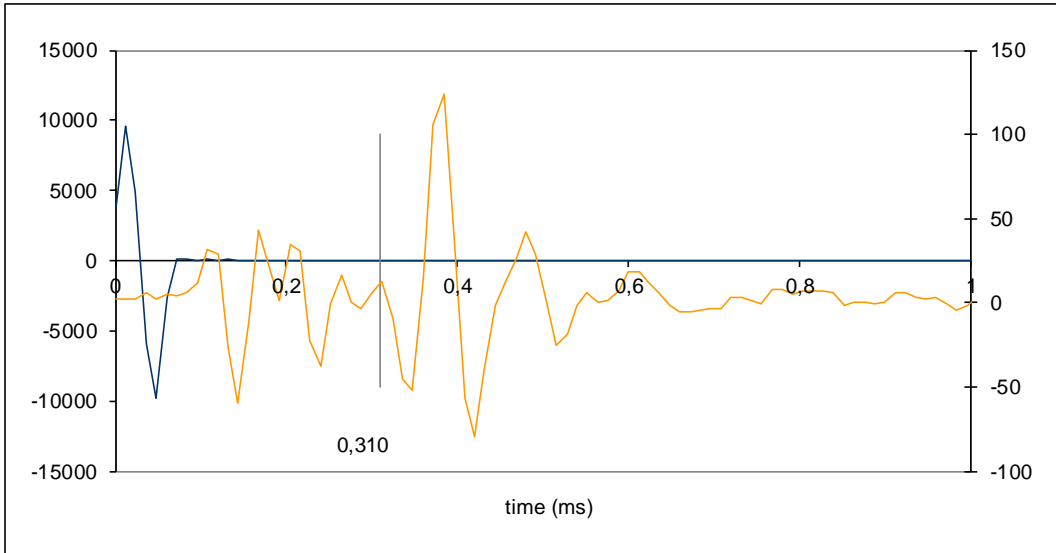


Figure A.52 – Sample 04: sweep 11, 15kHz

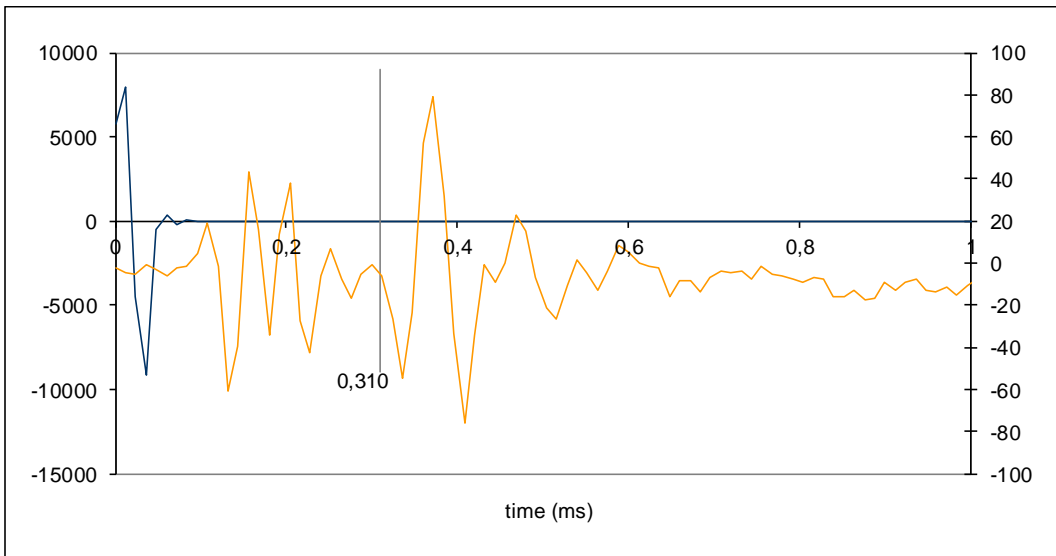


Figure A.53 – Sample 04: sweep 11, 20kHz

Table A.1.14 – Sample 04: logarithmic decrement method for sweep 11

04-CRBE-s11-1-1						
	Voltage [mV]					
	2kHz	4kHz	8kHz	10kHz	15kHz	20kHz
Max peak		50,073		147,29	123,755	78,815
Following peaks		15,265		54,303	41,956	23,503
		23,993		27,863	17,97	8,38
Signal Quality	-	Low	-	High	High	Low

Nr. of successive peaks	Logarithmic decrement, $\delta$					
	2kHz	4kHz	8kHz	10kHz	15kHz	20kHz
2		1,187919		0,997824	1,081682	1,209975
3		0,36786		0,832552	0,9648	1,120628

Nr. of successive peaks	Damping [%]					
	2kHz	4kHz	8kHz	10kHz	15kHz	20kHz
2		18,6		15,7	17,0	18,9
3		5,8		13,1	15,2	17,6

red value = peak value similar to the previous one

Table A.1.15 – Sample 04: summary of results with logarithmic decay method

Sweep	Damping [%]					
	2kHz	4kHz	8kHz	10kHz	15kHz	20kHz
03	5,6	X	X	X	X	-
04	5,4	5,6*	X	X	3,7	X
10	-	9,9	-	18,8	21,2	18,2
11	-	5,8*	-	14,4	17,0	18,9

X = discarded result due to very low signal quality; red value = low quality test result; - = untested frequency; \*=test with high variation on damping value

A.3.1.2. Sample 02

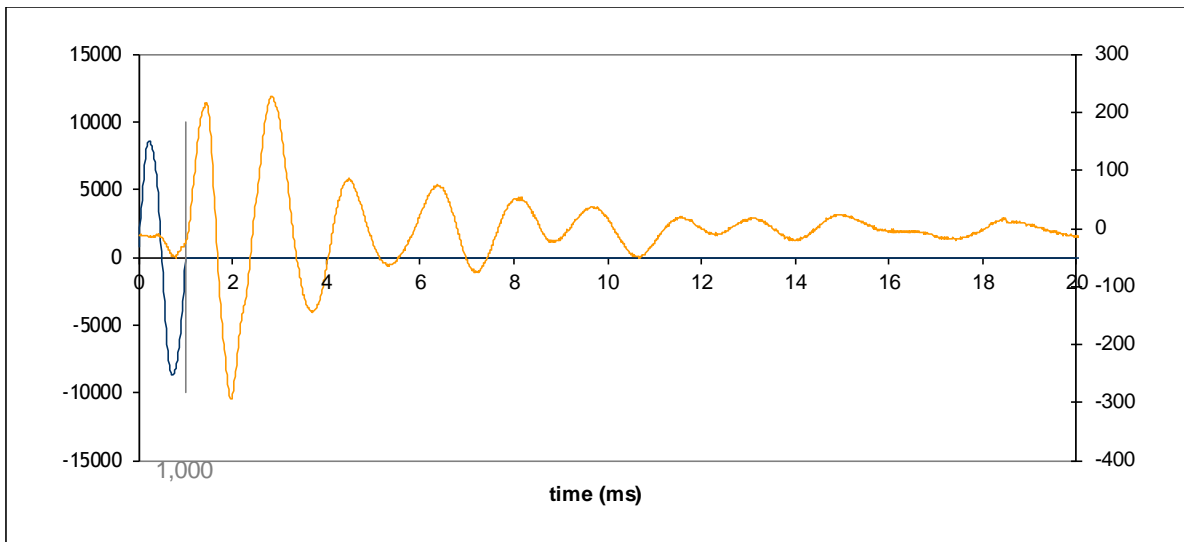


Figure A.54 – Sample 02, sweep 00, 1kHz

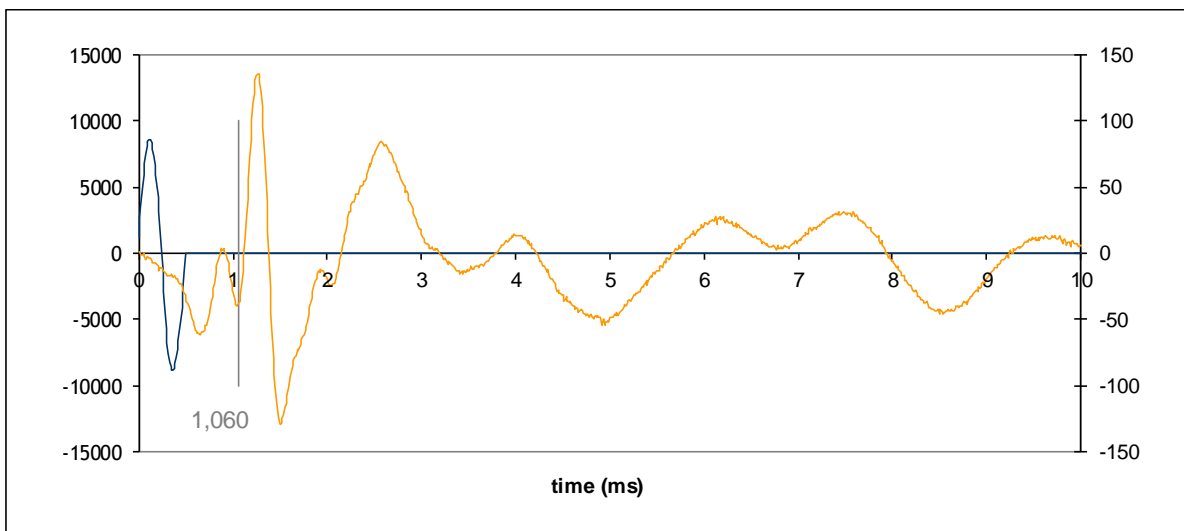


Figure A.55 – Sample 02: sweep 00, 2kHz



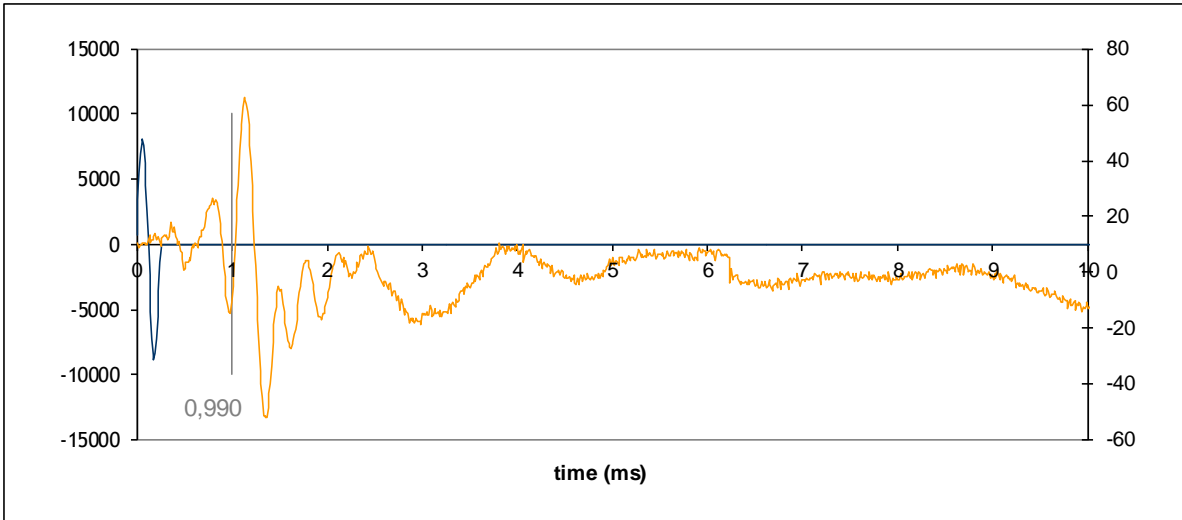


Figure A.56 – Sample 02: sweep00, 4kHz

Table A.1.16 – Sample 02: logarithmic decrement method for sweep 00

02-s00			
Voltage [mV]			
	1kHz	2kHz	4kHz
Max peak	211,136	134,445	
Following peaks	74,524	76,721	
	63,156	9,277	
	43,594	25,955	
	37,704		
Signal Quality	High	Low	Very low
Logarithmic decrement, $\delta$			
Nr. of successive peaks	1kHz	2kHz	4kHz
2	1,041381	0,56098	
3	0,603447	1,336808	
4	0,178734	0,36127	
5	0,12896		
Damping [%]			
Nr. of successive peaks	1kHz	2kHz	4kHz
2	16,4	8,9	
3	9,6	20,8	
4	2,8	5,7	
5	2,1		

red value = peak value similar to the previous one

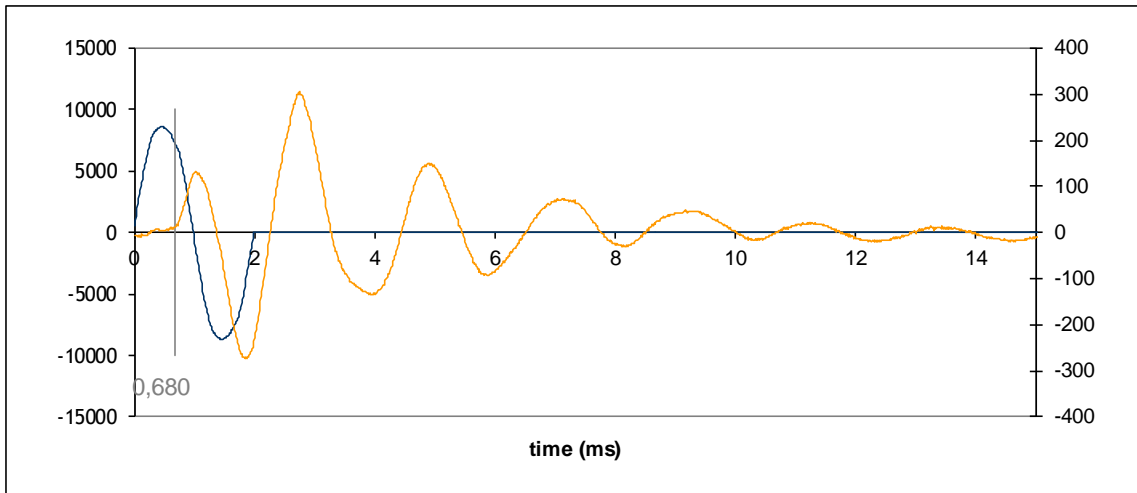


Figure A.57 – Sample 02: sweep 01, 0.5kHz

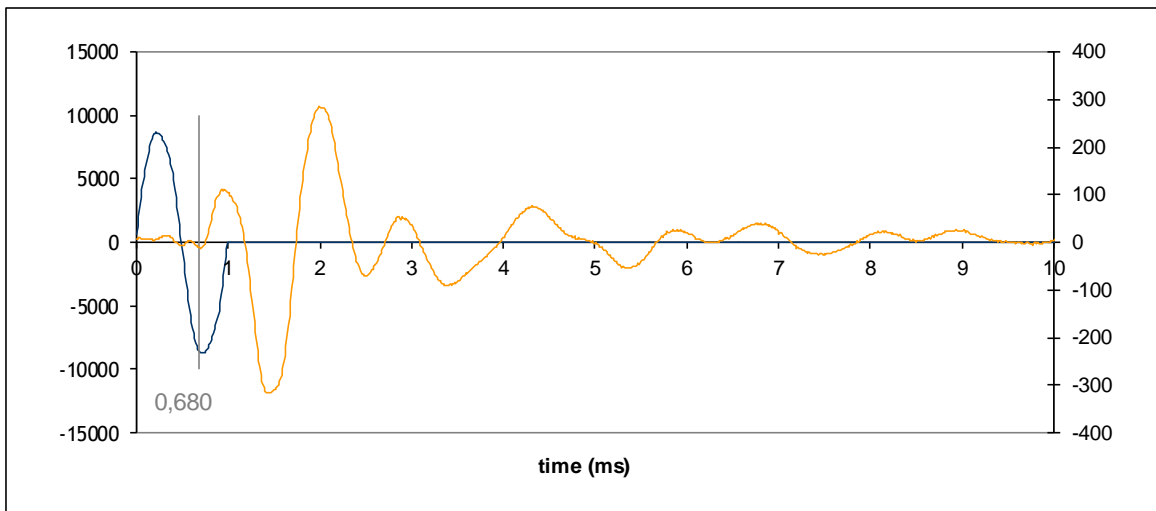


Figure A.58 – Sample 02: sweep 01, 1kHz

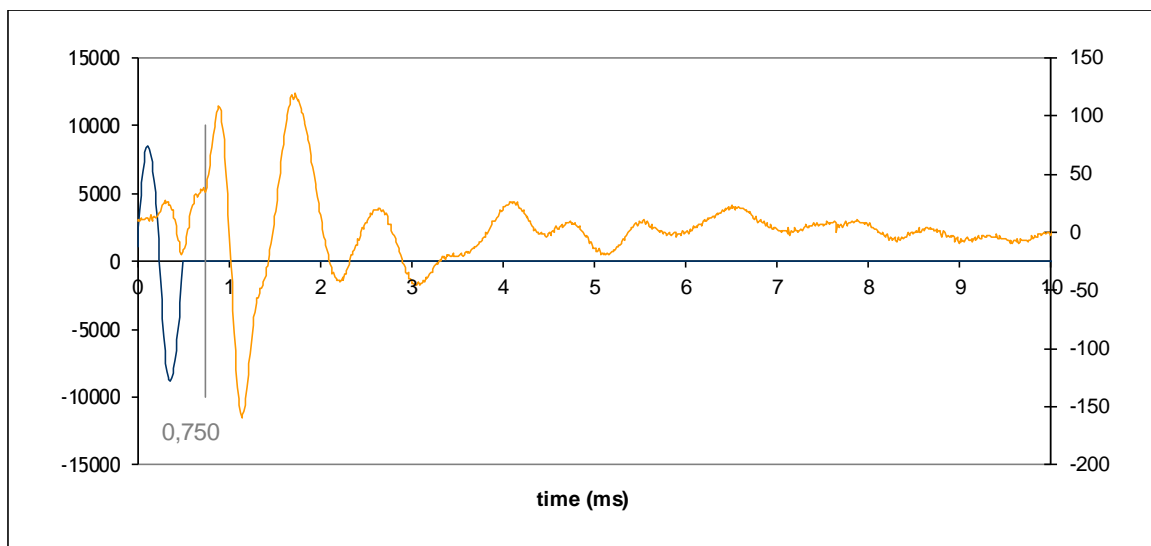


Figure A.59 – Sample 02: sweep 01, 2kHz

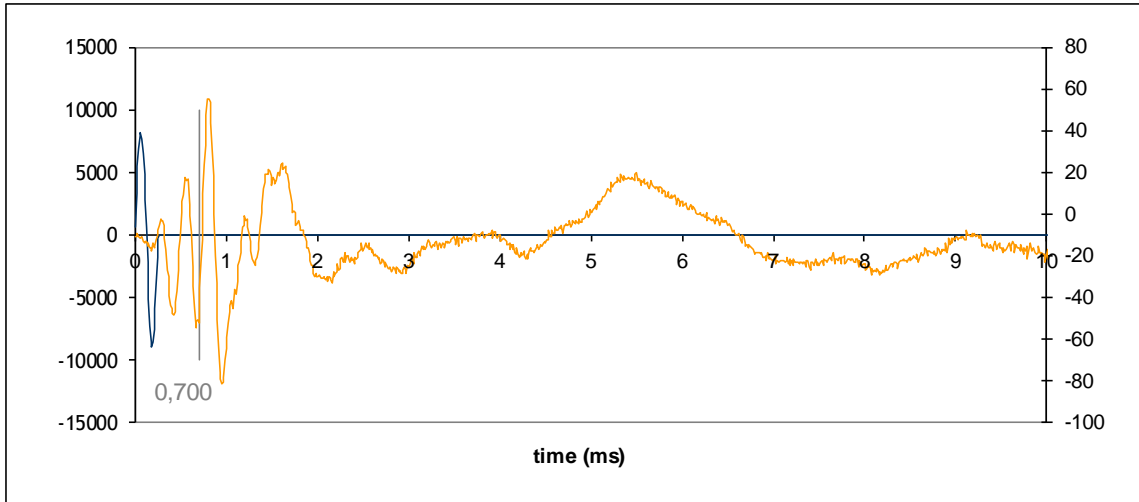


Figure A.60 – Sample 02: sweep 01, 4kHz

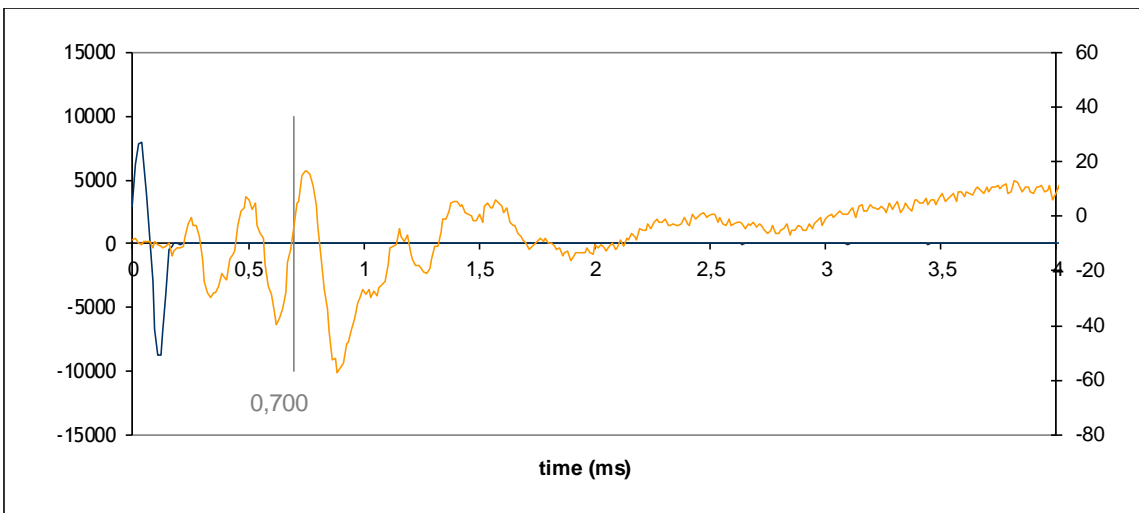


Figure A.61 – Sample 02: sweep 01, 6kHz

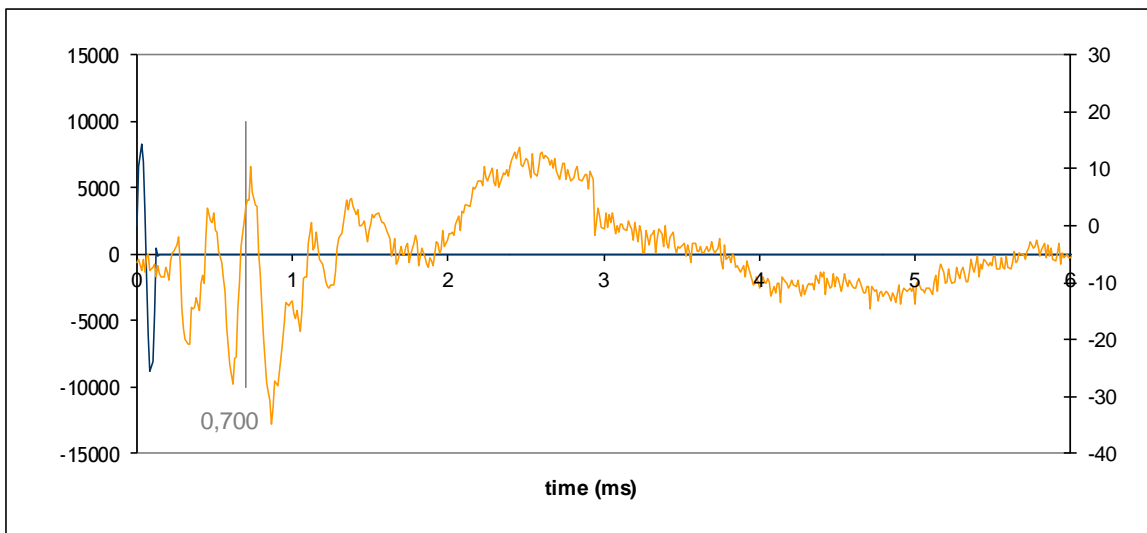


Figure A.62 – Sample 02: sweep 01, 8kHz

Table A.1.17 – Sample 02: logarithmic decrement method for sweep 01

02-s01						
	Voltage [mV]					
	0,5kHz	1kHz	2kHz	4kHz	6kHz	8kHz
Max peak	196,341	273,956	115,768			
Following peaks	139,008	85,09	12,711			
	69,321	68,954	21,866			
	42,892					
	18,997					
	10,849					
Signal Quality	Very high	Low	low	Very low	Very low	Very low

Nr. of peaks	Logarithmic decrement, $\delta$					
	0,5kHz	1kHz	2kHz	4kHz	6kHz	8kHz
2	0,345321	1,169258	2,20912			
3	0,520553	0,689764	0,833328			
4	0,507056					
5	0,723945					
6	0,579156					

Nr. of peaks	Damping [%]					
	0,5kHz	1kHz	2kHz	4kHz	6kHz	8kHz
2	5,5	18,3	33,2			
3	8,3	10,9	13,1			
4	8,0					
5	11,4					
6	9,2					

red value = peak value similar to the previous one

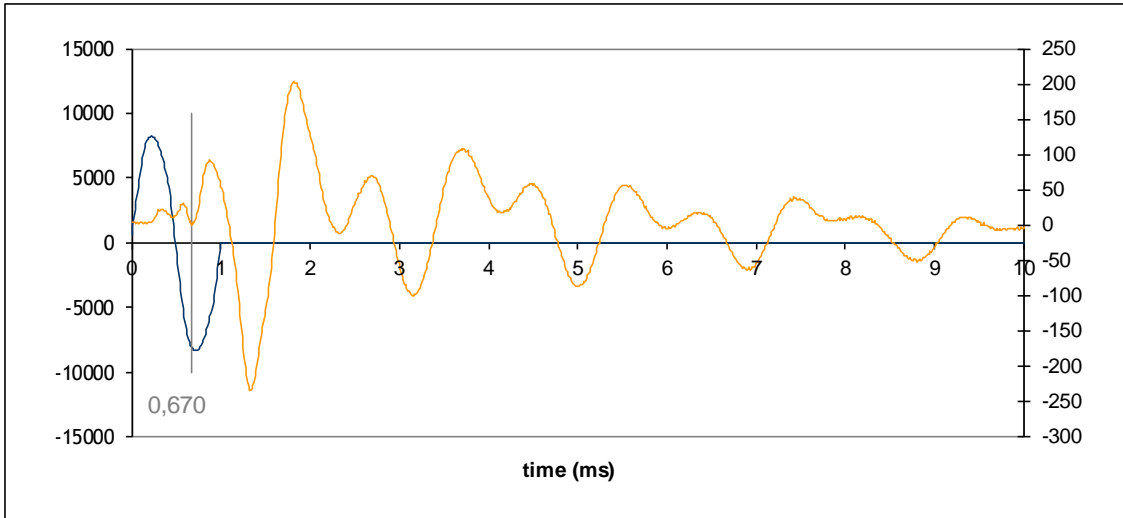


Figure A.63 – Sample 02: sweep 02, 1kHz

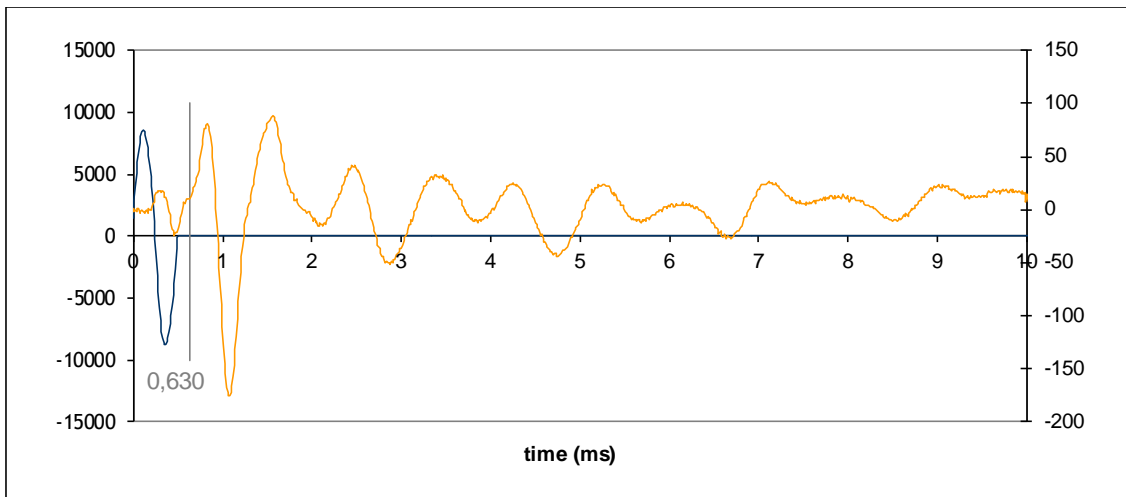


Figure A.64 – Sample 02: sweep 02, 2kHz

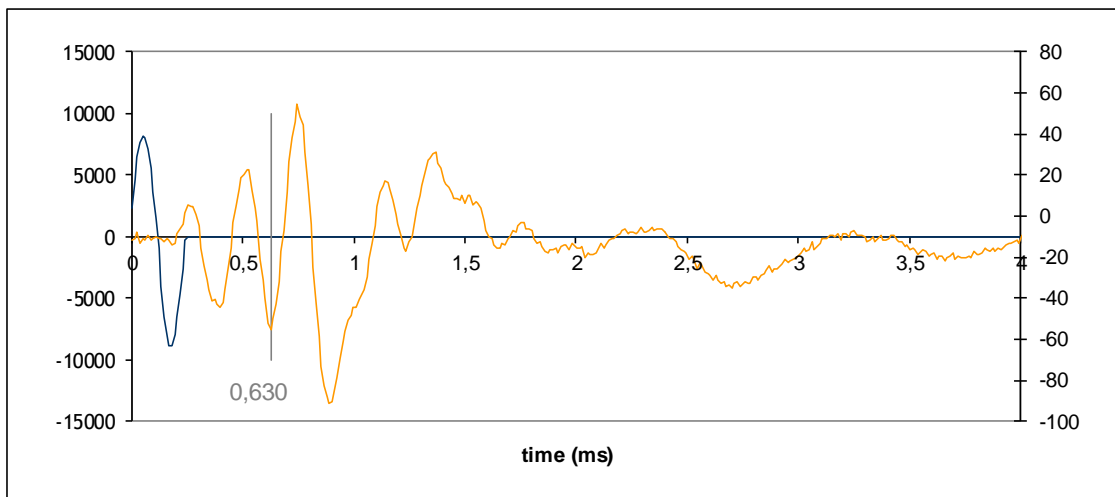


Figure A.65 – Sample 02: sweep 02, 4kHz

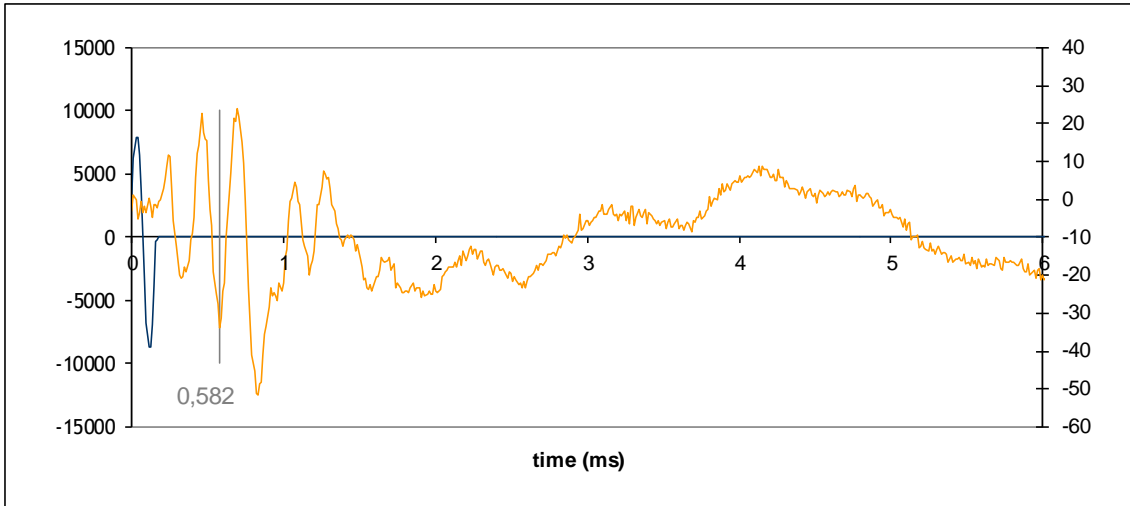


Figure A.66 – Sample 02: sweep 02, 6kHz

Table A.1.18 – Sample 02: logarithmic decrement method for sweep 02

02-s02				
	Voltage [mV]			
	1kHz	2kHz	4kHz	6kHz
Max peak	192,749	81,001		
	103,012	30,167		
Following peaks	53,356	29,602		
	32,303	20,889		
Signal Quality	Low	Low	Very low	Very low
Nr. of peaks	Logarithmic decrement, $\delta$			
	1kHz	2kHz	4kHz	6kHz
2	0,626543	0,987713		
3	0,642201	0,50331		
4	0,59541	0,451746		
Nr. of peaks	Damping [%]			
	1kHz	2kHz	4kHz	6kHz
2	9,9	15,5		
3	10,2	8,0		
4	9,4	7,2		

red value = peak value similar to the previous one

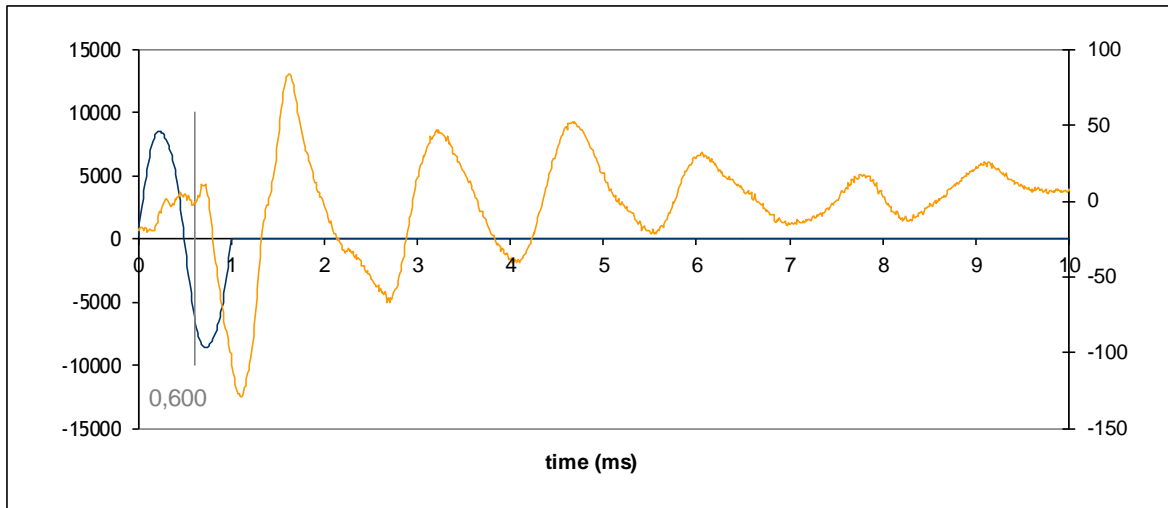


Figure A.67 – Sample 02: sweep 03, 1kHz

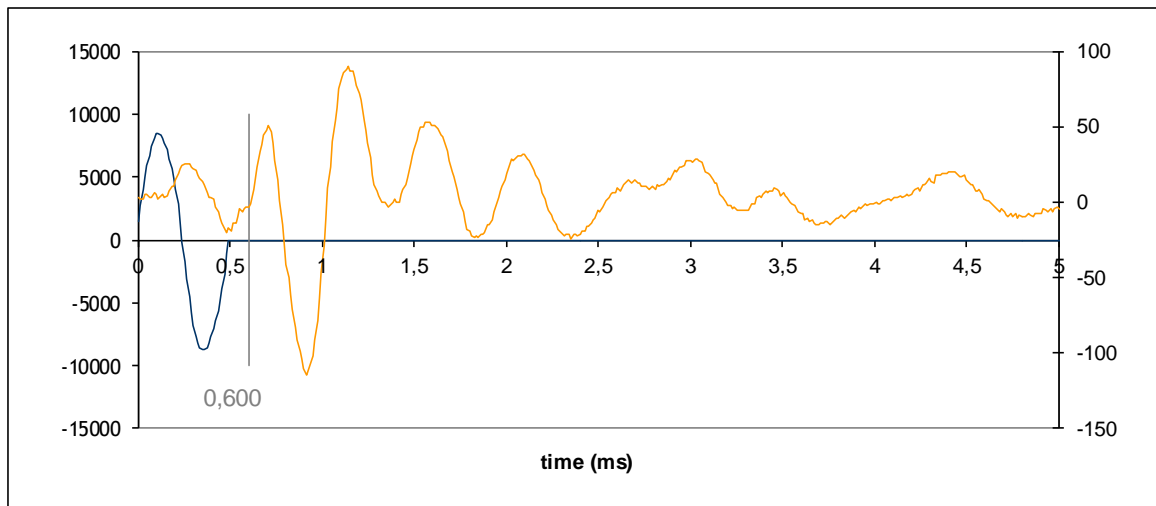


Figure A.68 – Sample 02: sweep 03, 2kHz

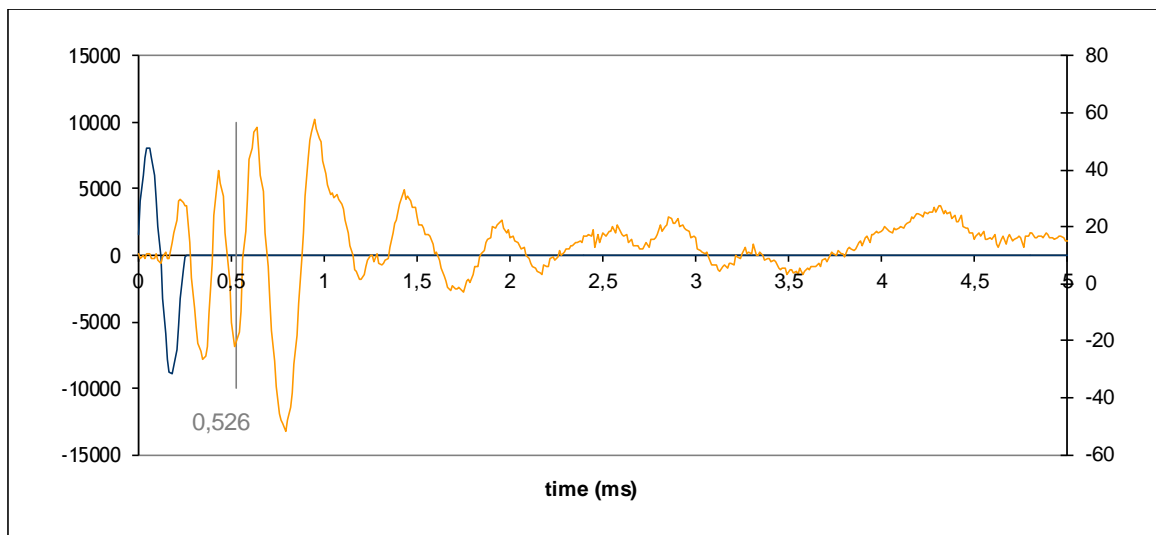


Figure A.69 – Sample 02: sweep 03, 4kHz

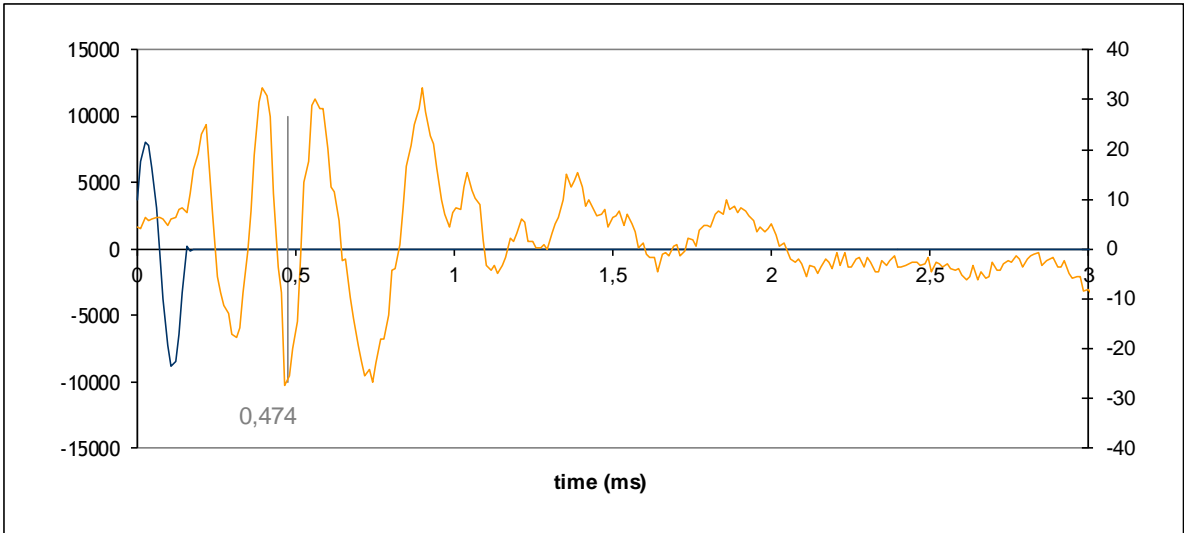


Figure A.70 – Sample 02: sweep 03, 6kHz

Table A.1.19 – Sample 02: logarithmic decrement method for sweep 03

02-s03				
	Voltage [mV]			
	1kHz	2kHz	4kHz	6kHz
Max peak	80,002	87,708	57,846	
Following peaks	43,93	50,217	33,188	
	50,766	30,106	21,423	
	27,679			
Signal Quality	Low	Low	Low	Very low
Logarithmic decrement, $\delta$				
Nr. of peaks	1kHz	2kHz	4kHz	6kHz
2	0,599454	0,55766	0,555596	
3	0,227412	0,534644	0,49666	
4	0,353793			
Damping [%]				
Nr. of peaks	1kHz	2kHz	4kHz	6kHz
2	9,5	8,8	8,8	
3	3,6	8,5	7,9	
4	5,6			

red value = peak value similar to the previous one



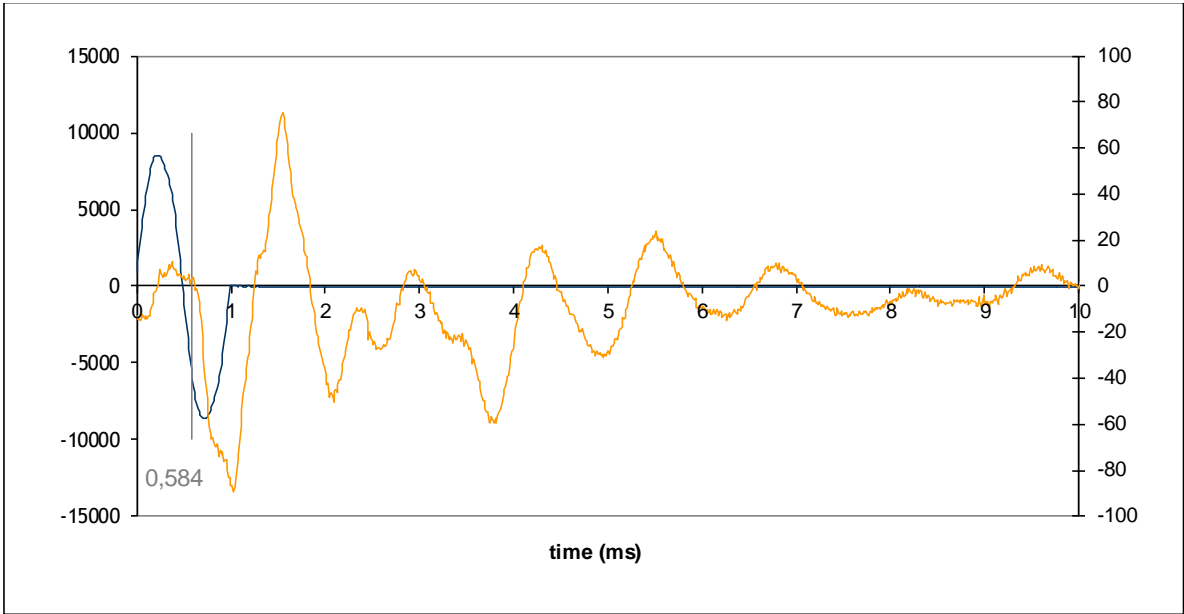


Figure A.71 – Sample 02: sweep 04, 1kHz

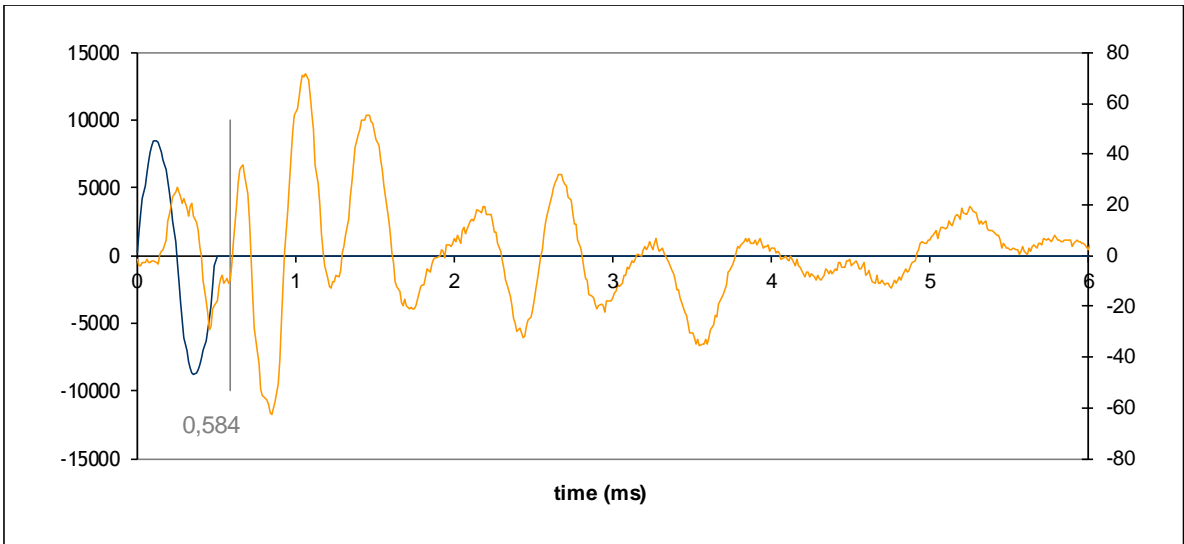


Figure A.72 – Sample 02: sweep 04, 2kHz

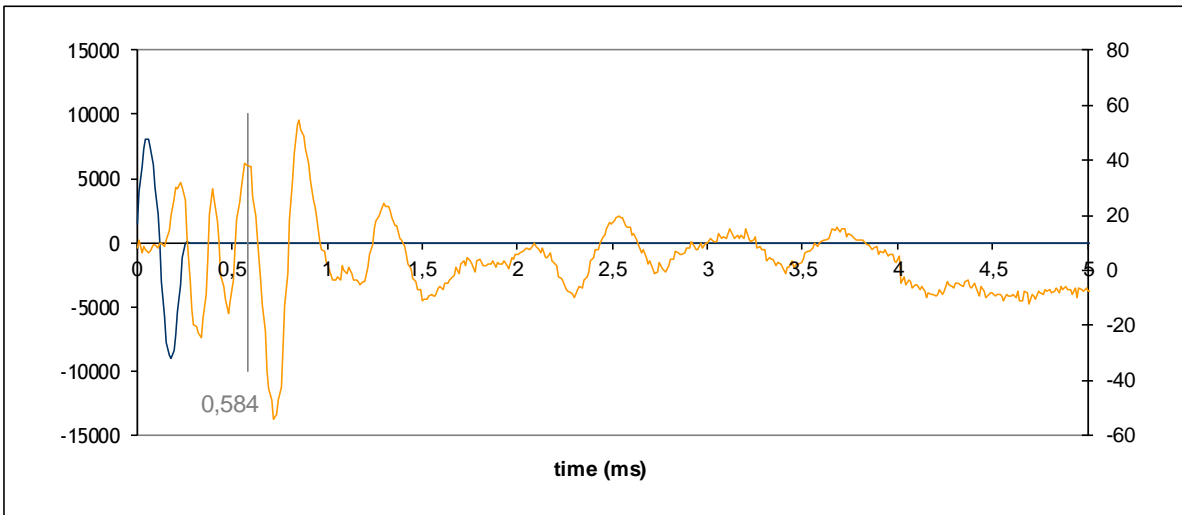


Figure A.73 – Sample 02: sweep 04, 4kHz

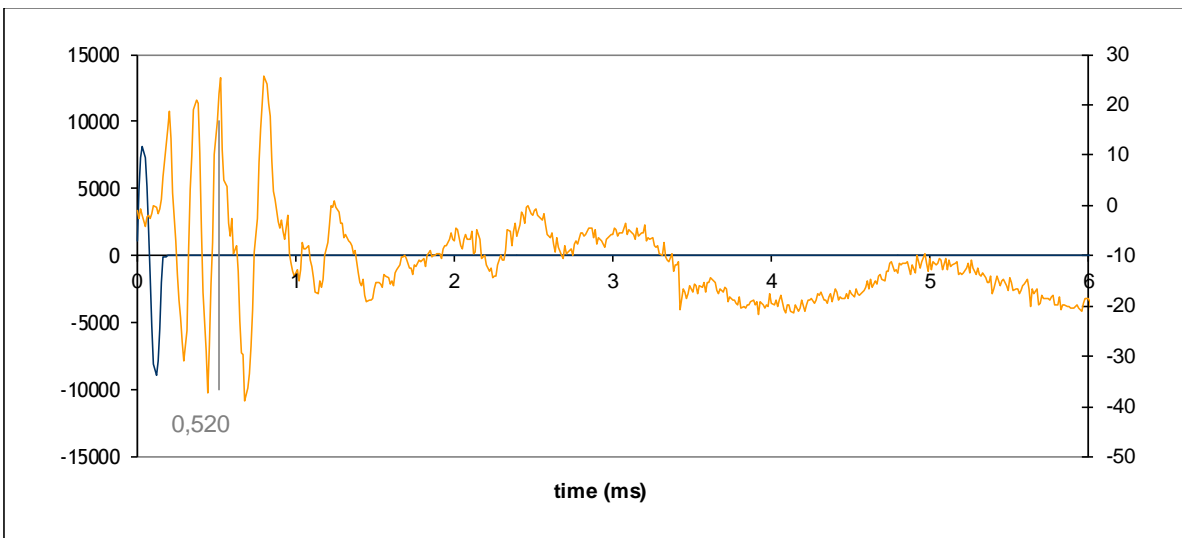


Figure A.74 – Sample 02: sweep 04, 6kHz

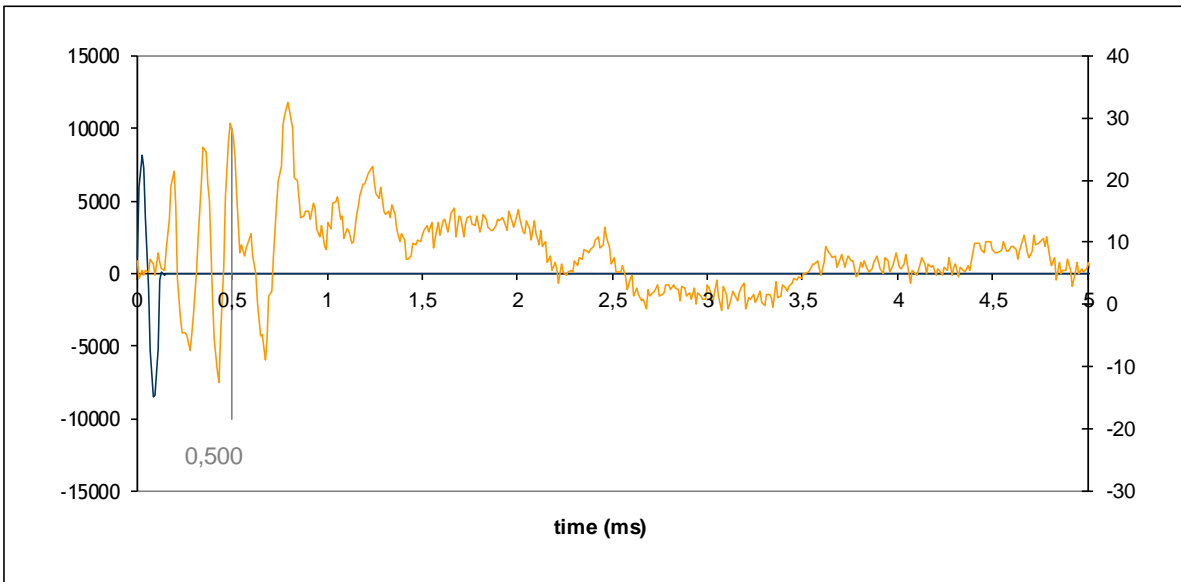


Figure A.75 – Sample 02: sweep 04, 8kHz

Table A.1.20 – Sample 02: logarithmic decrement method for sweep 04

02-s04					
Voltage [mV]					
	1kHz	2kHz	4kHz	6kHz	8kHz
Max peak		71,03	52,872		
Following peaks		53,513	17,822		
		16,513			
		30,365			
Signal Quality	Very low	High	Low	Very low	Very low
Logarithmic decrement, $\delta$					
Nr. of peaks	1kHz	2kHz	4kHz	6kHz	8kHz
2		0,283178	1,08744		
3		0,729477			
4		0,188878			
Damping [%]					
Nr. of peaks	1kHz	2kHz	4kHz	6kHz	8kHz
2		4,5	17,1		
3		11,5			
4		3,0			

red value = peak value similar to the previous one

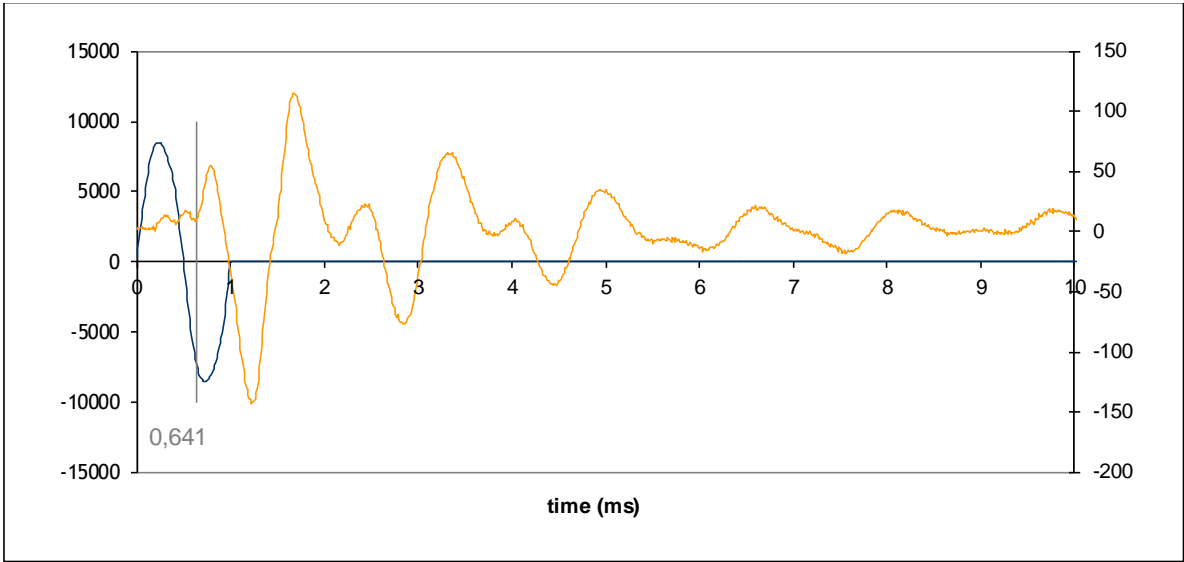


Figure A.76 – Sample 02: sweep 05, 1kHz

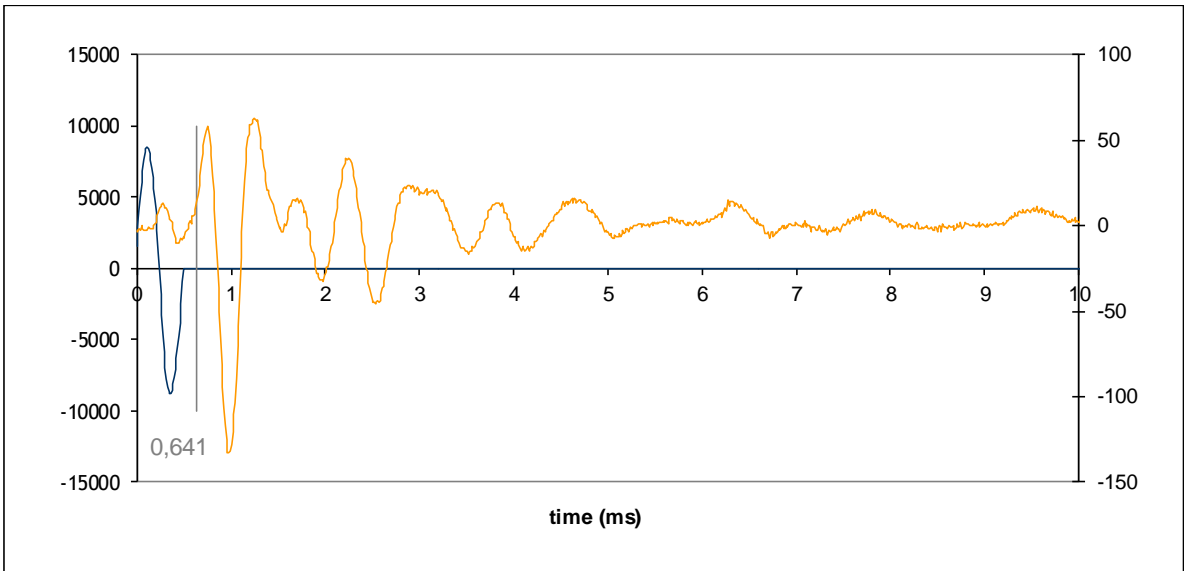


Figure A.77 – Sample 02: sweep 05, 2kHz

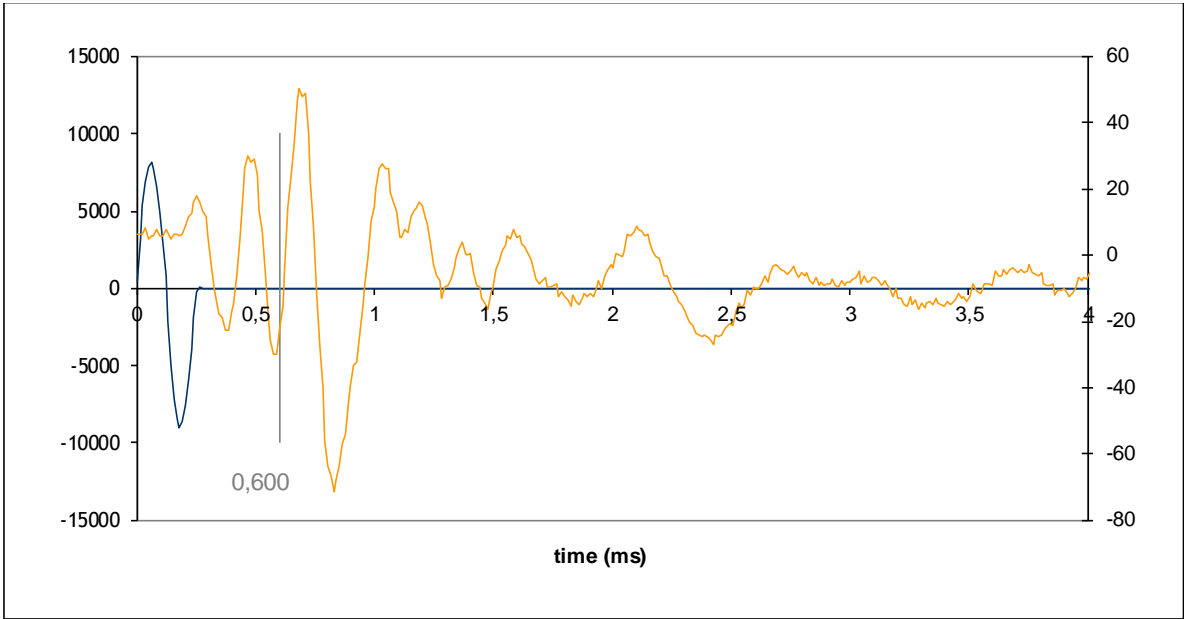


Figure A.78 – Sample 02: sweep 05, 4kHz

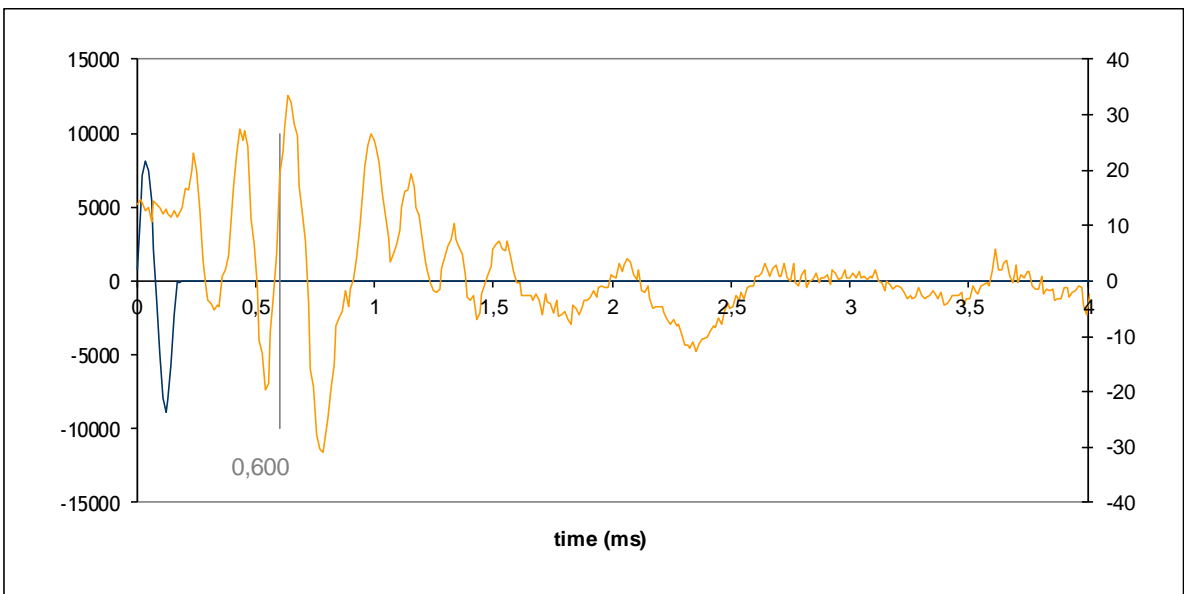


Figure A.79 – Sample 02: sweep 05, 6kHz

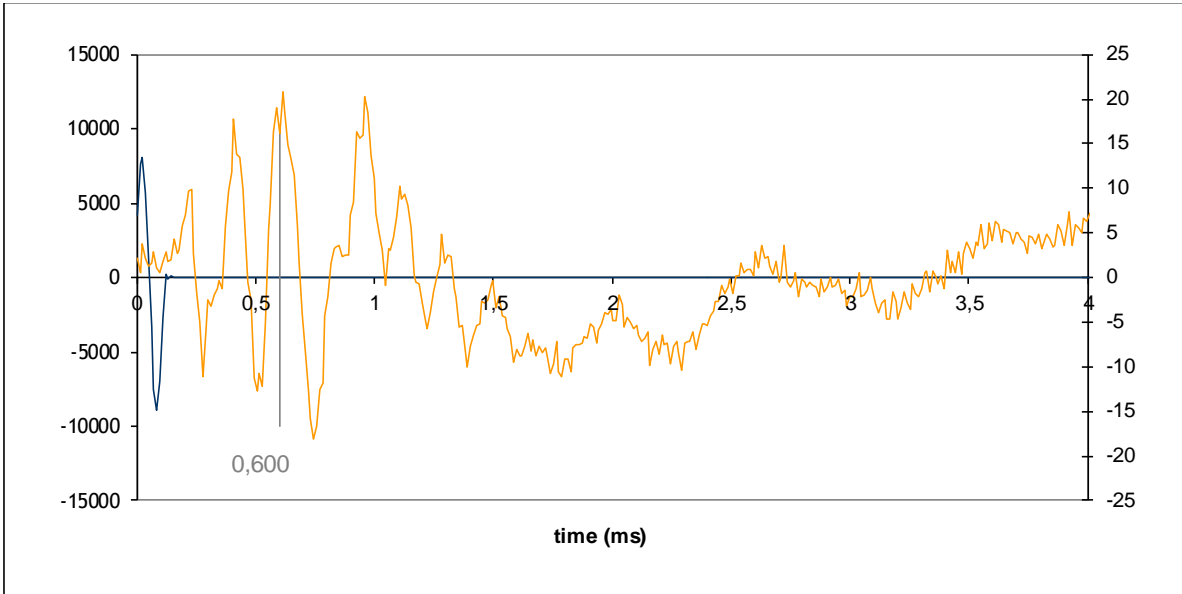


Figure A.80 – Sample 02: sweep 05, 8kHz

Table A.1.21 – Sample 02: logarithmic decrement method for sweep 05

02-s05					
	Voltage [mV]				
	1kHz	2kHz	4kHz	6kHz	8kHz
Max peak	107,071	59,28			
	59,097	36,469			
Following peaks	31,036	22,705			
	17,715	12,619			
Signal Quality	Low	Low	Very low	Very low	Very low
Nr. of peaks	Logarithmic decrement, $\delta$				
	1kHz	2kHz	4kHz	6kHz	8kHz
2	0,594312	0,485809			
3	0,619172	0,479843			
4	0,401589	0,353753			
Nr. of peaks	Damping [%]				
	1kHz	2kHz	4kHz	6kHz	8kHz
2	9,4	7,7			
3	9,8	7,6			
4	6,4	5,6			

red value = peak value similar to the previous one

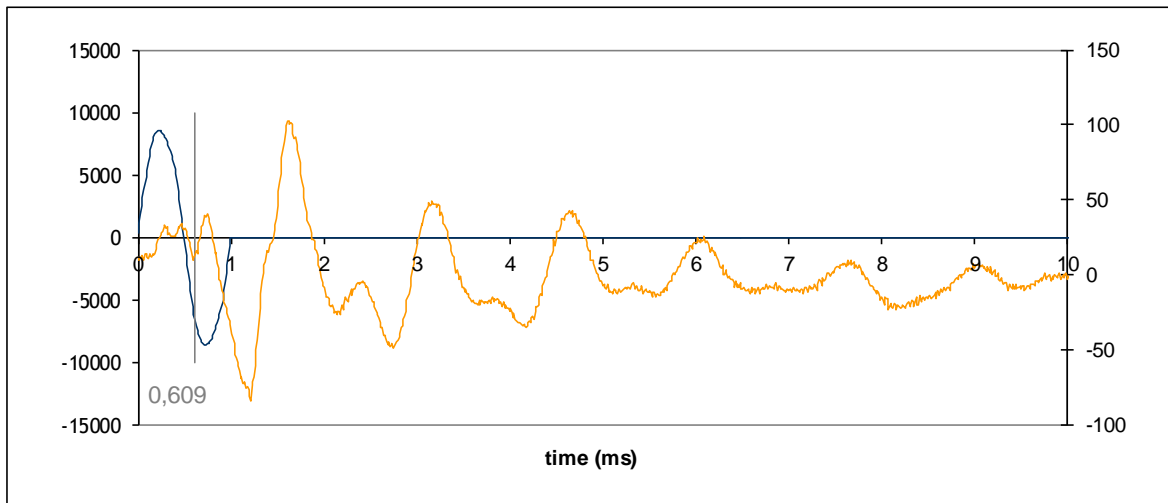


Figure A.81 – Sample 02: sweep 06, 1kHz

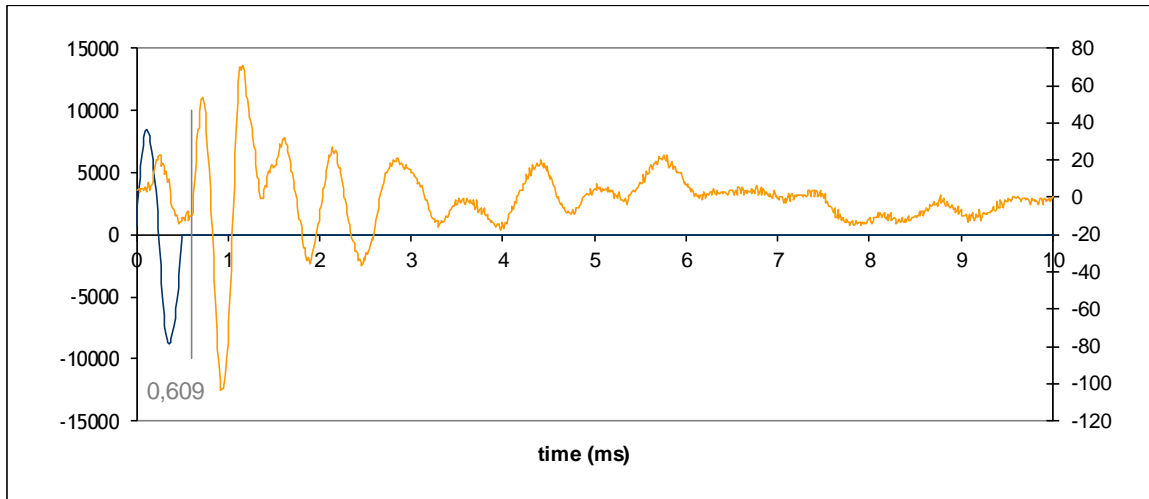


Figure A.82 – Sample 02: sweep 06, 2kHz

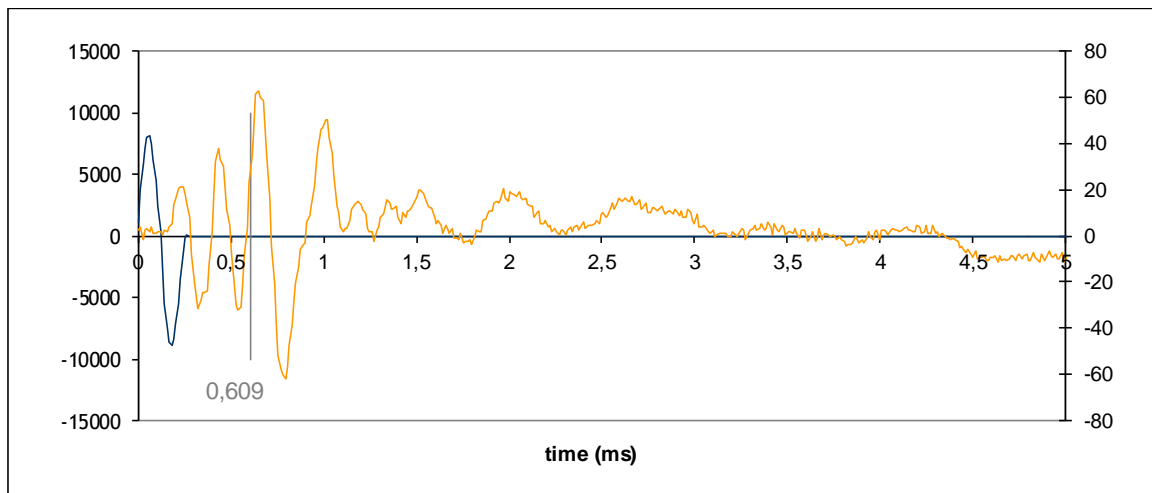


Figure A.83 – Sample 02: sweep 06, 4kHz

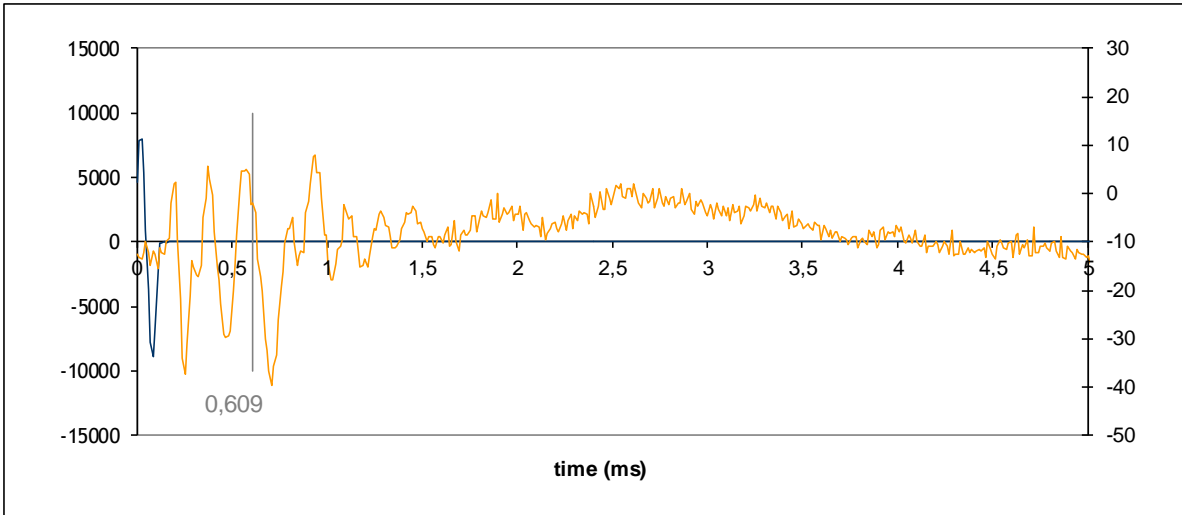


Figure A.84 – Sample 02: sweep 06, 8kHz

Table A.1.22 – Sample 02: logarithmic decrement method for sweep 06

02-s06				
Voltage [mV]				
	1kHz	2kHz	4kHz	8kHz
Max peak	99,319	69,962		
	46,585	31,494		
Following peaks	38,91	22,903		
		19,348		
Signal Quality	High	Low	Very low	Very low
Logarithmic decrement, $\delta$				
Nr. of peaks	1kHz	2kHz	4kHz	8kHz
2	0,757058	0,798155		
3	0,468543	0,558342		
4		0,428454		
Damping [%]				
Nr. of peaks	1kHz	2kHz	4kHz	8kHz
2	12,0	12,6		
3	7,4	8,9		
4		6,8		

red value = peak value similar to the previous one



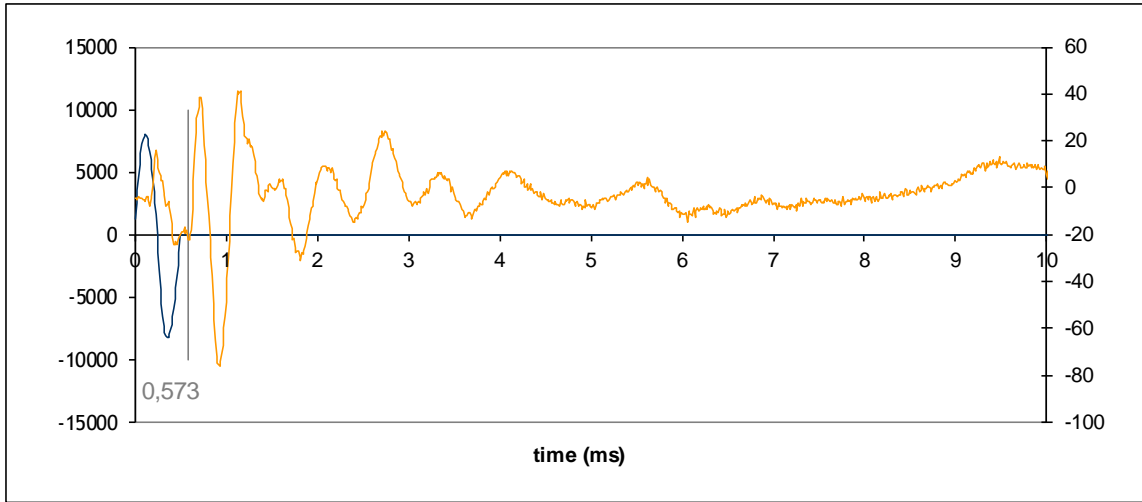


Figure 1.85 – Sample 02: sweep 07, 2kHz

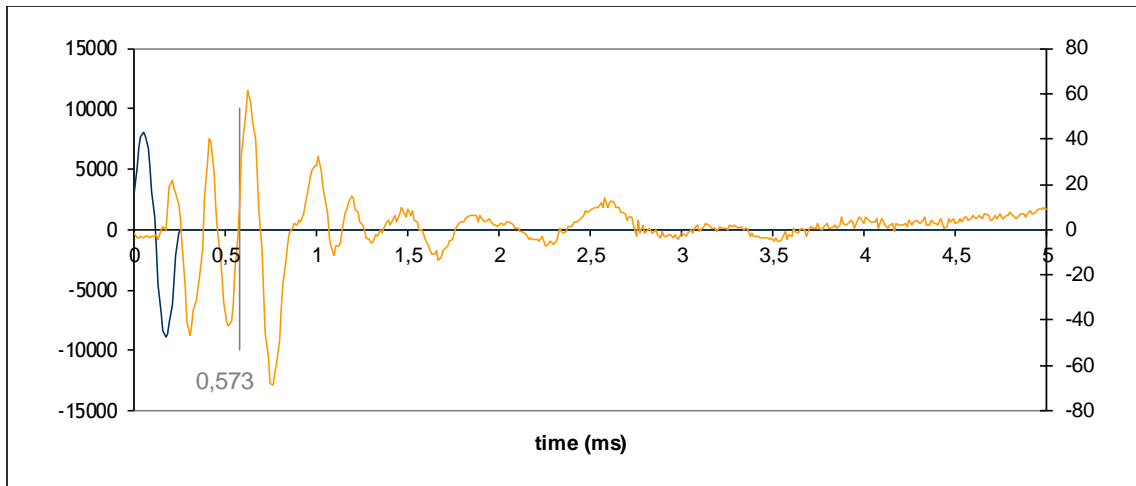


Figure 1.86 Sample 02: sweep 07, 4kHz

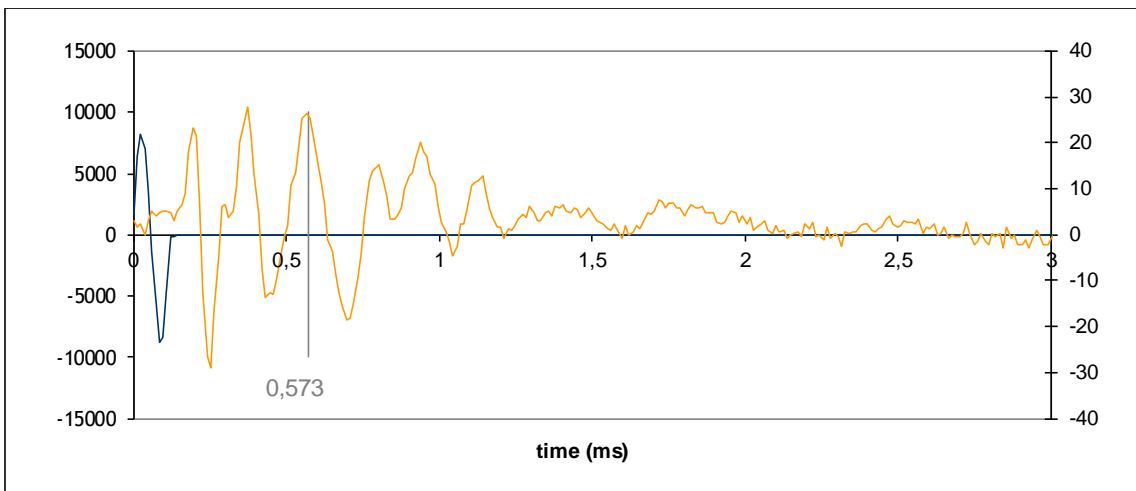


Figure 1.87 – Sample 02: sweep 07, 8kHz

Table A.23 – Sample 02: logarithmic decrement method for sweep 07

02-s07			
	Voltage [mV]		
	2kHz	4kHz	8kHz
Max peak		61,356	
Following peaks		28,259	
		10,086	
Signal Quality	Very low	Low	Very low
Logarithmic decrement, $\delta$			
Nr. of peaks	2kHz	4kHz	8kHz
2		0,775281	
3		0,902772	
Damping [%]			
Nr. of peaks	2kHz	4kHz	8kHz
2		12,2	
3		14,2	

red value = peak value similar to the previous one

Table A.24 – Sample 02: summary of results with logarithmic decay method

Sweep	Damping [%]					
	0,5kHz	1kHz	2kHz	4kHz	6kHz	8kHz
00	-	6,2*	7,3	X	-	-
01	8,5*	14,6*	33,2	X	X	X
02	-	9,8	7,6	X	X	-
03	-	3,6	8,7	8,4	X	-
04	-	X	3,8	17,1	X	X
05	-	8,5	6,7	X	X	X
06	-	9,7*	9,4*	X	-	X
07	-	-	X	13,2	-	X

X = discarded result due to very low signal quality; red value = low quality test result; - = untested frequency; \*=test with high variation on damping value

## A.3.2. FREQUENCY DOMAIN

### A.3.2.1. Sample 04

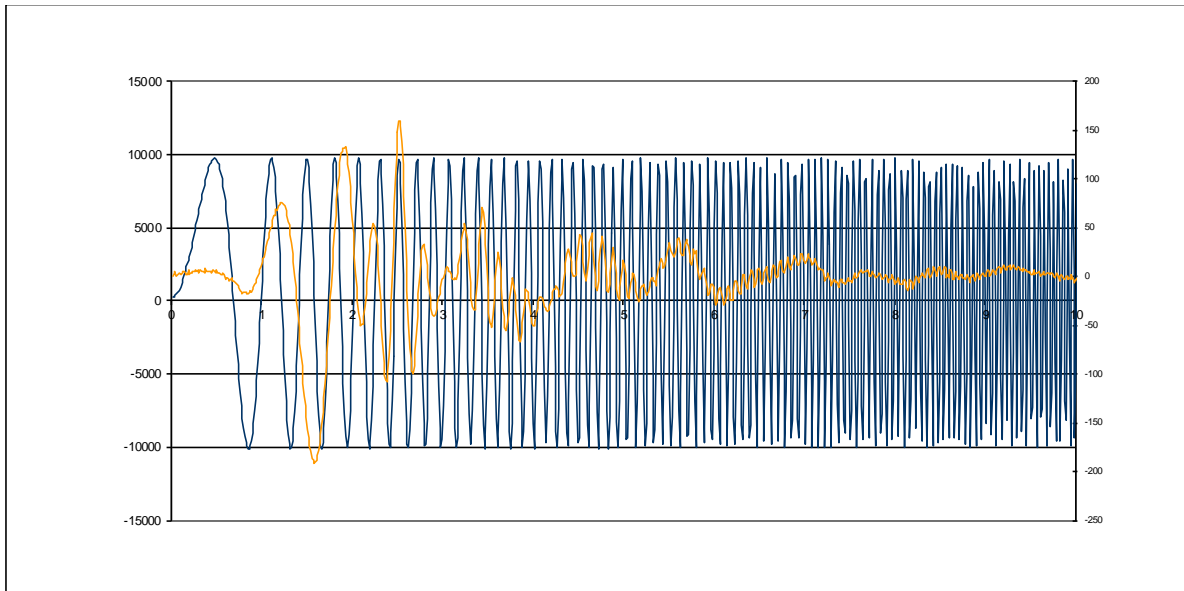


Figure A.88 – Sample 04: sweep 01 (ABETS)

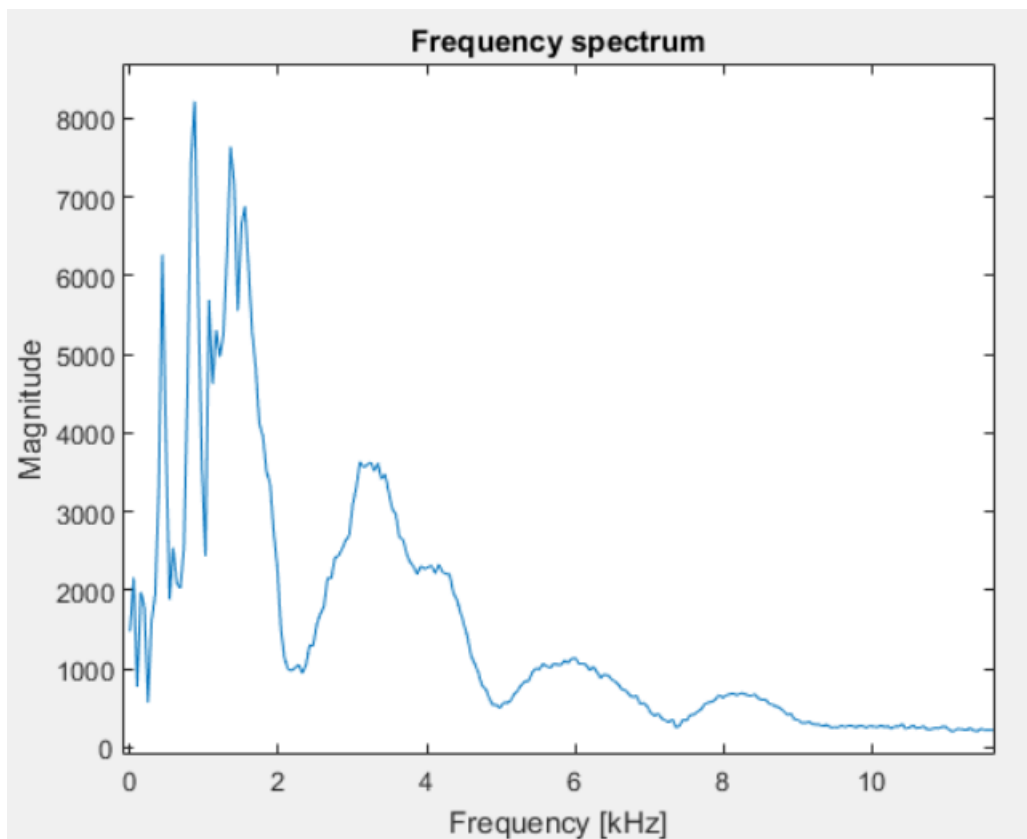


Figure A.89 – Sample 02: frequency spectrum for sweep 01

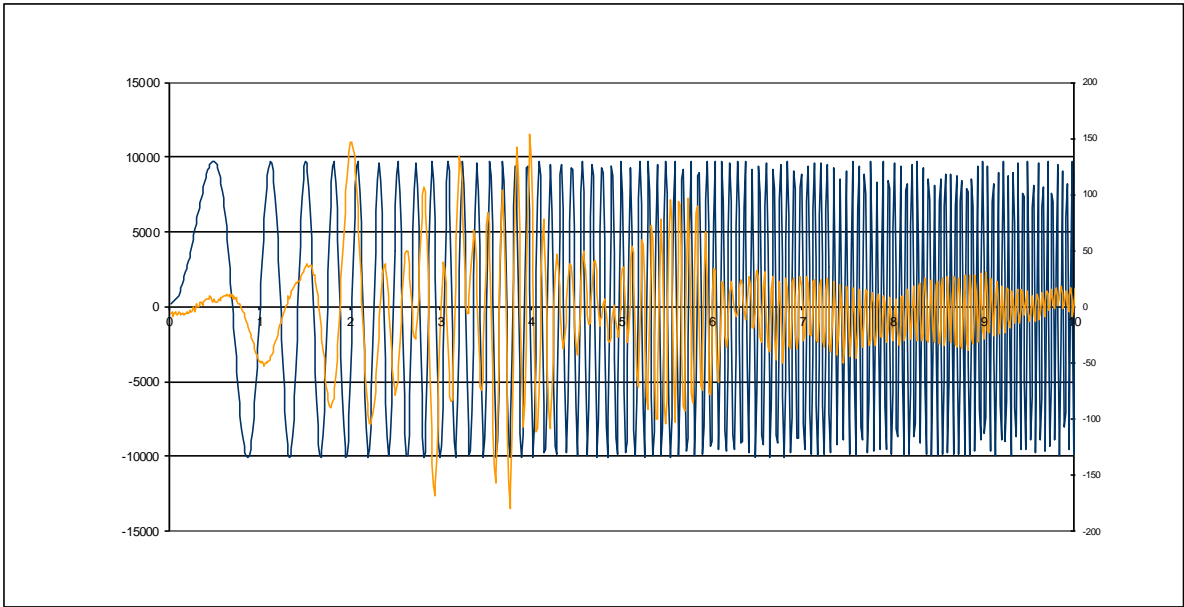


Figure A.90 – Sample 04: sweep 03 (ABETS)

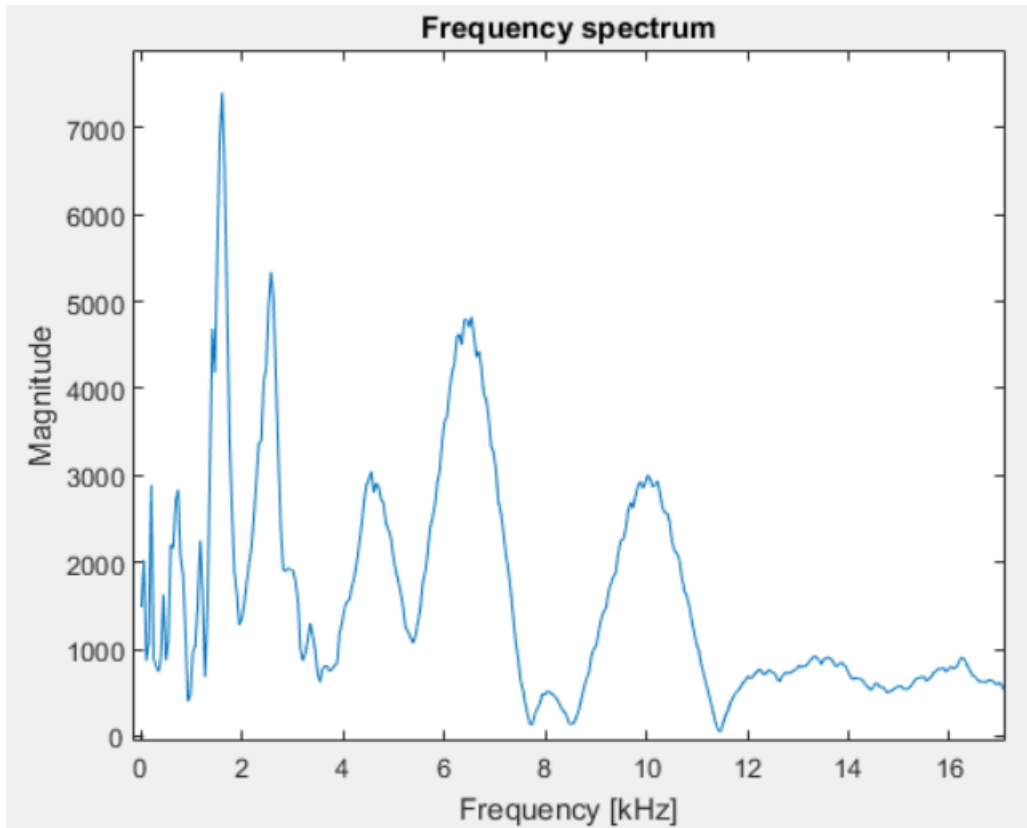


Figure A.91 – Sample 02: frequency spectrum for sweep 03

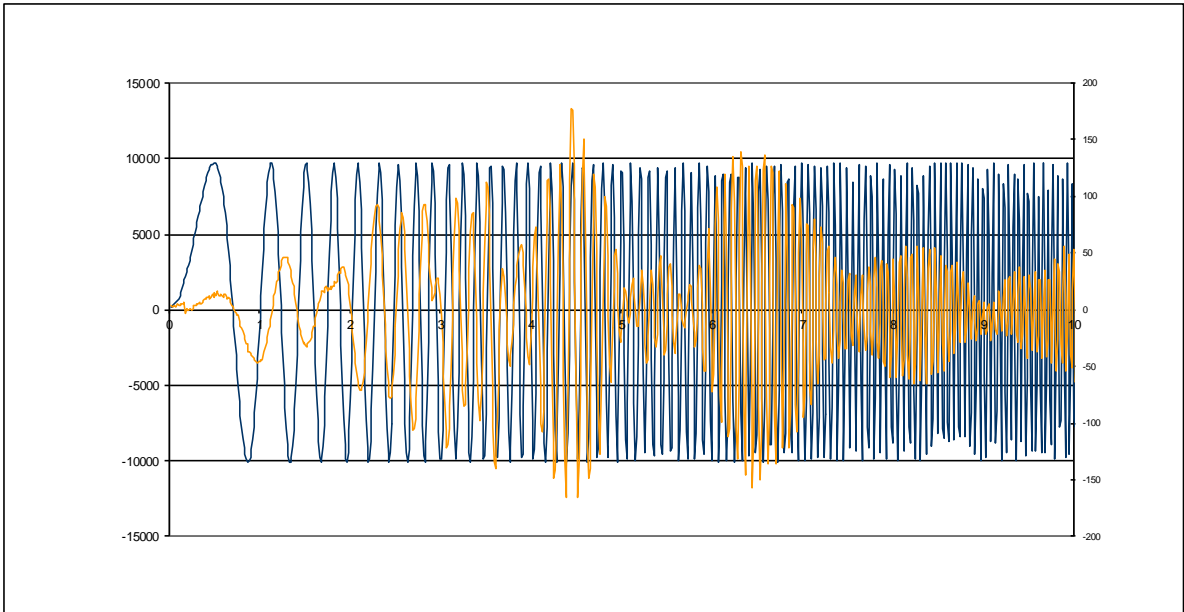


Figure A.92 – Sample 04: sweep 04 (ABETS)

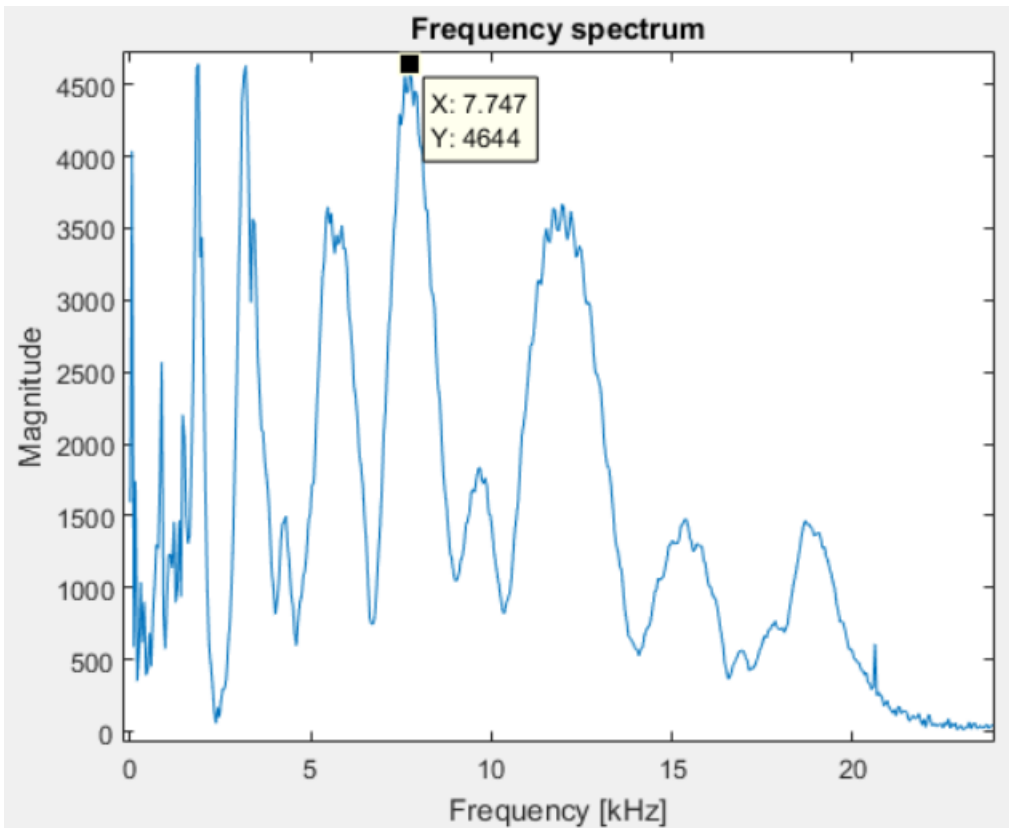


Figure A.93 – Sample 02: frequency spectrum for sweep 04

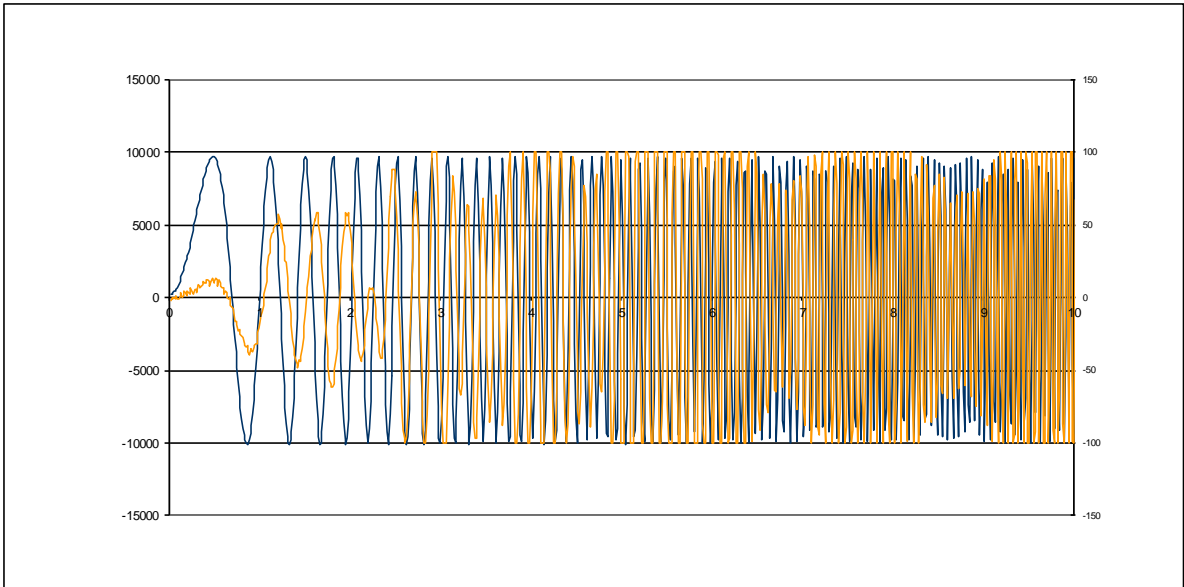


Figure A.94 – Sample 04: sweep 04 (ABETS)

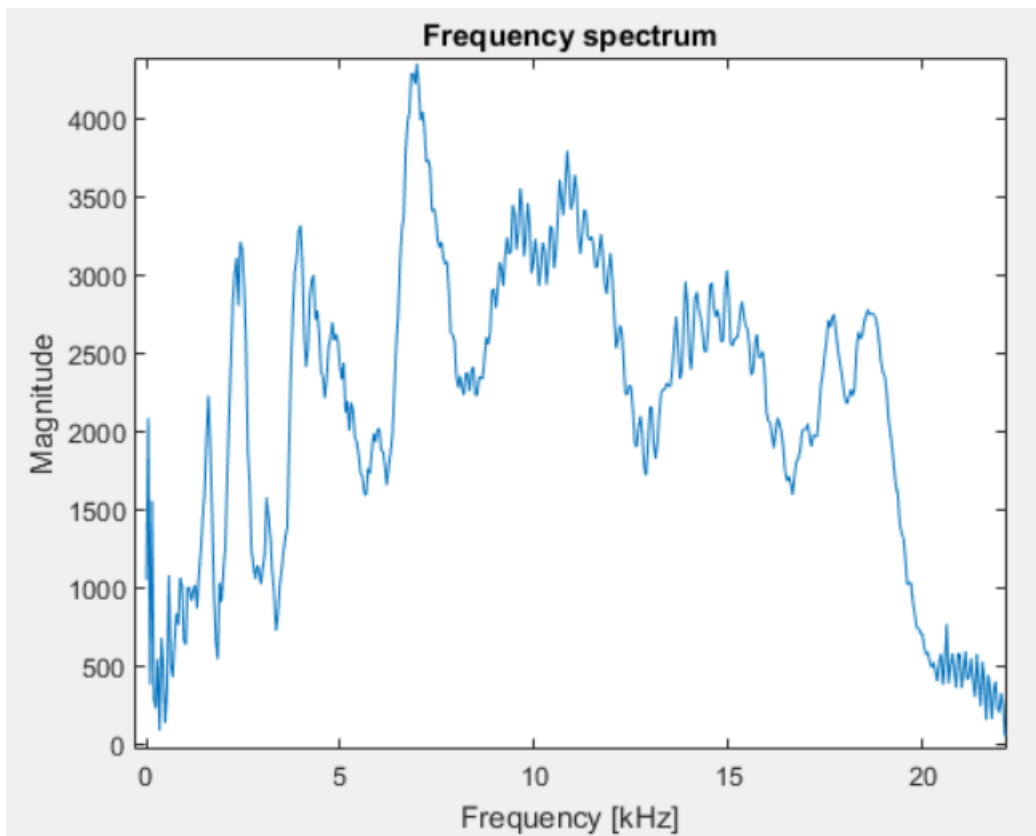


Figure A.95 – Sample 02: frequency spectrum for sweep 07

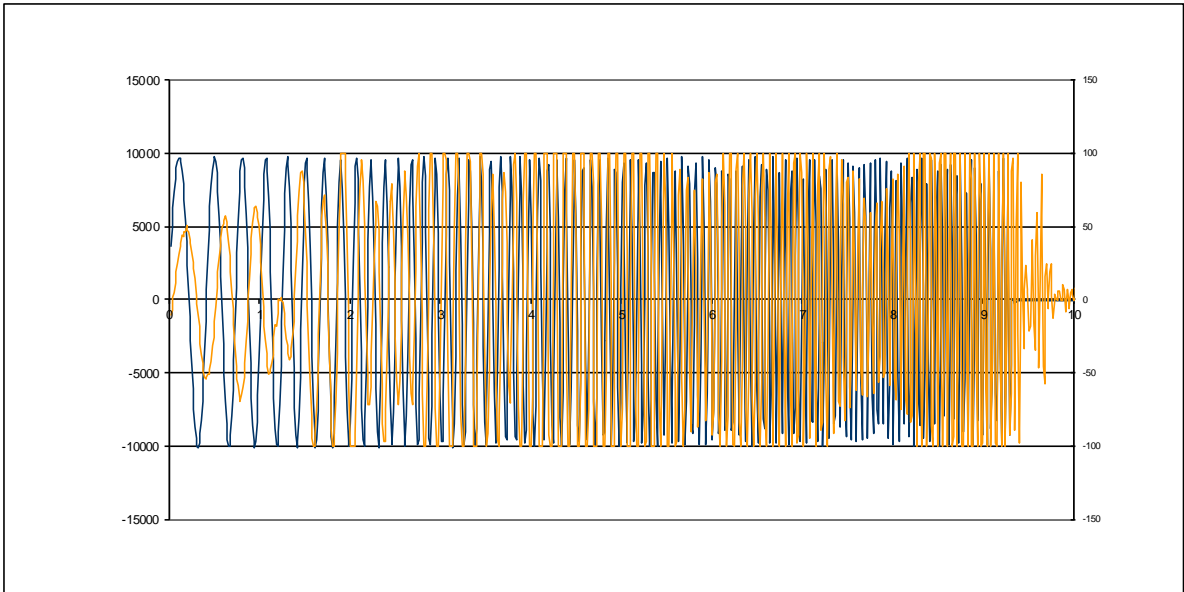


Figure A.96 – Sample 04: sweep 08 (ABETS)

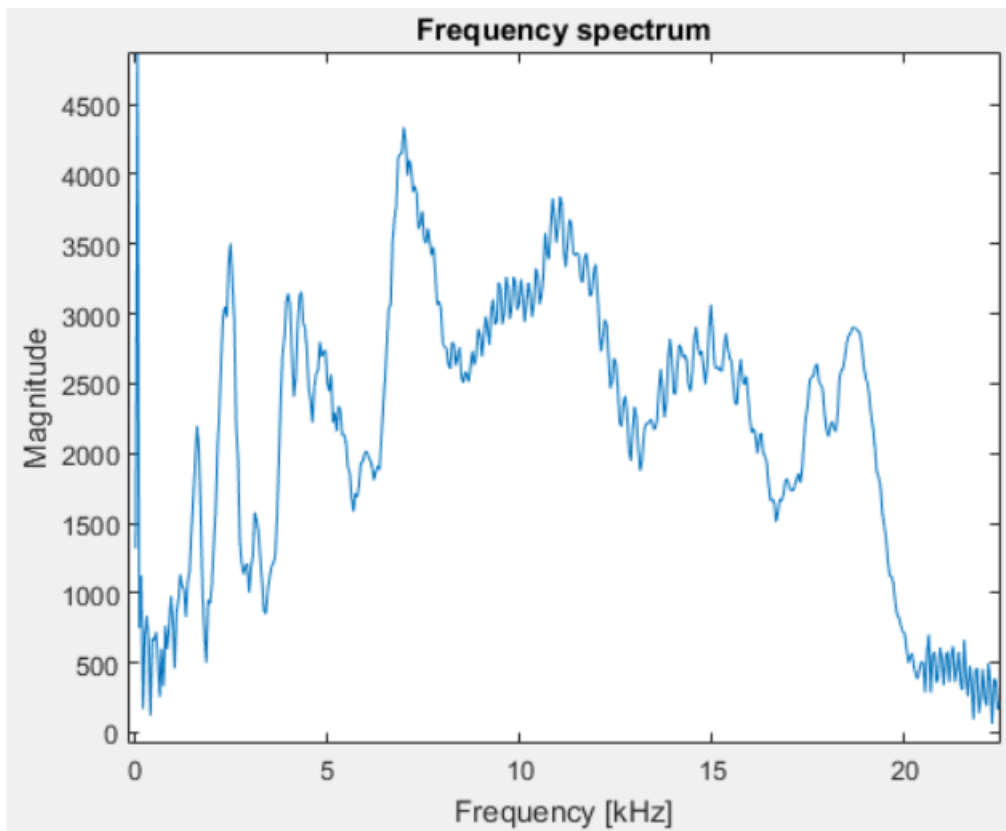


Figure A.97 – Sample 02: frequency spectrum for sweep 08

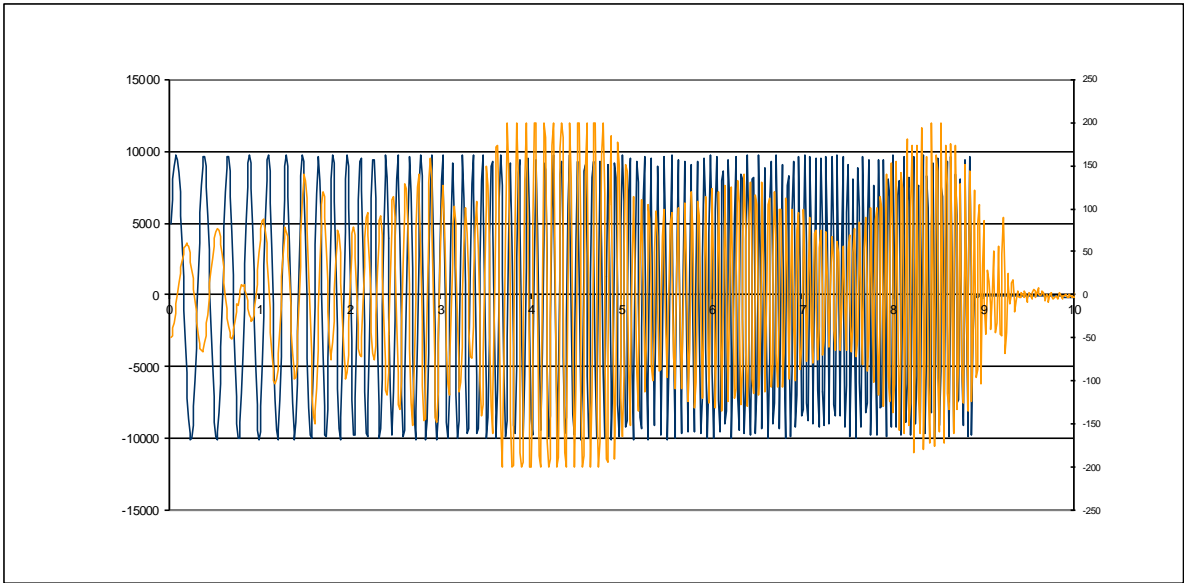


Figure A.98 – Sample 04: sweep 10 (ABETS)

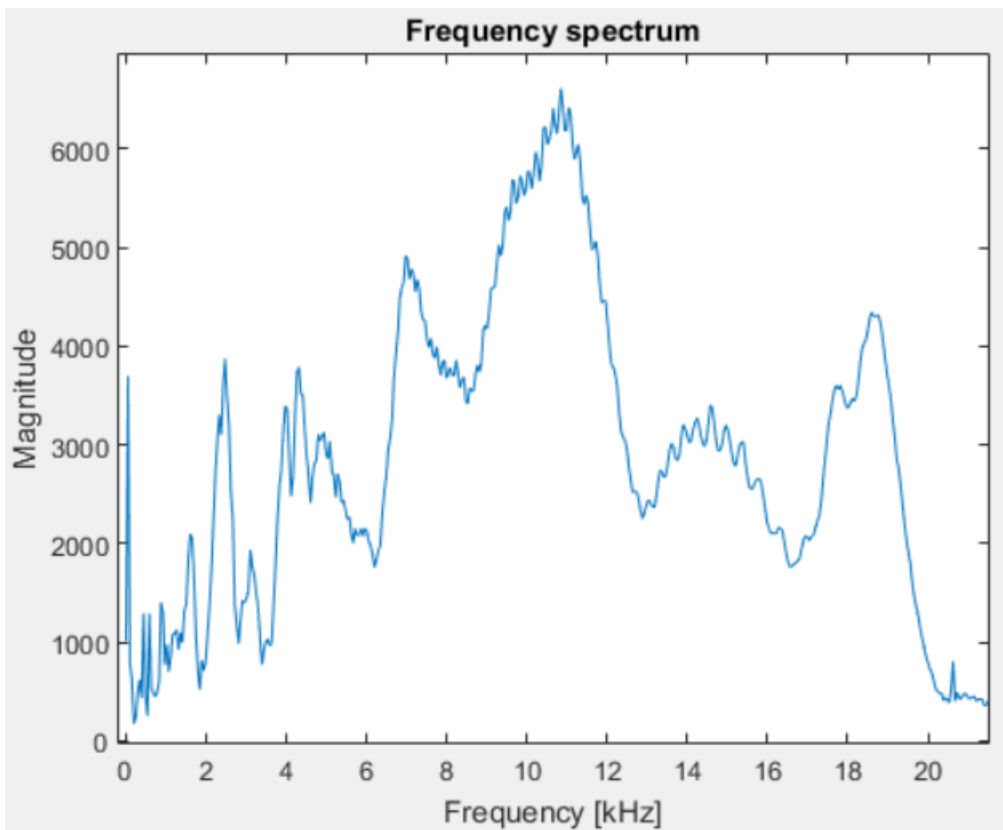


Figure A.99 – Sample 02: frequency spectrum for sweep 10



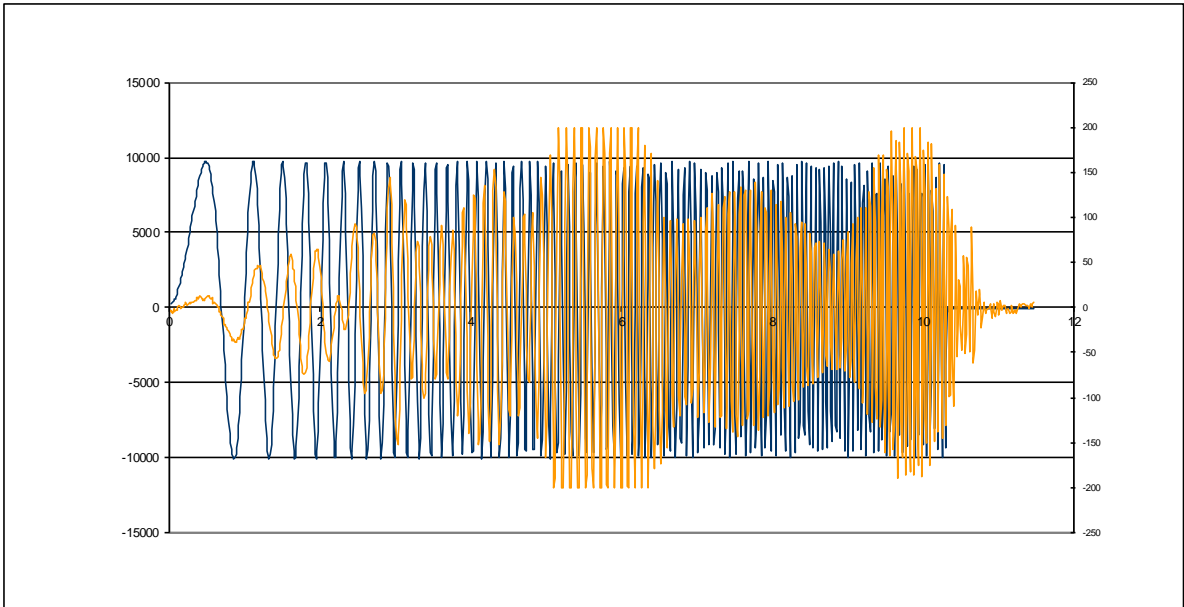


Figure A.100 – Sample 04: sweep 11 (ABETS)

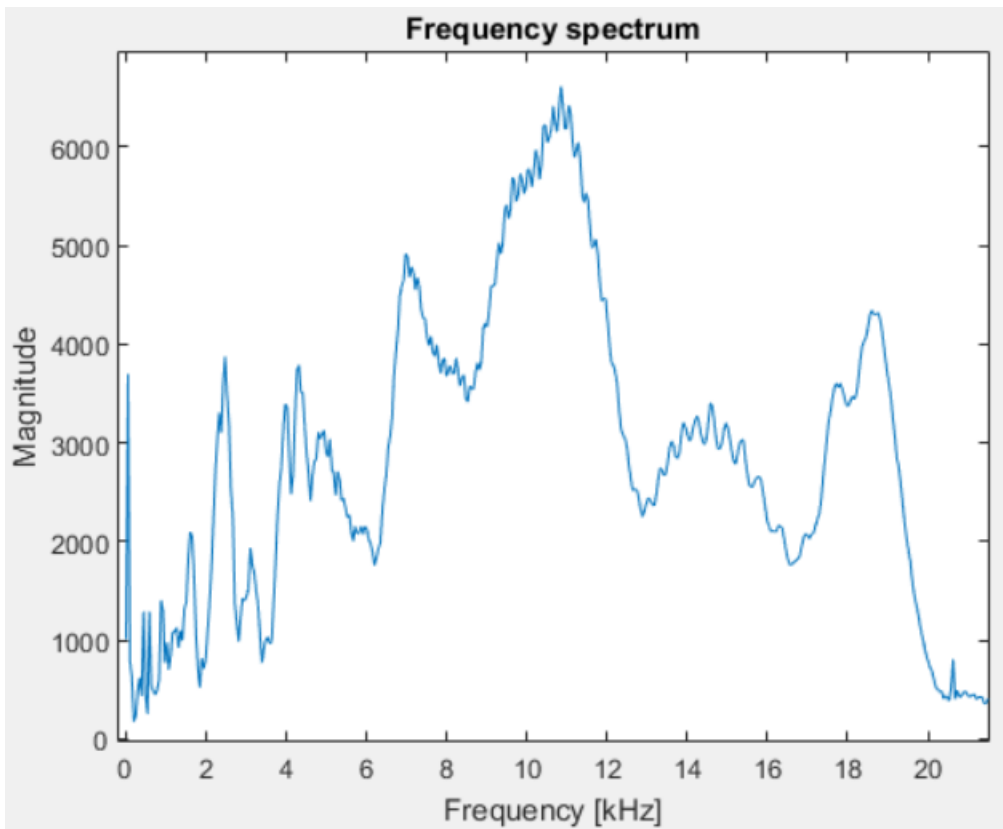


Figure A.101 – Sample 02: frequency spectrum for sweep 11

Table A.1.25 – Sample 04: results for the half-power bandwidth method

Sweep	$A_m$	$f_m$ [kHz]	$A_{not}$	$f_1$ [kHz]	$f_2$ [kHz]	$\xi_{BR}$	$\xi_K$
01	8.2134e+03	0.87	5.8078e+03	0.80	0.92	6.96	6.98
03	7.4031e+03	1.60	5.2348e+03	1.49	1.69	6.16	6.17
04	4.6441e+03	7.74	3.2839e+03	7.26	8.29	6.65	6.66
07	4.3508e+03	6.97	3.0765e+03	6.54	7.75	8.88	8.89
08	4.3368e+03	6.97	3.0666e+03	6.63	7.84	8.97	9.00
10	6.6118e+03	10.85	4.6753e+03	10.21	11.81	7.46	7.48
11	6.6938e+03	10.85	4.7332e+03	10.13	11.82	7.89	7.91

A.3.2.2. Sample 02

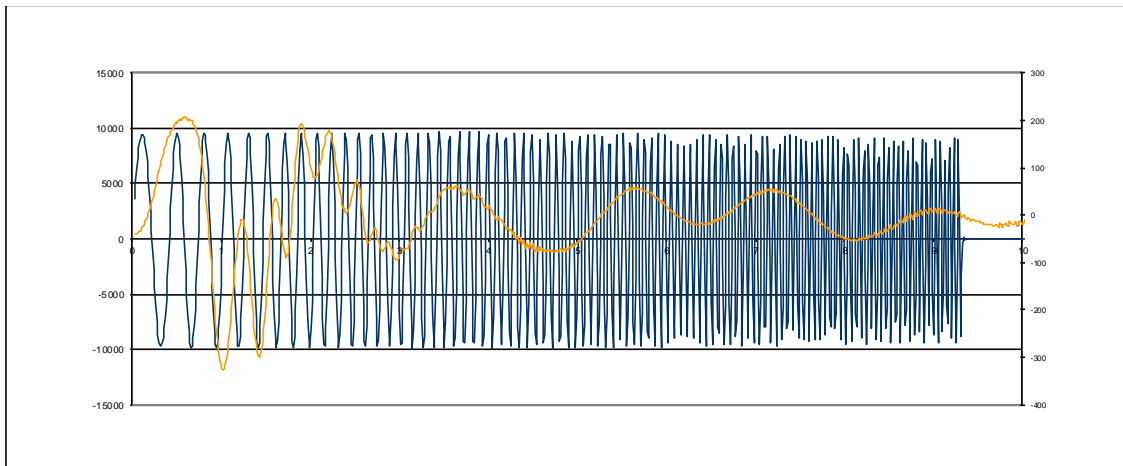


Figure A.102 – Sample 02: sweep 00 (ABETS)

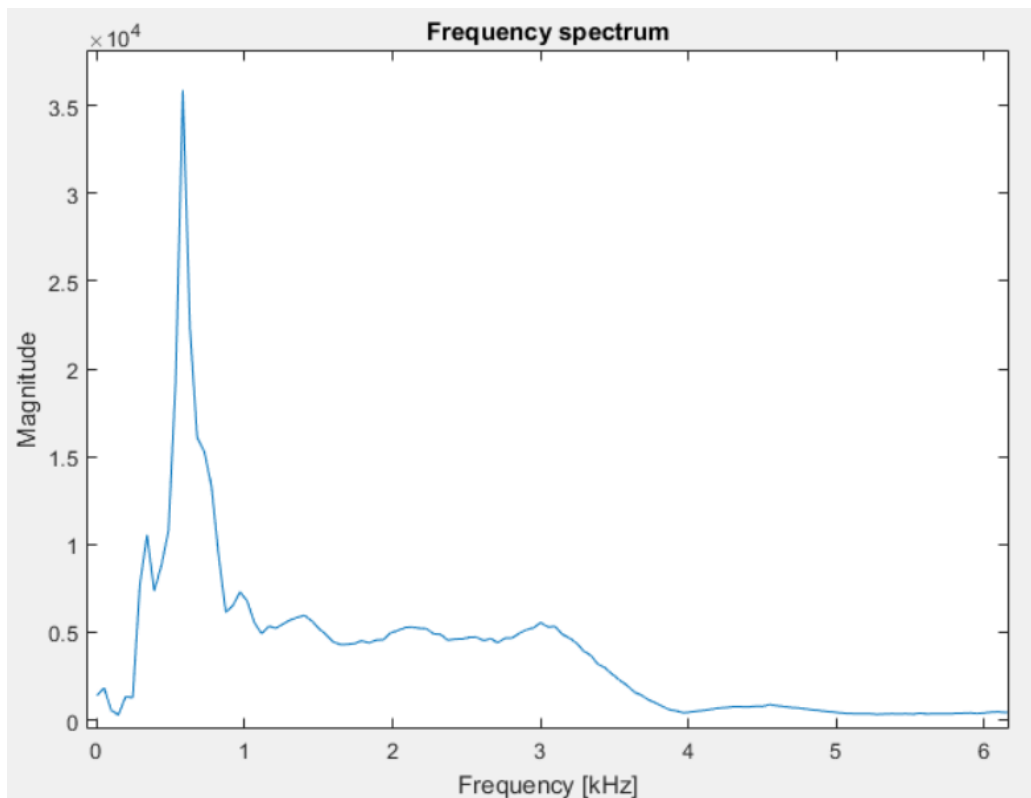


Figure A.103 – Sample 02: frequency spectrum for sweep 00

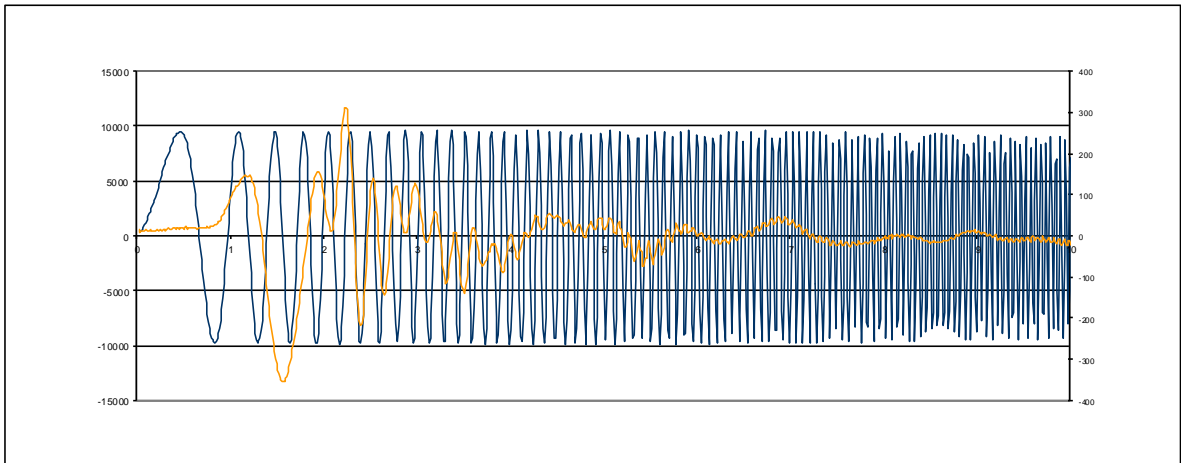


Figure A.104 – Sample 02: sweep 01 (ABETS)

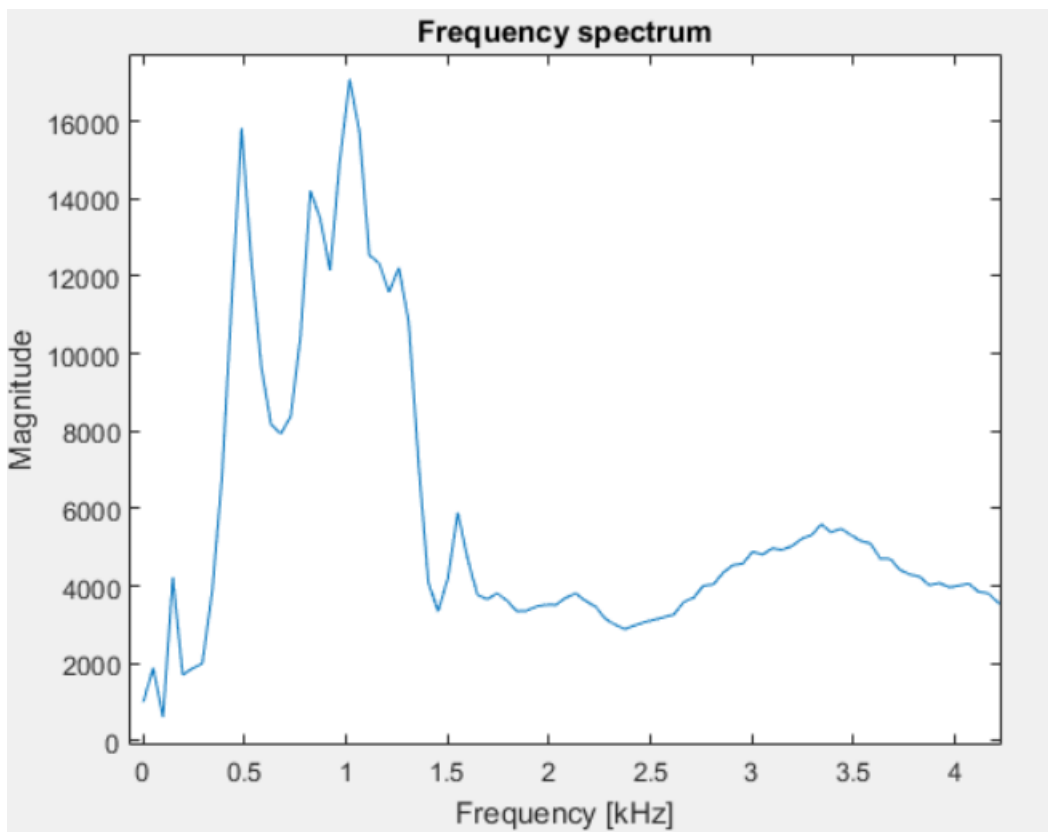


Figure A.105 – Sample 02: frequency spectrum for sweep 01

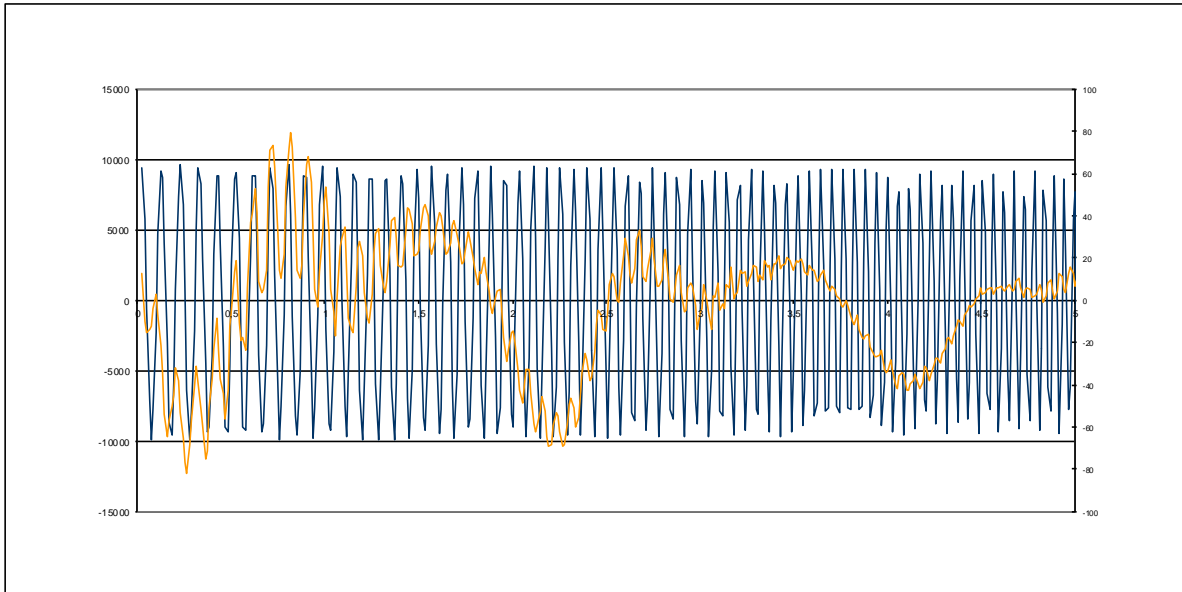


Figure A.106 – Sample 02: sweep 02 (ABETS)

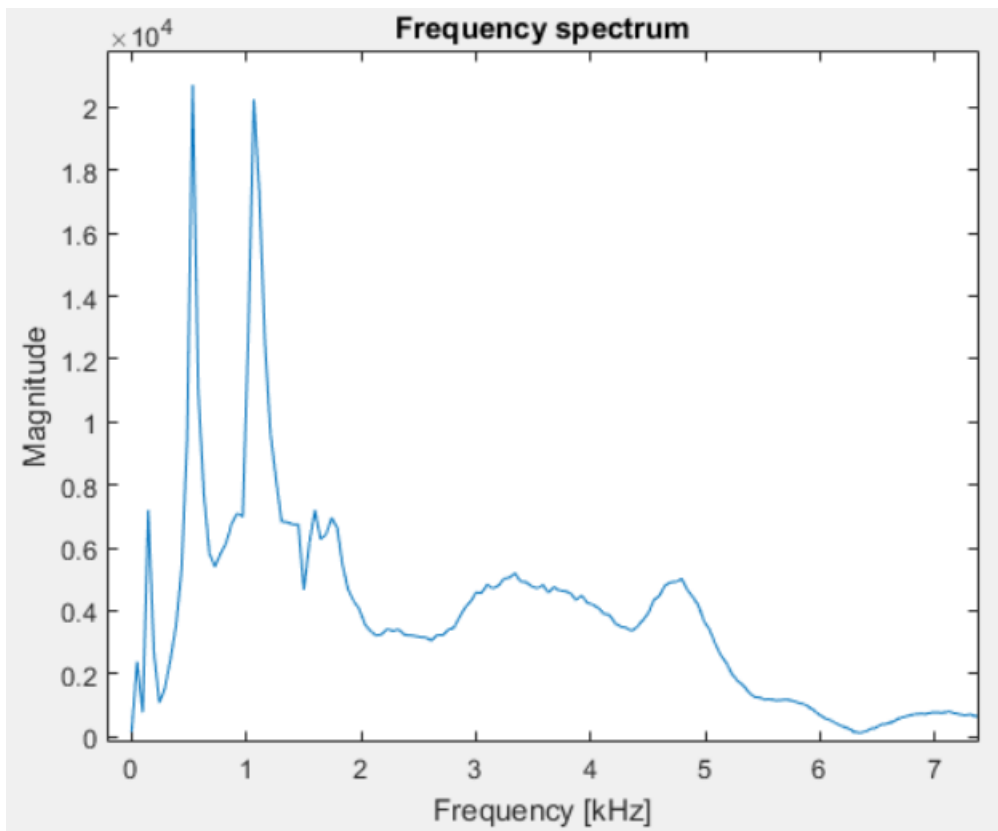


Figure A.107 – Sample 02: frequency spectrum for sweep 02

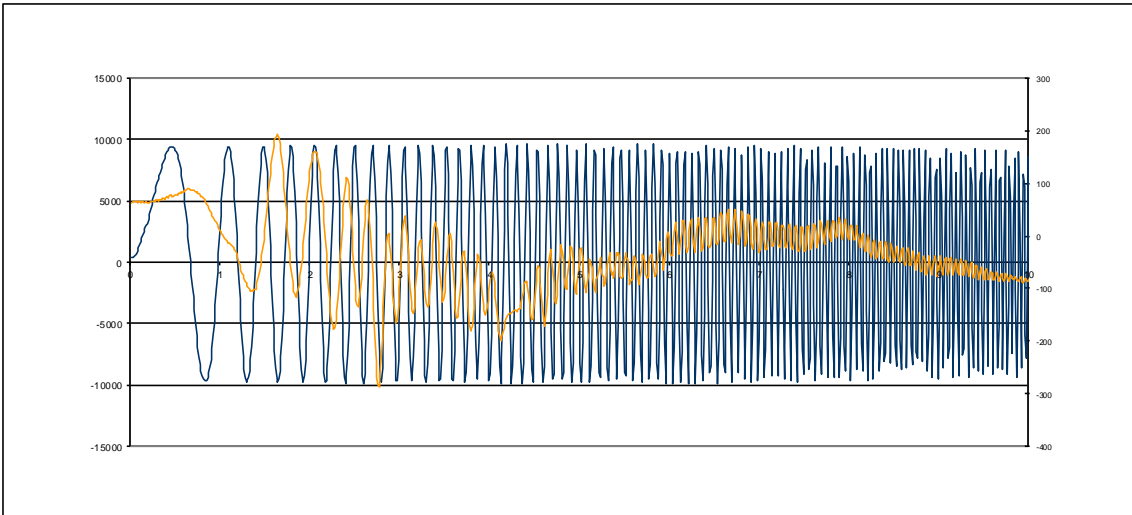


Figure A.108 – Sample 02: sweep 03 (ABETS)

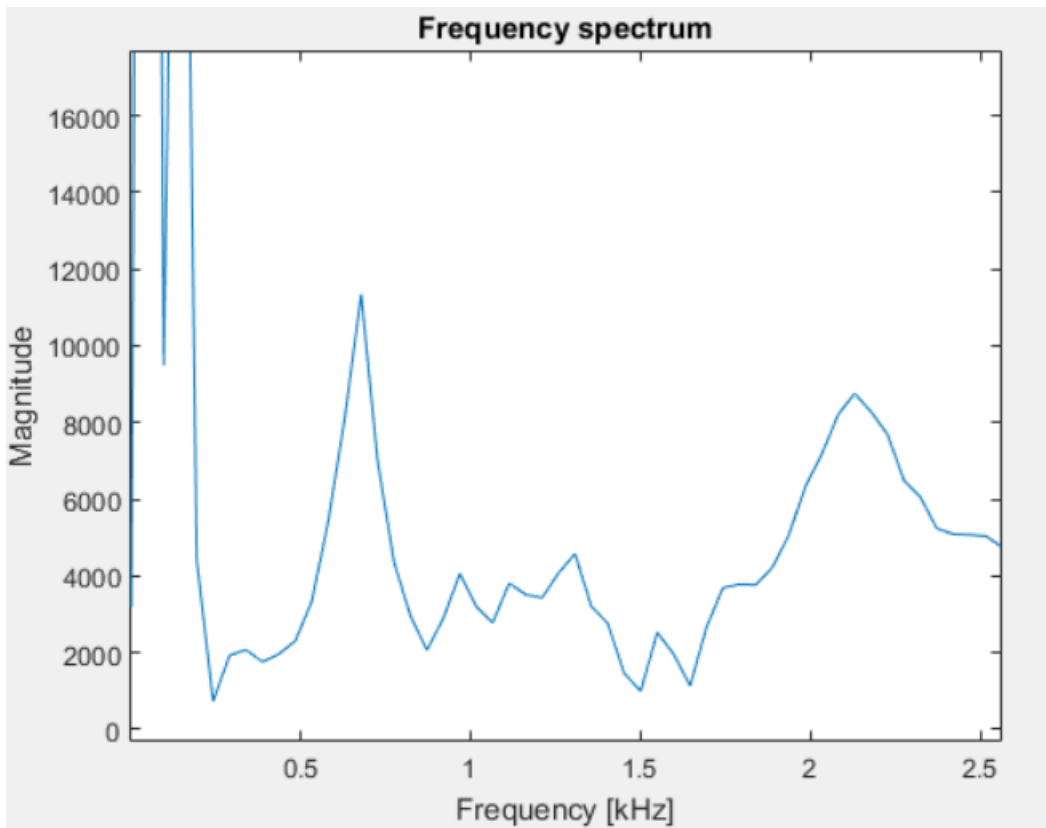


Figure A.109 – Sample 02: frequency spectrum for sweep 03

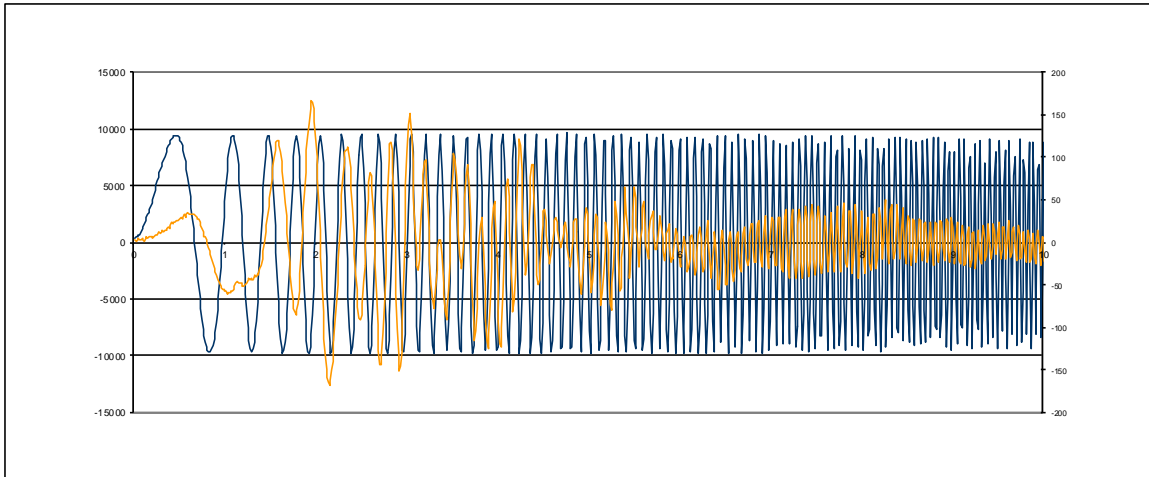


Figure A.110 – Sample 02: sweep 04 (ABETS)

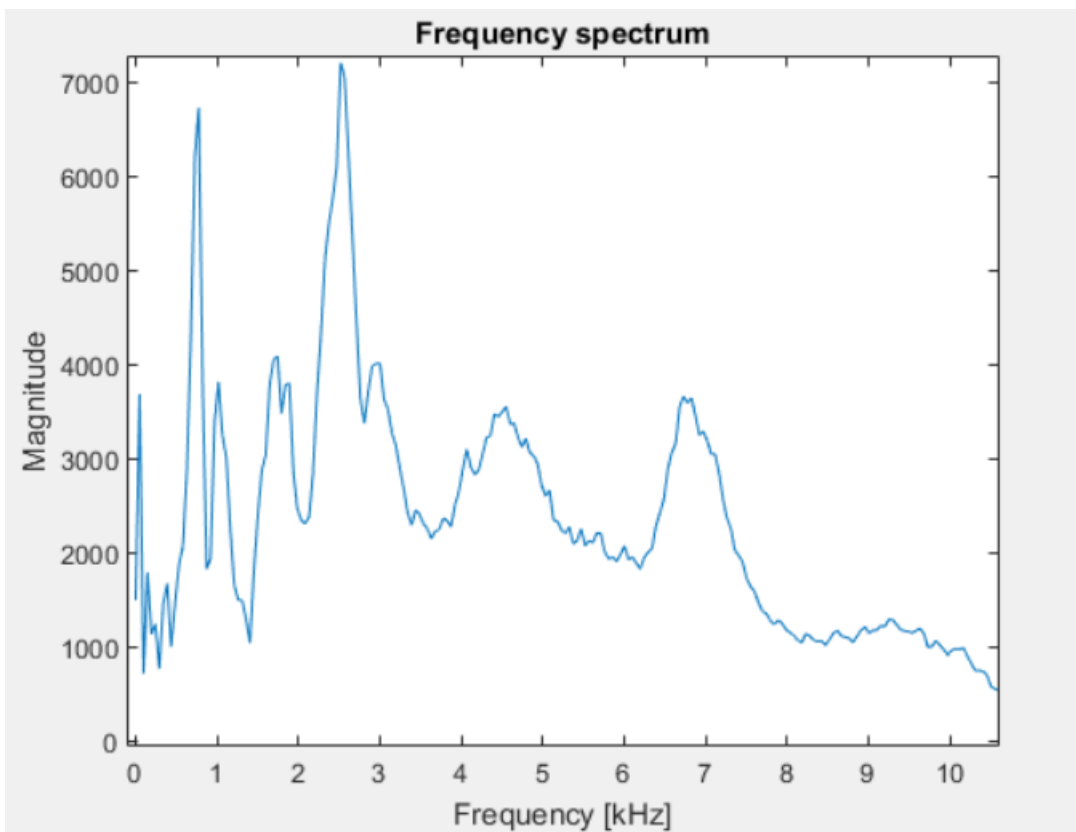


Figure A.111 – Sample 02: frequency spectrum for sweep 04

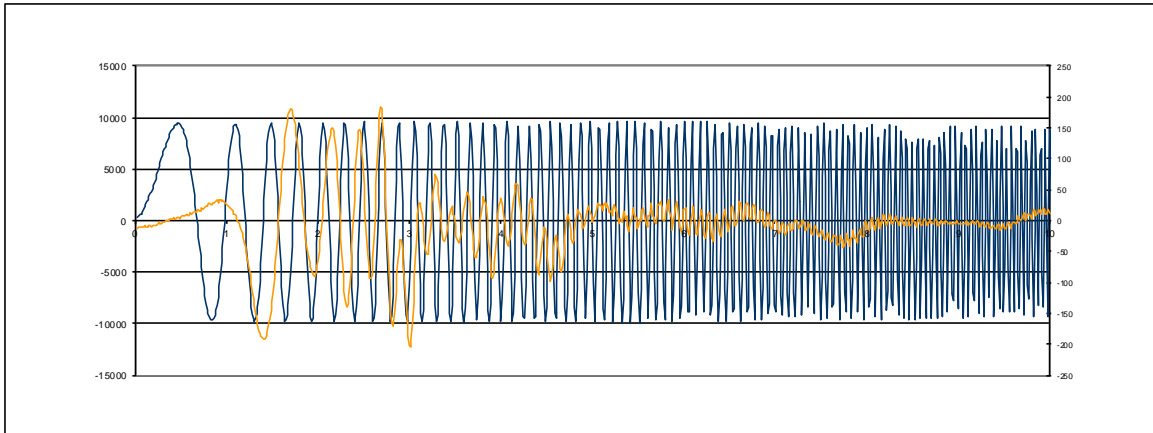


Figure A.112 – Sample 02: sweep 05 (ABETS)

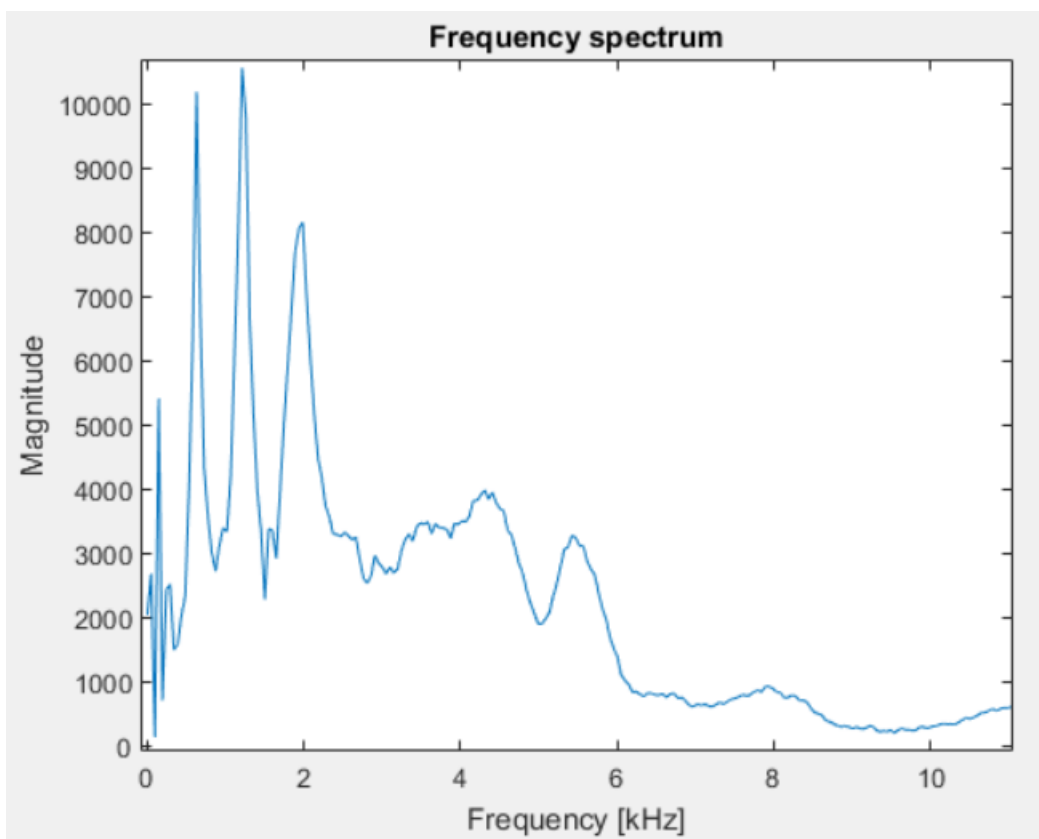


Figure A.113 – Sample 02: frequency spectrum for sweep 05

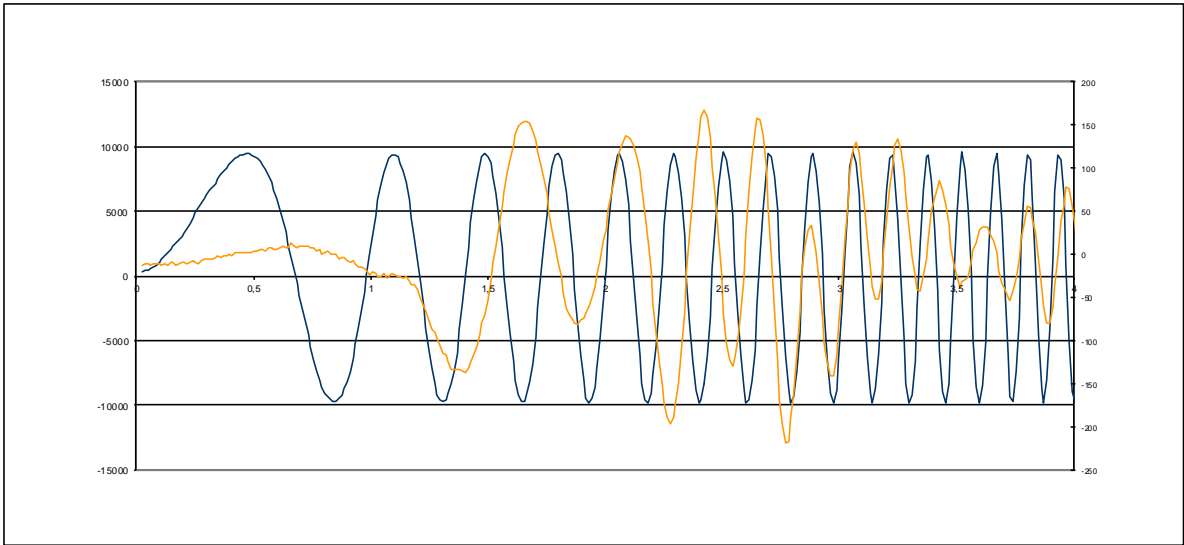


Figure A.114 – Sample 02: sweep 06 (ABETS)

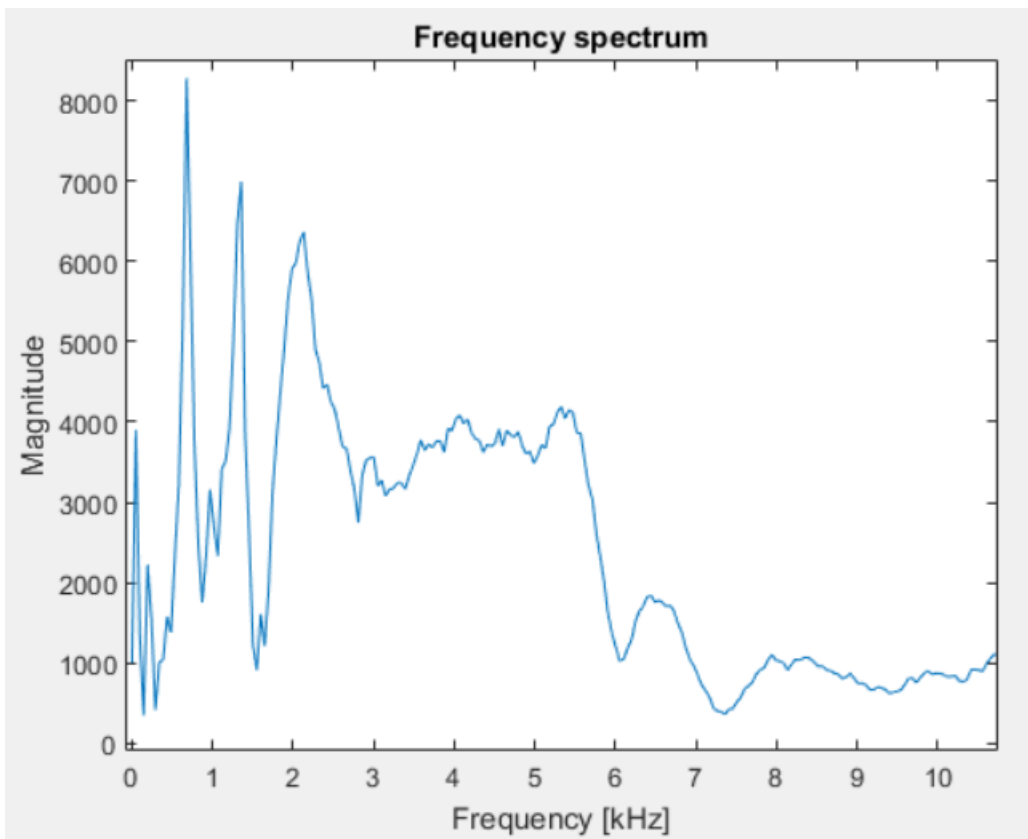


Figure A.115 – Sample 02: frequency spectrum for sweep 06



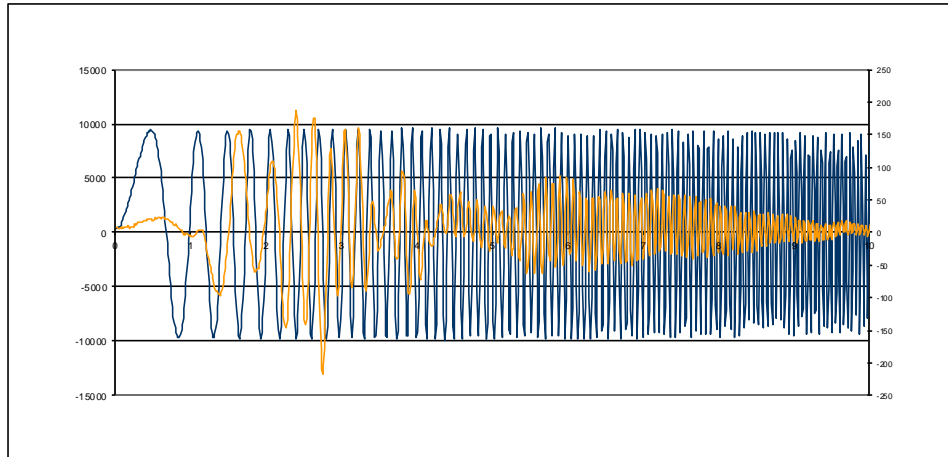


Figure A.116 – Sample 02: sweep 07 (ABETS)

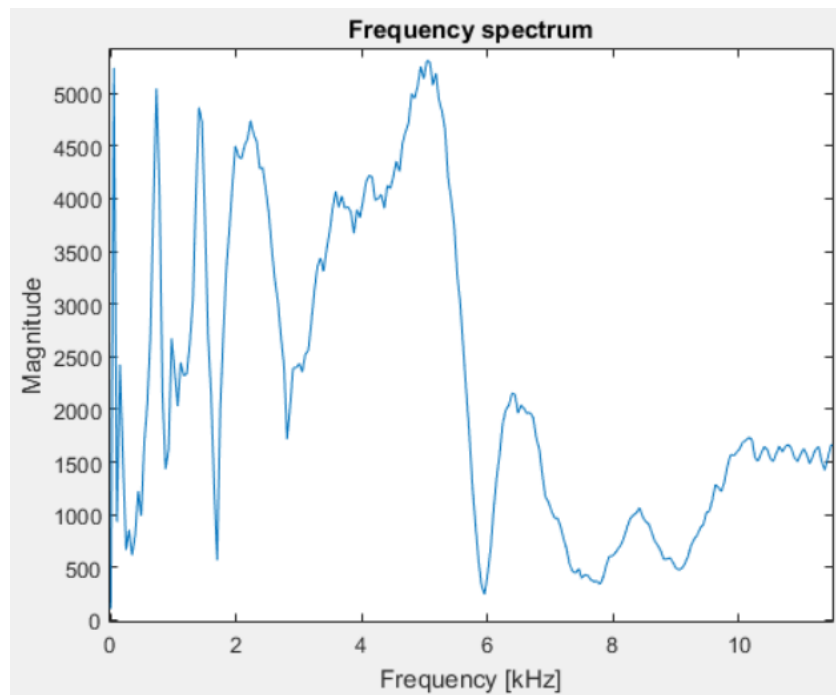


Figure A.117 – Sample 02: frequency spectrum for sweep 08

Table A.1.26 – Sample 02: results for the half-power bandwidth method

Sweep	$A_m$	$f_m$ [kHz]	$A_{not}$	$f_1$ [kHz]	$f_2$ [kHz]	$\xi_{BR}$	$\xi_K$
00	3.5862e+04	0.48	2.5328e+04	0.55	0.62	5.91	5.92
01	1.7082e+04	1.02	1.2079e+04	0.92	1.26	17.75	18.04
02	2.0721e+04	0.53	1.4652e+04	0.51	0.56	5.30	5.31
03	1.1341e+04	0.68	0.8019e+04	0.63	0.71	6.34	6.35
04	7.2085e+03	2.52	5.0972e+03	2.32	2.68	6.95	6.97
05	1.0553e+04	1.21	0.8056e+04	1.15	1.29	6.13	6.14
06	8.2270e+03	0.68	5.2127e+03	0.64	0.73	6.70	6.72
07	5.3090e+03	5.06	3.7540e+03	4.01	5.47	13.50	13.63

A.3.2.3. Sample 05

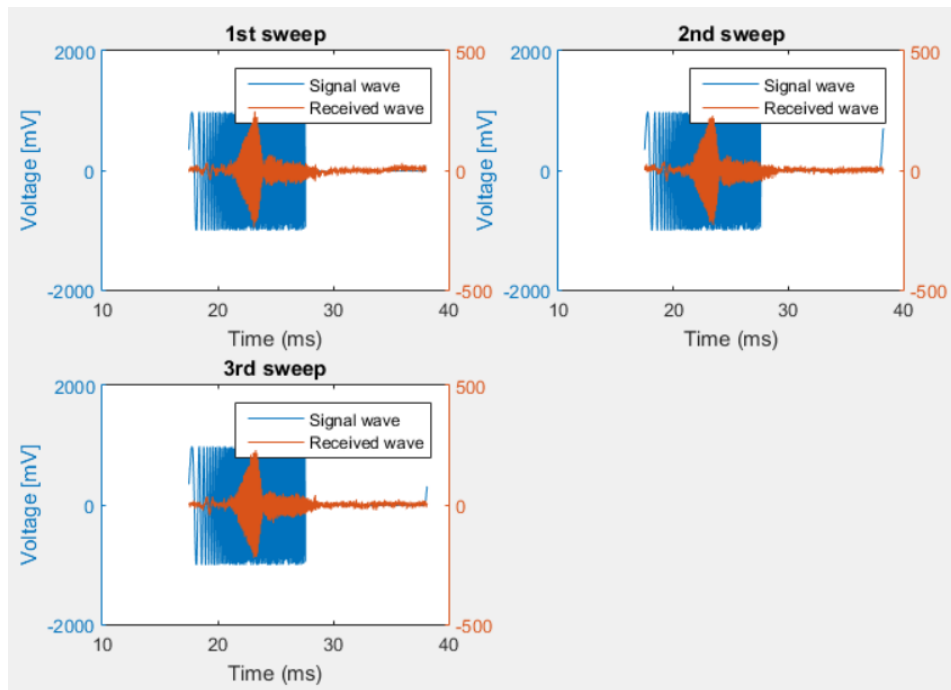


Figure A.118 – Sample 05: acquired sweeps

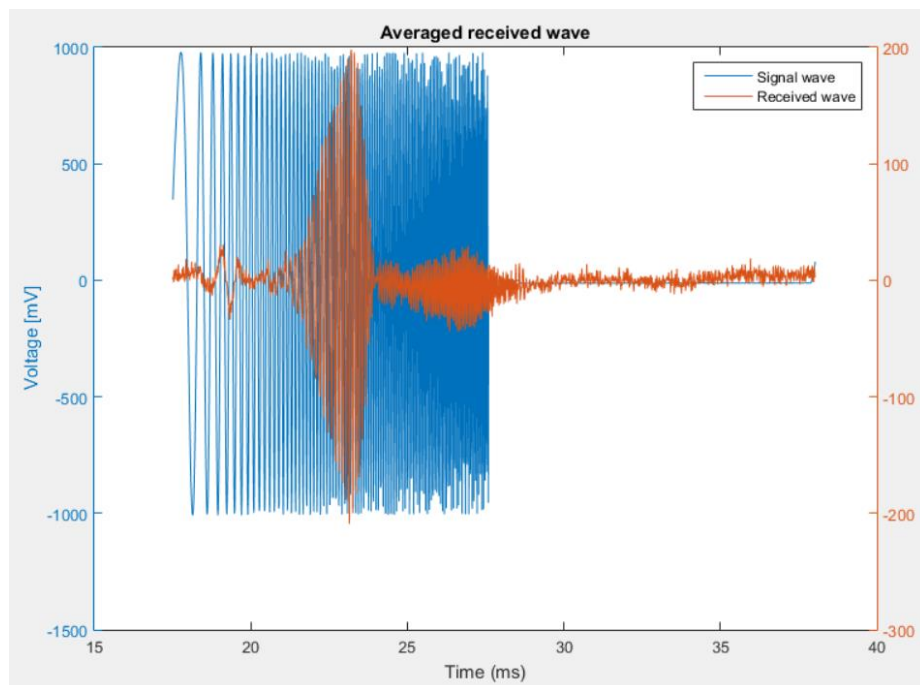


Figure A.119 – Sample 05: averaged signal

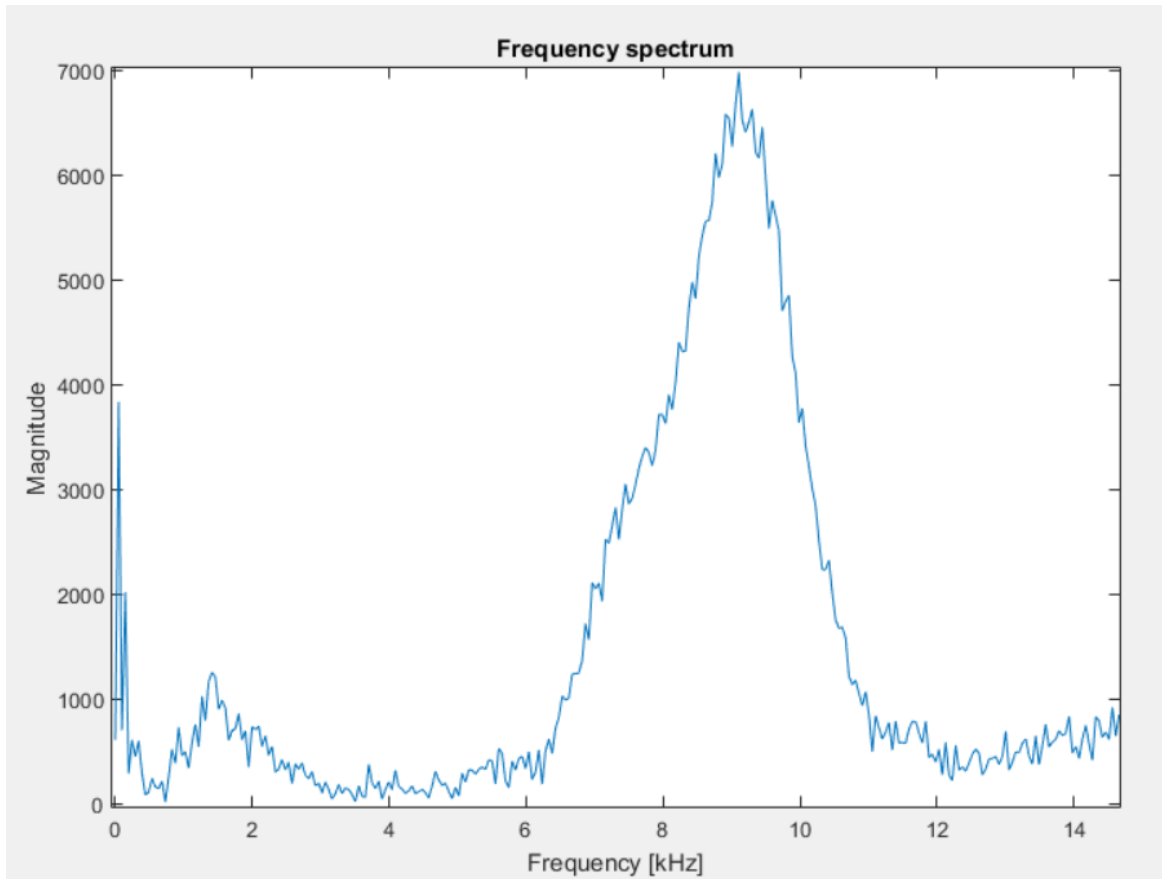


Figure A.120 – Sample 05: frequency spectrum

Table 1.27 – Sample 05: results for the half-power bandwidth method

$A_m$	$f_m$ [kHz]	$A_{not}$	$f_1$ [kHz]	$f_2$ [kHz]	$\xi_{BR}$	$\xi_K$
6.9837e+05	9.11	4.9382e+05	8.4176	9.7261	7.14	7.16

**A.4. SOIL CHARACTERIZATION**



## LABORATÓRIO DE GEOTECNIA DA F.E.U.P.

Rua Dr. Roberto Frias, s/n 4200-465 Porto

Telef. : 225081988 - Fax: 225081446 - Web: <http://www.fe.up.pt/labgeo>

DATA 02/03/2015	<b>ANÁLISE GRANULOMÉTRICA</b> CEN ISO/TS 17892-4	Amostra : Bloco 7 (Material do saco)
--------------------	---	---

MASSA TOTAL DA AMOSTRA ( gf )	$m_t =$	<b>274,20</b>
MASSA RETIDA NO PENEIRO DE 2,00 mm ( nº 10 ) ( gf )	$m_{10} =$	<b>44,20</b>
MASSA PASSADA NO PENEIRO DE 2,00 mm ( nº 10 ) ( gf )	$m'_{10} =$	<b>230,00</b>
% RETIDA NO PENEIRO DE 2,00 mm ( nº 10 )	$N'_{10} =$	<b>16,1</b>

FRACÇÃO RETIDA NO PENEIRO DE 2,00 mm ( nº 10 )								
PENEIROS	3"	2"	1,5"	1"	3/4"	3/8"	nº4	nº10
ABERTURA ( mm )	76,1	50,8	38,1	25,4	19,0	9,51	4,76	2,00
MASSA RETIDA ( gf )	( $m_x$ )	0,00	0,00	0,00	0,00	0,00	2,30	41,90
% RETIDA	[ $N_x = (m_x/m_t) \times 100$ ]	0,00	0,00	0,00	0,00	0,00	0,84	15,28
% RETIDA ACUMULADA	( $N'_x$ )	0,00	0,00	0,00	0,00	0,00	0,84	16,12
% PASSADA ACUMULADA	( $N''_x = 100 - N'_x$ )	100,0	100,0	100,0	100,0	100,0	99,16	83,88

FRACÇÃO PASSADA NO PENEIRO DE 2,00 mm ( nº 10 )							
NÚMERO DA PROVETA :	5	TEMP. MÉDIA DO ENSAIO, (°C) T=	20,8	PROV. SECO AO AR, $m_a =$	74,59		
NÚMERO DO DENSÍMETRO :	1	K = $30\mu / (980(\gamma_s - \gamma_w)^{0,5}) =$	0,01334	PROVETE SECO ( gf ) :			
CORRECÇÕES :		A = $(100/m_b)(\gamma_s / (\gamma_s - 1)) =$	2,1340	SEM PRÉ-TRATAMENTO, $m_b =$	74,59		
MENISCO, $C_M =$	0,0005	Nº da cápsula		COM PRÉ-TRATAMENTO, $m_b =$			
ANTIFLOCULANTE, $C_A =$	0,0025	Peso Solo humido, gf		PERDA NO PRÉ-TRATAMENTO ( gf ) , $n_p =$			
P. VOL. PART. SÓLIDAS, $\gamma_s =$	2,69	Peso Solo seco, gf		( % ) , $N_p =$			
		T. água w, (%)					

MASSA DA AMOSTRA SECA A ENSAIAR ( gf )							
				$m_b =$	<b>74,59</b>		
PENEIROS	nº20	nº40	nº60	nº80	nº140	nº200	
ABERTURA ( mm )	0,841	0,425	0,250	0,180	0,106	0,075	
MASSA RETIDA ( gf )	( $m_x$ )	10,31	6,06	4,41	2,82	4,68	2,77
% RETIDA	$n_x = (m_x/m_b) \times 100$	13,82	8,12	5,91	3,78	6,27	3,71
% RETIDA ACUMULADA	( $n'_x$ )	13,82	21,95	27,86	31,64	37,91	41,63
% PASSADA ACUMULADA	$n''_x = 100 - n'_x$	86,18	78,05	72,14	68,36	62,09	58,37
% PASSADA ACUM. TOTAL	$N''_x = n''_x (100 - N'_{10}) / 100$	72,3	65,5	60,5	57,3	52,1	49,0

FRACÇÃO PASSADA NO PENEIRO DE 75 µm - SEDIMENTAÇÃO											
TEMPO ( min. )	TEMPERATURA ( °C )	CORREC. DA TEMP. $C_T$	LEIT. NO DENSÍMET. $L_s$	$L_s + C_M - C_A + C_T$	$L_c$	Z ( cm )	Z / t	$D = K(Z/t)^{0,5}$	$B = 10^3(L_c - 1)$	A x B $n_b$ ( % )	$n_b(100 - N'_{10}) / 100$ $N_b$ ( % )
1	20,9	0,0000	1,0280	1,0260		9,105	9,105	0,0403	26,00	55,48	46,5
2	20,9	0,0000	1,0255	1,0235		9,782	4,891	0,0295	23,50	50,15	42,1
5	20,9	0,0000	1,0230	1,0210		10,458	2,092	0,0193	21,00	44,81	37,6
15	20,9	0,0000	1,0190	1,0170		11,541	0,769	0,0117	17,00	36,28	30,4
30	20,7	0,0000	1,0165	1,0145		12,217	0,407	0,0085	14,50	30,94	26,0
60	20,6	0,0000	1,0140	1,0120		12,894	0,215	0,0062	12,00	25,61	21,5
250	21,1	0,0002	1,0090	1,0072		14,247	0,057	0,0032	7,20	15,36	12,9
1440	20,8	0,0000	1,0047	1,0027		15,410	0,011	0,0014	2,70	5,76	4,8
2880	20,6	0,0000	1,0041	1,0021		15,573	0,005	0,0010	2,10	4,48	3,8

ENTIDADE:	OBRA:
ENSAIOU :	CALCULOU :
	VERIFICOU :



**LABORATÓRIO DE GEOTECNIA DA F.E.U.P.**

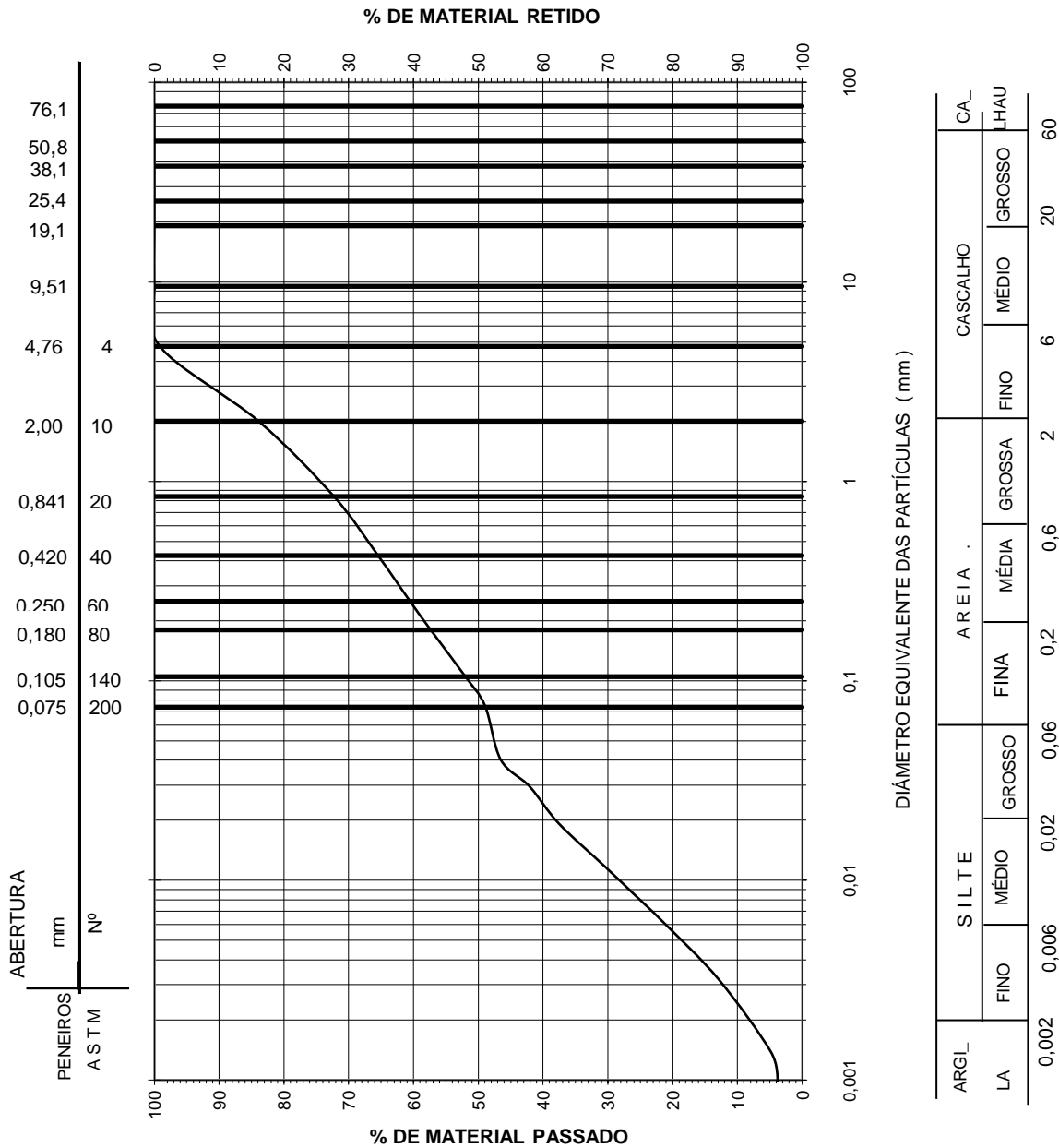
Rua Dr. Roberto Frias, s/n 4200-4654 Porto

Telef. : 225081988 - Fax: 225081446 - Web: <http://www.fe.up.pt/labgeo>

DATA  
02/03/15

**CURVA GRANULOMÉTRICA**

Amostra :  
Prof.:



ENTIDADE:

OBRA:

ENSAIOU :

CALCULOU :

VERIFICOU :



**LABORATÓRIO DE GEOTECNIA**  
**FACULDADE DE ENGENHARIA DA UNIVERSIDADE DO PORTO**  
Rua Dr. Roberto Frias, s/n 4200-465 Porto

Telef. : 225081988 - Fax: 225081446 - web : <http://www.fe.up.pt/labgeo>

DATA 02/03/2015	<b>PESO VOLUMICO DAS PARTÍCULAS SÓLIDAS</b> CEN ISO/TS 17892-3	Amostra: solo residual, amostra total (3m profundidade)
--------------------	---	---

**1-CALIBRAGEM**

t <sub>1</sub>	TEMPERATURA DE CALIBRAGEM DO PICNÓMETRO (° C)	26,0	25,9
m <sub>1</sub>	PESO DO PICNÓMETRO (gf)	55,74	55,91
m <sub>2</sub>	PESO DO PICNÓMETRO + ÁGUA DESTILADA (gf)	155,39	155,53

**2-DETERMINAÇÃO DO PESO VOLÚMICO**

-	NÚMERO DO PICNÓMETRO (gf)	18	20
m <sub>3</sub>	PICNÓMETRO + ÁGUA DESTILADA (gf)	163,77	155,63
m <sub>5</sub>	PICNÓMETRO + PROVETE +ÁGUA DESTILADA (gf)	173,79	174,07
-	NÚMERO DA CÁPSULA (gf)	18	20
A	PESO DA CÁPSULA (gf)	264,40	263,59
B	PESO DO PROVETE SECO + CÁPSULA (gf)	293,38	292,86
m <sub>4</sub> =B-A	PESO DO PROVETE SECO (gf)	28,98	29,27
tx	TEMPERATURA DO ENSAIO (° C)	21,7	22,0
K	RAZÃO ENTRE AS DENSIDADES DA ÁGUA À TEMPERATURA DO ENSAIO A 20° C	1,000	1,000
$\gamma_s = k \frac{m_4}{m_3 - (m_5 - m_4)} \cdot 981$	PESO VOLÚMICO DAS PARTÍCULAS (kN/m <sup>3</sup> )	14,99	26,51
MÉDIA DOS PESOS VOLÚMICOS DAS PARTÍCULAS (kN/m <sup>3</sup> )		20,8	

**Observações:**

ENTIDADE:		OBRA:	
ENSAIOU:	CALCULOU:	VERIFICOU:	



**LABORATÓRIO DE GEOTECNIA**  
**FACULDADE DE ENGENHARIA DA UNIVERSIDADE DO PORTO**  
Rua Dr. Roberto Frias, s/n 4200-465 Porto

Telef. : 225081988 - Fax: 225081446 - web : <http://www.fe.up.pt/labgeo>

DATA  
2/03/2015

**PESO VOLUMICO DAS PARTÍCULAS SÓLIDAS**  
CEN ISO/TS 17892-3

Amostra: Solo residual, passados  
peneiro #10 (3m profundidade)

**1-CALIBRAGEM**

t <sub>1</sub>	TEMPERATURA DE CALIBRAGEM DO PICNÓMETRO (° C)	26,3	26,1
m <sub>1</sub>	PESO DO PICNÓMETRO (gf)	55,97	54,45
m <sub>2</sub>	PESO DO PICNÓMETRO + ÁGUA DESTILADA (gf)	155,66	154,09

**2-DETERMINAÇÃO DO PESO VOLÚMICO**

-	NÚMERO DO PICNÓMETRO (gf)	17	19
m <sub>3</sub>	PICNÓMETRO + ÁGUA DESTILADA (gf)	155,79	154,21
m <sub>5</sub>	PICNÓMETRO + PROVETE +ÁGUA DESTILADA (gf)	174,12	174,14
-	NÚMERO DA CÁPSULA (gf)	17	19
A	PESO DA CÁPSULA (gf)	213,34	223,19
B	PESO DO PROVETE SECO + CÁPSULA (gf)	242,62	254,80
m <sub>4</sub> =B-A	PESO DO PROVETE SECO (gf)	29,28	31,61
tx	TEMPERATURA DO ENSAIO (° C)	21,0	21,1
K	RAZÃO ENTRE AS DENSIDADES DA ÁGUA À TEMPERATURA DO ENSAIO A 20° C	1,000	1,000
$\gamma_s = k \frac{m_4}{m_3 - (m_5 - m_4)} \cdot 981$	PESO VOLÚMICO DAS PARTÍCULAS (kN/m <sup>3</sup> )	26,23	26,55
MÉDIA DOS PESOS VOLÚMICOS DAS PARTÍCULAS (kN/m <sup>3</sup> )		26,4	

**Observações:**

ENTIDADE:		OBRA:	
ENSAIOU:	CALCULOU:	VERIFICOU:	